Delft Laminar Hump in vertical stabilizer design

D.D.P. van der Tuin

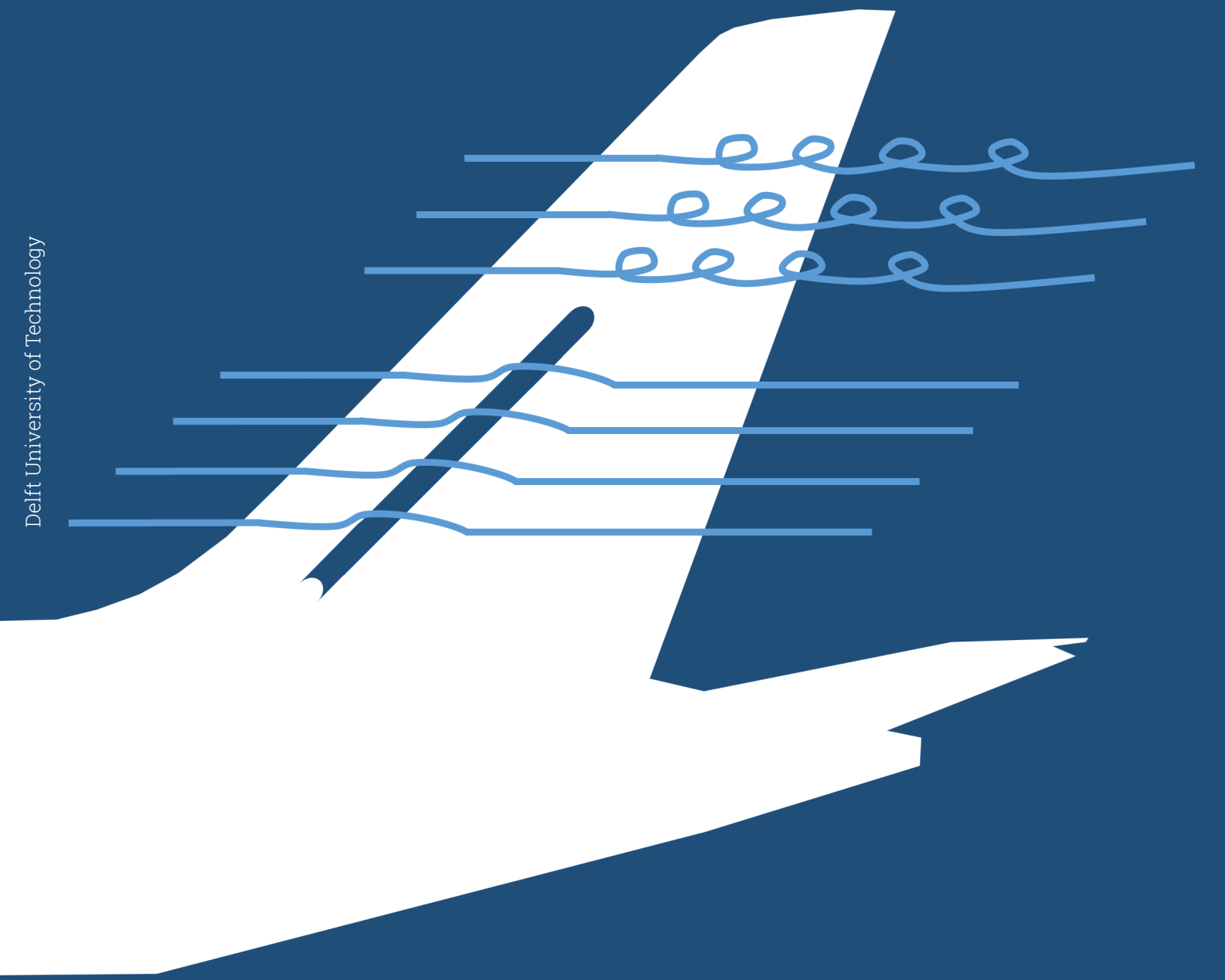

Delft University of Technology

TU Delft

Delft Laminar Hump in vertical stabilizer design

by

D.D.P. van der Tuin

To obtain the degree of Master of Science at the Delft University of Technology, to be defended publicly on March 24, 2025.

This report makes use of confidential information. In places where the information is confidential, this is indicated with 'CONFIDENTIAL', and the text/figure is censored.

Student Number:	4575806
Project Duration:	February 5, 2024 - March 24, 2025
Faculty:	Faculty of Aerospace Engineering, Delft
Thesis committee:	Dr.Ir. M.F.M. Hoogreef (TU Delft, Supervisor)
	Ir. M. Barahona Lopez (TU Delft, Supervisor)
	Prof.Dr.Ir. M. Kotsonis (TU Delft, Examiner)
	Prof.Dr.Ir. L.L.M. Veldhuis (TU Delft, Chair)

TU Delft Report Style, with modifications by D. Zwaneveld.

An electronic version of this thesis is available at `http://repository.tudelft.nl/`.

TU Delft

Abstract

The Delft Laminar Hump (DeLaH), discovered by the Aerodynamics Department of the Faculty of Aerospace Engineering at the Delft University of Technology, is a symmetrical smooth hump that is placed at a set distance parallel to the leading edge of the wing that reduces skin friction drag as it attenuates the growth of the crossflow instabilities (CFI). With the hump, transition can be delayed up to 14%. The only requirements are that the hump needs an natural laminar flow (NLF) airfoil and a condition where CFI is the dominant transition mechanism to be effective. Generally, CFI dominates when the wing sweep is greater than $30 - 35\ deg$, making the vertical stabilizer the best candidate for implementing the hump.

This research implements the Delft Laminar Hump on the vertical stabilizer of subsonic transport aircraft by modeling the effect of the hump as a shift in transition location. By using a Quasi-3D aerodynamic analysis in combination with a transition location database, the effect of the hump on the lift and drag coefficient of the vertical stabilizer is analyzed. The transition location database is constructed by using the external velocity of airfoil sections of the vertical tailplane and the boundary layer solver and stability analysis developed by the Group of Flow Control and Stability within the Delft University of Technology. With this, the N-factor curves along the chord can be calculated. Knowing the respective N-factors of the clean and hump configuration, the associated transition locations can be determined, which are then used to calculate the lift and drag coefficients of the vertical tailplane. To evaluate the aerodynamic effect of the hump on the full aircraft directional and lateral stability a stability analysis based on a method by Fokker / Obert is performed and checked against the CS-25 for Large Aeroplanes regulations by European Aviation Safety Authority (EASA).

It was found that the Delft Laminar Hump (DeLaH) on the vertical stabilizer of a subsonic transport aircraft does not affect the vertical tailplane lift curve slope, thus not affecting the stability of the aircraft. In contrast, the vertical tailplane drag coefficient is reduced by the hump. Retrofitting the hump on Airbus A320 (conventional tail) and the Fokker F-28 Mk1000 (T-tail) results in a reduction of the vertical tailplane drag coefficient of 6.73% and 8.72%, respectively. Translating this vertical tail drag reduction to the full aircraft drag coefficient results in a reduction of 0.17% and 0.34%. To evaluate the effect of the hump on weight and fuel consumption, additional weight and mission analyses are performed. Evaluating the harmonic range, an fuel reduction due to the hump of 0.16% and 0.32% is established, for the Airbus A320 and Fokker F-28 Mk1000, respectively. The aircraft weight is reduced by the same percentage through the fuel reduction, as it is assumed that the added weight due to the hump itself is negligible.

Additionally, two sensitivity analyses were performed, namely, sweep angle variation and surface area scaling to analyze the effectiveness of the hump for different vertical tailplane geometries. The effect of sweep angle on hump effectiveness does not affect the vertical tailplane lift curve slope and thus also not the stability coefficients. For the full aircraft drag coefficient, the hump effectiveness has an exponential relation with sweep angle and is most effective at lower sweep angles. A maximum full aircraft drag reduction was found of 0.41% at 30 deg sweep with an equivalent fuel reduction of 0.39%. Overall it is concluded that lower sweep angles are beneficial as the hump is most effective and results in reduced vertical tailplane weight, less fuel weight as well as an increased stability margin. Analyzing the effect of surface area scaling, the hump has no effect on the vertical tailplane lift curve slope regardless of surface area, again retaining the aircraft's stability. For the full aircraft drag coefficient, the hump effectiveness increases linearly for increasing surface area up to 0.37% at a surface scaling factor of 1.2 times the original vertical tailplane surface area. In terms of fuel reduction, a maximum value of 0.35% was found. There will be an optimal vertical tailplane surface area, since the hump effectiveness increases for increasing surface area, whilst for the full aircraft drag, vertical tailplane weight, and fuel weight a smaller surface area is preferred. The stability margin becomes the limiting factor as a minimum surface area is required for sufficient stability. Comparing the baseline aircraft, the hump is

more effective for the Fokker F-28 Mk1000 over the entire range of scaling factors and sweep angles. This leads to the suspicion that taper- and aspect ratio, and cruise speed play an important role in the effectiveness of the hump, but more research is required.

This research shows that the Delft Laminar Hump has a significant drag-reducing effect on the overall aircraft, whilst not affecting the aircraft's stability. Even though the fuel savings for an individual aircraft are not very large, on a fleet level this would be significant. The hump can be retrofitted on existing aircraft by gluing it on the outer skin, making it a relatively simple and cheap way to improve efficiency for aircraft manufacturers. Nevertheless, more research is required before implementing the hump on commercial aircraft as it is still unknown whether the hump also works on the suction side of the wing as well as whether the hump causes a shock at cruise Mach. Also, interaction effects with the horizontal stabilizer and fuselage need to be taken into account, to fully quantify the effectiveness of the hump. Dedicated wind tunnel experiments, flight tests, and/or CFD simulations are necessary.

Preface

With this research, my time at the Delft University of Technology comes to an end. After almost 9 years I completed my Bachelor in Mechanical Engineering and Master in Aerospace Engineering, but more importantly, I have met some incredible people along the way.

First, I would like to thank my supervisors Maurice Hoogreef and Marina Barahona Lopez for their time and expertise during this research. It has been a pleasure working with you.

My parents, who allowed me to study in the first place, for their emotional support throughout the years and during this project. It has not always been easy, but you were always there for me.

My brother, whom I consider to be my friend as well, for always looking on the bright side of things and always being interested in what I am up to.

All my friends, that I met during my time in Delft as well as the ones from before that time, for making my life a whole lot more fun and providing the opportunity to let me blow off some steam every once in a while.

Finally, the Delft University of Technology, for the hard but rewarding educational programs with all the incredible facilities, free to use for us as students.

D.D.P. van der Tuin
Delft, March 2025

Contents

List of Figures

List of Tables

Nomenclature

Symbols

Roman

A	Aspect ratio	$-$
$A_{i_{fan}}$	Fan inlet area	m^2
$A_{i_{primary}}$	Primary flow inlet area	m^2
A_{nz}	Nozzle area	m^2
$A_{nz_{fan}}$	Fan nozzle area	m^2
$A_{nz_{primary}}$	Primary flow nozzle area	m^2
$A_{_V}$	Vertical tailplane aspect ratio	$-$
$A_{_{V_{eff}}}$	Effective aspect ratio	$-$
$A_{_W}$	Wing aspect ratio	$-$
$b_{_{fl}}$	Wing flap span	m
$b_{_H}$	Horizontal tailplane span	m
B_p	Number of propeller blades	$-$
$b_{_V}$	Vertical tailplane span	m
$b_{_W}$	Wing span	m
C_1	Empirical taper ratio constant	$-$
$\left(C_{_{D_f}}\right)_{XFoil}$	Friction drag coefficient from XFoil	$-$
$\left(C_{_{D_p}}\right)_{NumSim}$	Pressure drag coefficient from numerical simulations	$-$
$\left(C_{_{D_p}}\right)_{XFoil}$	Pressure drag coefficient from XFoil	$-$
$\Delta\left(C_DS\right)_{as_{_{\delta_R}}}$	Drag area due to rudder deflection in asymmetric flight	m^2
$\Delta\left(C_DS\right)_{as_{_V}}$	Drag area due to asymmetric flight	m^2
$\Delta\left(C_DS\right)_{_{E_i}}$	Drag area due to inoperative engine	m^2
$\Delta\left(C_DS\right)_{prop}$	Drag area due to propeller	m^2
$\Delta\left(C_DS\right)_{wm}$	Drag area due to windmilling	m^2
$(C_{_D})_{total}$	Total drag coefficient	$-$
$(C_{_D})_{_V}$	Vertical tailplane drag coefficient	$-$
$(C_{_D})_{_{V,\alpha=0}}$	Vertical tailplane drag coefficient at $\alpha = 0$ (no sideslip)	$-$

$(C_D)_{V,off}$	Drag coefficient of aircraft without vertical tailplane	–
$\left((C_D)_V\right)_{original}$	Original vertical tailplane drag coefficient	–
c_f	Skin friction coefficient	–
c_{f_i}	Strip flap chord	m
c_i	Strip chord	m
C_{l_0}	Rolling moment coefficient when β, δ_R, and δ_a are set to zero	–
C_l	Rolling moment coefficient	–
C_{L_α}	Lift curve slope	deg^{-1}
$\left(C_{L_\alpha}\right)_V$	Vertical tailplane lift curve slope	deg^{-1}
$(C_{L_\alpha})_{V+df}$	Effective vertical tailplane lift curve slope including dorsal fin	deg^{-1}
C_{l_β}	Rolling-moment-due-to-sideslip derivative	deg^{-1}
$\left(\Delta C_{l_\beta}\right)_\Gamma$	Contribution to rolling-moment-due-to-sideslip derivative due to wing dihedral	deg^{-1}
$\left(C_{l_\beta}\right)_H$	Horizontal tailplane rolling-moment-due-to-sideslip derivative	deg^{-1}
$\left(C_{l_\beta}\right)_{T-O}$	Tail-off rolling-moment-due-to-sideslip derivative	deg^{-1}
$\left(C_{l_\beta}\right)_{T-O,C_L=0}$	Tail-off rolling-moment-due-to-sideslip derivative at zero lift coefficient	deg^{-1}
$\left(C_{l_\beta}\right)_V$	Vertical tailplane rolling-moment-due-to-sideslip derivative	deg^{-1}
$C_{l_{\delta_a}}$	Rolling-moment-due-to-aileron-deflection derivative	deg^{-1}
$\frac{c_{l_\delta}}{c_{l_\alpha}}$	Rudder control effectiveness	–
$\left(\frac{\partial C_L}{\partial \delta_f}\right)_i$	Strip lift coefficient due to aileron deflection	deg^{-1}
$\left(\frac{\partial C_l}{\partial \delta_f}\right)_i$	Strip lift coefficient due to aileron deflection at strip MAC	deg^{-1}
$(C_l)_{\delta_R}$	Rolling-moment-due-to-rudder-deflection coefficient	–
$C_{l_{\delta_R}}$	Rolling-moment-due-to-rudder-deflection derivative	deg^{-1}
$\left(C_{L_{\delta_R}}\right)_V$	Vertical tailplane lift coefficient due to rudder deflection	deg^{-1}
$C_{L_{des}}$	Design lift coefficient	–
$C_{L_{max_{1-g}}}$	Maximum lift coefficient at 1-g load factor	–
$C_{L_{max}}$	Maximum lift coefficient	–
$(C_{l_{max}})_{\delta_R}$	Maximum rolling-moment-due-to-rudder-deflection coefficient	–
$(C_L)_{T-O}$	Tail-off lift coefficient	–

$(C_l)_V$	Vertical tailplane rolling moment coefficient	$-$
C_{L_W}	Wing/tail-off lift coefficient ($\frac{L}{qS_W}$)	$-$
C_{n_0}	Yawing moment coefficient when β, δ_R, and δ_a are set to zero	$-$
C_n	Yawing moment coefficient	$-$
C_{n_β}	Yawing-moment-due-to-sideslip derivative	deg^{-1}
$\left(\Delta C_{n_\beta}\right)_{fl}$	Contribution to yawing-moment-due-to-sideslip derivative due to flap deflection	deg^{-1}
$\left(C_{n_\beta}\right)_{T-O}$	Tail-off yawing-moment-due-to-sideslip derivative	deg^{-1}
$\left(C_{n_\beta}\right)_V$	Vertical tailplane yawing-moment-due-to-sideslip derivative	deg^{-1}
$C_{n_{\delta_a}}$	Yawing-moment-due-to-aileron-deflection derivative	deg^{-1}
$(C_n)_{\delta_R}$	Yawing-moment-due-to-rudder-deflection coefficient	$-$
$C_{n_{\delta_R}}$	Yawing-moment-due-to-rudder-deflection derivative	deg^{-1}
$(C_{n_{max}})_{\delta_R}$	Maximum yawing-moment-due-to-rudder-deflection coefficient	$-$
$(C_n)_{OEI}$	Yawing moment coefficient due to one engine inoperative	$-$
$(C_n)_V$	Vertical tailplane yawing moment coefficient	$-$
c_R	Rudder chord	m
$0\%c_{r_V}$	Longitudinal position of 0%-point of vertical tailplane root chord	m
c_{r_V}	Vertical tailplane root chord	m
c_{r_W}	Wing root chord	m
c_{t_V}	Vertical tailplane tip chord	m
c_V	Vertical tailplane chord	m
$\bar{c}_V$	Vertical tailplane mean aerodynamic chord	m
$^1/_4\bar{c}_V$	Vertical tailplane quarter mean aerodynamic chord	m
c_W	Wing chord	m
$\bar{c}_W$	Wing mean aerodynamic chord	m
C_{y_0}	Side force coefficient when β, δ_R, and δ_a are set to zero	$-$
C_y	Side force coefficient	$-$
C_{y_β}	Side-force-due-to-sideslip derivative	deg^{-1}
$\left(\Delta C_{y_\beta}\right)_{fl}$	Contribution to side-force-due-to-sideslip derivative due to flap deflection	deg^{-1}
$\left(C_{y_\beta}\right)_{T-O}$	Tail-off side-force-due-to-sideslip derivative	deg^{-1}
$\left(C_{y_\beta}\right)_V$	Vertical tailplane side-force-due-to-sideslip derivative	deg^{-1}

$C_{y_{\delta_a}}$	Side-force-due-to-aileron-deflection derivative	deg^{-1}
$(C_y)_{\delta_R}$	Side-force-due-to-rudder-deflection coefficient	$-$
$C_{y_{\delta_R}}$	Side-force-due-to-rudder-deflection derivative	deg^{-1}
C_{y_ϕ}	Yawing-moment-due-to-bank-angle derivative	deg^{-1}
$(C_y)_{bank}$	Side force coefficient due to bank angle	$-$
$(C_{y_{max}})_{\delta_R}$	Maximum side-force-due-to-rudder-deflection coefficient	$-$
$(C_y)_V$	Vertical tailplane side force coefficient	$-$
D	Drag or diameter	N *or* m
d_D	DRE nominal diameter	mm
ΔD_{E_i}	Difference in drag of the inoperative and operative engine	N
D_f	Skin friction drag	N
D_{fus}	Fuselage diameter	m
$D_{fus_{max}}$	Maximum fuselage diameter	m
D_i	Engine inlet diameter	m
D_p	Pressure drag	N
D_p	Propeller diameter	m
D_V	Fuselage height at vertical tailplane quarter mean aerodynamic chord	m
d_V	Fuselage height at vertical tailplane quarter mean aerodynamic chord	m
g	Gravitational constant	m/s^2
h_1	Height of fuselage at $0.25l_B$	m
h_2	Height of fuselage at $0.75l_B$	m
h	Average height of fuselage at the wing root chord	m
h_R	Rudder height	m
h_W	Wing root height relative to fuselage center line ($h_W = -z_W$)	m
i_H	Horizontal tailplane incidence angle	deg
i_V	Vertical tailplane incidence angle	deg
K_σ	Factor for drag due to asymmetric flight	$-$
K_{as}	Factor for drag due to asymmetric flight	$-$
k_D	DRE numerical height	μm
K_{f_i}	Empirical correction factor to adjust for larger flap deflections of a strip	$-$
K_{FV}	Fuselage-vertical-tailplane lift carry-over effect	$-$
K_i	Wing-body interference factor for wing-body sideslip derivative C_{y_β}	$-$

K_{M_Γ}	Compressibility correction factor to uniform-geometric-dihedral-effect	$-$
K_N	Empirical factor related to sideslip derivative C_{n_β} for body + wing-body interference	$-$
K_{R_l}	Reynolds number correction factor	$-$
k_V	Correction factor for the tailplane configuration	$-$
K_{VH}	Horizontal-to-vertical tailplane endplate effect	$-$
L	Lift or rolling moment	$N\ or\ Nm$
l_B	Fuselage length	m
$(L)_V$	Vertical tailplane rolling moment	Nm
$l_{x_{S_V}}$	Vertical tailplane yawing moment arm in stability frame	m
l_{x_V}	Vertical tailplane yawing moment arm in body frame	m
$l_{x_{V_{ref}}}$	Exposed vertical tailplane yawing moment arm in body frame	m
$l_{x_{V+df}}$	Effective vertical tailplane yawing moment arm including dorsal fin in body frame	m
l_{y_E}	Engine yawing moment arm	m
$l_{z_{S_V}}$	Vertical tailplane rolling moment arm in stability frame	m
l_{z_V}	Vertical tailplane rolling moment arm in body frame	m
$l_{z_{V_{ref}}}$	Exposed vertical tailplane rolling moment arm in body frame	m
M	Mach number	$-$
$MTOW$	Maximum take-off weight	kg
ΔN	Change in N-factor (amplification factor) due to hump	$-$
N	Yawing moment or N-factor (amplification factor)	$Nm\ or -$
N_{clean}	Clean (no hump) N-factor (amplification factor)	$-$
$(N)_{E_i}$	Yawing moment due to difference in drag of the inoperative and operative engine	Nm
$(N)_{E_o}$	Yawing moment due to difference in thrust of the inoperative and operative engine	Nm
N_{hump}	Hump N-factor (amplification factor)	$-$
$(n_{nac})_F$	Number of fuselage-mounted nacelles	$-$
$(n_{nac})_W$	Number of wing-mounted nacelles	$-$
$(N)_{OEI}$	Yawing moment due to one engine inoperative	Nm
$(N)_V$	Vertical tailplane yawing moment	Nm
n_{zw}	Load factor normal to the flight path at $V_{C_{L^{MAX}}}$	$-$
q	Free-stream dynamic pressure	Pa

q_∞	Free-stream dynamic pressure	Pa
q_H	Horizontal tailplane average dynamic pressure	Pa
q_V	Vertical tailplane average dynamic pressure	Pa
R	Range	m
Re	Reynolds number	$-$
Re_{cr}	Critical Reynolds number	$-$
$Re_{l_{fuselage}}$	Fuselage Reynolds number	$-$
S_{B_S}	Body side area	m^2
S_{df}	Dorsal fin surface area	m^2
$S_{fus.cross}$	Maximum fuselage cross section	m^2
S_H	Horizontal tailplane surface area	m^2
S_i	Strip surface area	m^2
S_R	Rudder surface area	m^2
S_V	Vertical tailplane surface area	m^2
$(S_V)_{original}$	Original vertical tailplane surface area	m^2
S_{V_R}	Part of vertical tailplane surface area affected by rudder	m^2
$S_{V_{ref}}$	Exposed vertical tailplane surface area	m^2
S_W	Wing surface area	m^2
T	Thrust	N
t	Airfoil thickness	m
$\left(\frac{t}{c}\right)_{W,a}$	Thickness-to-chord ratio wing at aileron	$-$
ΔT_{E_o}	Difference in thrust of the inoperative and operative engine	N
$\Delta T_{E_o+wm+prop}$	Difference in thrust of the inoperative and operative engine plus drag due to windmilling and propeller	N
t_i	Strip airfoil thickness	m
$TSFC$	Thrust specific fuel consumption	$kg/(Ns)$
u_e	Velocity at outer edge of boundary layer	m/s
$V_2 + xx$	Airspeed approved for all-engines operating initial climb	m/s
V	Airspeed	m/s
V_∞	Free-stream velocity	m/s
V_C	Design cruise speed	m/s
$V_{C_{L^{MAX}}}$	Calibrated airspeed at the moment that the load factor-corrected lift coefficient is at the maximum	m/s
V_{CW}	Crosswind speed	m/s
V_D	Design dive speed	m/s

V_{FC}/M_{FC}	Maximum speed for stability characteristics dependent on Mach number with flaps and landing gear retracted	m/s
V_{FE}	Maximum flap extended speed	m/s
V_{LE}	Landing gear extended speed	m/s
V_{MO}/M_{MO}	Maximum operating speed limit dependent on Mach number	m/s
V_{nz}	Flow velocity at engine nozzle exit	m/s
V_{REF}	Reference landing speed	m/s
V_{SR0}	Reference landing stall speed	m/s
V_{SR1}	Reference stall speed at given condition	m/s
V_{SR}	Reference stall speed	m/s
$\bar{V}_V$	Vertical tailplane volume coefficient	$-$
W	Gross weight	N
w	Maximum body width (equal to $D_{fus_{max}}$ if fuselage is perfectly cylindrical)	m
W_{end}	Weight at end	N
W_{fuel}	Fuel weight	N
W_{start}	Weight at start	N
W_V	Vertical tailplane weight	kg
x	X-axis in body frame	$-$
Δx_{ac_V}	Horizontal displacement of the vertical tailplane aerodynamic center	m
x_{ac_V}	Distance from fuselage nose to vertical tailplane aerodynamic center including dorsal fin	m
x_{cr}	Transition location	m
x_D	DRE distance from leading edge in normal-to-leading-edge direction	m
x_E	X-axis in vehicle carried normal Earth frame	$-$
x_{exh}	Longitudinal position of the engine exhaust	m
x_H	Longitudinal position of horizontal tailplane (distance between leading edge vertical tail at height of horizontal tail and aerodynamic center horizontal tail)	m
x_m	Longitudinal distance nose to C.G.	m
x_S	X-axis in stability frame	$-$
(x_{tr}/c)	Transition location normalized by chord	$-$
$(x_{tr}/c)_{clean}$	Clean (no hump) transition location normalized by chord	$-$
$(x_{tr}/c)_{hump}$	Hump transition location normalized by chord	$-$
y^*	Spanwise position of the centroid of span loading as a fraction of the semi-span	$-$
Y	Side force	N

y	Y-axis in body frame	$-$
$(Y)_{bank}$	Side force due bank angle	N
$y_{_E}$	Y-axis in vehicle carried normal Earth frame	$-$
Y_i	Strip moment arm	m
$y_{_S}$	Y-axis in stability frame	$-$
$(Y)_{_V}$	Vertical tailplane side force	N
$\bar{y}_{_W}$	Spanwise location wing mean aerodynamic chord	m
z	Z-axis in body frame	$-$
$z_{cl,nac}$	Vertical position of the nacelle center line	m
$z_{_E}$	Z-axis in vehicle carried normal Earth frame	$-$
$z_{_H}$	Vertical position of horizontal tailplane	m
$z_{_R}$	Vertical position of rudder	m
$z_{_S}$	Z-axis in stability frame	$-$
$\bar{z}_{_V}$	Spanwise location vertical tailplane mean aerodynamic chord	m
$z_{_W}$	Wing root height relative to fuselage center line ($z_{_W} = -h_{_W}$)	m

Greek

α_0	Zero-lift angle of attack	deg
α	Angle of attack	deg
$\frac{\Delta\alpha_0}{\Delta\delta}$	Rudder control effectiveness	$-$
$\alpha_{_{C_{L_{max}}}}$	Stall angle of attack	deg
$\alpha^*_{_H}$	Horizontal tailplane zero-lift angle of attack relative to tailplane reference plane	deg
$\alpha_{_H}$	Effective horizontal tailplane angle of attack	deg
$\alpha_{_R}$	Angle of attack relative to a reference line, usually the fuselage centerline (note that R does not refer to the rudder in this case)	deg
$\alpha_{_V}$	Effective vertical tailplane angle of attack	deg
β	Sideslip angle	deg
$\beta_{CWL,FRS}$	Sideslip angle full rudder sideslips	deg
$\beta_{CWL,SSS}$	Sideslip angle crosswind landing for steady, straight sideslips	deg
β_{OEI}	Sideslip angle one engine inoperative	deg
δ_{99}	99% boundary layer thickness	m
$\Delta\alpha_{_{0L}}$	Change in zero-lift angle of attack	deg
$\frac{\delta\sigma}{\delta\beta}$	Sidewash-angle-to-sideslip-angle ratio	$-$
$\left(\Delta\frac{\delta\sigma}{\delta\beta}\right)_{\Gamma}$	Effect of wing dihedral on the sidewash-angle-to-sideslip-angle ratio	$-$

$\left(\Delta\frac{\delta\sigma}{\delta\beta}\right)_{C_{l_\beta}}$	Effect of rolling-moment-due-to-sideslip on the sidewash-angle-to-sideslip-angle ratio	–
$\left(\Delta\frac{\delta\sigma}{\delta\beta}\right)_{fl}$	Effect of wing flap deflection on the sidewash-angle-to-sideslip-angle ratio	–
$\left(\Delta\frac{\delta\sigma}{\delta\beta}\right)_{fl,ldg}$	Effect of wing flap deflection in the landing position on the sidewash-angle-to-sideslip-angle ratio	–
$\left(\frac{\delta\sigma}{\delta\beta}\right)_{FV}$	Fuselage-vertical-tailplane interference factor	–
$\left(\Delta\frac{\delta\sigma}{\delta\beta}\right)_{h_W}$	Effect of relative wing height on the fuselage on the sidewash-angle-to-sideslip-angle ratio	–
$\left(\Delta\frac{\delta\sigma}{\delta\beta}\right)_{NF}$	Effect of rear-fuselage engine nacelles on the sidewash-angle-to-sideslip-angle ratio	–
$\left(\Delta\frac{\delta\sigma}{\delta\beta}\right)_{NW}$	Effect of engine nacelles on the wing on the sidewash-angle-to-sideslip-angle ratio	–
$\frac{d\sigma_V}{dC_L}$	Vertical tailplane sidewash angle to lift coefficient ratio	deg
δ_a	Aileron deflection angle	deg
$\delta_{a_{max}}$	Maximum aileron deflection angle	deg
δ_{f_i}	Strip flap deflection angle	deg
$\delta_{fl,2}$	Flap deflection angle of most aft flap of double-hinged flap	deg
δ_{fl}	Flap deflection angle	deg
δ_R	Rudder deflection angle	deg
$\delta_{R_{max}}$	Maximum rudder deflection angle	deg
δ_{sl}	Slat deflection angle	deg
$\left(\frac{\partial u}{\partial y}\right)_w$	Velocity gradient at the wall	
ϵ	Downwash angle	deg
γ	Flight path angle	deg
Γ_H	Horizontal tailplane dihedral angle	deg
Γ_V	Vertical tailplane dihedral angle	deg
Γ_W	Wing dihedral angle	deg
Λ	Sweep angle	deg
λ	Taper ratio	–
$\Lambda_{1/4c}$	Quarter-chord sweep angle	deg
$\Lambda_{1/2c_V}$	Vertical tailplane semi-chord sweep angle	deg
$\Lambda_{1/4c_V}$	Vertical tailplane quarter-chord sweep angle	deg
$\Lambda_{1/4c_W}$	Wing quarter-chord sweep angle	deg

Λ_{hl_i}	Strip hinge line sweep angle	deg
Λ_{HL}	Hinge line sweep angle	deg
Λ_{LE}	Leading edge sweep angle	deg
Λ_{TE}	Trailing edge sweep angle	deg
λ_V	Vertical tailplane taper ratio	$-$
λ_W	Wing taper ratio	$-$
$\lambda_{z,D}$	Wavelength of DRE parallel to leading edge	mm
μ	Dynamic viscosity	$Pa \cdot s$
μ_∞	Dynamic viscosity of the free-stream	$Pa \cdot s$
ϕ	Bank angle	deg
ϕ_{max}	Maximum bank angle	deg
ρ_∞	Density of the free-stream	kg/m^3
ρ_e	Density at outer edge of the boundary layer	kg/m^3
σ	Sidewash angle	deg
σ_V	Vertical tailplane sidewash angle	deg
τ	Shear stress	Pa
τ_w	Shear stress at the wall	Pa

Subscripts

∞	Free-stream
a	Aileron
as	Asymmetric flight
D	DRE
df	Dorsal fin
E	Vehicle carried normal Earth frame
e	Outer edge of the boundary layer
E_i	Inoperative engine
E_o	Operative engine
F, fus	Fuselage
fl	Flap
H	Horizontal tailplane
HL	Hinge line
i	Engine inlet or i-th strip in strip method
LE	Leading edge
N	Nacelle

nz	Nozzle
OEI	One engine inoperative
$prop$	Propeller
R	Rudder
r	Root
S	Stability frame
sl	Slat
$T-O$	Tail-off
t	Tip
TE	Trailing edge
V	Vertical tailplane
W	Wing
w	Wall
WFN	Wing, fuselage, and nacelles
wm	Windmilling

Abbreviations

3E	Energy, Economy, Environment
ALT	attachment line transition
ALTTA	Application of Hybrid Laminar Flow Technology on Transport Aircraft
AVL	Athena Vortex Lattice
BLADE	Breakthrough Laminar Demonstrator in Europe
CG	center of gravity
CFI	crossflow instabilities
DBD	dielectric barrier discharge
DeLaH	Delft Laminar Hump
DRE	discrete roughness element
EASA	European Aviation Safety Authority
ELFIN	European Laminar Flow Investigation
ESDU	Engineering Sciences Data Unit (refers to ESDU 82010 [1])
HLFC	hybrid laminar flow control
HYLDA	Hybrid Laminar Flow Demonstration on Aircraft
ICAO	International Civil Aviation Organization
ILR	Institute of Aerospace Systems
KPI	key performance indicator
LATEC	Laminar Technology
LFC	laminar flow control
LTAG	long-term aspirational goal
MAC	mean aerodynamic chord
MTOW	maximum take-off weight
MZFW	maximum zero fuel weight
NLF	natural laminar flow
OEI	one engine inoperative
OEW	operational empty weight
RANS	Reynolds-averaged Navier-Stokes
TSFC	thrust specific fuel consumption
TSI	Tollmien Schlichting instabilities
USAF DATCOM	United States Air Force Data Compendium (refers to USAF Stability and Control DATCOM [2])
VeDSC	Vertical tail Design, Stability, and Control (refers to method by Nicolosi et al. [3])
VLM	vortex lattice method

1

Introduction

Ever since the start of aviation aircraft have become more and more energy efficient. Now, with the current climate crisis in full swing, even more effort is put into making aircraft more sustainable. Following the Paris Climate Agreement [4], the International Civil Aviation Organization (ICAO) drafted Resolution A41-21 [5] which includes the long-term aspirational goal (LTAG) for international civil aviation CO2 emission reductions [6]. The LTAG for international civil aviation is net-zero carbon emissions by 2050.

One of the areas of focus is to make improvements in the aerodynamic design of aircraft. For subsonic transport aircraft, friction drag is responsible for about half of the total drag [7][8]. It would therefore make sense to try to reduce this friction drag component, which can be established by delaying the transition from laminar to turbulent flow. This can be obtained by using laminar flow control (LFC). LFC is an umbrella term for systems that change the boundary layer flow in such a way that transition from laminar to turbulent flow is delayed. This includes the passive flow control, known as NLF, which uses geometry, active flow control (LFC), which uses active methods such as suction or cooling, and hybrid laminar flow control (HLFC), which uses a combination of the passive and active flow control strategies. The general idea for LFC already stems from the 1930s and various systems and configurations have been tested on aircraft throughout the 20th century as described by Braslow [9] and Joslin [10]. However, they have never been widely implemented in subsonic transport aircraft, often because these systems were too large, heavy, or complex.

In 2021, Rius-Vidales and Kotsonis discovered that a forward-facing step of a certain height can delay transition [11]. This phenomenon was developed into the DeLaH[1], by the Aerodynamics Department of the Faculty of Aerospace Engineering at the Delft University of Technology. The DeLaH is a symmetrical smooth hump that is placed at a set distance parallel to the leading edge of the wing that reduces skin friction drag as it attenuates the growth of crossflow instabilities (CFI). With the hump, transition can be delayed up to 14%. The effectiveness of the hump is dependent on the hump height, width, chordwise location, and perturbation amplitude of the CFI. Currently, the hump is still being investigated by a research group led by Prof. M. Kotsonis.

With this recent development, the time might have come to integrate a LFC device into commercial aircraft. The DeLaH can be (retro)fitted by gluing it on an aircraft wing. This makes it a very simple and cost-effective solution compared to HLFC systems. However, there is very limited knowledge of how such a device affects the aircraft's conceptual design and performance in terms of weight and drag. Moreover, when retrofitting the DeLaH on an existing aircraft, the aerodynamic behavior of the aircraft will change and potentially impact the overall geometry required to meet the lifting, stabilizing, and controlling requirements.

[1] Delft University of Technology. (2023). ERC Proof of Concept grant for the Delft Laminar Hump. Retrieved January 27, 2024, from https://www.tudelft.nl/en/2023/lr/erc-proof-of-concept-grant-for-the-delft-laminar-hump

1.1. Research objective

This research will look into the impact of the Delft Laminar Hump, implemented on the vertical stabilizer on conceptual subsonic transport aircraft design and performance in terms of weight and drag. As the DeLaH attenuates the growth of the CFI, it requires a condition where CFI is the dominant transition mechanism to be effective. CFI dominate when the wing sweep is greater than $30 - 35\,deg$ [12]. Therefore, the vertical stabilizer is chosen as the sweep angle generally lies in this range (see Table 2.1), whilst the main wing and horizontal stabilizer often have lower sweep angles, making them less suitable. Another reason to investigate the vertical stabilizer is relative geometric simplicity since it must be able to provide a side force in both directions and therefore it is symmetrical. The available data on the DeLaH also uses a symmetric airfoil. Moreover, the vertical stabilizer is relatively small compared to other components suitable for LFC, such as the main wing, reducing computational time and resources.

Constraints and assumptions

To simplify the research problem and to tighten the scope, there are several constraints and assumptions:

- Only subsonic transport aircraft are considered, with a cruise velocity of up to Mach 0.8.
- Only jet/turbofan aircraft are considered, therefore no asymmetric flow profiles due to propellers are present. Thus it may be assumed that the vertical tailplane incidence angle (or mounting angle) $i_v = 0$ and only symmetric airfoil shapes are used.
- Only conventional empennage layouts are used, namely fuselage- or fin-mounted designs (including T-tails). V-tails, twin vertical tails, or other unconventional designs are not considered.
- The DeLaH is implemented on both sides of the vertical stabilizer.
- For LFC to be useful it is required that there is laminar flow at the vertical tail. Therefore only cruise conditions will be considered in the performance evaluation. High lift conditions (landing and take-off) will not be considered, because in that case there is a lot of induced drag, making the skin-fiction drag reduction due to LFC at the vertical tail negligible. The same holds for unfavorable weather conditions.

Research areas

Based on the research objective, the main research areas are vertical tail design, laminar flow control, and subsonic transport aircraft performance, which are shown in Figure 1.1. Where all the research areas overlap the main research objective (1+2+3) is found.

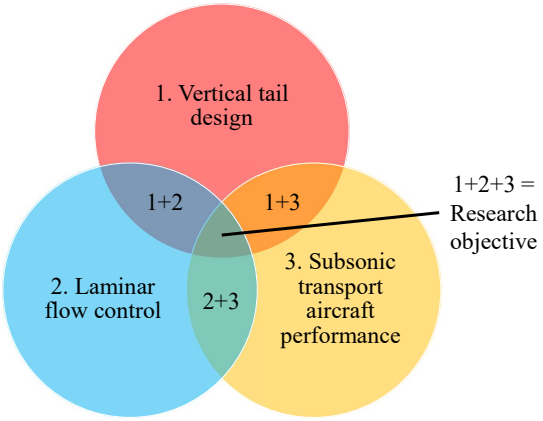

Figure 1.1: Research areas.

Main research question

From this diagram and research objective, the main research question follows. The main research question is phrased as follows:

- *What is the impact of the Delft Laminar Hump, implemented on the vertical stabilizer, on conceptual subsonic transport aircraft design and performance in terms of weight and drag?*

Sub-questions

To answer the main question, the three research areas, and their overlap are used to formulate sub-questions, each contributing to the answer to the main research question. The numbers in Figure 1.1 are also indicated at each corresponding sub-question.

TECHNICAL BACKGROUND

[1] - Vertical tail design:
- *How are vertical stabilizers typically parameterized?*

[1+3] - Vertical tail integration in subsonic transport aircraft:
- *How are vertical stabilizers designed and integrated into the full aircraft?*
- *What are the critical design requirements (geometry and aerodynamic performance) for vertical stabilizers?*

[2] - Laminar flow control:
- *What is LFC/DeLaH and how does it work?*

RESEARCH

[1+2] - Laminar flow control integration in vertical tail:
- *How can the aerodynamics of the LFC/DeLaH implemented on a vertical stabilizer be modeled?*
- *How does the vertical tail design affect the aerodynamic impact of LFC/DeLaH?*

[3] - Subsonic transport aircraft performance:
- *What are the typical flight missions and conditions, that subsonic transport aircraft are tested for?*

[2+3] - Laminar flow control integration in subsonic transport aircraft:
- *What metrics are used to assess the impact of LFC/DeLaH on aircraft performance (drag reduction, mass penalties, fuel/emission reduction)?*

1.2. General method and report layout

Based on the sub-questions a general method is proposed in Figure 1.2.

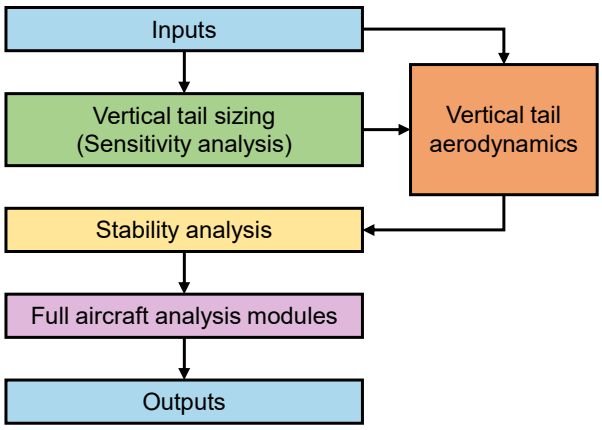

Figure 1.2: General overview of method.

The key idea behind this method is that DeLaH is implemented on a vertical tailplane by modeling the aerodynamic effect of the hump as a shift in transition location. Starting with the vertical tail sizing, the geometry of the vertical tailplane is parametrized. With the parametrization known, the vertical tail aerodynamics can be analyzed. This is done with the use of a Quasi-3D analysis (Q3D) and an aero-

dynamic database, which provides the shift in transition location due to the hump. To analyze whether the vertical tailplane with the hump still provides sufficient stability and control when implemented on the full aircraft, a stability analysis is performed and the critical design requirements are checked. The stability analysis is connected to the vertical tail aerodynamics through the vertical tailplane lift curve slope. After the stability analysis, the impact of the hump on the full aircraft is assessed with full aircraft analysis modules, namely a weight-, mission- and drag analysis. Finally, to see what the effect of the vertical tailplane geometry on the effectiveness of the hump is, a sensitivity analysis is performed. Specific geometry variables are varied and the effectiveness of the hump in terms of the full aircraft performance is studied.

The report is divided into two main parts: the technical background and the research. The technical background provides the work done during the literature study and forms the basis for the research. The technical background starts with the vertical stabilizer parametrization, stability analysis, and critical design requirements, presented in chapter 2. Next, chapter 3 discusses LFC aerodynamics as well as the different types of LFC, and wind tunnel and flight tests performed in previous research. This puts the DeLaH into context of research on other LFC devices. The research part starts with the methodology in chapter 4, which is a much more elaborate and in-depth version of the general method provided here. This is where the actual integration of the DeLaH into a vertical stabilizer is discussed. In essence, it connects the vertical tail sizing and stability analysis, provided in the technical background, with the vertical tail aerodynamics. Next to the vertical tail aerodynamic analysis, the full aircraft analysis modules are discussed in this chapter, as well as the main test cases and the sensitivity analysis. Next, in chapter 5, the various intermediate steps of the methodology are verified and validated. Thereafter, the results of the baseline cases and sensitivity analysis are presented in chapter 6. Finally, chapter 7 provides the conclusion, discussion, and future work.

TECHNICAL BACKGROUND

2

Vertical stabilizer parametric design

In this chapter, the vertical stabilizer will be discussed by exploring its purposes and types in section 2.1 and the general parametrization in section 2.2. In section 2.3 the most common methods for stability analysis are compared, followed by section 2.4 that discusses the reference frames and main derivatives for the stability analysis. Subsequently, section 2.5 presents the chosen stability analysis method in detail. Finally, the critical design requirements of vertical stabilizers are investigated in section 2.6.

2.1. Vertical stabilizer purpose and types

2.1.1. Vertical stabilizer purpose

The vertical stabilizer has several purposes. First, the vertical stabilizer provides stability for the aircraft, both static and dynamic. Static stability is the tendency of the aircraft to return to its initial equilibrium after a disturbance. In contrast, dynamic stability is the damping of the transient motion of the aircraft regaining (a new) equilibrium after a disturbance [13]. Since there are three axes of rotation, there are also three types of stability: lateral, longitudinal, and directional. For the vertical stabilizer, directional and lateral stability are the ones of interest. Second, the vertical stabilizer provides control over the aircraft. This control is provided by the rudder, which is part of the vertical stabilizer. Third, the vertical stabilizer creates a state of equilibrium in different conditions of flight [14][15][16].

The purpose of the rudder can be defined in more detail. First, it helps to create a steady state of equilibrium with or without a control force. Second, it facilitates the maneuvering of the aircraft. Third, it helps to correct for perturbations, keeping the aircraft on course [14][17].

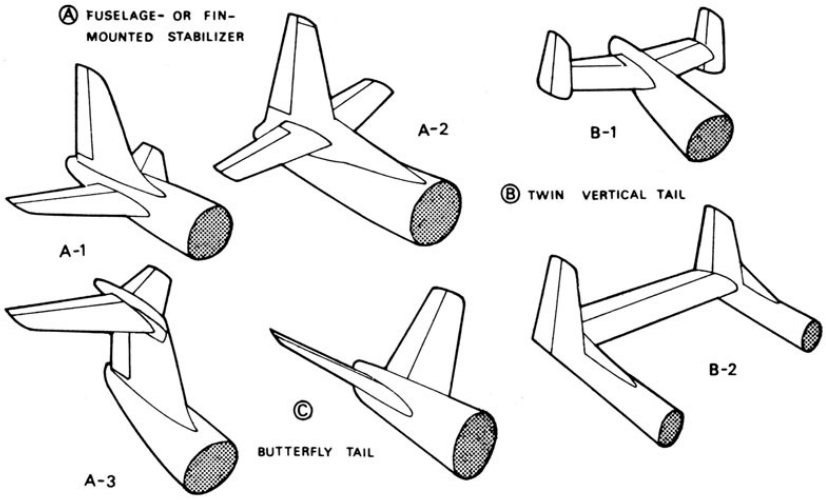

Figure 2.1: Tailplane types [15].

2.1.2. Vertical stabilizer types

There are three main types of tailplanes, namely the fuselage- or fin-mounted stabilizer, twin vertical tail, and butterfly tail. Figure 2.1 shows several examples of each type. Fuselage- or fin-mounted stabilizers are the most common, especially in subsonic transport aircraft. This is the most simple design regarding structural design. A special case of the fin-mounted stabilizer is the T-tail (A-3 in Figure 2.1). Twin vertical tails are often used when the vertical tail fins must be relatively small, to prevent a too large rolling moment as a result of the use of the rudder. Butterfly tails are a more complex configuration, as they double as an elevator and rudder at the same time, making the control system also more complex. This configuration is therefore less common [15]. There are even more types of vertical tails comprehensively described by Raymer [16], but these are far outside the scope of this research.

2.2. Parametrization of vertical stabilizers

First, the parametrization will be provided in subsection 2.2.1. Subsequently, in subsection 2.2.2, the design range for the parameters is provided. The design range contains the acceptable values for the various parameters that are used in the sizing of the vertical stabilizers.

2.2.1. Parametrization

For the parametrization of the vertical stabilizer, the definitions of Obert [14] are used. A visualization of the parametrization is shown in Figure 2.2 (its positioning relative to the fuselage can be seen in Figure 2.3). The vertical tailplane planform is simply defined as any other wing or fin. It can be described by a vertical tailplane root chord c_{r_V}, vertical tailplane span b_V, vertical tailplane taper ratio λ_V (defined in Equation 2.1), and vertical tailplane quarter-chord sweep angle $\Lambda_{1/4c_V}$. Since the vertical tailplane is mounted straight upwards in the z-direction, there is no vertical tailplane dihedral Γ_V.

$$\lambda_V = \frac{c_{t_V}}{c_{r_V}} \quad \textit{, where } c_{t_V} \textit{ is the vertical tailplane tip chord} \tag{2.1}$$

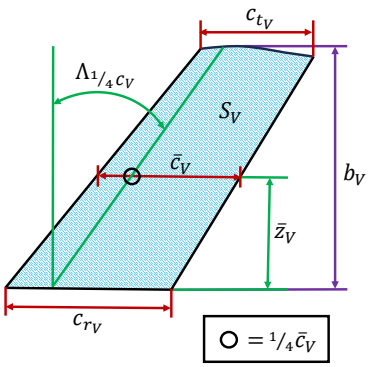

Figure 2.2: Vertical stabilizer parametrization based on [14].

The parameters above can be used to obtain the vertical tailplane aspect ratio A_V with Equation 2.2 and the vertical tailplane surface area S_V with Equation 2.3 [2]. Here the original formula for a wing is converted into one for the vertical stabilizer. Note that for this vertical stabilizer definition, the vertical tail surface area S_V continues into the fuselage, where the vertical tail half-root-chord, $1/2c_{r_V}$, intersects with the center line of the fuselage. This is visualized in Figure 2.3 and specific for the parametrization of Obert [14], thus not always the same for other common methods such as ESDU [1]. Differences between these methods will be discussed in subsection 2.3.2. Also note that in this parametrization, the dorsal fin parametrization is not provided. The only relevant parameter regarding the dorsal fin is the dorsal fin surface area, S_{df}. Why this is relevant is discussed in subsection 2.5.5 in the subsection on the effect of the dorsal fin on the vertical tailplane lift curve. In addition, the vertical tail tip shape is ignored, because the vertical tail side force derivative is mainly dependent on the tail span and to a first order, not dependent on the tip shape [14].

$$A_V = \frac{b_V^2}{S_V} \tag{2.2}$$

$$S_W = 2\int_0^{b_W/2} c_W(y)dy \quad \rightarrow \quad S_V = \int_0^{b_V} c_V(z)dz \quad \textit{(general planform)} \tag{2.3}$$

The vertical tailplane MAC $\bar{c}_V$ and the spanwise location of the MAC $\bar{z}_V$ can also be obtained. The latter is the distance between c_{r_V} and $\bar{c}_V$ as seen in Figure 2.2. Note that there are two methods for calculating both $\bar{c}_V$ and $\bar{z}_V$. The version for a general planform is shown in Equation 2.4 and Equation 2.6 and the version for a straight-tapered or trapezoidal planform in Equation 2.5 and Equation 2.7 all based on USAF DATCOM [2]. Again all the original formulas for a wing are converted into one for the vertical stabilizer. The general planform version should always work, however, if only straight-tapered vertical tailplane planforms are considered, the straight-tapered version might be easier to use.

$$\bar{c}_W = \frac{2}{S_W}\int_0^{b_W/2} c_W(y)^2 dy \quad \rightarrow \quad \bar{c}_V = \frac{1}{S_V}\int_0^{b_V} c_V(z)^2 dz \quad \textit{(general planform)} \tag{2.4}$$

$$\bar{c}_W = \frac{2}{3}c_{r_W}\frac{1+\lambda_W+\lambda_W^2}{1+\lambda_W} \quad \rightarrow \quad \bar{c}_V = \frac{2}{3}c_{r_V}\frac{1+\lambda_V+\lambda_V^2}{1+\lambda_V} \quad \textit{(straight-tapered planform)} \tag{2.5}$$

$$\bar{y}_W = \frac{2}{S_W}\int_0^{b_W/2} c_W(y)ydy \quad \rightarrow \quad \bar{z}_V = \frac{1}{S_V}\int_0^{b_V} c_V(z)zdz \quad \textit{(general planform)} \tag{2.6}$$

$$\bar{y}_W = \left(\frac{1-\frac{\bar{c}_W}{c_{r_W}}}{1-\lambda_W}\right)\frac{b_W}{2} = \frac{1}{3}\left(\frac{1+2\lambda_W}{1+\lambda_W}\right)\frac{b_W}{2} \quad \rightarrow \quad \bar{z}_V = \left(\frac{1-\frac{\bar{c}_V}{c_{r_V}}}{1-\lambda_V}\right)b_V = \frac{1}{3}\left(\frac{1+2\lambda_V}{1+\lambda_V}\right)b_V \tag{2.7}$$

(straight-tapered planform)

In Figure 2.3 the vertical tailplane yawing moment arm is l_{x_V}, which is the distance between the center of gravity (CG) of the whole aircraft and the vertical tailplane quarter MAC, namely $^1/_4\bar{c}_V$. The fuselage height D_V is measured along the $^1/_4\bar{c}_V$ in the spanwise direction of the vertical tail (= z-direction). The vertical position of the horizontal tail z_H is also measured in the spanwise direction of the vertical tail (= z-direction). Although not stated in the parametrization from Obert [14], it is assumed that, if the horizontal tailplane has an incidence angle, z_H is measured at the horizontal tailplane quarter root chord. Nowadays, most transport aircraft have a horizontal tailplane that can be trimmed (incidence can be changed depending on the location of the CG).

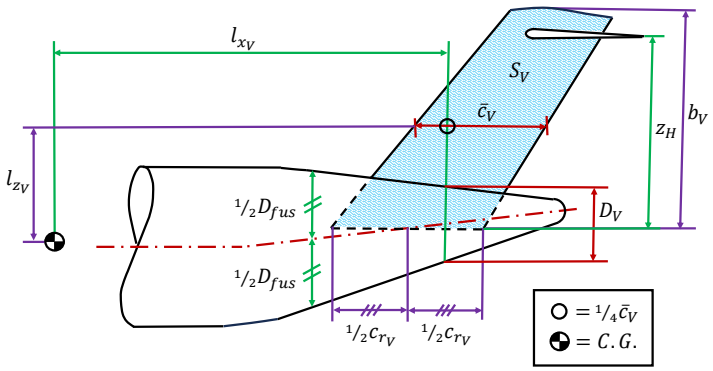

Figure 2.3: Empennage parametrization based on [14].

The rudder parametrization is shown in Figure 2.4, where the rudder surface area S_R is visualized. This surface starts a distance z_R from the vertical tailplane root chord and has a height of h_R. The depth of the rudder (chord length) is often expressed in the rudder-chord-to-tailplane-chord ratio, c_R/c_V, which consists of the rudder chord c_R over the vertical tailplane chord. In general rudder-chord-to-tailplane-chord ratio is even over the whole rudder height. However, if that is not the case, the rudder-chord-to-tailplane-chord ratio at the half-rudder height, $^1/_2 h_R$, can be used as suggested by ESDU [18]. In

addition to the regular rudder surface area, there is also a part of the vertical tailplane surface area affected by the rudder, namely S_{V_R}. This is needed for the Fokker / Obert method [14], which will be explained in section 2.5. This surface is bounded by the top and bottom of the rudder surface as shown in Figure 2.5.

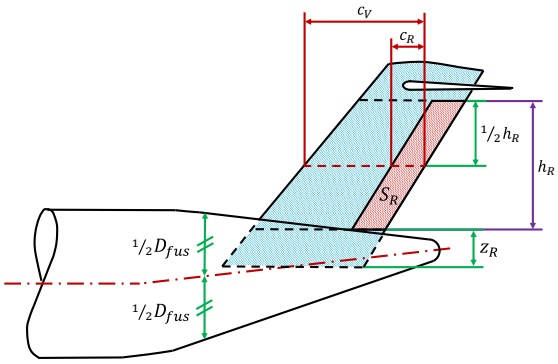

Figure 2.4: Side view vertical tailplane on fuselage with rudder surface area

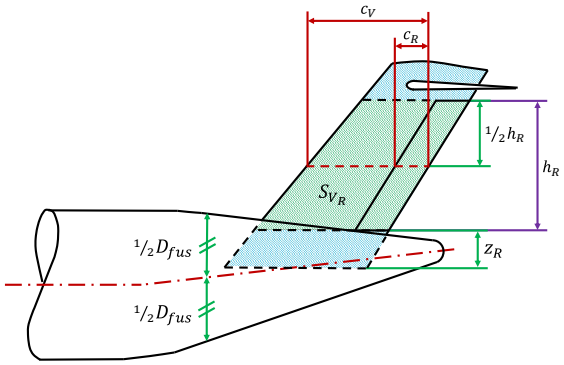

Figure 2.5: Side view vertical tailplane on fuselage with part of vertical tailplane surface area affected by the rudder.

With the side view parametrization established, Figure 2.6 shows the top view of the parametrization. The vertical tailplane consists of airfoils, which can differ throughout the span from root to tip. It is common to choose a root and tip airfoil with a smooth transition between these. Normally the airfoil shapes used for the vertical tail are symmetric. The incidence angle, i_V, is the angle between the fuselage center line and the root chord of the vertical tailplane, which is set to zero in Figure 2.6. This may not always be zero, for instance when considering propeller/turboprop aircraft, to counteract the forces on the aircraft due to the rotating flow coming from the propeller. This means that the pilot does not have to give a constant rudder input to counteract this rotating flow effect. For this research, however, only turbofan/jet engines are considered, and therefore it may be assumed that $i_V = 0$. Figure 2.7 shows the the rudder deflection angle δ_R.

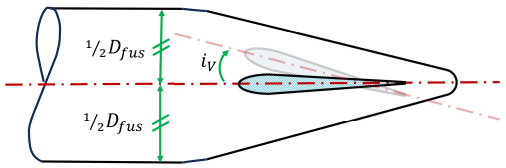

Figure 2.6: Top view vertical tailplane on fuselage with positive incidence angle.

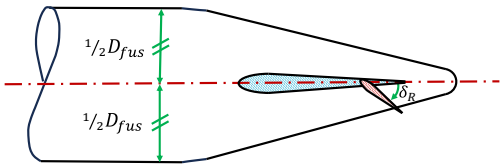

Figure 2.7: Top view vertical tailplane on fuselage with positive rudder deflection angle.

For a complete parametrization of all parameters involved in the Fokker/ Obert method [14], some additional definitions are needed, shown in Figure 2.8. The maximum fuselage diameter $D_{fus_{max}}$ is taken as the reference of which the wing root height h_W is defined. The wing root height is measured vertically from $^1/_2 D_{fus_{max}}$. Note that h_W is positive when the wing is above the fuselage center line. Conversely, z_W, the wing root height relative to the fuselage center line, is positive when the wing is below the fuselage center line because $z_W = -h_W$.

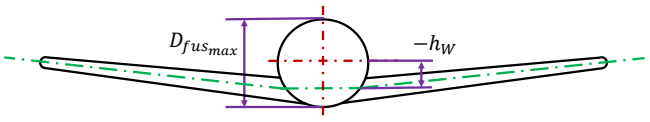

Figure 2.8: Wing root height based on [14].

2.2.2. Design range

Table 2.1 shows the design range for the design parameters of the vertical tail. Some notes about the data used are given below. For ESDU [1], the horizontal tailplane root chord is expected to be of

a similar length as the vertical tailplane root chord for fuselage-mounted horizontal tailplanes. In the case of a fin-mounted horizontal tailplane, the horizontal tailplane root chord is expected to be the same as the vertical tailplane chord at z_H. For Obert [17], only the data of jet aircraft is taken into account. Propeller aircraft data was excluded since the focus of this research is turbofan/jet-powered aircraft as explained in subsection 2.2.1. Also note that the Fokker/Obert method [14], assumes $A_V \leq 1.5$, but the data provided by Obert [17] also includes aspect ratios up to 2. For Torenbeek [15], only data for the transport aircraft were taken into account, excluding small single/four/six seaters. In addition, to reduce vertical tail stall, Torenbeek [15] advises $A_V < 1.8$.

Normally the airfoil shapes used for the vertical tail are symmetric. Common airfoils are the symmetrical NACA-00-series, with a certain thickness ratio. The average thickness ratio, t/c_V, varies between 9-15%, and quite often is 12% according to Torenbeek [15].

A note should be made that the maximum overall height of vertical stabilizers is not defined in literature. However, the height of the vertical stabilizer is constrained by structural requirements as well as maximum height limitations in hangars. No official maximum hangar height was found in literature. The highest transport aircraft currently in use is the Airbus A380-800 has a maximum height of 24.1 meters[1]. So a maximum height of 25 meters of the full aircraft including the vertical tail seems reasonable, giving enough clearance to the hangar roof.

Finally, the location of the vertical tailplane, and all tail surfaces for that matter, may not be in the efflux of the engines. Generally, the efflux is a cone with a 6 deg half-angle. Tail surfaces cannot be placed within this area, because of acoustic fatigue of the tail surfaces and the altered airflow, which may make the tail surfaces ineffective in terms of stability and control. So the placement of the engines might influence the location of the vertical tailplane. Another solution might be to point the engines slightly in another direction (downwards), to make sure the efflux does not interfere with the tail surfaces [15]. More on the effect of engine nacelles on the vertical tailplane can be found in subsection 2.5.6.

Table 2.1: Geometric constraints and design range (*C = conventional tail, *T = T-tail)

	Range				
Parameter	**ESDU** [1]	**Obert** [17][14]	**Raymer** [16]	**Roskam** [19]	**Torenbeek** [15]
A_V	1.0 - 5.0	1.0 - 1.9 (*C) 0.85 - 1.5 (*T)	1.3 - 2.0 (*C) 0.7 - 1.2 (*T)	0.7 - 2.0	0.78 - 1.96
$\Lambda_{1/4c_V}$ $[deg]$	0 - 60	35 - 60 (*C) 30 - 50 (*T)	35 - 55	33 - 53	31 - 55
λ_V	0 - 1	0.25 - 0.4 0.25 - 0.75	0.3 - 0.6 (*C) 0.6 - 1.0 (*T)	0.26 - 0.73	-
S_V/S_W	0.05 - 0.27	-	-	-	0.106 - 0.268
z_H/b_V	0.25 - 1	-	-	-	-
Average t/c_V	-	-	-	-	9 - 15%
c_R/c_V	0.25 - 0.40 (*C) 0.20 - 0.40 (*T)	0.20 - 0.35	0.25-0.5	-	max. 0.30 - 0.35

2.3. Vertical tailplane sizing

2.3.1. Volume coefficients

One of the more simple, but common, methods to size the vertical tail is the method that uses the volume coefficient. This method is based on the similarity between comparable aircraft as their requirements for stability, provided by their vertical tails, are similar. The main features for aircraft to be considered comparable are wing position, horizontal stabilizer position, and engine location. The vertical tail volume coefficient $\bar{V}_V$ in Equation 2.8 consists of a fraction between the vertical tail surface S_V multiplied by the vertical tailplane yawing moment arm l_{x_V}, and the wing surface S_W multiplied by

[1] Lufthansa group. (n.d.). Airbus A380-800. Retrieved January 9, 2024, from https://www.lufthansagroup.com/en/company/fleet/lufthansa-and-regional-partners/airbus-a380-800.html

the wingspan b_w. The method simply takes the same volume coefficient for comparable aircraft and with the overall geometry of the aircraft (l_{x_V}, S_w, and b_w) known, the required vertical tail surface S_V can then be estimated [14], [15], [16], [3], [20], and [21].

$$\bar{V}_V = \frac{S_V l_{x_V}}{S_w b_w} \tag{2.8}$$

2.3.2. Comparison of stability analyses

Since the goal of the research is to implement the DeLaH in the vertical stabilizer, as laid out in chapter 1, a link needs to be found to connect the aerodynamics to the stability requirements of the vertical stabilizer. The volume coefficient method, in the previous section, does not provide such a link. Therefore a more advanced method to size the vertical tail is discussed here, which must provide the link to the aerodynamics. Several different methods found in literature are United States Air Force Data Compendium (USAF DATCOM) [2], Engineering Sciences Data Unit (ESDU) [1], the Fokker / Obert [14] and Vertical tail Design, Stability, and Control (VeDSC) [3]. All these methods are used to obtain the stability derivatives.

The USAF DATCOM [2] is a very comprehensive method that is intended for early design/concept development. It provides approaches for subsonic, transonic, and supersonic velocity regimes. It uses a combined theoretical and empirical approach to calculate the stability derivatives. The empirical data takes the (aerodynamic) interference effects of other aircraft components into account. It assumes small angles of attack in the linear angle of attack range. It also considers only horizontal tailplanes that are body-mounted. This makes this method limited to conventional fuselage-mounted tail designs.

ESDU [1] also uses a combined theoretical and empirical approach. Again taking the (aerodynamic) interference effects of other aircraft components into account, however, this method is intended only for subsonic speeds. It also assumes small angles of attack. Moreover, the flow is fully attached and wholly subsonic over the configuration. This may not always be the case in reality, since there might be local transonic velocities on high subsonic aircraft. One very important prerequisite for ESDU is that the body/fuselage cross-section must be near circular. This means that more unconventional fuselage designs are not covered by this method.

The Fokker / Obert method [14] is intended for high subsonic transport aircraft and combines parts of USAF DATCOM and ESDU and empirical data from Fokker aircraft as well as well as some models from Airbus. The method is intended for conventional fuselage- and fin-mounted tailplanes, therefore limiting for unconventional tailplane configurations. The main difference of this method compared to the previously mentioned is that it considers many different sources that may influence the sidewash and interference effects of other components. The sidewash at the vertical tailplane is the result of various aircraft components upstream altering the velocity and direction of the flow. The more upstream aircraft components are taken into account, the more accurate the estimation of the sidewash becomes. The sidewash described by Fokker / Obert consists of seven different components and related effects, namely the effect of the fuselage-vertical-tailplane interference, wing-fuselage interference, wing dihedral and sweep, rolling-moment-due-to-sideslip, wing flap deflection in landing position, engine nacelles on the wing, and engine nacelles on the rear-fuselage. In addition, the Fokker / Obert method also considers an improved version of the endplate effect that the horizontal tail has on the vertical tail. Similar to USAF DATCOM it considers the vertical position of the horizontal tail and the tailplane area ratio, but in addition, it also takes the effective angle of attack of the horizontal tailplane into account. This is important since the lift generated by the horizontal tailplane and the crossflow that occurs with swept horizontal tailplanes affect the endplate effect. The improved version is based on empirical data. The Fokker / Obert method also offers the possibility to implement dorsal fins.

Finally, VeDSC [3] is different from the other methods named before in the sense that it heavily relies on numerical Reynolds-averaged Navier-Stokes (RANS) simulations. It does use a similar approach as ESDU, but the correction factor is not based on empirical data, but on RANS simulations of turboprop transport aircraft, validated through wind tunnel tests. Since it is focused on turboprops, it uses a slightly lower speed regime compared to the other methods.

To decide which of the above-mentioned methods is most appropriate, a comparison is made. For each of the methods, the main characteristics are summarized in Table A.1 regarding the input, output, conditions, configurations, and various other specifics (remarks). Subsequently, the pros and cons of each method are discussed Table 2.2. Based on these points it is chosen to use the Fokker / Obert method. VeDSC is not an option since it is focused on turboprops, which fly in a lower speed regime than conventional high-subsonic transport aircraft. Also, the use of turboprops may result in slightly different correction factors as compared to turbofan/jet engines used by conventional transport aircraft. The main reasons to choose the Fokker / Obert method over USAF DATCOM and ESDU, is that the Fokker / Obert method uses the improved version of the endplate effect as well as the large amount of upstream aircraft components taken into account for the sidewash, making it more accurate. USAF DATCOM and ESDU only consider sidewash due to the fuselage and the wing's dihedral and vertical position, whilst the Fokker / Obert method also considers other sources. Moreover, the Fokker / Obert method was (most likely) used by Fokker to develop tailplanes of their transport aircraft models. This makes it very useful for this research since the main focus is on conventional fuselage- or fin-mounted stabilizers for subsonic transport aircraft. The working principle of the Fokker / Obert method will be discussed in detail in section 2.5.

Table 2.2: Choice of stability analyses

	Pros	**Cons**
USAF DATCOM [2]	· Well known in other literature · Interference effects of other components	· Limited cases of sidewash and crossflow · Horizontal tailplane must be mounted to body · No dorsal fins · Empirical data based on older aircraft · Limiting for unconventional tailplane configurations
ESDU [1]	· Well known in other literature · Interference effects of other components · Dorsal fins can be implemented	· Limited cases of sidewash and crossflow · Body/fuselage cross-section must be (near) circular · Less accurate for large aspect ratios and twist due to assumption of constant induced sidewash · Limiting for unconventional tailplane configurations
Fokker / Obert [14]	· Many cases of sidewash and crossflow · Interference effects of other components · Dorsal fins can be implemented · Endplate effects are taken into account	· Unknown in other literature · Limiting for unconventional tailplane configurations
VeDSC [3]	· Based on more recent aircraft	· Unknown in other literature · Focusses on turboprops · Data based on RANS and wind tunnel tests, no real empirical data · Limiting for unconventional tailplane configurations

2.4. Stability and control analysis: Reference frames and derivatives

As discussed in section 2.1, the main purpose of the vertical stabilizer is to provide directional and lateral stability. For these, only the side force Y, rolling moment L and yawing moment N are of interest. (Note that L refers to the rolling moment and not to lift in this context.) It is of great importance to define in what reference frame these forces are expressed.

2.4.1. Reference frames

There are three different reference frames to consider, namely the body (fixed) frame, the stability frame, and the vehicle carried normal Earth frame, all visualized in Figure 2.9 based on [22] and [23]. All of the reference frames are centered at the CG, have the x-axis pointing towards the aircraft nose, the y-axis towards the right wing, and the z-axis downwards. The difference between them is their relative rotations around the y-axis. First, the vehicle carried normal Earth frame (denoted with subscript E) has its z-axis always perpendicular to the Earth horizon and its x- and y-axis parallel to the horizon. Second, the stability frame (denoted with subscript S) is rotated around the y-axis by the flight path angle γ

relative to the vehicle carried normal Earth frame. Third, the body (fixed) frame (with no subscript) is again rotated around the y-axis by the angle of attack α relative to the stability frame. It could also be said that the stability frame is in the direction of the aircraft's velocity direction V (or airspeed) in terms of pitch and the body frame is in the direction of the aircraft fuselage centerline.

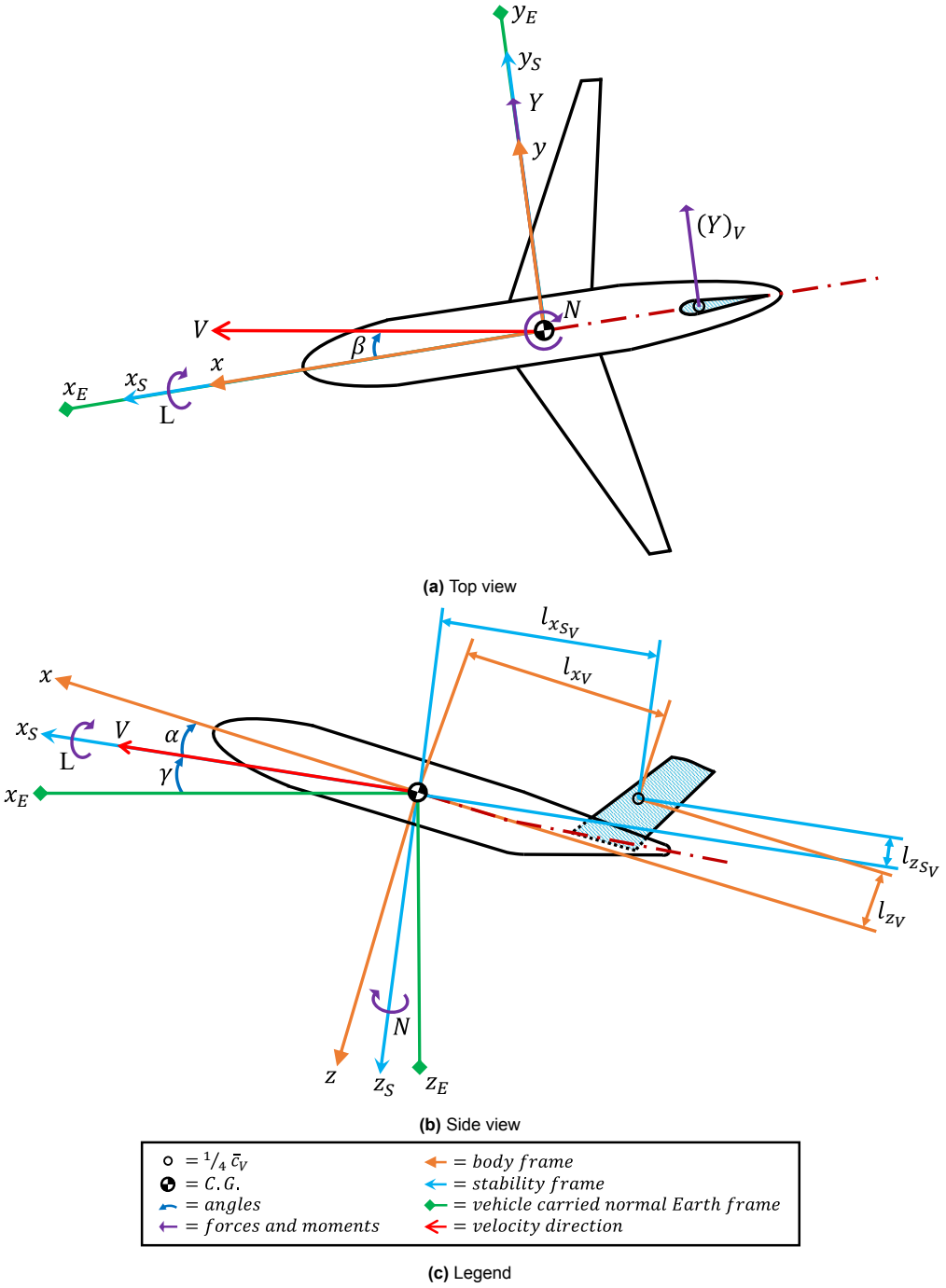

Figure 2.9: Reference frames based on [22] and [23]. Note that all coordinate system axes, angles, forces, and moments are drawn in the positive direction. Moments are based on right-hand rule.

The reason why these reference frames are relevant is because of the vertical tail moment arms, which are needed in the vertical tailplane stability analysis. It is assumed the moment arms are the distance between the CG and the vertical tailplane mean aerodynamic quarter chord (assumed to coincide with the aerodynamic center), where the CG is taken to be at the 25% wing mean aerodynamic chord, although Fokker often uses the 30% wing mean aerodynamic chord [14]. In most stability analy-

sis methods, the yawing moment arm l_{x_V} and rolling moment arm l_{z_V} are expressed in the body frame, whilst the yawing moment and rolling moment (and thus the coefficients) are expressed in the stability frame. This is not a problem when small angles of attack are assumed, which is the case for steady flight during cruise, but this becomes relevant when looking at high angles of attack during high lift conditions. It can be seen in Figure 2.9b that for large angles of attack, the yawing and rolling moment arms change in length and even can change in sign. Hence, adjusted moment arms are needed, expressed in the stability frame. Equation 2.9 and Equation 2.10 are the yawing and rolling moment arms in the stability frame [23]. Based on these equations it can be said that for conventional aircraft the relative change in moment arm due to angle of attack is much more significant for the rolling moment arm $l_{z_{S_V}}$ since the components of l_{x_V} and l_{z_V} have similar magnitudes [1].

$$l_{x_{S_V}} = l_{x_V} \cos\alpha + l_{z_V} \sin\alpha \tag{2.9}$$

$$l_{z_{S_V}} = l_{z_V} \cos\alpha - l_{x_V} \sin\alpha \tag{2.10}$$

2.4.2. Stability and control derivatives

With the reference frames clear, the forces and moments need to be expressed as coefficients. To express these in coefficients, the side force, rolling, and yawing moments are normalized as seen in Equation 2.11, Equation 2.12, and Equation 2.13, resulting in the side force coefficient, rolling moment coefficient, and yawing moment coefficient respectively. Here $q = {}^1\!/_2 \rho V^2$ is the dynamic pressure, S_W the wing surface, and b_W the wing span.

$$C_y = \frac{Y}{qS_W} \tag{2.11}$$

$$C_l = \frac{L}{qS_W b_W} \tag{2.12}$$

$$C_n = \frac{N}{qS_W b_W} \tag{2.13}$$

Each of these coefficients is built up out of several components shown in Equation 2.14. They consist of the stability derivatives with respect to sideslip angle β, shown in Figure 2.9, and control derivatives with respect to rudder deflection angle δ_R and aileron deflection angle δ_a.

$$\begin{Bmatrix} C_y \\ C_l \\ C_n \end{Bmatrix} = \begin{bmatrix} C_{y_0} & C_{y_\beta} & C_{y_{\delta_R}} & C_{y_{\delta_a}} \\ C_{l_0} & C_{l_\beta} & C_{l_{\delta_R}} & C_{l_{\delta_a}} \\ C_{n_0} & C_{n_\beta} & C_{n_{\delta_R}} & C_{n_{\delta_a}} \end{bmatrix} \begin{Bmatrix} 1 \\ \beta \\ \delta_R \\ \delta_a \end{Bmatrix} \tag{2.14}$$

Technically, derivatives for slats and spoilers could also be added to this analysis as proposed by USAF DATCOM [2] for instance. Moreover, every moving component on the wing that influences the forces and moments could be added as long as they are used asymmetrically or create an asymmetric force distribution, otherwise, there is no influence on the lateral and directional stability and control. However, most analyses, such as Obert [14], Raymer [16] and Roskam [22], just use most or all of the derivatives shown in Equation 2.14. The terms for C_{y_0}, C_{l_0}, and C_{n_0} are the C_y, C_l, and C_n when β, δ_R, and δ_a are set to zero. However, these terms can be assumed to be zero for airplane configurations that are symmetrical. This results in the final set of derivatives in Equation 2.15.

$$\begin{Bmatrix} C_y \\ C_l \\ C_n \end{Bmatrix} = \begin{bmatrix} C_{y_\beta} & C_{y_{\delta_R}} & C_{y_{\delta_a}} \\ C_{l_\beta} & C_{l_{\delta_R}} & C_{l_{\delta_a}} \\ C_{n_\beta} & C_{n_{\delta_R}} & C_{n_{\delta_a}} \end{bmatrix} \begin{Bmatrix} \beta \\ \delta_R \\ \delta_a \end{Bmatrix} \tag{2.15}$$

Keep in mind that the overall objective of this research is to implement the DeLaH in the vertical tail. Therefore a link between the aerodynamics of the vertical tail and the stability analysis is required. This link is provided by the vertical tail lift curve slope $\left(C_{L_\alpha}\right)_V$. The $\left(C_{L_\alpha}\right)_V$ affects the stability analysis through the stability and control derivatives with respect to sideslip and rudder deflection angle as seen

in Equation 2.15. This approach will also discussed in chapter 4, and the individual derivatives will be discussed in the next section (section 2.5).

2.5. Stability and control analysis: Fokker / Obert

In the next sections the Fokker / Obert [14] method to obtain these stability and control derivatives will be discussed. It should be stressed that the method assumes steady-state conditions for the vertical tailplane sizing. Also, the method is intended for conventional transport aircraft, which is in the high-subsonic-speed regime.

2.5.1. Stability derivatives: Components

As discussed in section 2.1, the main purpose of the vertical stabilizer is to provide directional and lateral stability. The stability derivatives of interest are the derivatives with respect to sideslip angle β. The sideslip angle is defined as clockwise positive as seen from above as shown in Figure 2.9. The derivatives of interest are the side-force-due-to-sideslip derivative C_{y_β}, the rolling-moment-due-to-sideslip derivative C_{l_β}, and the yawing-moment-due-to-sideslip derivative C_{n_β}. Based on Figure 2.9 it can be determined that for adequate static stability C_{y_β} is negative, C_{l_β} is desired to be negative, and C_{n_β} is desired to be positive [22].

To be able to size the vertical tail, the contribution of the vertical tail to the stability derivative needs to be found. This is done by dividing the stability derivatives in a component without the tail, the so-called tail-off component, the horizontal tail component, and the vertical tail component as seen in Equation 2.16, Equation 2.17, and Equation 2.18. The tail-off component uses the subscript $T-O$ and is the whole aircraft without the vertical tail. Sometimes this component is also referred to with the subscript WFN, which stands for the wing, fuselage, and nacelles, respectively. Note that the horizontal tailplane is only included for the rolling moment derivative since it only influences the rolling moment and not the side-force, and yawing moment. The wing, fuselage, nacelle, and horizontal stabilizer interference are included as an interference factor in the vertical tail component via the sidewash. More on this will be discussed later in this chapter.

$$C_{y_\beta} = \left(C_{y_\beta}\right)_{T-O} + \left(C_{y_\beta}\right)_V \tag{2.16}$$

$$C_{l_\beta} = \left(C_{l_\beta}\right)_{T-O} + \left(C_{l_\beta}\right)_V + \left(C_{l_\beta}\right)_H \tag{2.17}$$

$$C_{n_\beta} = \left(C_{n_\beta}\right)_{T-O} + \left(C_{n_\beta}\right)_V \tag{2.18}$$

2.5.2. Stability derivatives: Tail-off components

First, the tail-off components are presented in Equation 2.19, Equation 2.20, Equation 2.21, and Equation 2.22. Starting with $\left(C_{y_\beta}\right)_{T-O}$, which is based on USAF DATCOM [2] and NACA TN D-6946 [24]. The only difference, however, is that a correction is applied for the number of nacelles for both wing and fuselage-mounted nacelles, $(n_{nac})_W$ and $(n_{nac})_F$, respectively. This correction for the nacelles is based on various wind tunnel tests. The factor K_i is the wing-body interference factor for wing-body sideslip derivative C_{y_β} and values can be obtained by using Figure B.1. In addition, $\left(\Delta C_{y_\beta}\right)_{fl}$ is also added. This is the contribution to the side-force-due-to-sideslip derivative due to flap deflection of the wing flaps δ_{fl}. The corresponding values for various degrees of flap deflection can be found in Figure B.2, which gives average values for wings with slats as well as wings without slats. Both the added correction for the nacelles as well as the flap deflection have a small but still considerable influence on the tail-off side force derivative and are therefore included.

$$\left(C_{y_\beta}\right)_{T-O} = -\frac{S_{fus.cross}}{S_W} K_i \frac{2}{57.3} - 0.0001\Gamma_W + \left(\Delta C_{y_\beta}\right)_{fl} - 0.00175\,(n_{nac})_W - 0.00025\,(n_{nac})_F \tag{2.19}$$

Next, $\left(C_{l_\beta}\right)_{T-O}$, in Equation 2.20, is also based on on USAF DATCOM [2] and NACA TN D-6946 [24]. The influence of the wing dihedral, $\frac{C_{l_\beta}}{\Gamma_W}$, is obtained from Figure B.3. The wing aspect ratio, sweep, and taper influence is incorporated in $\frac{C_{l_\beta}}{C_{L_W}}$, which is the lift-dependent tail-off roling-moment-due-to-sideslip and is determined with either Figure B.4, and Figure B.5 or with Equation 2.21.

$$\left(C_{l_\beta}\right)_{T-O} = \left(\frac{C_{l_\beta}}{C_{L_W}}\right)\frac{C_{L_W}}{57.3} + \left(\frac{C_{l_\beta}}{\Gamma_W}\right)\Gamma_W - \left(-0.042\frac{z_W}{D_{fus_{max}}} + 0.0005\Gamma_W\right)\sqrt{A_W}\left(\frac{D_{fus_{max}}}{b_W}\right)^2 \tag{2.20}$$

$$\left(\frac{C_{l_\beta}}{C_{L_W}}\right) = -\frac{1}{2}\left[\frac{3}{A_W(1+\lambda_W)} + y^*\left(\tan\Lambda_{1/4c_W} - \frac{6}{A_W}\frac{1-\lambda_W}{1+\lambda_W}\right)\right] + 0.05 \quad \textit{(per rad.)} \tag{2.21}$$

Equation 2.22 shows $\left(C_{n_\beta}\right)_{T-O}$ that is again based on USAF DATCOM [2] and NACA TN D-6946 [24], but the contribution of the flap deflection of the wing flaps δ_{fl} is added, similar to tail-off side-force derivative. The value for $\left(\Delta C_{n_\beta}\right)_{fl}$ can be obtained from Figure B.2. Different from the tail-off side force derivative, the nacelles do not influence the tail-off yawing moment. The empirical factor related to sideslip derivative C_{n_β} for body and wing-body interference, K_N, is determined with Figure B.6. Note that this factor K_N incorporates the effect of the fuselage Reynolds number, $Re_{l_{fuselage}}$, directly in the graph, whilst the original USAF DATCOM splits this in a K_N without fuselage Reynold number effect and a separate fuselage Reynolds number correction factor K_{R_l}. The USAF DATCOM approach may be useful if fuselage Reynolds numbers between $80 \cdot 10^{-6}$ and $350 \cdot 10^{-6}$ occur, as found in Figure B.7.

$$\left(C_{n_\beta}\right)_{T-O} = -K_N\frac{S_{B_S}}{S_W}\frac{l_B}{b_W} + \left(\Delta C_{n_\beta}\right)_{fl} \tag{2.22}$$

2.5.3. Stability derivatives: Horizontal tail component

Second, the horizontal tail component is discussed. $\left(C_{l_\beta}\right)_H$, as seen in Equation 2.23, is based on Roskam [22]. The dihedral term, $\left(\frac{C_{l_\beta}}{\Gamma_H}\right)\Gamma_H$, is obtained in the same way as in Equation 2.20 by using Figure B.3 for $\frac{C_{l_\beta}}{\Gamma_H}$. One consideration is that in USAF DATCOM [2], an additional compressibility correction factor is used in the form of K_{M_Γ}, which is multiplied with the dihedral term. The value for this factor can be obtained from Figure B.8. However, this compressibility correction factor is not used by Roskam, and therefore Equation 2.23 is used directly. Another important thing to consider is that $\left(C_{l_\beta}\right)_H$ is positive when the horizontal tailplane is mounted on the fuselage or low on the vertical tailplane, negative when mounted high on the vertical tailplane and has no influence on the overall rolling-moment-due-to-sideslip when mounted halfway on the vertical tailplane span [2]. The dynamic pressure ratio, $\frac{q_H}{q}$, is obtained from Torenbeek [15], where $\frac{q_H}{q}$ is 0.85 for fuselage-mounted horizontal tailplanes, 1.0 for T-tails, and 0.95 for fin-mounted horizontal tailplanes.

$$\left(C_{l_\beta}\right)_H = \left(\frac{C_{l_\beta}}{\Gamma_H}\right)\Gamma_H\frac{q_H}{q}\frac{S_H b_H}{S_W b_W} \tag{2.23}$$

2.5.4. Stability derivatives: Vertical tail components

Third, the vertical tail components are discussed. First, the forces and moments at the vertical tail are defined, Equation 2.24, Equation 2.25, and Equation 2.26, respectively. Figure 2.3 can be used as a reference for the rolling and yawing moment arms l_{z_V} and l_{x_V}. Also, note that the vertical tailplane lift curve slope is $(C_{L_\alpha})_V$, which is the most common notation in stability analysis literature. Technically, this refers to the vertical tailplane as a standalone component. In the context of full aircraft, this should

be C_{Y_β}. However, this may be confused with the very similar notation for vertical tailplane side-force-due-to-sideslip derivative $\left(C_{y_\beta}\right)_V$, which will be introduced later in this section. To prevent confusion $(C_{L_\alpha})_V$ will be used for the vertical tailplane lift curve slope throughout this report.

$$(Y)_V = (C_{L_\alpha})_V \, \alpha_V \, q_V \, S_V \tag{2.24}$$

$$(L)_V = (C_{L_\alpha})_V \, \alpha_V \, q_V \, S_V \, l_{z_V} \tag{2.25}$$

$$(N)_V = (C_{L_\alpha})_V \, \alpha_V \, q_V \, S_V \, l_{x_V} \tag{2.26}$$

The angle of attack at the vertical tailplane is described by Equation 2.27. Here β is the sideslip angle and σ is the sidewash angle, which is a result of various aircraft components altering the flow, as seen in Figure 2.10a and Figure 2.10b. The effects on the spanwise circulation distribution and downwash are shown in Figure 2.10c and Figure 2.10d. The incidence angle of the vertical tailplane, i_V, is the angle between the vertical tail chord and the fuselage centerline. As explained earlier, the vertical tailplane incidence angle is not always zero. For instance when considering propeller/turboprop aircraft, where the vertical tailplane must counteract the forces on the aircraft due to the rotating flow coming from the propeller. This means that the pilot does not have to give a constant rudder input to counteract this rotating flow effect. For this research, however, only turbofan/jet engines are considered, and therefore it may be assumed that $i_V = 0$.

$$\alpha_V = \beta + \sigma + i_V \tag{2.27}$$

Next, the sideslip and sidewash angles can be substituted as seen in Equation 2.28, Equation 2.29, and Equation 2.30.

$$(Y)_V = (C_{L_\alpha})_V \, (\beta + \sigma) \, q_V \, S_V \quad \textit{(assuming } i_V = 0 \textit{ degrees)} \tag{2.28}$$

$$(L)_V = (C_{L_\alpha})_V \, (\beta + \sigma) \, q_V \, S_V \, l_{z_V} \quad \textit{(assuming } i_V = 0 \textit{ degrees)} \tag{2.29}$$

$$(N)_V = (C_{L_\alpha})_V \, (\beta + \sigma) \, q_V \, S_V \, l_{x_V} \quad \textit{(assuming } i_V = 0 \textit{ degrees)} \tag{2.30}$$

To obtain the coefficients, all should be normalized by using Equation 2.31 based on [22].

$$(C_y)_V = \frac{(Y)_V}{qS_W} \quad , \quad (C_l)_V = \frac{(L)_V}{qS_W b_W} \quad , \quad (C_n)_V = \frac{(N)_V}{qS_W b_W} \tag{2.31}$$

This gives the side force, rolling moment, and yawing moment coefficients in Equation 2.32, Equation 2.33, and Equation 2.34, respectively.

$$(C_y)_V = (C_{L_\alpha})_V \, (\beta + \sigma) \, \frac{q_V}{q} \frac{S_V}{S_W} \tag{2.32}$$

$$(C_l)_V = (C_{L_\alpha})_V \, (\beta + \sigma) \, \frac{q_V}{q} \frac{S_V l_{z_V}}{S_W b_W} \tag{2.33}$$

$$(C_n)_V = (C_{L_\alpha})_V \, (\beta + \sigma) \, \frac{q_V}{q} \frac{S_V l_{x_V}}{S_W b_W} \tag{2.34}$$

Finally, the derivatives with respect to sideslip angle, β, are taken to obtain the final vertical tailplane side-force-due-to-sideslip derivative $\left(C_{y_\beta}\right)_V$, vertical tailplane rolling-moment-due-to-sideslip derivative $\left(C_{l_\beta}\right)_V$, and vertical tailplane yawing-moment-due-to-sideslip derivative $\left(C_{n_\beta}\right)_V$, presented in Equation 2.35, Equation 2.36, and Equation 2.37, respectively.

$$\left(C_{y_\beta}\right)_V = (C_{L_\alpha})_V \left(1 + \frac{\delta\sigma}{\delta\beta}\right) \frac{q_V}{q} \frac{S_V}{S_W} \tag{2.35}$$

Figure 2.10: CONFIDENTIAL Flow in sideslip [14].

$$\left(C_{l_\beta}\right)_V = (C_{L_\alpha})_V \left(1 + \frac{\delta\sigma}{\delta\beta}\right) \frac{q_V}{q} \frac{S_V l_{z_V}}{S_W b_W} \tag{2.36}$$

$$\left(C_{n_\beta}\right)_V = (C_{L_\alpha})_V \left(1 + \frac{\delta\sigma}{\delta\beta}\right) \frac{q_V}{q} \frac{S_V l_{x_V}}{S_W b_W} \tag{2.37}$$

With these derivatives now established and the geometric variables assumed to be known, expressions need to be found for the lift curve slope, $(C_{L_\alpha})_V$, and the sidewash parameter, $\left(1 + \frac{\delta\sigma}{\delta\beta}\right)\frac{q_V}{q}$, which will be done in subsection 2.5.5 and subsection 2.5.6, respectively. Be careful that these derivatives are still expressed in the body frame and not in the stability frame as they use l_{x_V}, l_{z_V} and not $l_{x_{S_V}}$, $l_{z_{S_V}}$. Furthermore, the signs of $\left(C_{y_\beta}\right)_V$ and $\left(C_{l_\beta}\right)_V$ are negative due to their direction relative to the aircraft CG.

2.5.5. Stability derivatives: Vertical tailplane lift curve slope

The vertical tailplane lift curve slope in 2D is dictated by the airfoil shape. When going to 3D the geometry of the vertical tail also becomes part of the estimation of the lift curve slope. Also, the dorsal fin may affect the lift curve slope, as well as the endplate effect due to the presence of the horizontal tailplane.

Effect of vertical tailplane geometry on vertical tailplane lift curve slope

Looking at Figure B.9, Figure B.10, and Figure B.11, it can be seen that for vertical tail surfaces, or for all lifting surfaces for that matter, with low aspect ratios ($A_{V} \leq 1.5$) the lift curve slope is affected by the shape of the planform very little. The geometric parameters that dictate the shape of the planform are the sweep Λ, taper ratio λ, and aspect ratio A. In addition to these characteristics, the tip shape also has very little effect on the lift curve slope, because the vertical tail side force derivative is mainly dependent on the tail span and to a first order, not dependent on the tip shape according to Obert [14].

Effect of dorsal fin on vertical tailplane lift curve slope

In general, one could argue that a properly designed vertical tail does not need a dorsal fin, however, for completeness, the general effects of a dorsal fin on the lift curve slope will be discussed shortly. The dorsal fin is normally added to the vertical tail to increase the angle of attack at which it stalls. Figure B.12 shows that the dorsal fin shape and size do not change the yawing moment for small to medium yaw angles. Figure B.13 and Figure B.15 give the horizontal displacement of the vertical tailplane aerodynamic center, $\frac{\Delta x_{ac_{V}}}{\bar{c}_{V}}$ (normalized by $\bar{c}_{V}$), against the dorsal fin over vertical tail surface ratio, $\frac{S_{df}}{S_{V}}$. This proves that the larger the dorsal fin size, the more the vertical tail aerodynamic center moves forward. Knowing this and since the yawing moment does not change with dorsal fin size, it can be concluded that the side force must increase and therefore also the vertical tailplane lift curve slope. This is also reflected by Figure B.14 and Figure B.16, which show the combined vertical tailplane + dorsal fin lift curve slope over dorsal fin lift curve slope, $\frac{(C_{L_{\alpha}})_{V+df}}{(C_{L_{\alpha}})_{V}}$, against the dorsal fin over vertical tail surface ratio, $\frac{S_{df}}{S_{V}}$. Here an increase in dorsal fin size results in an increase in vertical tailplane lift curve slope.

To incorporate the effect of the increased vertical tailplane lift curve slope due to the dorsal fin in the stability derivatives, the moment arm simply needs to be adjusted. Based on the relations found above, the new effective vertical tailplane yawing moment arm including dorsal fin, $l_{x_{V+df}}$, can be found by using Equation 2.38 in combination with Figure B.13, Figure B.14, Figure B.15, and Figure B.16.

$$l_{x_{V+df}} = l_{x_{V}} - \frac{\Delta x_{ac_{V}}}{\bar{c}_{V}} \bar{c}_{V} = \frac{(C_{L_{\alpha}})_{V}}{(C_{L_{\alpha}})_{V+df}} l_{x_{V}} \tag{2.38}$$

Endplate effect on vertical tailplane lift curve slope

USAF DATCOM [2] uses the effective aspect ratio $A_{V_{eff}}$ from Figure B.17, which includes a correction factor that accounts for the horizontal to vertical tailplane surface ratio (or tailplane area ratio) S_{H}/S_{V}, to calculate the lift curve slope of the vertical tailplane including the endplate effect of the horizontal tail. Fokker / Obert [14], uses a slightly different approach based on empirical data, which will also be the approach used in this research. With Equation 2.39 the endplate effect of horizontal tailplane at zero horizontal tailplane angle of attack can be calculated and it consists of two components. First, the effect of the relative vertical mounting position of the horizontal tailplane, $\left((K_{VH})_{S_{H}/S_{V}=1.33}\right)_{\alpha_{H}=0}$, where the vertical mounting position of the vertical tailplane is z_{H}/b_{V}. The values can be obtained from Figure B.18, Figure B.19, Figure B.20, Figure B.21, and Figure B.22. Second, the effect of the relative horizontal to vertical tailplane surface ratio, $\left(\frac{K_{VH}-1}{(K_{VH})_{S_{H}/S_{V}=1.33}-1}\right)_{\alpha_{H}=0}$, can be obtained with Figure B.23.

The two components are combined in Equation 2.39 and the resulting value $(K_{VH})_{\alpha_{H}=0}$ can be found in Figure B.24. It should be noted that in the data used to obtain these graphs, a distinction is made between $(K_{VH})_{\alpha_{H}=0}$ from $C_{y_{\beta}}$ and $C_{n_{\beta}}$. For this research the calculated value for $(K_{VH})_{\alpha_{H}=0}$ is assumed to be the same for $C_{y_{\beta}}$ and $C_{n_{\beta}}$, since the relationship in Equation 2.39 is based on the average values of both $C_{y_{\beta}}$ and $C_{n_{\beta}}$, even though the individual datapoints of $C_{y_{\beta}}$ and $C_{n_{\beta}}$ for the same aircraft are not the same.

$$(K_{V_H})_{\alpha_H=0} = \left(\left((K_{V_H})_{S_H/S_V=1.33} \right)_{\alpha_H=0} - 1 \right) \left(\frac{K_{V_H} - 1}{(K_{V_H})_{S_H/S_V=1.33} - 1} \right)_{\alpha_H=0} + 1 \tag{2.39}$$

With the endplate effect of the horizontal tailplane at zero horizontal tailplane angle of attack known, the total endplate effect of the horizontal tailplane on the vertical tailplane can be calculated. This is done with Equation 2.40, where the $(K_{V_H})_{\alpha_H=0}$ is corrected for the effective horizontal tailplane angle of attack. In this equation, the horizontal tailplane zero-lift angle of attack relative to the tailplane reference plane, α^*_H, is always $1.5\ deg$, according to the data that is used to construct the graphs to obtain $(K_{V_H})_{\alpha_H=0}$. Note that this equation sometimes uses the value 0.013 instead of 0.014 in the Fokker / Obert method [14] for unknown reasons. The horizontal tailplane angle of attack, α_H, can be found with Equation 2.41, where ϵ is the downwash and i_H is the horizontal tailplane incidence angle. The downwash may be calculated directly based on the aircraft design or the estimated values from Fokker / Obert [14] can be used. The latter are not included because they are very specific to the types of aircraft presented in the paper. Also Figure 2.10d shows the change in downwash when sideslipping, showing this gives an uneven downwash distribution, proving estimations are needed for the overall downwash.

$$K_{V_H} = (K_{V_H})_{\alpha_H=0} \left[1 - 0.014 \left(\alpha_H + \alpha^*_H \right) \right] \quad \textit{(assume } \alpha^*_H = 1.5\, deg\textit{)} \tag{2.40}$$

$$\alpha_H = \alpha + \epsilon + i_H \tag{2.41}$$

On a final note, the K_{V_H} factor found with Equation 2.40 can simply be used as a correction factor to $(C_{L_\alpha})_V$ to incorporate this endplate effect in the vertical tailplane lift curve slope.

2.5.6. Stability derivatives: Sidewash

Next to the vertical tail lift curve slope, an expression for the sidewash parameter, $\left(1 + \frac{\delta\sigma}{\delta\beta}\right) \frac{q_V}{q}$, to the stability derivatives is needed. $\frac{\delta\sigma}{\delta\beta}$ is officially the sidewash-angle-to-sideslip-angle ratio, but often referred to as sidewash or sidewash factor. Furthermore, $\frac{q_V}{q}$ is the effective-versus-free-stream dynamic pressure ratio, which accounts for the fuselage boundary layer effect.

The sidewash at the vertical tailplane is the result of various aircraft components upstream altering the velocity and direction of the flow. The more upstream aircraft components are taken into account, the more accurate the estimation of the sidewash becomes. The sidewash described by Fokker / Obert [14] consists of seven different components and related effects, namely the effect of the fuselage-vertical-tailplane interference, wing-fuselage interference, wing dihedral and sweep, rolling-moment-due-to-sideslip, wing flap deflection in landing position, engine nacelles on the wing, and engine nacelles on the rear-fuselage.

Note that the components discussed in this section are the main and most important components of transport aircraft that play a role in the formation of sidewash. One potential addition to these components could be the landing gear during landing and take-off. However, the main goal of this research is the implementation of the DeLaH into the vertical tail. A prerequisite for this is laminar flow at the vertical tail and this is most likely not the case during landing and take-off. Moreover, the contribution of the landing gear to the sidewash is most likely very small and therefore negligible.

Effective-versus-free-stream dynamic pressure ratio and fuselage-vertical-tailplane lift carry-over effect

Before going into the sidewash contributions, the effective-versus-free-stream dynamic pressure ratio and fuselage-vertical-tailplane lift carry-over effect should be addressed. The effective-versus-free-stream dynamic pressure ratio is $\frac{q_V}{q}$, as addressed earlier, and accounts for the fuselage boundary layer effect. To incorporate the additional lift generated by the vertical tail because of the fuselage being nearby, the so-called fuselage-vertical-tailplane lift carry-over effect, K_{FV}, is introduced. Both of these combined $\frac{q_V}{q} K_{FV}$ can be obtained through Figure B.25. All sidewash contributions in the next sections are either already or should be multiplied by this value.

Effect of fuselage-vertical-tailplane interference on sidewash

The first effect contributing to the sidewash is the fuselage-vertical-tailplane interference, which is visualized in Figure 2.10c and Figure 2.10b. In Equation 2.42 is the expression to quantify the fuselage-vertical-tailplane interference on sidewash, where $\left(1+\frac{\delta\sigma}{\delta\beta}\right)_{FV}$ is the fuselage-vertical-tailplane interference factor. Figure B.26 can be used to obtain the value for this sidewash contribution.

$$\left(1+\frac{\delta\sigma}{\delta\beta}\right)_{FV}\frac{q_{V}}{q}K_{FV} \tag{2.42}$$

Effect of wing-fuselage interference on sidewash

The second effect contributing to the sidewash is the wing-fuselage interference, $\left(\Delta\frac{\delta\sigma}{\delta\beta}\right)_{h_W}$, which can be calculated with Equation 2.43. Next to the equation, Figure B.27, Figure B.28, and Figure B.29 show the graph where the equation is based upon, for further reference. For the geometric definitions of h_W and $D_{fus_{max}}$, refer to Figure 2.8.

$$\left(\Delta\frac{\delta\sigma}{\delta\beta}\right)_{h_W}\frac{q_{V}}{q}K_{FV}=-0.40\frac{h_W}{D_{fus_{max}}} \tag{2.43}$$

Effect of wing dihedral and sweep on sidewash

The third effect contributing to the sidewash is $\left(\Delta\frac{\delta\sigma}{\delta\beta}\right)_{\Gamma}$, which is the wing dihedral and sweep. Equation 2.44 is used to obtain the corresponding values for the wing dihedral and sweep contribution. The equation is based on Figure B.30 (bottom) where the $\left(\Delta C_{l_\beta}\right)_{\Gamma}$ was implemented to also cover the wing sweep, instead of just the wing dihedral as seen in Figure B.30 (top). The rolling-moment-due-to-sideslip due to wing dihedral, $\left(\Delta C_{l_\beta}\right)_{\Gamma}$, can be found with Equation 2.45, which is just the part of Equation 2.20 that is governed by the wing dihedral. The influence of the wing dihedral, $\frac{C_{l_\beta}}{\Gamma_W}$, is obtained from Figure B.3. Again, for the geometric definitions of h_W and $D_{fus_{max}}$, refer to Figure 2.8.

$$\left(\Delta\frac{\delta\sigma}{\delta\beta}\right)_{\Gamma}\frac{q_{V}}{q}K_{FV}=+\left(110+50\frac{h_W}{D_{fus_{max}}}\right)\left(\Delta C_{l_\beta}\right)_{\Gamma} \tag{2.44}$$

$$\left(\Delta C_{l_\beta}\right)_{\Gamma}=\left(\frac{C_{l_\beta}}{\Gamma_W}\right)\Gamma_W-0.0005\Gamma_W\sqrt{A_W}\left(\frac{D_{fus_{max}}}{b_W}\right)^2 \tag{2.45}$$

Effect of rolling-moment-due-to-sideslip on sidewash

The fourth effect contributing to the sidewash is the rolling-moment-due-to-sideslip, $\left(\Delta\frac{\delta\sigma}{\delta\beta}\right)_{C_{l_\beta}}$, described by Equation 2.46. It consists of the tail-off rolling-moment-due-to-sideslip, $\left(C_{l_\beta}\right)_{T-O}$, which is calculated with Equation 2.20 and Equation 2.21, also making use of Figure B.3 Figure B.4, and Figure B.5. Next to that, the tail-off rolling-moment-due-to-sideslip at zero lift coefficient, $\left(C_{l_\beta}\right)_{T-O,C_L=0}$, is required. This is calculated in the same way as the $\left(C_{l_\beta}\right)_{T-O}$ described above, but the term that contains the lift coefficient is set to zero. In other words, in Equation 2.20 $\left(\frac{C_{l_\beta}}{C_{L_W}}\right)\frac{C_{L_W}}{57.3}$ is set to zero.

$$\left(\Delta\frac{\delta\sigma}{\delta\beta}\right)_{C_{l_\beta}}=-0.50\left[\left(C_{l_\beta}\right)_{T-O}-\left(C_{l_\beta}\right)_{T-O,C_L=0}\right] \tag{2.46}$$

Effect of wing flap deflection in landing position on sidewash

The fifth effect contributing to the sidewash is the wing flap deflection in landing position, $\left(\Delta\frac{\delta\sigma}{\delta\beta}\right)_{fl,ldg}$, and is described by Equation 2.47. The equation is derived from Figure B.31 and it is dependent on the relative flap span, namely b_{fl}.

$$\left(\Delta\frac{\delta\sigma}{\delta\beta}\right)_{fl,ldg} = -0.80\left(\frac{b_{fl}}{b_w} - 0.67\right) \tag{2.47}$$

In the case of smaller wing flap deflection when not in landing, the effect of wing flap deflection on the sidewash is proportional to the wing flap deflection angle [14]. This is shown in Equation 2.48, where δ_{fl} is the wing flap deflection and $\delta_{fl,ldg}$ the wing flap deflection during landing, assuming the latter is equal to the maximum flap deflection.

$$\left(\Delta\frac{\delta\sigma}{\delta\beta}\right)_{fl} = -0.80\left(\frac{b_{fl}}{b_w} - 0.67\right)\frac{\delta_{fl}}{\delta_{fl,ldg}} \tag{2.48}$$

Effect of engine nacelles on the wing on sidewash

The sixth effect contributing to the sidewash is the engine nacelles on the wing. Based on a comparison between the calculated sidewash of aircraft without nacelles and the measured sidewash of the same aircraft with nacelles on the wing, an average effect of nacelles on the wing on the sidewash was found. The value presented in Equation 2.49 can, depending on the aircraft type, be positive or negative. Based on the available data it is chosen to use a negative sign, since for similar aircraft types with more engines, the sidewash due to the the engine nacelles on the wing decreases. Note that this value also may be -0.04 instead of -0.03 because the Fokker / Obert method [14] gives different values throughout the report for unknown reasons.

$$\left(\Delta\frac{\delta\sigma}{\delta\beta}\right)_{NW} \approx +/-0.03 \tag{2.49}$$

Effect of engine nacelles on the rear-fuselage on sidewash

The seventh and final effect contributing to the sidewash is the engine nacelles on the rear-fuselage $\left(\Delta\frac{\delta\sigma}{\delta\beta}\right)_{NF}$. To quantify this effect the position of the nacelles on the rear-fuselage is needed. For this, the longitudinal and the vertical position are used. The lateral position is not used, because the nacelles are mounted on the fuselage, so therefore little variation in the lateral positioning. The longitudinal position is described by $\frac{x_{exh}-0\%c_{r_V}}{c_{r_V}}$, which is the distance between the longitudinal position of the engine exhaust, x_{exh}, and the longitudinal position of 0%-point of vertical tailplane root chord, $0\%c_{r_V}$, normalized by the vertical tailplane root chord, c_{r_V}. This distance is defined as positive when x_{exh} is aft of $0\%c_{r_V}$. Figure 2.11 visualizes this longitudinal positioning. The vertical position is described by $\frac{z_{cl,nac}}{D_{fus}}$, where $z_{cl,nac}$ is the vertical position of the nacelle center line, normalized by D_{fus}, the fuselage diameter. This is defined as positive when $z_{cl,nac}$ is above the fuselage center line. With the location of the nacelles known, Figure B.33 and Figure B.34 can be used to determine $\left(\Delta\frac{\delta\sigma}{\delta\beta}\right)_{NF}$. Both figures are combined and summarized in Figure B.35. This figure shows several cases for different vertical nacelle positions, $\frac{z_{cl,nac}}{D_{fus}}$, angle of attacks, α, and flap deflection angles, δ_{fl}.

$$\left(\Delta\frac{\delta\sigma}{\delta\beta}\right)_{NF} \tag{2.50}$$

Total sidewash

Combining all sidewash effects discussed before results in the total sidewash parameter Equation 2.51. Note that all terms are summed and subsequently multiplied by the effective-versus-free-stream dynamic pressure ratio and fuselage-vertical-tailplane lift carry-over effect. Also the effect of wing flap deflection in landing position on sidewash $\left(\Delta\frac{\delta\sigma}{\delta\beta}\right)_{fl,ldg}$ can be changed to $\left(\Delta\frac{\delta\sigma}{\delta\beta}\right)_{fl}$, when not in landing.

$$\begin{aligned}&\left(1+\frac{\delta\sigma}{\delta\beta}\right)\frac{q_V}{q}K_{FV} = \\ &\left(\left(1+\frac{\delta\sigma}{\delta\beta}\right)_{FV} + \left(\Delta\frac{\delta\sigma}{\delta\beta}\right)_{h_W} + \left(\Delta\frac{\delta\sigma}{\delta\beta}\right)_{\Gamma} + \left(\Delta\frac{\delta\sigma}{\delta\beta}\right)_{C_{l_\beta}} + \left(\Delta\frac{\delta\sigma}{\delta\beta}\right)_{fl,ldg} + \left(\Delta\frac{\delta\sigma}{\delta\beta}\right)_{NW} + \left(\Delta\frac{\delta\sigma}{\delta\beta}\right)_{NF}\right)\frac{q_V}{q}K_{FV}\end{aligned} \tag{2.51}$$

Figure 2.11: CONFIDENTIAL Position of rear-fuselage engine nacelles [14].

Be careful with the endplate correction factor as this equation sometimes uses the value 0.013 instead of 0.014. Also, be careful with the effect of engine nacelles on the wing on sidewash as this value sometimes is -0.04 instead of -0.03. For both, it is unknown why these values vary throughout the report of the Fokker / Obert method [14].

2.5.7. Control derivatives: Rudder

As discussed in section 2.1, the main purpose of the vertical stabilizer is to provide control over the aircraft. This control is provided by the rudder. The control derivative with respect to rudder deflection angle $\delta_{_R}$ is therefore required. This can be done with Equation 2.52, which shows the side-force-due-to-rudder-deflection coefficient, $(C_y)_{\delta_{_R}}$. This can be split into the side-force-due-to-rudder-deflection derivative, $C_{y_{\delta_{_R}}}$, and the rudder deflection angle, $\delta_{_R}$. In essence, this equation is very similar to the derivatives due to sideslip, only using $\frac{c_{l_\delta}}{c_{l_\alpha}}$ instead. This is the control effectiveness of the rudder, which is the effect of the rudder lift curve slope on the vertical tailplane lift curve slope. The value can be obtained from Figure B.36 by using the rudder-chord-to-tailplane-chord ratio, namely $c_{_R}/c_{_V}$. This value is based on the chord lengths shown in Figure 2.5 and Figure 2.4. In general rudder-chord-to-tailplane-chord ratio is even over the whole rudder height. However, if that is not the case the rudder-chord-to-tailplane-chord ratio at the half-rudder height, $^1/_2 h_{_R}$, can be used as suggested by ESDU [18]. By using $c_{_R}/c_{_V}$ in Figure B.36 and knowing $\frac{c_{l_\delta}}{c_{l_\alpha}} = \frac{\Delta\alpha_0}{\Delta\delta}$, the required value for $\frac{c_{l_\delta}}{c_{l_\alpha}}$ is obtained. In addition, Figure B.37 shows roughly the same graph as Figure B.36, but is based on 3-dimensional data rather than on airfoil sections and the rudder data is normalized to full-span rudders with $S_{_{V_R}}/S_{_V}$.

$$(C_y)_{\delta_{_R}} = C_{y_{\delta_{_R}}}\,\delta_{_R} = (C_{L_\alpha})_{_V}\,\frac{q_{_V}}{q}K_{_{FV}}K_{_{VH}}\frac{c_{l_\delta}}{c_{l_\alpha}}\frac{S_{_{V_R}}}{S_{_W}}\delta_{_R} \tag{2.52}$$

With the side-force-due-to-rudder-deflection now obtained, the rolling- and yawing-due-to-rudder-deflection can be easily found by multiplying them with their respective moment arms based on the exposed vertical tailplane. This results in Equation 2.53 and Equation 2.54. Observe that the moment arm for Equation 2.54 is increased by $0.30\bar{c}_{_V}$, since the rudder located is further aft than the $^1/_4\bar{c}_{_V}$. Also note that if there is a dorsal fin the yawing moment arm also needs to incorporate the effect of the presence of the dorsal fin. More on this in subsection 2.5.5 on the effect of the dorsal fin on vertical tailplane lift curve slope. Additionally, these derivatives are still expressed in the body frame and not in the stability frame as they use $l_{x_{_V}}$, $l_{z_{_V}}$ and not $l_{x_{S_{_V}}}$, $l_{z_{S_{_V}}}$, which should be accounted for. Finally, the sign of $(C_n)_{\delta_{_R}}$ is negative due to its relative direction to the aircraft CG.

$$(C_l)_{\delta_{_R}} = C_{l_{\delta_{_R}}}\,\delta_{_R} = (C_{L_\alpha})_{_V}\,\frac{q_{_V}}{q}K_{_{FV}}K_{_{VH}}\frac{c_{l_\delta}}{c_{l_\alpha}}\frac{S_{_{V_R}}}{S_{_W}}\frac{l_{z_{_{V_{ref}}}}}{b_{_W}}\delta_{_R} \tag{2.53}$$

$$(C_n)_{\delta_R} = C_{n_{\delta_R}} \delta_R = (C_{L_\alpha})_V \frac{q_V}{q} K_{FV} K_{VH} \frac{c_{l_\delta}}{c_{l_\alpha}} \frac{S_{V_R}}{S_W} \frac{l_{x_{V_{ref}}} + 0.30\bar{c}_V}{b_W} \delta_R \tag{2.54}$$

For the case with a maximum rudder deflection Equation 2.55, Equation 2.56 and Equation 2.57 are used. Generally, δ_R is about 35 deg for the maximum side force at c_R/c_V between 0.20 and 0.35, which is the normal range for the rudder-chord-to-tailplane-chord ratio. Also, the side force due to rudder deflection is linear up to $\delta_R = 25\ deg$, but between 25 and 35 deg it reduces by 10 to 15%, which is reflected by the 0.90 in the equations.

$$(C_{y_{max}})_{\delta_R} = 0.90 C_{y_{\delta_R}} \delta_{R_{max}} \tag{2.55}$$

$$(C_{l_{max}})_{\delta_R} = 0.90 C_{l_{\delta_R}} \delta_{R_{max}} \tag{2.56}$$

$$(C_{n_{max}})_{\delta_R} = 0.90 C_{n_{\delta_R}} \delta_{R_{max}} \tag{2.57}$$

2.5.8. Control derivatives: Aileron

The second and final contribution to control derivatives is the control derivative with respect to the aileron deflection angle δ_a, where $\delta_a = \left((\delta_a)_{right} - (\delta_a)_{left}\right)/2$. These derivatives are not provided by the Fokker / Obert method [14], thus other sources are used. According to Roskam [22], $C_{y_{\delta_a}}$ can be neglected. That still leaves the other two derivatives. These can be obtained with the so-called strip method, for which the geometry is shown in Figure 2.12. The aileron is seen as a simple flap. This method cuts the wing area with the aileron up into i small strips, with their respective strip surface area S_i, strip chord c_i, and strip flap chord c_{f_i}. Of each strip, the lift due to aileron deflection, $\left(\frac{\partial C_L}{\partial \delta_f}\right)'_i$, is determined, which is then used to calculate the moment around the aircraft centerline with a strip moment arm Y_i up to the MAC of the strip. The centerline is passing through the CG of the aircraft when seen from above in Figure 2.12. Therefore this moment is taken around the CG, just as all other moments calculated before. Each strip is also multiplied by an empirical correction factor K_{f_i} and by $cos(\Lambda_{hl_i})$, which is to account for the sweep angle at the hinge line. All the strip rolling moments are summed, resulting in the overall rolling-moment-due-to-aileron-deflection derivative $C_{l_{\delta_a}}$, presented in Equation 2.58 provided by Raymer [16]. The two in front of the summation sign is to account for both ailerons.

$$C_{l_{\delta_a}} = \frac{2 \sum K_{f_i} \left(\frac{\partial C_L}{\partial \delta_f}\right)'_i Y_i S_i \cos \Lambda_{hl_i}}{S_W b_W} \tag{2.58}$$

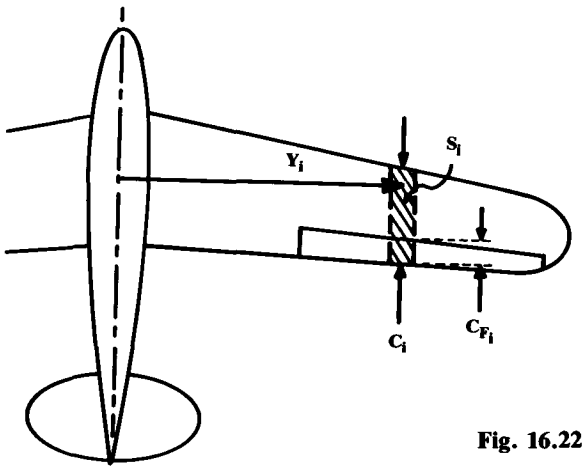

Figure 2.12: Aileron strip geometry [16].

To obtain the value for $\left(\frac{\partial C_L}{\partial \delta_f}\right)_i$ Equation 2.59 can be used. K_{f_i} adjusts for larger flap deflections and is used in both Equation 2.59 and Equation 2.58. The value is obtained from Figure B.39. It uses the flap deflection of the strip δ_{f_i} and the strip flap chord over strip chord ratio c_{f_i}/c_i. This ratio is taken at the MAC of the strip. $\left(\frac{\partial C_l}{\partial \delta_f}\right)_i$ (note the lower case l) is the theoretical lift increment for a plain flap and is obtained from Figure B.38. This again uses the strip flap chord over strip chord ratio and the thickness over chord ratio of the strip at the MAC, namely t_i/c_i. $\frac{S_i}{S_W}$ is the ratio of the strip area and the reference area (in this case the wing). Finally, $cos(\Lambda_{hl_i})$ accounts for the sweep angle at the hinge line of the strip. Note that the 0.9 is originally used to adjust for the tip losses of the flap, however, only the first and last strips have tip losses. It is not yet determined how to account for this. Potentially by using the value 0.95 for the first and last strip and 1.0 for all strips in between. Also, the hinge gap influences the lift increment. If the gap is unsealed, the lift increment is reduced by 15%.

$$\left(\frac{\partial C_L}{\partial \delta_f}\right)_i = 0.9 K_{f_i} \left(\frac{\partial C_l}{\partial \delta_f}\right)_i \frac{S_i}{S_W} \cos \Lambda_{hl_i} \tag{2.59}$$

Equation 2.60 provided by Raymer [16] is based on a simplified version from USAF DATCOM [2]. It uses the rolling-moment-due-to-aileron-deflection as seen in Equation 2.58, and is multiplied by the wing lift coefficient, C_{L_W}.

$$C_{n_{\delta_a}} = -0.2 C_{L_W} C_{l_{\delta_a}} \tag{2.60}$$

2.6. Critical design requirements

With the parametrization, design range, and method to size the vertical tailplane (stability analysis) known, the critical design requirements are the last step in designing a vertical tail. Critical design requirements are the (extreme) flight conditions in which a vertical tail must still provide a certain performance in terms of stability (and control). Apart from the extreme flight conditions, the static stability requirements should still be met of course. Therefore, the static stability requirements are discussed first in this chapter, and thereafter the extreme flight conditions. The main cases are shown below and will be discussed throughout this chapter.

- Static stability
- One engine inoperative (OEI)
- Crosswind landing
- Stall
- Dynamic stability
  - Dutch roll
  - Spiral
- Spin

Before starting, the velocities and rudder and aileron deflection angles are discussed. These vary for every critical design requirement.

CS-25: velocities

Most of the critical design requirements are specified in the certification specifications CS-25 for Large Aeroplanes [25] as compiled by EASA. These regulations use several different speeds, which are specified in Table 2.3.

To obtain the reference stall speed, V_{SR}, Equation 2.61 can be used. $V_{C_{L_{MAX}}}$ is the calibrated airspeed at the moment that the load factor-corrected lift coefficient is at the maximum, where the load factor-corrected lift coefficient is $\left(\frac{n_{zw} W}{q S_W}\right)$. Here, n_{zw} is the load factor normal to the flight path at $V_{C_{L_{MAX}}}$, W is the gross weight of the aircraft, q the dynamic pressure, and S_W the wing surface area.

$$V_{SR} \geq \frac{V_{C_{L_{MAX}}}}{\sqrt{n_{zw}}} \tag{2.61}$$

The landing speed V_{REF} is taken to be 1.23 times the reference landing stall speed V_{SR0}, which is assumed to have a 1-g load factor, shown in Equation 2.62, based on CS 25.125 [25].

$$V_{REF} = 1.23 V_{SR0} = 1.23 \frac{V_{C_{L}MAX}}{\sqrt{n_{zw}}} \tag{2.62}$$

Where $V_{C_{L}MAX}$ can be obtained through Equation 2.63, where $MTOW$ is used for W.

$$C_{L_{max_{1-g}}} = \frac{n_{zw} W}{\frac{1}{2}\rho V^2_{C_{L}MAX} S_W} \qquad \textit{, where } n_{zw} = 1 \tag{2.63}$$

Table 2.3: Speed types used by EASA [25].

Speed type	Definition	Source
V	Airspeed	AMC 25.177(c)
V_{SR}	Reference stall speed	CS 25.103(a)
$V_{C_{L}MAX}$	Calibrated airspeed at the moment that the load factor-corrected lift coefficient is at the maximum	CS 25.103(a)
V_{SR0}	Reference landing stall speed	CS 25.125
V_{SR1}	Reference stall speed at given condition	
V_{FE}	Maximum flap extended speed	AMC 25.21(g) 6.9.2 table 2
V_{LE}	Landing gear extended speed	CS 25.1515(b)
V_{FC}/M_{FC}	Maximum speed for stability characteristics dependent on Mach number with flaps and landing gear retracted	CS 25.253(b)
V_{MO}/M_{MO}	Maximum operating speed limit dependent on Mach number	AMC 25.21(g) 6.9.2 table 2
V_{CW}	Crosswind speed	AMC 25.177(c)
$V_2 + xx$	Airspeed approved for all-engines operating initial climb	AMC 25.177(d)1.3
V_{REF}	Reference landing speed	AMC 25.21(g) 6.9.2 table 2
$V_{REF} - 9.3\ km/h$	Reference landing speed minus 9.3 km/h	AMC 25.21(g) 6.9.2g

Rudder and aileron deflections

Most of the critical design requirements use varying rudder and aileron deflection angles. Table 2.4 shows these angles for the different critical design requirements and from various sources. For one engine inoperative and crosswind landing, the maximum aileron deflection angle values could not be found. Based on this data, the maximum allowable rudder deflection used for this research is 35 deg, and the maximum aileron deflection is 25 deg.

Table 2.4: Maximum rudder and aileron deflection angles for different critical design requirements.

	Critical design requirement	**Obert** [14]	**Raymer** [16]	**Roskam** [19]	**Torenbeek** [15]
$\delta_{R_{max}}$	General	25 deg (linear) 35 deg (max side force)	-	25 deg 35 deg (double hinged)	25 - 30 deg
	One engine inoperative	-	20 deg	-	-
	Crosswind landing	-	20 deg	-	-
$\delta_{a_{max}}$	General	-	30 deg	25 deg	20 deg
	One engine inoperative	-	-	-	-
	Crosswind landing	-	-	-	-

2.6.1. Static stability

The first critical design requirement is static stability. In general it can be said that C_{l_β} is desired to be negative, and C_{n_β} is desired to be positive (also C_{y_β} is negative) to obtain static stability [22]. CS25.177 [25] states the static stability requirements in a more precise manner. The static directional stability has to be positive. This requirement must hold at any flap and landing gear deflection and the symmetrical power condition (all engine operative) at a speed between $1.13V_{SR1}$ and V_{FE}, V_{LE} or V_{FC}/M_{FC}. The static lateral stability may not be negative. Again, this requirement must hold at any flap and landing gear deflection and the symmetrical power condition (all engine operative) at a speed between: a) $1.13V_{SR1}$ and V_{FE}, V_{LE} or V_{FC}/M_{FC} or b) V_{MO}/M_{MO} and V_{FC}/M_{FC}, unless the divergence is gradual, easily recognizable and controllable.

Static stability can be established by making sure the vertical tailplane uses relatively small aspect ratios ($A_V < 1.8$), a large vertical tail span, large sweep angles, and optionally a dorsal fin [15]. Regarding the aspect ratio, it can be said that for this research $A_V \leq 1.5$ as a result of using the Fokker / Obert method [14] described in section 2.5. The large vertical tail span has a big impact on the side force derivative, whilst at the first order not dependent on the shape and chord length [14][17]. As for the sweep angle and dorsal fin, they both increase the lift coefficient maximum as well as the angle of the sideslip at which stall occurs. For small angles of sideslip, the dorsal fin also does not change the yaw stability.

2.6.2. One engine inoperative

The second critical design requirement is the one engine inoperative condition (OEI), which is the case when one engine of an aircraft with two wing-mounted engines seizes. Technically one could also use this condition for an aircraft with two fuselage-mounted engines, but the moment arms would be much smaller and therefore the influence on the rolling and yawing moment much smaller. Aircraft with more than two engines could also be analyzed, but for simplicity, a two-engine configuration is used, since this is most common. The critical design requirement for the OEI condition as stated in AMC 25.143(b)(1) [25] is that when an engine becomes completely and instantly inoperative, the aircraft control should be regained without reaching a dangerous fight condition. There are two flight conditions to be considered for this case, namely take-off and steady flight.

The conditions for take-off consist of:

- Flap settings for take-off
- Lowest speed for a steady climb
- Engines at maximum take-off thrust
- Propeller control settings for take-off (does not apply to jet/turbofan aircraft)
- Landing gear retracted
- Trimmed

The conditions for steady flight consist of:

- Flaps retracted
- Speed of 1.23V_{SR1}
- Engines at maximum continuous thrust
- Propeller control settings for steady flight (does not apply to jet/turbofan aircraft)
- Landing gear retracted
- Trimmed

The failure of the engine has to occur flying straight and with level wings. Two seconds after the engine failure the recovery should be initiated by the pilot and should be done with normal control inputs only (no trim controls). When recovering, the bank angle may not exceed 45 deg. Additionally, AMC 25.121 [25] states that in climb the maximum allowable bank angle is 3 deg. To analyze this condition a stability analysis can be performed, which is done in the next section. A representation of the OEI condition is visualized in Figure 2.13.

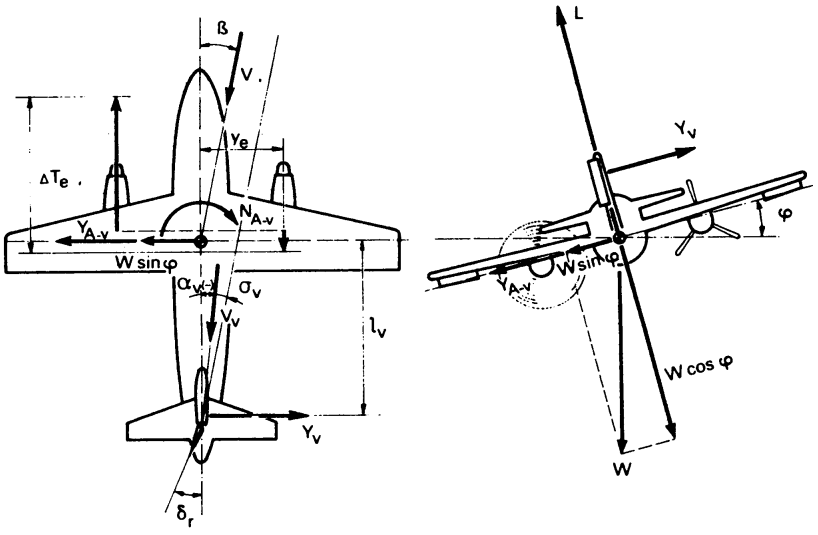

Figure 2.13: OEI condition for aircraft with two wing-mounted engines [15] (note that $Y_e = l_{y_E}$ and $l_V = l_{x_V}$ in text).

One engine inoperative stability analysis

First, there is a yawing moment due to the difference in thrust as seen in Equation 2.64 [15]. When one engine is fully inoperative, the ΔT_{E_o} is the thrust of the operative engine, where E_o is the operative engine.

$$(N)_{E_o} = \Delta T_{E_o} l_{y_E} \tag{2.64}$$

Additionally, Equation 2.65 shows the yawing moment due to the additional drag of the inoperative engine ΔD_{E_i}, where E_i is the inoperative engine. The calculation for the drag due to one engine inoperative can be found in Equation 2.82 in the section on drag of an inoperative engine.

$$(N)_{E_i} = \Delta D_{E_i} l_{y_E} \tag{2.65}$$

The previous two results are combined in Equation 2.66, which is the total yawing moment due to one engine being inoperative.

$$(N)_{OEI} = (N)_{E_o} + (N)_{E_i} = \Delta T_{E_o} l_{y_E} + \Delta D_{E_i} l_{y_E} = (\Delta T_{E_o} + \Delta D_{E_i}) l_{y_E} \tag{2.66}$$

The yawing moment can be normalized with Equation 2.67.

$$(C_n)_{OEI} = \frac{(N)_{OEI}}{q S_W b_W} \tag{2.67}$$

This gives Equation 2.68.

$$(C_n)_{OEI} = \frac{(\Delta T_{E_o} + \Delta D_{E_i}) l_{y_E}}{q S_W b_W} \tag{2.68}$$

Next to the contribution of the engines themselves, there is also a contribution of the weight of the aircraft to the side force due to the bank angle ϕ, shown in Equation 2.69 [15].

$$(Y)_{bank} = W \sin\phi = L \tan\phi \approx L\phi \quad \text{for } \phi \leqslant 5\, deg \tag{2.69}$$

The side force can be normalized with Equation 2.70.

$$(C_y)_{bank} = \frac{(Y)_{bank}}{q S_W} \tag{2.70}$$

This gives Equation 2.71.

$$(C_y)_{bank} = \frac{L\phi}{qS_W} \tag{2.71}$$

Taking the derivative of $(C_y)_{bank}$ with respect to ϕ results in Equation 2.72.

$$C_{y_\phi} = \frac{L}{qS_W} \tag{2.72}$$

Combining Equation 2.68 and Equation 2.72 with the stability derivatives from Equation 2.15 gives a set of equations as seen in Equation 2.73. The maximum rudder deflection angle for one engine inoperative may be 35 deg and the maximum aileron deflection angle may be 25 deg. As explained earlier, the maximum allowable bank angle during climb is 3 deg. The maximum sideslip angle is not prescribed, however, the vertical tailplane may not stall, thus the sideslip angle from Equation 2.83 can be used. With all above the required vertical tailplane size in case of one engine inoperative can be calculated.

$$\begin{Bmatrix} C_y \\ C_l \\ C_n \end{Bmatrix} = \begin{bmatrix} C_{y_\beta} & C_{y_{\delta_R}} & C_{y_{\delta_a}} & C_{y_\phi} \\ C_{l_\beta} & C_{l_{\delta_R}} & C_{l_{\delta_a}} & 0 \\ C_{n_\beta} & C_{n_{\delta_R}} & C_{n_{\delta_a}} & 0 \end{bmatrix} \begin{Bmatrix} \beta \\ \delta_R \\ \delta_a \\ \phi \end{Bmatrix} + \begin{Bmatrix} 0 \\ 0 \\ (C_n)_{OEI} \end{Bmatrix} = \begin{Bmatrix} 0 \\ 0 \\ 0 \end{Bmatrix} \tag{2.73}$$

Drag of an inoperative engine

The drag components are based on the method proposed by Torenbeek [15]. The drag of an inoperative engine, shown in Equation 2.82, consists of three parts: windmilling drag, propeller drag, and drag due to asymmetric flight. First, the windmilling drag is the drag that comes from the windmilling of the engine, which is when the propeller or blades in a jet/turbofan freely rotate. This drag can be split up into external and internal components. The external drag originates from the inlet spillage, which is not a well-understood phenomenon but can be estimated. The internal component of the windmilling drag is the difference between the flow velocities of the incoming and exiting flow of the engine multiplied by the windmilling mass flow. It is assumed that the static nozzle exit pressure is the same as the ambient pressure and the nozzle exit temperature is the same as the sum of the static temperature and 0.8 times the change in temperature from stagnation. This results in a combined windmilling drag area described by Equation 2.74. The value for $\frac{V_{nz}}{V}$ depends on the type of engine used as seen in Table 2.5. Note that the windmilling drag must be calculated separately for the bypass engines with multiple nozzles (hot and cold).

$$\Delta (C_D S)_{wm} = 0.0785 D_i^2 + \frac{2}{1 + 0.16M^2} A_{nz} \frac{V_{nz}}{V} \left(1 - \frac{V_{nz}}{V}\right) \tag{2.74}$$

Table 2.5: Values for $\frac{V_{nz}}{V}$ for various engine types based on [15].

Engine type / component	Value
Straight turbojet and turboprop engines	0.25
Low bypass ratio engines, mixed flow	0.42
Primary airflow of high bypass engines	0.12
Fan airflow of high bypass engines	0.92

Second, the propeller drag, as shown in Equation 2.75, uses the number of propeller blades and diameter, B_p and D_p, respectively. This value can be neglected for jet/turbofan engines as will be done in this research.

$$\Delta (C_D S)_{prop} = 0.00125 B_p D_p^2 \tag{2.75}$$

Third, the drag due to asymmetric flight consists of five components, namely induced drag as a result of vertical tail normal force and change in lift distribution, profile drag from control surface deflection (rudder and ailerons) and components in the engine (propeller) slipstream, and drag of the airframe as a consequence of sideslipping. The induced drag as a result of the vertical tail normal force is presented

in Equation 2.76 with Equation 2.77, where the effective aspect ratio is $A_{V_{eff}}$, which can be obtained from Figure B.17.

$$\Delta\left(C_D S\right)_{as_V} = \frac{\left(C_y\right)_V^2 S_V}{\pi A_{V_{eff}}} + \left(C_y\right)_V S_V \sin\sigma_V \tag{2.76}$$

$$\left(C_y\right)_V = \frac{\Delta T_{E_o+wm+prop}}{q_V S_V} \frac{l_{y_E}}{l_{x_V}} \tag{2.77}$$

The profile drag from rudder deflection is covered by Equation 2.78.

$$\Delta\left(C_D S\right)_{as_{\delta_R}} = \frac{2.3}{\pi}\sqrt{S_R S_V}\left(A_{V_{eff}}\right)^{-4/3}\left(\cos\Lambda_{1/4c_V}\right)^{1/3}\left(C_y\right)_V^2 \tag{2.78}$$

By combining all the equations above, the combined drag area of an inoperative engine can be calculated with Equation 2.79, Equation 2.80, and Equation 2.81. Note that the yawing moment arm should be adjusted for the effect of the dorsal fin as well as being expressed in the stability frame.

$$\Delta\left(C_D S\right)_{E_i} = K_{as}\left(\frac{thrust\ per\ engine}{q} + \Delta\left(C_D S\right)_{wm} + \Delta\left(C_D S\right)_{prop}\right)^2 + K_\sigma \frac{thrust\ per\ engine}{W} \tag{2.79}$$

$$K_{as} = \left(\frac{l_{y_E}}{l_{x_V}}\right)^2 \frac{1}{S_V}\frac{1}{\pi A_{V_{eff}}}\left(1 + 2.3\sqrt{\frac{S_R}{S_V}}\left(A_{V_{eff}} / \cos\Lambda_{1/4c_V}\right)^{-1/3}\right) \tag{2.80}$$

$$K_\sigma = \frac{l_{y_E}}{l_{x_V}}\frac{d\sigma_V}{dC_L} S_W \tag{2.81}$$

Finally, to obtain the actual drag due the inoperative engine Equation 2.82 is used.

$$\Delta D_{E_i} = \Delta\left(C_D S\right)_{E_i} q \tag{2.82}$$

One engine inoperative design requirements and recommendations

A yaw damper can be used, which changes the rudder setting to counteract the unwanted yaw due to the inoperative engine. The yaw damper is controlled by the autopilot [15]. Making sure the tailplane is not too large can be done with the following [15]:

- Engines not too far outboard
- Twin vertical tail
- Double-hinged rudder
- Not too low vertical tailplane aspect ratio
- Increase vertical tailplane moment arm

2.6.3. Crosswind landing

The third critical design requirement is the ability to perform crosswind landings. Crosswind landings are landings under a (large) sideslip angle. Various sources state that the vertical tail must be able to deal with sideslip angles up to 25 deg [14][17][15]. The critical design requirement specified by CS 25.177 [25] makes a distinction between steady, straight sideslips and full rudder sideslips. According to AMC 25.177(c) [25] the appropriate sideslip angle for steady, straight sideslips is dependent on the airspeed and can be calculated with Equation 2.83, with $V_{CW} = 30\ knots$, and V in $KCAS$. The maximum allowable rudder deflection angle for crosswind landing for steady, straight sideslips may not exceed half the maximum rudder deflection angle of 17.5deg and the maximum aileron deflection angle is 25 deg. The maximum bank angle is not prescribed, and therefore 3 deg is assumed, which is the same as for the OEI condition.

$$\beta = arcsin\left(\frac{V_{CW}}{V}\right) \tag{2.83}$$

For full rudder sideslips, according to AMC 25.177(d), no rudder reversal may occur, and for increased sideslip angles, a larger rudder deflection is required. In this case, the maximum allowable rudder deflection is 35 deg and the aileron, and bank angles are 25 deg and 3 deg again. As the rudder deflection is known, the rudder reversal can be checked by comparing the signs of the associated sideslip angles of the straight, steady sideslips, and full rudder sideslips, as they should be the same. The second criterion is met when the sideslip angle for full rudder sideslips is larger than the straight, steady sideslip angle, since also here the rudder deflections are known. The velocities for the full rudder sideslips vary for different conditions seen in Table 2.6. Equation 2.84 shows the set of equations that is used to assess the crosswind landing condition.

$$\begin{Bmatrix} C_y \\ C_l \\ C_n \end{Bmatrix} = \begin{bmatrix} C_{y_\beta} & C_{y_{\delta_R}} & C_{y_{\delta_a}} & C_{y_\phi} \\ C_{l_\beta} & C_{l_{\delta_R}} & C_{l_{\delta_a}} & 0 \\ C_{n_\beta} & C_{n_{\delta_R}} & C_{n_{\delta_a}} & 0 \end{bmatrix} \begin{Bmatrix} \beta \\ \delta_R \\ \delta_a \\ \phi \end{Bmatrix} = \begin{Bmatrix} 0 \\ 0 \\ 0 \end{Bmatrix} \tag{2.84}$$

Table 2.6: Speed and power conditions for full rudder sideslips with all engines operative, where flight condition dictates flap and landing gear deflection based on AMC 25.177(d)1.3 [25].

Flight condition	**Speed**	**Power**
Take-off	$V_2 + xx$ to V_{FE} or V_{LE}	Take-off power
Flaps up	$1.23V_{SR}$ to V_{LE} or V_{MO}/M_{MO}	Maximum continuous power
Approach	$1.23V_{SR}$ to V_{FE} or V_{LE}	Idle to go-around power
Landing	$V_{REF} - 9.3\ km/h$ to V_{FE} or V_{LE}	Idle to go-around power (at V_{REF} km/h to V_{FE}/V_{LE}) Idle (at $V_{REF} - 9.3\ km/h$)

2.6.4. Stall

The fourth critical design requirement is that the vertical stabilizer should not stall when experiencing high sideslip angles and deflection of the rudder in either direction in line with CS 25.177 [25] for steady, straight sideslips and full rudder sideslips. The stall angle can be calculated with the USAF DATCOM approach [2], which is an empirical method that makes a distinction between low- and high-aspect ratio wings. High-aspect-ratio wings are defined by Equation 2.85, low-aspect-ratio wings by Equation 2.86, and the borderline case by Equation 2.87, where C_1 is an empirical taper ratio constant [2]. For all of the cases, the wing is assumed to be straight-tapered, have no twist, and have a constant airfoil section.

$$A > \frac{4}{(C_1 + 1)cos(\Lambda_{LE})} \tag{2.85}$$

$$A < \frac{3}{(C_1 + 1)cos(\Lambda_{LE})} \tag{2.86}$$

$$\frac{3}{(C_1 + 1)cos(\Lambda_{LE})} \leq A \leq \frac{4}{(C_1 + 1)cos(\Lambda_{LE})} \tag{2.87}$$

In the subsonic regime ($0.2 \leq M \leq 0.6$), the high-aspect-ratio wing stall angle is calculated with Equation 2.88 and Equation 2.89. In these equations, the first term is for Mach of 0.2, whilst the second term is for the increase between Mach 0.2 to 0.6. All terms are obtained from empirical data [2] and the zero-lift angle of attack α_0 can be assumed zero for vertical tailplanes as they are symmetrical.

$$C_{L_{max}} = \left(\frac{C_{L_{max}}}{c_{l_{max}}}\right) c_{l_{max}} + \Delta C_{L_{max}} \tag{2.88}$$

$$\alpha_{C_{L_{max}}} = \frac{C_{L_{max}}}{C_{L_\alpha}} + \alpha_0 + \Delta\alpha_{C_{L_{max}}} \tag{2.89}$$

The low-aspect-ratio wing stall angle in subsonic conditions is calculated by Equation 2.90. Again the terms are obtained through empirical data [2], where the first (base) term is dependent on aspect- and taper ratio, sweep angle, and Mach number. The second term is a shift to this base value again dependent on aspect- and taper ratio, sweep angle, and Mach number.

$$\alpha_{C_{L_{max}}} = \left(\alpha_{C_{L_{max}}}\right)_{base} + \Delta\alpha_{C_{L_{max}}} \tag{2.90}$$

For the subsonic borderline case, either the high- and low-aspect ratio approach may be used.

For the transonic regime ($0.6 < M \leq 1.2$), there is no method available for high-aspect-ratio wings. For the low-aspect-ratio wings, Equation 2.91 is used, where the first term is calculated with the method for subsonic speeds (Equation 2.90) at a Mach number of 0.6. The second term is the change due to Mach number between 0.6 and 1.2. Again all of the terms are obtained through empirical data [2].

$$\left(\alpha_{C_{L_{max}}}\right)_M = \left(\alpha_{C_{L_{max}}}\right)_{M=0.6} + \Delta\alpha_{C_{L_{max}}} \tag{2.91}$$

Finally, the stall angle is also affected by rudder deflection, which is accounted for with a method by Raymer [16]. In Equation 2.92, $\left(\alpha_{C_{L_{max}}}\right)_{\delta_R=0}$ is the stall angle without rudder deflection calculated with the USAF DATCOM method described before. This value is adjusted by a change in zero-lift angle, which consists of the change zero-lift angle itself, $\Delta\alpha_{0L}$, and an adjustment for the amount of the rudder deflection relative to the maximum rudder deflection.

$$\alpha_{C_{L_{max}}} = \left(\alpha_{C_{L_{max}}}\right)_{\delta_R=0} - \Delta\alpha_{0L}\left(\frac{\delta_R}{\delta_{R_{max}}}\right) \tag{2.92}$$

The zero-lift angle is calculated with Equation 2.93, where the airfoil zero-lift angle is assumed to be 15 deg for landing and 10 deg for take-off, according to Raymer [16]. This value is proportional to the flapped surface and adjusted for the hinge line sweep angle.

$$\Delta\alpha_{0L} = \left(\Delta\alpha_{0L}\right)_{airfoil}\left(\frac{S_{flapped}}{S_{ref}}\right)cos(\Lambda_{HL}) \tag{2.93}$$

As a design recommendation, the stall angle can be increased by changing the sweep angle and adding a dorsal fin, as they both increase the lift coefficient maximum as well as the angle of the sideslip at which stall occurs. For small angles of sideslip, the dorsal fin also does not change the yaw stability. Also note that the earlier requirement, that the vertical tail may not be in the efflux of the engines [15], applies to the stall condition as well. Refer to subsection 2.2.2 on how to apply this requirement.

2.6.5. Dynamic stability

The two dynamic stability cases to consider are Dutch roll and spiral.

Dutch roll

The Dutch roll is an oscillatory yawing and rolling motion due to a perturbation, shown in Figure 2.14. According to CS 25.181 (b) [25], at a speed between $1.13V_{SR}$ and V_{FE}, V_{LE} or V_{FC}/M_{FC}, Dutch roll must be damped with controls free as well as possible to be controlled by the pilot with primary controls. One way to ensure that the Dutch roll can be damped is by ensuring C_{n_β} is of a relatively large positive value [22][23]. It is common to have $0.04 \leq C_{n_\beta} \leq 0.10$ for subsonic aircraft with one engine and $0.10 \leq C_{n_\beta} \leq 0.25$ for transport aircraft. However, when wing sweep is present, the lift coefficient and flap setting also become important. Therefore, to ensure the Dutch roll is properly damped, a yaw damper is used. This yaw damper changes the rudder setting to counteract the unwanted yaw of the Dutch roll. The yaw damper is controlled by the autopilot [15]. In addition, the C_{l_β} is desired to be of a relatively small negative value to dampen the Dutch roll [22][23].

Spiral

Spiraling is yawing to one side and over time an increased rolling motion due to a perturbation. This results in a downward spiral trajectory with an increasing bank angle over time, shown in Figure 2.15. It is desired to dampen this spiraling motion. According to CS 25.181 (a) [25], at a speed between $1.13V_{SR}$ and V_{FE}, V_{LE} or V_{FC}/M_{FC}, it must be possible to damp the spiraling motion with the primary controls free as well as fixed. For increased spiraling motion damping a relatively large negative C_{l_β} is desired and a relatively small positive value for C_{n_β} [22][23]. Nevertheless, with the use of an autopilot, a bit of spiral instability is allowable [15].

Dutch roll versus Spiral

As established before, Dutch roll and spiral need to be damped, but the means to do that are conflicting in terms of C_{l_β} and C_{n_β}, as visualized in Figure 2.16. To obtain enough damping for both, the vertical tailplane surface, S_V, and vertical tail moment arm, l_{x_V}, can be increased, which increases C_{n_β} and the wing dihedral, Γ_W, can be increased to decrease C_{l_β} [23]. For the Dutch roll damping, the negative effect of the decrease of the value of C_{l_β} is outweighed by the increase in C_{n_β} [22].

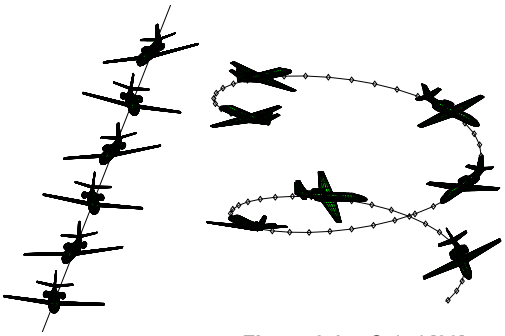

Figure 2.14: Dutch roll [23]

Figure 2.15: Spiral [23]

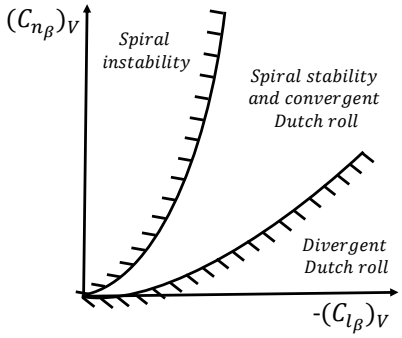

Figure 2.16: Lateral stability diagram based on [23]

2.6.6. Spin

When in a spin the aircraft must be able to restore to non-spinning flight. Spin is different from a spiral, since spin is the result of a stall, whilst the spiral is the result of a perturbation. The spin can be controlled with the rudder and therefore the rudder must work under these conditions. One important factor is the horizontal stabilizer placement, because the horizontal stabilizer may stall during the spin, making the rudder ineffective. The horizontal stabilizer must therefore be placed in such a way that a part or the whole rudder is not in the separated flow region behind the horizontal tail. This is shown in Figure 2.17. It is advisable that for a 45 deg angle of attack, a third of the rudder surface area must be out of the separated flow region from the horizontal tailplane. This is based on the assumption that in this case, the horizontal tailplane separated flow region has an angle of 60 deg from the leading edge and 30 deg from the trailing edge [15]. Other improvements are the use of a dorsal fin or anti-spin fillets, which are dorsal fins for the horizontal stabilizer [26].

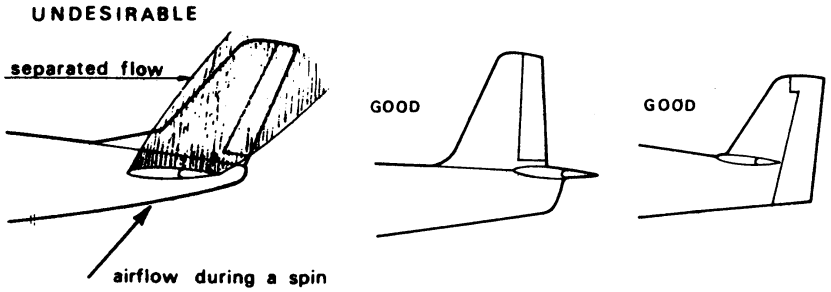

Figure 2.17: Rudder affected by the horizontal stabilizer placement [15].

2.6.7. Overview of critical design requirements

Table 2.7 shows the critical design requirements for every critical case. Subsequently, design recommendations to fulfill the critical design requirements are also summarized.

Table 2.7: Overview of critical design requirements

Case	Requirements	Design recommendations
Static stability	CS25.177 [25]: At any flap and landing gear deflection and the symmetrical power condition (all engine operative): 1) static directional stability must be positive at a speed between $1.13V_{SR1}$ and V_{FE}, V_{LE} or V_{FC}/M_{FC}. 2) static lateral stability may not be negative at a speed between: a) $1.13V_{SR1}$ and V_{FE}, V_{LE} or V_{FC}/M_{FC} b) V_{MO}/M_{MO} and V_{FC}/M_{FC}, unless the divergence is gradual, easily recognizable and controllable.	· Small vertical tailplane aspect ratio ($A_V < 1.8$ [15] or $A_V \leq 1.5$ when using Fokker / Obert method [14]) · Large vertical tailplane span [15][14] · Large vertical tailplane sweep angles [15][14] · Dorsal fin (optionally) [15][14]

One engine inoperative	AMC 25.143(b)(1) [25]:
	The aircraft control should be regained without reaching a dangerous fight condition using normal control inputs only (no trim controls). There are two flight conditions to be considered for this case, namely take-off and steady flight. The bank angle may not exceed 45 deg when recovering.
	AMC 25.121 [25]:
	In climb the maximum allowable bank angle is 3 deg.
		· Install a yaw damper [15]
		· Making sure the tailplane is not too large:
		  · Engines not too far outboard [15]
		  · Twin vertical tail [15]
		  · Double-hinged rudder [15]
		  · Not too low vertical tailplane aspect ratio [15]
		  · Increase vertical tailplane moment arm [15]

Crosswind landing	AMC 25.177(c) [25]: *Steady, straight sideslips* Crosswind landings can be performed up to a sideslip angle $\beta = arcsin\left(\frac{V_{CW}}{V}\right)$, with $V_{CW} = 30\ knots$. The maximum allowable rudder deflection angle may not exceed half the maximum rudder deflection. AMC 25.177(d) [25]: *Full rudder sideslips* No rudder reversal may occur, and for increased sideslip angles, a larger rudder deflection is required.	· Ensure enough S_V [3] and l_{x_V} · Ensure rudder size large enough
Stall	The vertical stabilizer should not stall when experiencing high sideslip angles and deflection of the rudder in either direction.	· Large vertical tailplane sweep angles [15][14] · Dorsal fin (optionally) [15][14] · Vertical tailplane not in efflux of engines (assume efflux as cone with 6 deg half-angle [15])
Dynamic stability: Dutch roll	CS 25.181 (b) [25]: At a speed between $1.13V_{SR}$ and V_{FE}, V_{LE} or V_{FC}/M_{FC}, Dutch roll must be damped with controls free as well as possible to be controlled by the pilot with primary controls.	· Increase C_{n_β} by increasing S_V and l_{x_V} [22][23] (note that this is directly coupled to the spin design recommendation) · Subsonic aircraft with one engine $0.04 \leq C_{n_\beta} \leq 0.10$ · Transport aircraft $0.10 \leq C_{n_\beta} \leq 0.25$ · If wing sweep, then install a yaw damper [15] (yaw damper is standard for modern aircraft) · Autopilot for yaw damper control [15]
Dynamic stability: Spiral	CS 25.181 (a) [25]: At a speed between $1.13V_{SR}$ and V_{FE}, V_{LE} or V_{FC}/M_{FC}, the spiraling motion must be damped with the primary controls free as well as fixed.	· Decrease C_{l_β} (larger negative value) by increasing Γ_W [22][23] (note that this is directly coupled to the Dutch roll design recommendation) · Autopilot allows minimal spiral instability [15]
Spin	Restore to non-spinning flight with pilot control inputs.	· Third of the rudder surface area outside of separated flow region from horizontal tailplane [15] (when 45 deg angle of attack and separated flow region 60 deg at leading edge and 30 deg at trailing edge) · Dorsal fin or antispin fillets [26]

3

Laminar flow control

3.1. Boundary layer theory

To explain the concepts of natural laminar flow and (hybrid) laminar flow control in subsection 3.2.1, subsection 3.2.2 and subsection 3.2.3, a basic understanding of boundary layer theory is required. Flow around a body can be divided into two types; inviscid and viscous flow. Inviscid flow is assumed to have no friction, diffusion, or thermal conduction. This occurs when the Reynolds number becomes infinite. In reality, this does not occur, but when the Reynolds number is large enough, inviscid flow is a satisfactory representation of the flow. However, a discrepancy between this inviscid representation and the real world is observed when looking at the flow along a surface. At the surface, the no-slip condition must be satisfied, but this is not the case for the inviscid solution. The no-slip condition states that the velocities at the wall are zero. To satisfy the no-slip condition, viscous flow comes into play in the form of a boundary layer. The boundary layer, first described by Prandtl in 1904 [27], is a thin layer of fluid flowing along a surface, where, due to the friction between the surface and the fluid, the flow is altered [28][29].

3.1.1. Viscous flow

For viscous flow, the viscosity, diffusion, and thermal conduction need to be taken into account. However, it is assumed that there is no gradient in the chemical composition of the air and therefore (mass) diffusion may be neglected. This leaves us with viscosity and thermal conduction [29].

The viscosity has several effects on the flow. First, when the fluid is moving along the surface, there is a friction force between the two. This is expressed as the shear stress at the wall τ_w in Equation 3.1, where friction force is expressed per unit area. This shear stress can be used to obtain the skin friction coefficient in Equation 3.2 and results in the so-called skin friction drag D_f [29].

$$\tau_w = \mu \left(\frac{\partial u}{\partial y} \right)_w \tag{3.1}$$

$$c_f = \frac{\tau}{q_\infty} = \frac{\tau_w}{\frac{1}{2}\rho_e u_e^2} \tag{3.2}$$

Next to the shear stress, an adverse pressure gradient is imposed on the flow by the shape of the body. The adverse pressure gradient slows the flow down as it goes further downstream. If the flow slows down enough it can reverse its direction, called reversed flow. This may cause flow separation from the surface, which in turn makes the flow see a larger effective body. The changed pressure distribution due to this larger effective body results in additional drag. This type of drag is called *pressure drag due to separation*, D_p, also known as form drag. To summarize, the viscous boundary layer has two types of drag associated with it, D_f due to shear stress and D_p due to separation. The combined drag is called profile drag (2D) or parasite drag (3D) [29].

In addition to viscosity that results in shear stress and separation, there is another aspect of viscous flow of importance, namely thermal conduction. When the fluid is flowing along a body, the flow is

slowed down due to friction, which increases the temperature in the fluid. This change from kinetic energy to thermal energy in the boundary layer is called viscous dissipation. Since there now is a temperature difference between the fluid and the body, the heat will go from the warm fluid to the colder body. This is called aerodynamic heating [29].

3.1.2. Laminar versus turbulent

The shear stress, separation, and aerodynamic heating discussed before all depend on the type of flow or, in other words, whether the flow is laminar or turbulent. Laminar flow is when the flow of the fluid elements is smooth, steady, and regular [29][30]. Turbulent flow is when the flow of the fluid elements is fluctuating, agitated, and irregular [29][30]. Whether the flow is laminar or turbulent, can greatly change the velocity profile in the boundary layer. For turbulent flow, the flow is more energized close to the wall, meaning that the flow velocity near the wall is higher for turbulent flow. This results in that for turbulent flow, the shear stress and aerodynamic heating are larger compared to laminar flow. Separation however is less prone to occur for turbulent flow and the region of separation is not as large as for laminar flow [29].

With all previous sections in mind, Figure 3.1 summarizes everything. In addition, it shows the difference between slender and blunt bodies. The main difference is that for slender bodies the skin friction drag is much larger than the pressure drag due to separation. For blunt bodies, this is the other way around. This information can be combined with the fact that for laminar flow the reduction in skin friction drag outweighs the increase in pressure drag due to separation and for blunt bodies vice versa. Therefore, the overall conclusion is that to reduce drag for slender bodies, the laminar flow should be prolonged, whilst for blunt bodies, turbulent flow is preferable.

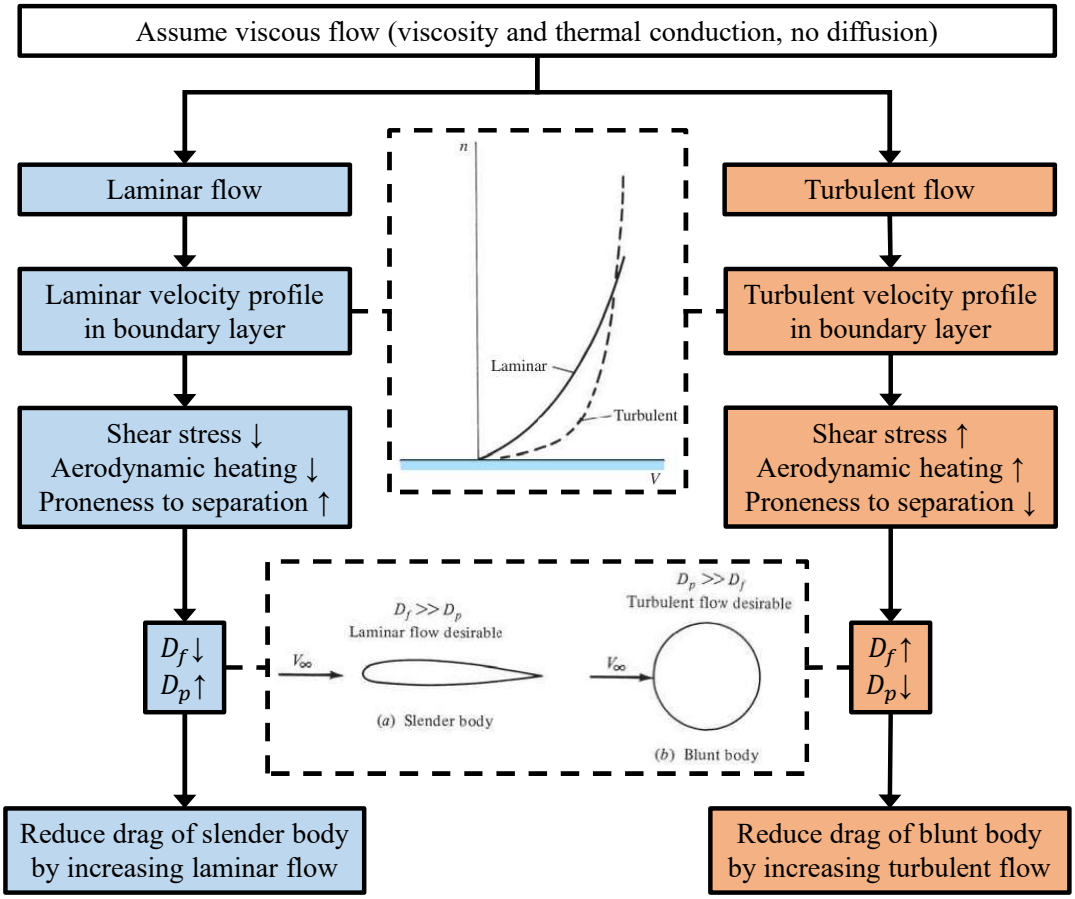

Figure 3.1: Laminar versus turbulent flow effect on boundary layer and drag. Dashed encircled images from [29].

3.1.3. Laminar-to-turbulent transition

Earlier the distinction was made between laminar and turbulent flow, however for most flows along a surface, they are both present (without any deliberate flow control or tripping). When there is a flow along a surface the flow starts as laminar and can change somewhere downstream to turbulent. This change from laminar to turbulent flow is called transition and the location of transition x_{cr} is measured as a distance from the leading edge, as seen in Figure 3.2. This transition location depends on surface roughness, the amount of turbulence in the freestream, favorable/adverse pressure gradients, and the temperature of the fluid by the surface. Equation 3.3 shows the Reynolds number at which transition occurs and is called the critical Reynolds number [29].

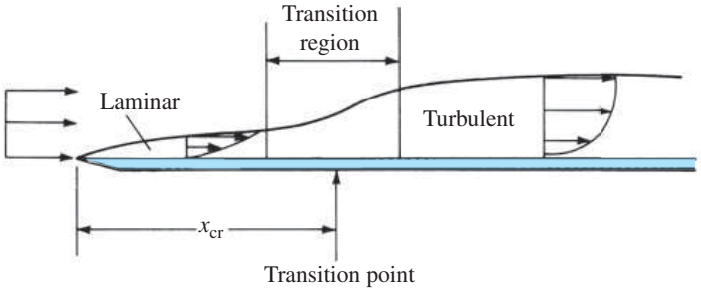

Figure 3.2: Boundary layer transition [29].

$$Re_{cr} = \frac{\rho_\infty V_\infty x_{cr}}{\mu_\infty} \tag{3.3}$$

There are three main mechanisms that initiate transition for swept wings:

- Tollmien Schlichting instabilities (TSI)
- crossflow instabilities (CFI)
- attachment line transition (ALT)

The precise inner workings of these instabilities are not relevant to the scope of this research. What is relevant is that for a swept wing one of the mechanisms may be dominant over the others, depending on the Reynolds number. This is visualized in Figure 3.3, which shows the dominant transition mechanism for an infinite $30\,deg$-swept wing at Mach 0.82 for a range of Reynolds numbers. In general, it can be said that for transition at low Reynolds number laminar separation and TSI are dominant, and for higher Reynolds numbers CFI and ALT are dominant [7]. Figure 3.4 shows that the transition location is also dependent on the sweep angle. It can be observed that to obtain the same transition location for higher Reynolds numbers as for lower Reynolds numbers, a lower sweep angle is required. The dominant transition mechanisms for varying sweep angles are shown in Table 3.1. The sources use quite different ranges for each transition mechanism, however the overall trend is clear. TSI is dominant at low sweep angles and CFI at high sweep angles. Note that the ranges from Schrauf [8] are obtained from a graph, making the ranges not very accurate.

Table 3.1: Dominant transition mechanisms at varying sweep angles.

Dominant transition mechanism	**Joslin** [10]	**Joslin** [12]	**Schrauf**[8]
TSI	0-10 deg	0-25 deg	0-15 deg
TSI and CFI	10-30 deg	25-30/35 deg	-
CFI	>30 deg	>30/35 deg	>15 deg

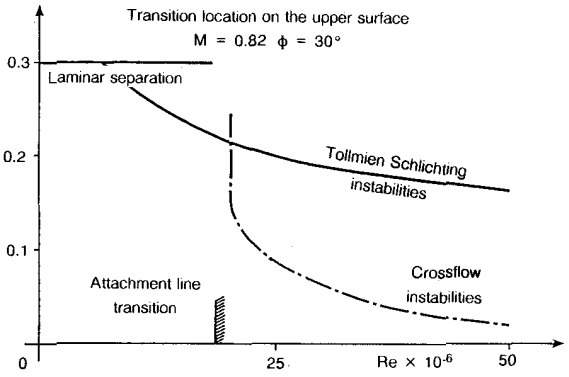

Figure 3.3: Transition mechanisms on infinite swept wing; Reynolds number against transition location [7] (y-label: transition location x/c).

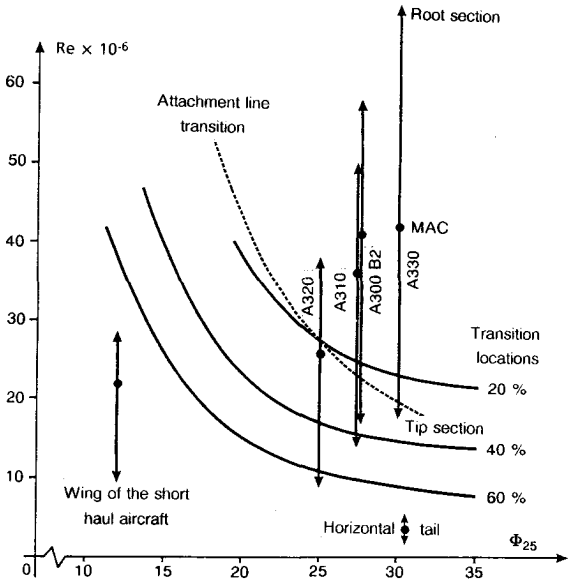

Figure 3.4: Transition mechanisms for infinite swept wing; sweep angle against Reynolds number [7].

3.2. Laminar flow control

Figure 3.5 and Figure 3.6 (left) show the drag components of generic transport aircraft. It can be observed that lift-dependent drag (or drag due to lift or lift-induced drag) and (skin) friction drag are the two main components. The friction drag component is responsible for about half ($\approx 48 - 52\%$) of the total drag of a standard transport aircraft. It would therefore make sense to try to reduce this friction drag component [7][8]. Based on Figure 3.6 (right), the distribution of the contributing aircraft components to friction drag can be observed, namely fuselage, wing, horizontal tailplane (HTP), vertical tailplane (FIN), nacelles, and pylons + fairings. As established in section 3.1 to reduce friction drag, it is beneficial to prolong the laminar flow. According to Schrauf [8] the fuselage cannot be made laminar due to the magnitude of the Reynolds numbers. This leaves the other components. Especially, the wing and winglike components (vertical and horizontal tailplanes) contribute greatly to the friction drag. Since these components are rather slender and using the reasoning from Figure 3.1, a drag reduction could be obtained with prolonged laminar flow.

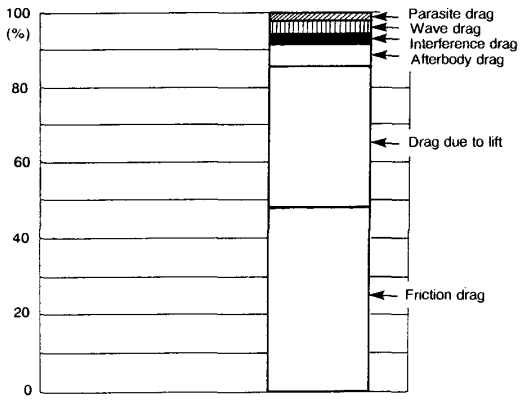

Figure 3.5: Drag components of transport aircraft, with friction drag $\approx 48\%$, drag due to lift $\approx 38\%$, afterbody drag $\approx 6\%$, interference drag $\approx 3\%$, wave drag $= 3\%$, and parasite drag $\approx 2\%$ [7].

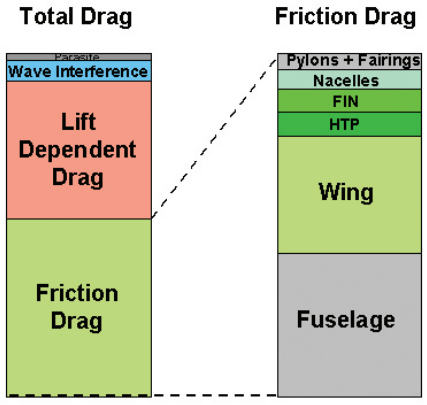

Figure 3.6: Drag components of transport aircraft, with friction drag due to the fuselage $= 22\%$, wing $= 18\%$, horizontal tailplane (HTP) $= 4\%$, vertical tailplane (FIN) $= 3\%$, nacelles $= 3\%$, and pylons + fairings $\approx 2\%$ [8].

The next question is how to prolong this laminar flow, or in other words, how to delay transition. As said before, the transition location is dependent on surface roughness, the amount of turbulence in

the freestream, favorable/adverse pressure gradients, and the temperature of the fluid by the surface. Therefore the goal is to influence these characteristics, which can be done in three ways, namely with natural laminar flow (NLF), laminar flow control (LFC), and hybrid laminar flow control (HLFC). NLF is a passive method and uses a favorable pressure gradient to delay transition. LFC requires an active system that influences the fluid in such a way that laminar flow is maintained even above the natural Re_{cr}. HLFC is the combination of passive and active systems, thus combining NLF and LFC [10]. Each of the laminar flow (control) types will be discussed in the following sections.

3.2.1. Passive flow control strategies: Natural laminar flow

NLF is a passive method and uses a favorable pressure gradient to delay transition. This can be obtained by changing the geometry of the wing.

The simplest method to delay transition is airfoil shaping. This is shaping the geometry of the airfoil in such a way a favorable pressure gradient is maintained throughout the airfoil [10]. This maximizes the natural laminar flow over the airfoil, thus delaying transition. Depending on the Reynolds number and sweep angle either TSI, CFI, or ALT is the dominating transition mechanism as explained in section 3.1. Many studies have been performed into NLF airfoils and when testing often a natural laminar glove is used [31][32]. This glove is like a natural laminar airfoil sleeve that is placed on the wing to study NLF.

Another option is the use of discrete roughness elements (DREs). These are very small elements with a height in the order of micrometers. The DRE can have various shapes, but often are cylindrical. The main advantage of DRE is that they can simply be applied to an existing wing in various configurations. No extra systems are required. However, the test performed with these DREs showed only limited success and the results were inconsistent [33][34][35].

Delft Laminar Hump

A more novel method to obtain prolonged laminar flow is the DeLaH[1], discovered by the Aerodynamics Department of the Faculty of Aerospace Engineering at the Delft University of Technology. Currently, the hump is still being investigated by a research group led by Prof. M. Kotsonis. The DeLaH is a symmetrical smooth hump that is placed at a set distance parallel to the leading edge of the wing. The hump could simply be glued on an existing aircraft wing. This makes it a very simple and cost-effective solution compared to HLFC systems. The hump attenuates the growth of the CFI, reducing skin friction drag. Wind tunnel tests were conducted with this hump on a $45\ deg$-swept wing at Reynolds numbers between $2.1-2.7\cdot10^6$ for angles of attack between $2-5deg$. The effectiveness of the hump is dependent on the hump height, width, chordwise location, and perturbation amplitude, where the perturbation is the CFI. With the hump, transition can be delayed up to 14%. The hump is discussed in more detail in section 4.6 as it is the main test case in this research.

3.2.2. Active flow control strategies: Laminar flow control

LFC requires an active system that influences the fluid in such a way that laminar flow is maintained even above the natural Re_{cr}. This can be done through suction, cooling, wing morphing, and even plasma actuators.

The most common method is suction. By applying suction through the wall where the boundary layer is developing, stability is improved because the momentum deficit is reduced due to changes in velocity profile, and thus the boundary layer thickness decreases. There are two main categories, discrete and continuous suction [36][9].

Discrete suction is through slots, which are discrete long and narrow openings along the span of the wing, through which the air can be sucked, as shown in Figure 3.7. This can either be one slot or several with space in between. This was first tested in 1941 by Zalovcik et al. [31] and continued up to the late 1980s [10], especially by Northrop [37][9], mainly by Pfenninger and Groth, and NASA [38][9].

Continuous suction can be done in two ways, with a perforated or porous surface, shown in Figure 3.8 and Figure 3.9. The main difference between perforated and porous surface suction is the size

[1] Delft University of Technology. (2023). ERC Proof of Concept grant for the Delft Laminar Hump. Retrieved January 27, 2024, from https://www.tudelft.nl/en/2023/lr/erc-proof-of-concept-grant-for-the-delft-laminar-hump

of the holes and therefore suitable materials [39]. The configuration of suction pumps, ducts, and inlets, differs from system to system, but for most systems packaging causes problems, due to limited space in wings. It is possible to reduce the size of these systems by adopting a HLFC setup and limiting the suction to a smaller area of the wing (leading edge). Considerable contributions to the investigation of this type of suction systems were made by Boeing [40][36] and Airbus [41][42][43][44], mainly by Schrauf.

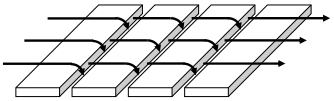

Figure 3.7: Slot suction.

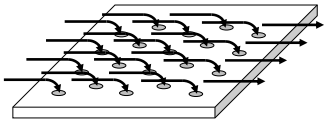

Figure 3.8: Perforated surface suction.

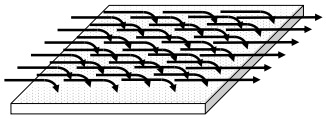

Figure 3.9: Porous surface suction.

Thermal laminar flow control uses cooling of the skin. Wall cooling greatly stabilizes TSI and to a lesser extent CFI as was found in various studies by Lekoudis [45], Mack [46], and Bertolotti [47]. One very promising application of wall cooling is for hydrogen aircraft. The liquid hydrogen can be pumped along the wing surface to cool the wall as proposed by Reshotko [48].

Morphing wings are wings that can actively change their shape by deforming their skin. With this, a morphing laminar wing can be made that actively changes its shape to prolong laminar flow as much as possible. There are many possibilities and ways to design such a system. For instance, using morphing segments with piezoelectric sensors that can detect whether the boundary layer is laminar, turbulent, or in transition as proposed by Stuber et al. [49] as well as a morphing leading edge device combined with an NLF wing as investigated by Lammering et al. [50].

Plasma actuators make use of the ionic wind concept. Here, air molecules are ionized with a large voltage, and subsequently, these ionized air molecules move due to the electric field. This ionic wind can be used to change the velocity profile and delay transition. One of the first to use plasma actuators for drag reduction was Malik et al. [51], which uses a corona discharge to ionize the air molecules. In newer research, dielectric barrier discharge (DBD) is used to control the TSI as well as the CFI, as investigated by Roth et al. [52], Tol et al. [53], and Chernyshev et al. [54]. Most research, however, is still in the experimental phase and is not at the stage of being implemented on an actual aircraft.

3.2.3. Active/passive flow control strategies: Hybrid laminar flow control

HLFC is a combination of the passive NLF and active LFC. It might seem that there is no case to be made for the use of HLFC since a passive system (NLF) is much less complex and has no energy consumption. However, for the speed regime of subsonic transport aircraft and the use of swept wings, CFI are dominant and these can be dealt with by using an active system (LFC). Using a combination of the passive NLF and active LFC would combine the best of both worlds. The active part of HLFC can deal with the CFI and the passive part minimizes the energy consumption, complexity, and expensive systems.

In theory, every combination of the NLF and LFC types described in the previous sections could be used in a HLFC system. However, not all combinations are feasible. The most promising combination is the combination of a suction system and airfoil shaping (NLF airfoil). This has been extensively tested by many aircraft manufacturing companies in wind tunnel experiments as well as flight tests. Especially the perforated and porous suction systems are the focus of research in recent years and are the closest to being implemented on commercial aircraft, next to passive NLF systems of course. The major wind tunnel and flight tests were performed throughout the years by both Boeing and Airbus. In 1990 Boeing performed flight tests with a Boeing 757 with an HLFC system on the wing, that consisted of a perforated titanium leading edge through which suction can be applied [40][55][56][10]. It was found that a local drag reduction of 29% could be obtained, which equates to a 6% overall drag reduction of the aircraft [56]. Between 1998 and 2018 a major effort was made to implement a HLFC suction system in the vertical stabilizer of an Airbus A320, under the name of the A320 HLF fin project [44][57][43][41][58][42]. Numerous flight tests and configurations have been tested, however, all variations of the hybrid laminar flow fin used a combination of wing shaping (NLF wing) and suction at the leading edge through a porous

wall. Significant delay in transition was found, resulting in a transition location up to 52% of the chord [57]. Nevertheless, there are still some problems left before being able to implement this system into commercial aircraft. For example, the problem of contamination (insects, debris, etc.) and combining the HLFC system with anti-icing systems still need to be tackled [8].

3.3. Laminar flow control wind tunnel and flight tests

Over the years many different wind tunnel and flight tests have been performed investigating LFC. Since there are too many to discuss here, an overview of all the research is given with the help of graphs to visualize the various flight and geometry conditions that were covered. The plots are comprised of data from various sources ([10][36][59][8][60]), but not all of the research was included in all of the plots as some data was not available. Appendix C provides a full timeline of all the different flight tests, wind tunnel tests, and research projects that have been performed in the field of LFC. To get an idea of what tests have been done in terms of aerodynamic characteristics, Figure 3.10 shows the Reynolds number versus sweep angle and Figure 3.11 the streamwise extend of LFC device against the laminar maximum, both in terms of percent x/c. In Figure 3.11 diagonals are added with a gradient of one for easier comparison of the data. Note that the Delft Laminar Hump is on the outer regions of what has been tested before in both figures. Several of these research and flight tests are explained in more detail in Appendix D, because of their importance for LFC implementation in modern subsonic transport aircraft. This concerns the Boeing 757 with HLFC, the Fokker 100 with a laminar flow glove, the Airbus A320 with a hybrid laminar flow fin, the Boeing 787 with a passive suction system, and the Airbus A340 BLADE project.

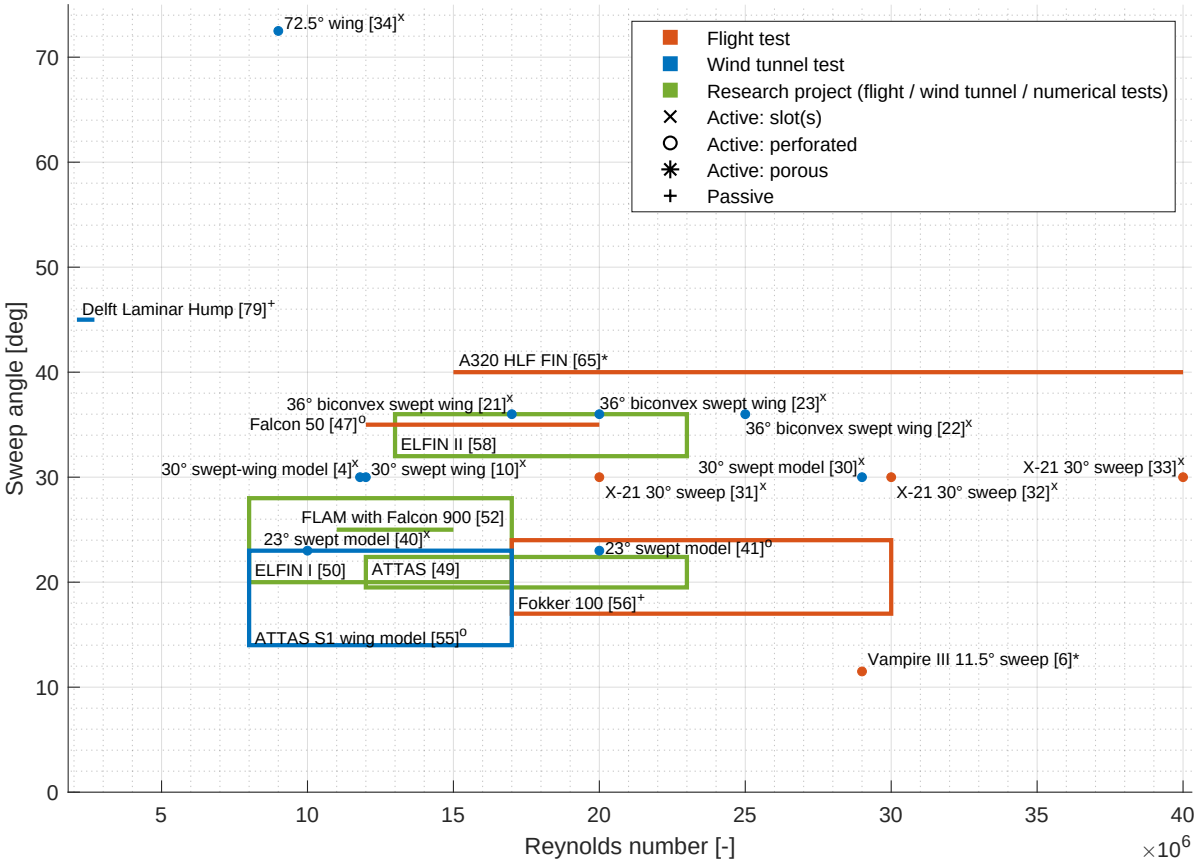

Figure 3.10: LFC research: Reynolds number vs. sweep based on [10][36][59][8][60] (Note: research project is a collaborative research which may include flight, wind tunnel and/or numerical tests. Some of the flight and wind tunnel tests shown in the figure are also part of the research projects shown in the same figure. Note: rectangles and/or lines mean that the corresponding tests were performed over a range of Reynolds numbers and sweep angles).

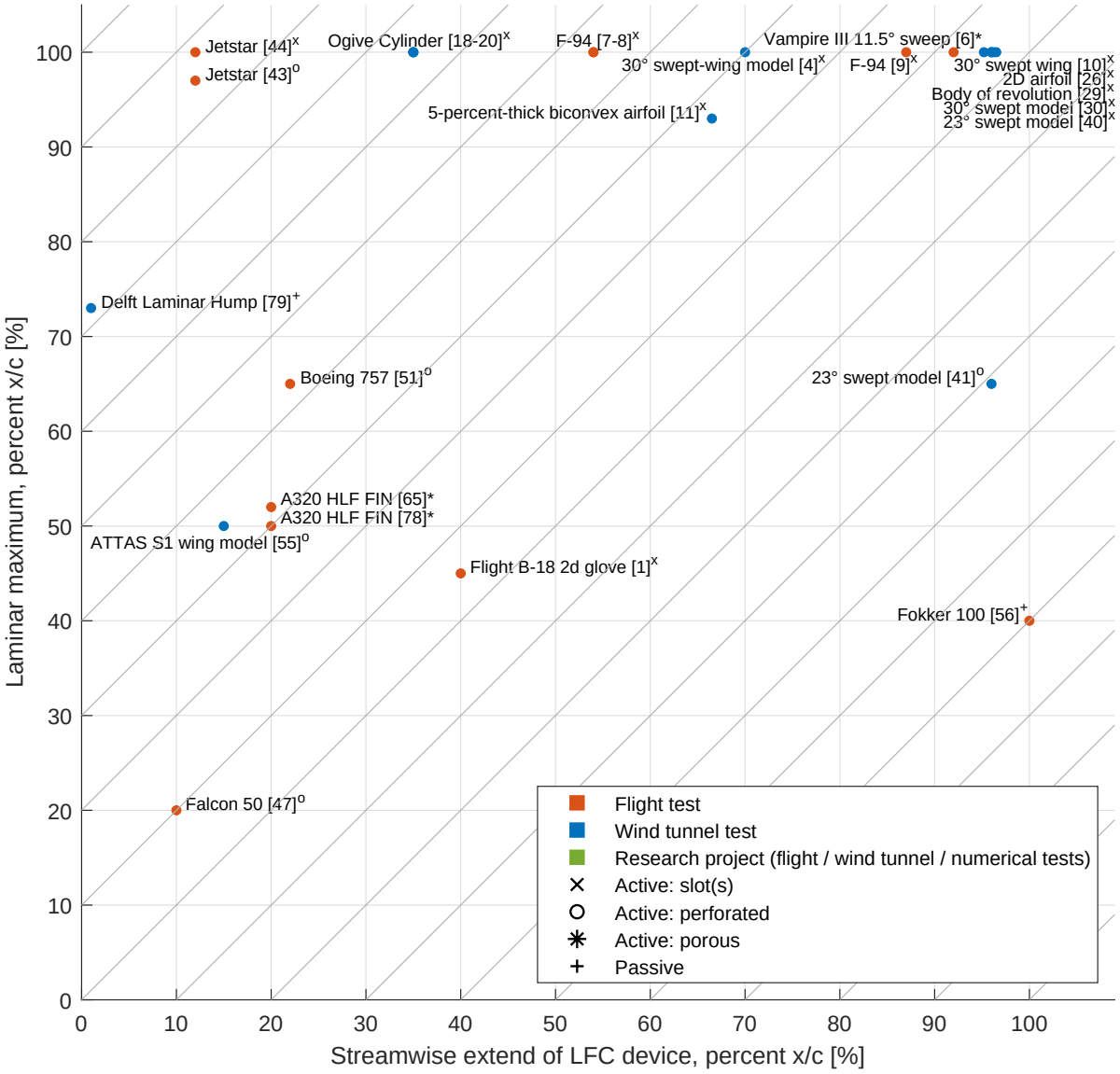

Figure 3.11: LFC research: Streamwise extend of LFC device, percent x/c vs. laminar maximum, percent x/c based on [10][36][59][8][60] (Note: research project is a collaborative research which may include flight, wind tunnel and/or numerical tests. Some of the flight and wind tunnel tests shown in the figure are also part of the research projects shown in the same figure).

RESEARCH

4

Methodology

In this chapter, the vertical stabilizer parametrization, stability analysis, and LFC aerodynamics will be combined and extended into one methodology to evaluate the DeLaH. Starting with section 4.1 the vertical tail sizing is discussed. With the vertical tail geometry, the aerodynamic analysis can be performed. In this aerodynamic analysis, the shift in transition location that models the aerodynamic effect of the hump is implemented. The method and programs involved are presented in section 4.2. In section 4.3 the implementation of the stability analysis by Fokker / Obert (as explained in section 2.5) and its link to the aerodynamics is discussed. After the stability analysis, the full aircraft analysis modules are presented in section 4.4, which consists of the weight, drag, and mission analysis, to evaluate the performance of the full aircraft. At the end of this, the complete method is visualized in section 4.5, which gives a more detailed flowchart of the whole system, including the inputs and outputs of each component.

With the main method established, the test cases are discussed. The main test case is the Delft Laminar Hump, which is explained in section 4.6. The DeLaH is evaluated on two aircraft (conventional and T-tail), which forms the baseline configuration in section 4.7. If there is enough margin left in the stability conditions, potentially the vertical tail can be reduced in size, resulting in additional drag reduction. This is investigated with the sensitivity analysis proposed in section 4.8

4.1. Vertical tail sizing

The goal of this research is to implement the DeLaH in the vertical stabilizer. Therefore, first, the geometry of the vertical tail needs to be established. The vertical tail can be described by the parametrization given in chapter 2.

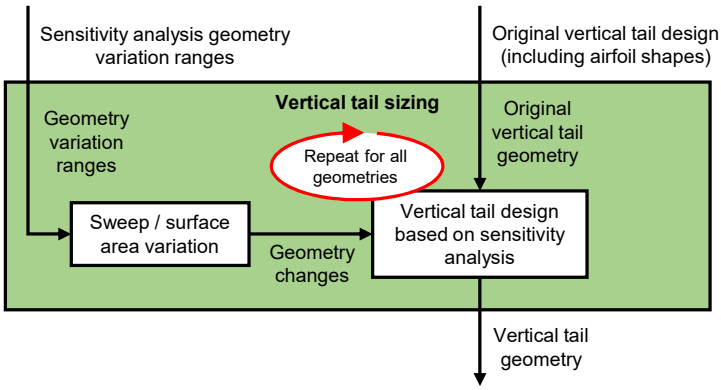

Figure 4.1: Vertical tailplane sizing flowchart.

Additionally, to obtain a good understanding of the interaction between the vertical tail geometry and the DeLaH, a sensitivity analysis is performed. Several vertical tail geometry variables will be

varied within a certain range to assess the effectiveness of the hump due to the geometry changes. A more detailed explanation of the sensitivity analysis can be found in section 4.8. Figure 4.1 shows how the vertical tailplane is sized based on the original vertical tail design and how it is combined with the geometry changes due to the sensitivity analyses to obtain the vertical tail geometry that is evaluated by the rest of the method.

4.2. Vertical tail aerodynamics

The aerodynamic evaluation method consists of two parts as seen in Figure 4.2, the Quasi-3D aerodynamic analysis (Q3D), discussed in subsection 4.2.1, and an aerodynamic database for LFC, discussed in subsection 4.2.2. The aerodynamic database for LFC provides the shift in transition location due to the LFC device (in this case the hump), which is used by Q3D to calculate the lift curve slope and drag coefficient.

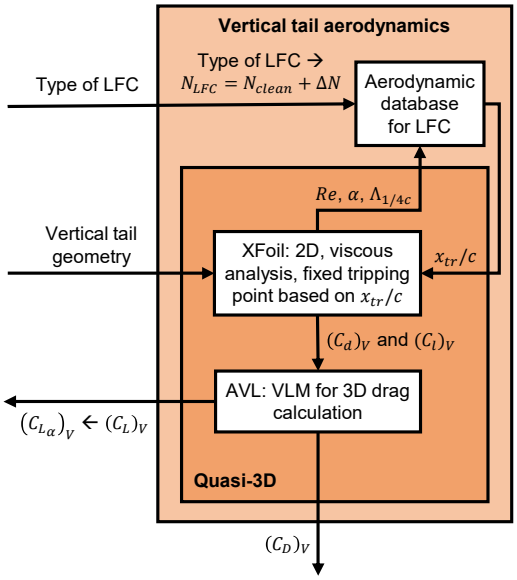

Figure 4.2: Vertical tail aerodynamics flowchart.

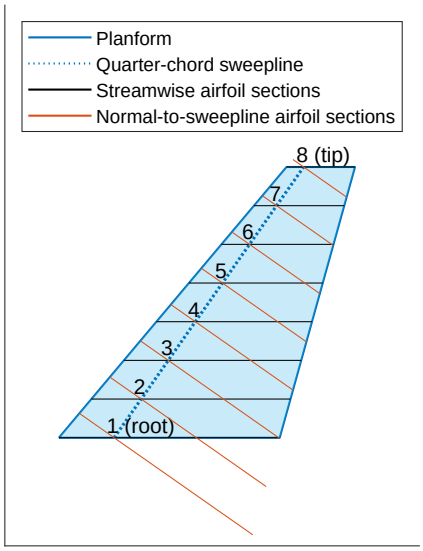

Figure 4.3: Vertical tailplane planform with airfoil sections as used by Q3D.

4.2.1. Quasi-3D

The overall objective of this research is to implement the hump in the vertical tail. Therefore a link between the modifications of the hump to the transition location and the stability analysis is required. This link is provided by the vertical tail lift curve slope $(C_{L_\alpha})_V$. This lift curve slope is calculated with the Quasi-3D analysis (Q3D) developed by Mariens et al. [61]. For subsonic analyses, this method uses XFoil[1] for the 2-dimensional viscous analysis of airfoils and Athena Vortex Lattice (AVL)[2] for the 3-dimensional inviscid analysis, which is a vortex lattice method (VLM). Some changes to the existing Q3D program are made to ensure it can handle semi-span wings (vertical tailplanes) as well as adjust the transition location in XFoil since this is required to model the effect of the hump. It will assess the semi-span wing (vertical tailplanes) as an isolated, free-floating wing, without any walls present (no fuselage interaction, etc.). Refer to subsection 5.3.4 for more information.

The Quasi-3D analysis consists of three main steps. Note that this is slightly different than the representation used in Figure 4.2, which is a simplified visualization. First, AVL is used to calculate wing lift distribution, wing lift coefficient, and wing induced drag coefficient. The Trefftz plane [62] analysis is used for the induced drag. Second, the wing is divided into airfoil sections and XFoil is used to find the profile (= form drag + skin friction drag) of the airfoils. Note that at subsonic speeds, no wave drag is present and that XFoil uses normal-to-sweepline airfoil sections, as seen in Figure 4.3. For this, the

[1] Drela, M., Youngren, H.. (2000). XFOIL Subsonic Airfoil Development System. Retrieved February 4, 2024, from `https://web.mit.edu/drela/Public/web/xfoil/`

[2] Drela, M., Youngren, H.. (2004). AVL. Retrieved February 4, 2024, from `https://web.mit.edu/drela/Public/web/avl/`

quarter-chord sweepline is used and the default value of 8 sections is used. By using the strip method [63][64] in combination with simple sweep theory [65] the profile drag is obtained. Third, the total wing drag is calculated by combining the inviscid drag from AVL and the inviscid/viscous drag components from XFoil, after integrating the 2D viscous drag components of the airfoils over the wing.

The vertical tail lift curve slope $(C_{L_\alpha})_V$ is obtained through the C_L values calculated by Q3D. By running the same wing at 3 different angles of attack the lift curve slope in the linear regime can be estimated. The vertical tail is evaluated at $\alpha =$ -1, 0, and 1 degree since Q3D sometimes diverges at larger angles of attack.

4.2.2. Laminar flow control aerodynamic database

The impact of the hump on the vertical tail aerodynamics is represented as a shift of the transition location. This shift in transition location due to the hump will form the aerodynamic database for LFC. In a more generalized approach, the volume (and dimensions) needed to implement all necessary systems that comprise the LFC device could also be included. For instance, a space for the pumps is required for a LFC system with suction. However, for the main test case in this research, no minimum volume is required as the hump is mounted on the outer skin.

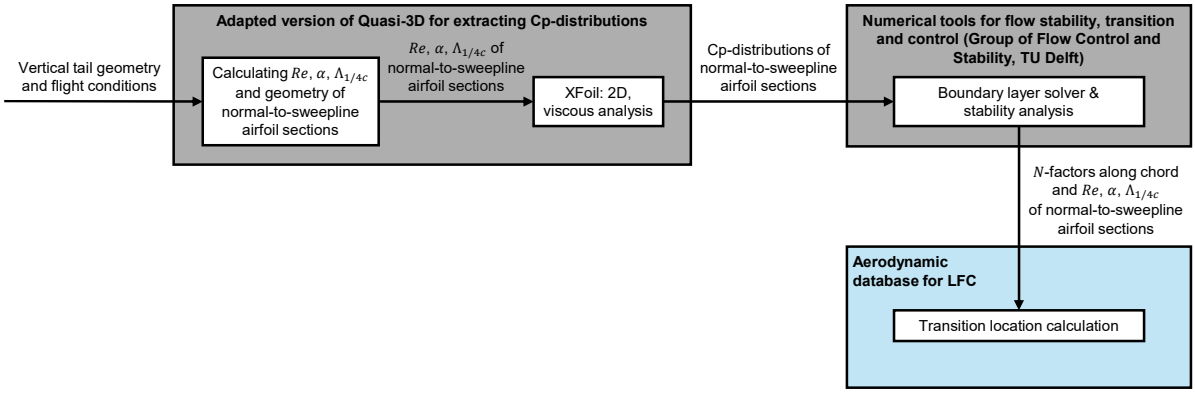

Figure 4.4: Aerodynamic database for LFC construction flowchart.

The aerodynamic database is constructed as shown in Figure 4.4. The vertical tail geometry and flight conditions are used as the initial input for an adapted version of Quasi-3D. It calculates the normal-to-sweepline airfoil sections and their respective local flight conditions, which are then fed to XFoil to calculate the pressure distributions over the normal-to-sweepline airfoil sections. These pressure distributions are used to perform a boundary layer stability analysis. For this, numerical tools developed by the Group of Flow Control and Stability within the Delft University of Technology are used (see subsection 5.3.1). With this, the N-factors along the chord of the airfoil sections are calculated (for both sides of the airfoil). This N-factor is the amplification factor in the e^n-method by Van Ingen [66]. An example of this N-factor along the airfoil chord calculated with the numerical tool is shown in Figure 4.5. It is assumed that transition occurs at $N_{clean} = 9$ for a clean configuration as is supported by literature [66].

To obtain the shift in transition location due to the LFC device a ΔN is introduced. For the hump $\Delta N \approx$ [redacted] CONFIDENTIAL, for the forcing case with a distributed roughness patch and is estimated from the (confidential) master thesis by Morais [67]. To model the shift in transition locations due to LFC $N_{LFC} = N_{clean} + \Delta N$ is used. In the case of the DeLaH, it is assumed that $N_{hump} = N_{clean} + \Delta N$, where $\Delta N \approx$ [redacted] CONFIDENTIAL, holds for every flight condition. Figure 4.5 shows that the increased N-factor results in a shift in transition location. This calculation is repeated for every normal-to-sweepline airfoil section for various Reynolds numbers, angles of attack, and sweep angles. All these results together form the transition location database (i.e. the Aerodynamic database for LFC). The ranges of Reynolds numbers, angles of attack, and sweep angles, for which the N-factors need to be calculated are dependent on several things. The Reynolds numbers are dependent on flight conditions (cruise or landing) and the chord length of the section since this varies when the surface area is scaled in the sensitivity analysis. The angles of attack only need to be calculated for -1, 0, and 1, since only these

small angles of attack are used to obtain the lift curve slope in the linear range. The sweep angles are dependent on the sweep angles used in the sensitivity analysis (discussed in section 4.8).

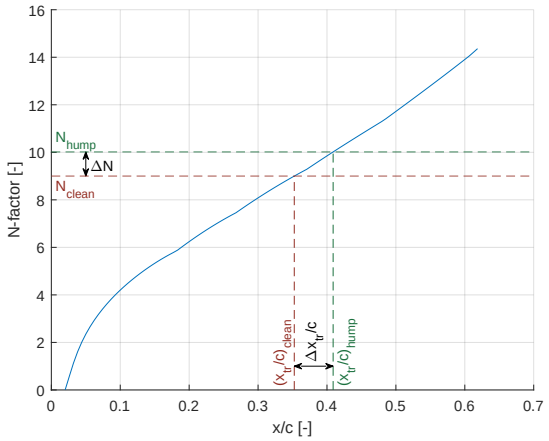

Figure 4.5: Example of obtaining the transition locations for clean and hump configurations. x/c vs. N-factor (Fokker F-28 Mk1000, mid-span section (4 of 8), $\Lambda_{1/4c_V} = 40\ deg$, cruise, $\alpha = 0\ deg$)

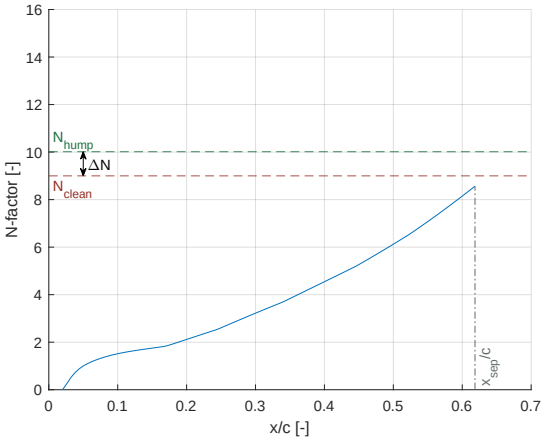

Figure 4.6: Example of separation occuring before transition. x/c vs. N-factor (Fokker F-28 Mk1000, mid-span section (4 of 8), $\Lambda_{1/4c_V} = 40\ deg$, cruise, $\alpha = 0\ deg$)

Finally, Figure 4.6 shows a special case. The boundary layer stability analysis tool only accounts for attached flow, and therefore it will only calculate N-factors up to the point of separation. Therefore it sometimes happens that the N-factor curve does not reach the values of N_{clean} and/or N_{hump}. In that case, it is assumed that the transition location coincides with the point of separation. Based on experimental evidence [68], it is known that a laminar separation bubble forms around $x/c \approx 0.70$ ($\alpha = 0\,deg$ and $Re = 2.12 \cdot 10^6$), in the adverse pressure region of the M3J wing. This NLF wing will also be used for the main test case in this research, as explained in section 4.6. Therefore it is assumed that a laminar separation bubble also occurs for this N-factor curve, where the flow is laminar up to the very end of the N-factor curve, and separation occurs at the end of this curve, which also directly results in transition. Due to the transition, the boundary layer will reattach, after which turbulent separation will happen further downstream or even at the trailing edge. Whether this assumption is valid will be tested in subsection 5.3.5.

4.3. Stability analysis

As established before, a link needs to be found to connect the aerodynamics to the stability requirements of the vertical stabilizer. The commonly used volume coefficient method, as described in subsection 2.3.1, does not provide such a link and therefore a more advanced method to size the vertical tail is used. The method used is the Fokker / Obert [14] that is based on a stability analysis as explained in section 2.5. The link to the aerodynamics is provided through the vertical tail lift curve slope $\left(C_{L_\alpha}\right)_V$. This vertical tail lift curve slope can be used in the stability analysis to see if the vertical tail provides sufficient stability. The $\left(C_{L_\alpha}\right)_V$ affects the stability analysis through the stability and control derivatives with respect to sideslip and rudder deflection angle as seen in Equation 2.15. The change in the stability and control derivatives will influence whether the critical design requirements (section 2.6) are met or not and whether the vertical tailplane meets the specifications of CS-25 for Large Aeroplanes by EASA. An overview of this procedure is shown in Figure 4.7.

The critical design requirements and their respective flight condition that will be checked are:

- Static stability - cruise
- One engine inoperative (OEI) - landing
- Crosswind landing:
  - Crosswind landing for steady, straight sideslips (CWL,SSS) - landing
  - Crosswind landing for full rudder sideslips (CWL,FRS) - landing
- Stall - landing

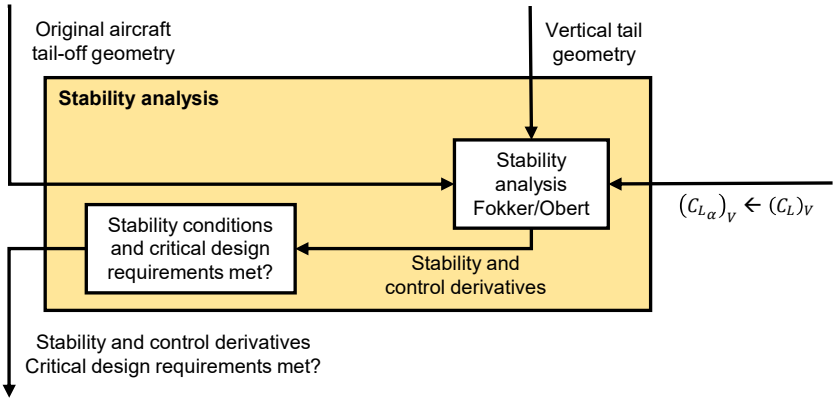

Figure 4.7: Stability analysis flowchart.

The exact implementation of the requirements for each critical design requirement is found in Table 6.3. Note that stall is checked for both one engine inoperative and crosswind landing, hence the landing condition. Also note that different from what was discussed in section 2.6, Dutch roll, spiral, and spin are not evaluated. The former two are part of dynamic stability, which in general is not used in evaluating conceptual vertical tailplane design. For spin, no clear EASA regulation could be found in the specifications of CS-25 for Large Aeroplanes by EASA.

4.4. Full aircraft analysis modules

Three full aircraft analysis modules will be used, namely the weight analysis, mission analysis, and drag analysis. Figure 4.8 shows how these modules are linked.

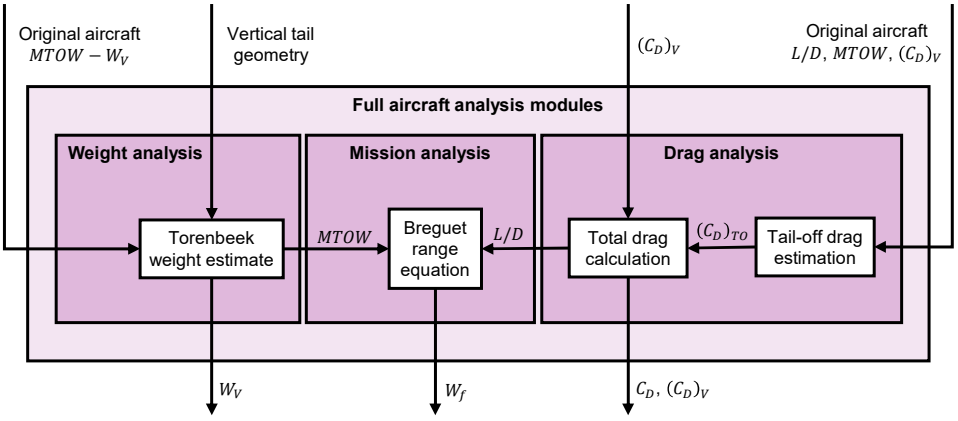

Figure 4.8: Full aircraft analysis modules flowchart.

4.4.1. Weight analysis

For the weight analysis, the vertical tailplane weight is estimated with an empirical method by Torenbeek [15]. For this method, the vertical tailplane weight is a function of the vertical tailplane geometry together with the design dive speed V_D (in EAS), as seen in Equation 4.1. The function is visualized in Figure 4.9. The design dive speed, V_D, is calculated with Equation 4.2 as a multiple of the design cruise speed, V_C, as prescribed by CS 25.335b Design airspeeds [25]. To account for the mounting location of the horizontal tailplane a correction factor k_V is introduced, where a distinction is made between fuselage- and fin-mounted horizontal tailplanes as seen in Equation 4.3 and Equation 4.4. The final $MTOW$ can be calculated by simply adding the vertical tailplane weight calculated with the method above to the $MTOW - W_V$ of the original aircraft.

$$\frac{W_{_V}}{S_{_V}} = k_{_V} \cdot f\left(\frac{S_{_V}^2 V_{_D}}{\sqrt{cos(\Lambda_{1/2c_{_V}})}}\right) \tag{4.1}$$

$$V_{_D} = \frac{V_{_C}}{0.8} \tag{4.2}$$

$$k_{_V} = 1.0 \quad \text{(fuselage-mounted horizontal tailplanes)} \tag{4.3}$$

$$k_{_V} = 1 + 0.15\frac{S_{_H} z_{_H}}{S_{_V} b_{_V}} \quad \text{(fin-mounted horizontal tailplanes)} \tag{4.4}$$

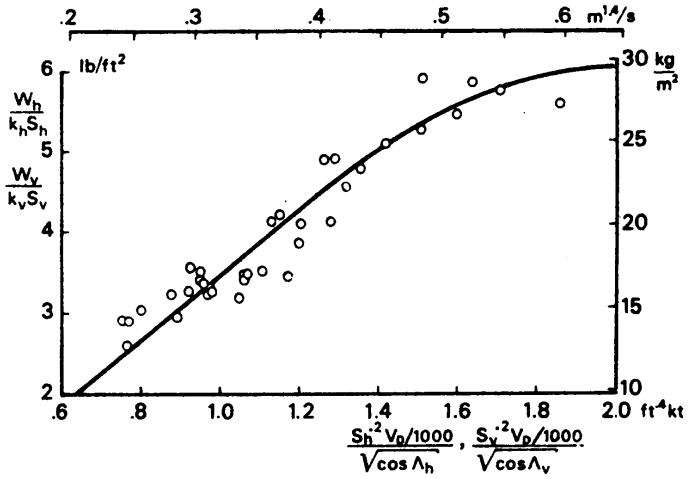

Figure 4.9: Vertical tailplane weight empirical relation [15].

4.4.2. Mission analysis

The mission analysis uses the Breguet range equation as seen in Equation 4.5. At the start of the mission, the weight is set to the maximum take-off weight (MTOW) of the aircraft. Depending on the required range the weight at the end of the mission can be calculated. It is assumed the range is equal to the harmonic range, which is the highest range for maximum payload [17]. In essence, this W_{end} is the maximum zero fuel weight (MZFW), and therefore the fuel weight for the harmonic range can be calculated with Equation 4.6.

$$R = \frac{V}{gTSFC}\frac{L}{D} ln\left(\frac{W_{start}}{W_{end}}\right) \tag{4.5}$$

$$W_{end} = W_{start} - W_{fuel} \tag{4.6}$$

For the fuel weight, the vertical tail is not really of importance in terms of fuel storage since this normally is not done in the vertical tail. This is because it is preferable to store the fuel as close to the CG as possible, to prevent large shifts in CG location during flight. Therefore it is also assumed that there is no CG shift during the mission due to fuel consumption. Nevertheless, the aerodynamic properties of the vertical tail are of importance to the fuel weight. If the drag of the vertical tail is reduced, the overall fuel consumption would also drop, which in turn reduces the fuel weight. The thrust specific fuel consumption (TSFC) is dependent on the engine type. To estimate the fuel volume from the fuel weight, Jet-A1 fuel at $15°C$, which is equal to $0.804\ kg/l$, is assumed[3]. For the CO_2 emission, a fuel conversion factor of $3.15\ kg_{CO_2}/kg_{Jet-A1}$ is assumed [69].

[3]Wikipedia. (2025). Jet fuel. Retrieved January 6, 2025, from `https://en.wikipedia.org/wiki/Jet_fuel`

4.4.3. Drag analysis

For the drag analysis, two main drag components are used, namely the drag coefficient of the full aircraft without vertical tailplane and the drag coefficient of the vertical tailplane, as seen in Equation 4.7. The drag coefficient of the full aircraft without vertical tailplane is estimated by subtracting the drag coefficient of the original vertical tailplane, $\left((C_D)_V\right)_{original}$, from the drag coefficient of the full aircraft, which is seen in Equation 4.8. The drag coefficient of the full aircraft is estimated by using the lift coefficient based on the $W_{mid-cruise}$ and lift-to-drag ratio in cruise. The $W_{mid-cruise}$ in Equation 4.9 assumes the harmonic range, which is the highest range for maximum payload, therefore halfway between MTOW and MZFW. The drag coefficient of the original vertical tailplane, $\left((C_D)_V\right)_{original}$, is calculated with Q3D. The drag coefficient of the (newly designed) vertical tailplane, $(C_D)_V$, is calculated in the same manner as $\left((C_D)_V\right)_{original}$, but is different from the drag coefficient of the original vertical tailplane when the vertical tailplane geometry changes. K_{FV} is a correction factor for the fuselage-vertical-tailplane interference, as introduced in subsection 2.5.6. Why this factor is included is discussed in subsection 5.3.4. The $\frac{q_V}{q}$ and $\frac{S_{V_{ref}}}{S_W}$ terms are to adjust for the effective-versus-free-stream dynamic pressure ratio and the reference area, respectively. Note that the reference area of the vertical tail is the full surface area (continuing in the fuselage as defined in Figure 2.3) and not the exposed vertical tailplane area. This will also be discussed in more detail in subsection 5.3.4.

$$C_D = (C_D)_{V,off} + (C_D)_V K_{FV} \frac{q_V}{q} \frac{S_V}{S_W} \tag{4.7}$$

$$(C_D)_{V,off} = \frac{W_{mid-cruise} g}{q S_W \frac{L}{D}} - \left((C_D)_V\right)_{original} K_{FV} \frac{q_V}{q} \frac{(S_V)_{original}}{S_W} \tag{4.8}$$

$$W_{mid-cruise} = MTOW - \frac{MTOW - MZFW}{2} \tag{4.9}$$

Since the drag coefficient in this analysis is calculated in cruise configuration the sideslip angle is assumed to be zero (i.e. the angle of attack of the vertical tailplane). Therefore the drag coefficient of the vertical tailplane will be fully comprised of viscous drag (profile drag (2D) or parasite drag (3D)) as the induced drag will be zero for the symmetric airfoil used for the vertical tailplane. As discussed in subsection 3.2.2, an LFC device will reduce the skin friction drag, which is a viscous drag component and therefore can be observed as a drag reduction even when no sideslip occurs.

4.5. Complete method overview

Figure 4.10 shows the complete method overview of implementing laminar flow control in a vertical tail. This flowchart combines the smaller flowcharts on the vertical tailplane sizing Figure 4.1, the vertical tailplane aerodynamics Figure 4.2, the stability analysis Figure 4.7, and the full aircraft analysis module Figure 4.8 into one flowchart. For a detailed explanation, refer to the earlier sections in this chapter. Only the main inputs and outputs have been added here for completeness.

The complete method overview proposed here is similar to other research on this topic by Risse et al. [70] and [71]. They use MICADO, the aircraft design platform by the Institute of Aerospace Systems (ILR). They propose a method for an initial wing design based on the full aircraft design and with an extensive quasi-3D analysis obtain the wing polars, to subsequently implement these into the full aircraft. This process is iterated and after convergence, a mission analysis is performed to obtain the block fuel, cost, emissions, and noise. The main benefit of the approach proposed in this research is the much simpler Q3D analysis, which will most likely result in much shorter computational times. This is beneficial for quick conceptual design iterations. In addition, this research focuses on the vertical tail instead of the wing, dealing with stability and control of the aircraft, rather than the lifting capabilities.

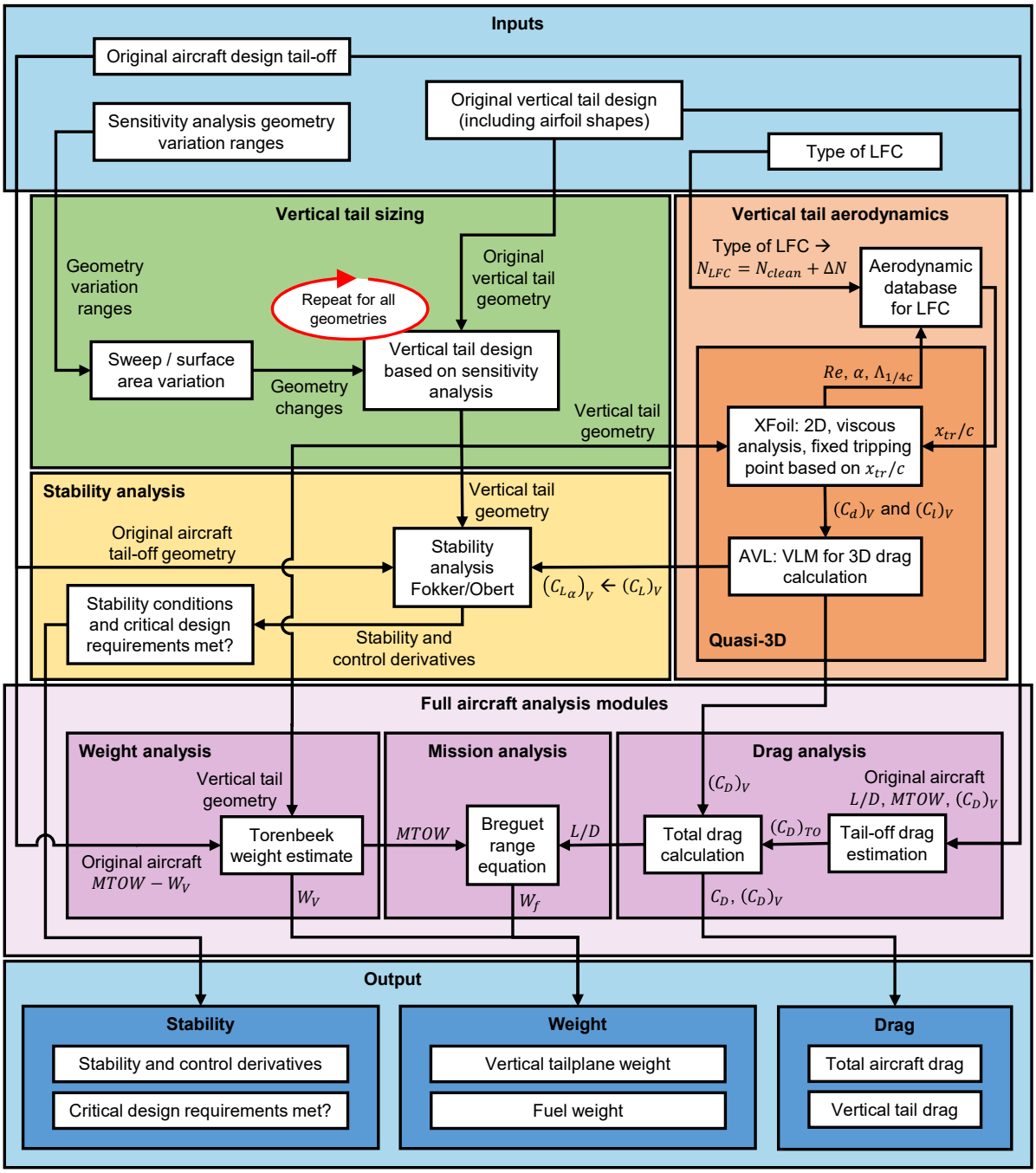

Figure 4.10: Complete method overview flowchart.

4.6. Main test case: Delft Laminar Hump

The main test case is the Delft Laminar Hump. In this section, first, the Delft Laminar Hump itself is discussed. Second, previously performed wind tunnel tests of the hump are discussed, and finally, the way the hump will be implemented on a vertical stabilizer.

4.6.1. Delft Laminar Hump

The Delft Laminar Hump (DeLaH)[4] is a novel way to delay transition. As mentioned in subsection 3.2.1, the DeLaH is a symmetrical smooth hump that is placed at a set distance parallel to the leading edge of the wing as shown in Figure 4.11[5] and Figure 4.12[5]. The hump has a hump height in the order of [redacted] CONFIDENTIAL, which implies that the hump is fully submerged in the boundary layer. From the wind tunnel experiments and numerical analyses, it was found that the effectiveness of the hump in delaying transition is dependent on the hump height, width, chordwise location, and perturbation amplitude, where the perturbation is the CFI. With the hump, the transition location could be moved aft up to 14%. Do note that the hump has the prerequisite that the airfoil it is implemented on, is a NLF airfoil. The hump can simply be glued on an existing aircraft wing, as shown in Figure 4.13[6] on a airfoil section. This would make it a very simple and cost-effective solution compared to HLFC systems. The wind tunnel experiments, however, were conducted only on a NLF swept wing and not yet implemented on an aircraft. This brings various uncertainties on aircraft level. It is uncertain what the drag reduction is on aircraft level as well as what the implications are on aircraft stability, especially when implemented on a vertical stabilizer. Therefore the hump will be the main test case in this research.

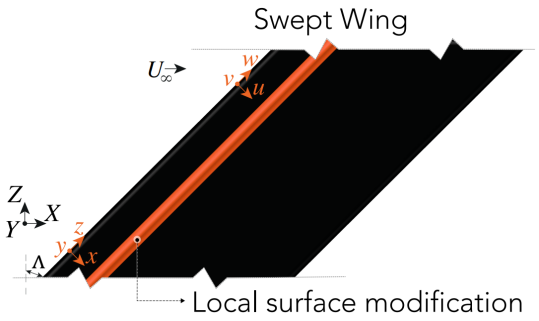

Figure 4.11: Swept wing with local surface modification[5].

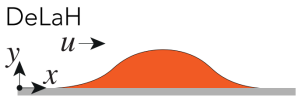

Figure 4.12: Local surface modification: the Delft Laminar Hump (DeLaH)[5].

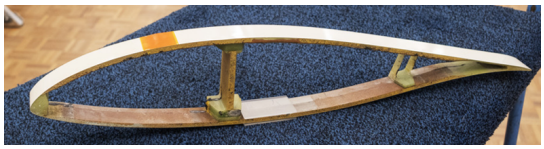

Figure 4.13: Airfoil with Delft Laminar Hump in orange [6].

4.6.2. Previously performed wind tunnel tests

Based on unpublished confidential documents of the Aerodynamics Department of the Faculty of Aerospace Engineering at the Delft University of Technology, wind tunnel tests were conducted with this hump on a $45\ deg$-swept, untapered, NLF wing at Reynolds numbers between $2.1 - 2.7 \cdot 10^6$ for angles of attack between $2 - 5\ deg$. Figure 4.14 shows a schematic drawing of the wind tunnel setup and Figure 4.15 shows the hump on the swept wing model. The airfoil used for this swept wing is the M3J airfoil, which is shown in Figure 4.16. This is a symmetrical airfoil and therefore ideal for use in the vertical tail. Figure 4.17 shows the corresponding pressure distribution of the pressure side of M3J airfoil, measured with pressure taps at the lower and upper side of the swept wing (also shown in Figure 4.14).

Figure 4.18[7] shows an image of the swept wing model in the wind tunnel (note that the hump is not actually present in this image). Two different types of forcing were used in the wind tunnel campaign, namely a distributed roughness patch and discrete roughness elements (DREs), as shown

[4] Delft University of Technology. (2023). ERC Proof of Concept grant for the Delft Laminar Hump. Retrieved January 27, 2024, from https://www.tudelft.nl/en/2023/lr/erc-proof-of-concept-grant-for-the-delft-laminar-hump

[5] Image provided by Dr. A.F. Rius Vidales

[6] Image by Van Wechem, S., from: Van de Weijer, B.. (2023). Soepeler door de lucht met een bult op de vliegtuigvleugel; Delfts team is er zelf door verrast. Retrieved January 29, 2024, from https://www.volkskrant.nl/wetenschap/soepeler-door-de-lucht-met-een-bult-op-de-vliegtuigvleugel-delfts-team-is-er-zelf-door-verrast~bc56f436/?referrer=https://www.google.com/

[7] Adapted image provided by Dr. A.F. Rius Vidales

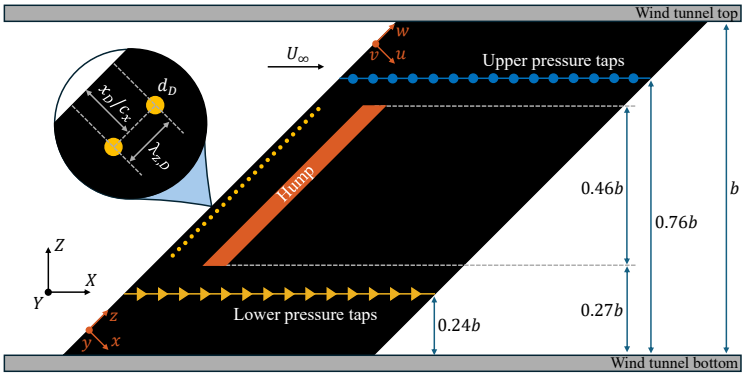

Figure 4.14: Swept wing with hump in wind tunnel, with $b = 1.25\ m$ and DRE parameterization, adapted figure [72] [67].

Figure 4.15: CONFIDENTIAL Hump on swept wing model with DREs [67].

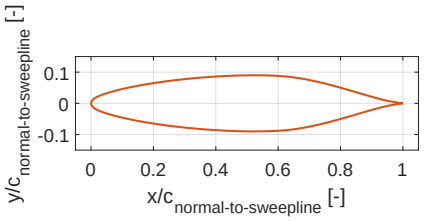

Figure 4.16: M3J airfoil.

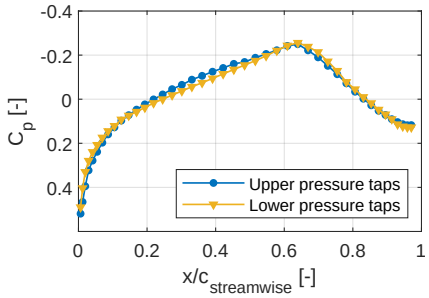

Figure 4.17: M3J pressure distribution of pressure side from wind tunnel measurements (with DREs and no hump), $\alpha = 3\ deg$ and $Re = 2.29 \cdot 10^6$.

in Figure 4.19 and Figure 4.20, respectively. The parameterization of the DREs is shown on the left side of Figure 4.14. The dimensions of the DREs used in the wind tunnel experiments are shown in Table 4.1. In what follows, when referring to DREs, these dimensions are meant. These DREs force a specific wavelength, whilst the distributed roughness patch forces a range of wavelengths. The ΔN due to the hump (discussed in subsection 4.2.2) is based on wind tunnel data that uses the distributed roughness patch because this is close(r) to real-world conditions.

Table 4.1: CONFIDENTIAL DRE dimensions based on parameterization Figure 4.14, where k_D is the element height [67].

$\lambda_{z,D}$	d_D	k_D	x_D/c_x

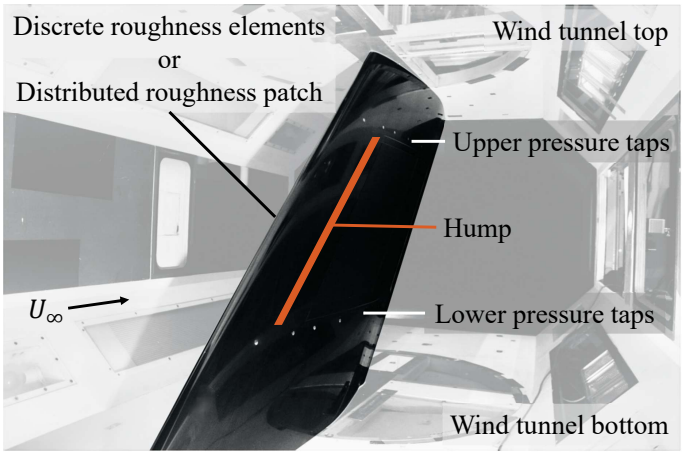

Figure 4.18: Swept wing model in wind tunnel, adapted image[7].

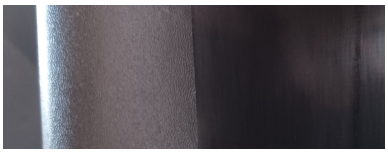

Figure 4.19: Distributed roughness patch on leading edge of swept wing model [67].

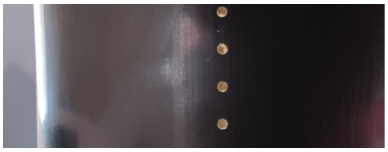

Figure 4.20: Discrete roughness elements (DREs) on leading edge of swept wing model [67].

To see the effect of the hump on the pressure distribution, the simulated pressure distribution over the hump is shown against the experimental wind tunnel data in Figure 4.21. The numerical simulations are obtained with the Harmonic Navier Stokes Solver [73]. The effect on the pressure distribution is

more clearly seen in the zoomed Figure 4.22, where the hump creates a small pressure drop, after which the pressure restores to a similar pressure as the clean configuration. Note that the effect of the hump geometry on the pressure distribution will be discussed in more detail in subsection 5.1.2.

Figure 4.21: CONFIDENTIAL M3J pressure distribution of pressure side from wind tunnel measurements (with DREs, no hump) and numerical simulations (clean and hump, both no roughness forcing), $\alpha = 3\,deg$ and $Re = 2.29 \cdot 10^6$.

Figure 4.22: CONFIDENTIAL Zoomed M3J pressure distribution of pressure side from wind tunnel measurements (with DREs, no hump) and numerical simulations (clean and hump, both no roughness forcing), $\alpha = 3\,deg$ and $Re = 2.29 \cdot 10^6$.

4.6.3. Implementation Delft Laminar Hump on vertical stabilizer

Based on the relatively small effect of the hump geometry on the pressure distribution in Figure 4.21 and the fact that the hump height is in the order of [redacted] CONFIDENTIAL, the geometry and thus the change in pressure drag are most likely negligible. This assumption will be verified in subsection 5.1.2. In case the hump geometry can be neglected, then the hump can be considered as a change in transition location, only dependent on Reynolds number, angle of attack, and sweep angle. The simulation of the hump on the vertical stabilizer can then be performed as described in subsection 4.2.2. The hump will be implemented on both sides of the vertical stabilizer since the vertical stabilizer is symmetric and must perform the same in both positive and negative sideslip conditions. It should be noted that the wind tunnel tests were only performed with the hump on the pressure side of the airfoil. Additional tests with the hump on the suction side would be useful to see whether the hump even works on the suction side or even has detrimental effects in terms of lift (side force) and drag. Also note that at large sideslip angles, the flow might already be transitioned before the hump, making the hump redundant. Therefore the main benefit of the hump would be in cruise conditions (no sideslip).

To be able to interpret the impact of the hump on a vertical tail, a reference case is required. Therefore this main test case will make use of the vertical tail of an existing aircraft and the hump is added to that vertical tail. This then can be compared to the same vertical tail without the hump installed. For a fair comparison, it is very important not to change the vertical tail geometry (baseline configuration) to isolate just the effect of the added hump in terms of weight and drag. It is a prerequisite for the hump to be used on a NLF airfoil, therefore it is also important to isolate the effect of the hump on the vertical tail design and performance from the effect of the NLF airfoil. This is done by running a case with the original airfoil of the aircraft and comparing it to the case with the NFL airfoil (M3J) to see the influence of the NLF airfoil on the vertical tail design. Subsequently, the case with the NLF airfoil (M3J) with the hump is run to see the effect of the hump.

4.7. Baseline configuration

There are many different aircraft that could be chosen to evaluate the DeLaH, but it was decided to use an Airbus A320 as well as the Fokker F-28 Mk1000. In the case of the A320, the exact type is often not specified in data. Since a lot of data is rather old, the earliest version of the A320 is used when

multiple variant data is available: A320-200. The aircraft are shown in Figure 4.23[8] and Figure 4.24[9].

Figure 4.23: Airbus A320[8].

Figure 4.24: Fokker F-28 Mk1000[9].

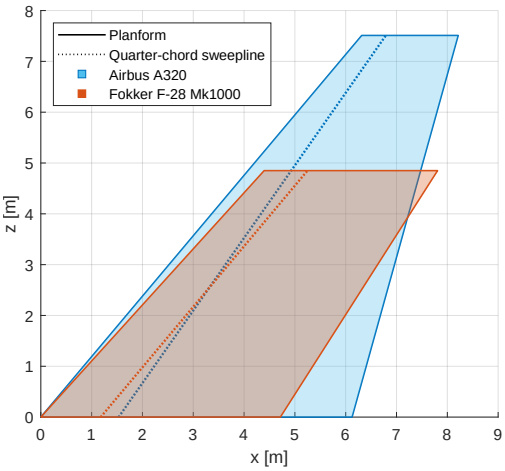

Figure 4.25: Vertical tailplane planform comparison

There are multiple reasons why these aircraft are chosen. The A320-type is one of the most common aircraft and has a very conventional layout with a fuselage-mounted stabilizer and wing-mounted engines. The Fokker F-28 Mk1000 is interesting since it has a T-tail and fuselage-mounted engines, this makes for a nice comparison to see what the influence of tail/engine layout has on the vertical tail design with a hump. In addition, for both these aircraft LFC investigations have been performed in the past. The Fokker F100 (evaluation of F-28) with a NLF glove and the Airbus A320 with a HLFC suction device in the vertical stabilizer, as discussed in section 3.3. Finally, for these aircraft, their geometry data and their stability analysis by the Fokker / Obert method are available, which is convenient for validation purposes.

The vertical tailplane planforms are shown in Figure 4.25 for comparison. It shows that the vertical tail of the Airbus A320 is significantly larger and is more tapered, whilst the Fokker F-28 Mk1000 has more sweep and little taper. The geometries and all other specifications required for the calculations of both aircraft are specified in detail in Table H.1, and Table H.2 for the Airbus A320 and Table H.3, and Table H.4 for the Fokker F-28 Mk1000. Note that section H.1 contains a short explanation of how the vertical tailplane rolling moment arm is estimated.

The flight conditions are specified in Table H.5, and Table H.6, for the Airbus A320 and Fokker F-28 Mk1000, respectively. They contain both a cruise and landing condition. These are required for the stability analysis and critical design requirements, discussed in section 4.3. The overall effect of the hump in terms of weight and drag will be evaluated in cruise. Mainly because skin friction is a large part of the aircraft drag in cruise as discussed in chapter 3. During landing and take-off, high lift conditions apply, which increase the lift-induced drag significantly. This means that the skin friction drag would become much less significant relative to the lift-induced drag. Moreover, at high-lift conditions, the flow at the vertical tail is most likely turbulent, which also makes the hump ineffective since it requires laminar flow to be effective. Weather circumstances during cruise that may result in turbulent flow at the vertical tail are not taken into account.

4.8. Sensitivity analysis

To see the effect of the vertical tail geometry on the effectiveness of the DeLaH, a sensitivity analysis is performed. There will be two main variations during the sensitivity analysis, namely the sweep variation and surface area variation. Both will be discussed in the next sections, including the calculation of the affected variables due to changing the main sensitivity variable.

[8] Image by Aragão, P.. (2013). Reg: F-WWIQ photos. Aircraft: Airbus A320-216. Airline: Airbus Industri. Serial #: 5098. Retrieved January 22, 2025, from `https://www.jetphotos.com/photo/7617615/`

[9] Image by Wallner, R.. (1989). Fokker F-28-1000 Fellowship - Piedmont Airlines. Retrieved January 22, 2025, from `https://www.airliners.net/photo/Piedmont-Airlines/Fokker-F-28-1000-Fellowship/451713/L`

The reason to vary the sweep and surface area is to exclude as many other variables as possible, to see the isolated effect of the main variable of interest. The sweep angle can be isolated by keeping the span, aspect ratio, and taper ratio constant. The sweep angle is relevant for the change in local Mach numbers. The more sweep, the lower the local Mach number, reducing the onset of shock waves, and increasing the critical Mach number. Another argument to analyze sweep is that at higher sweep angles the better the vertical tail can handle high sideslip angles (improved sideslip characteristics) according to Obert [17]. The surface area is of interest since the most important factor in the side force generated by the vertical tail is the span, whilst the planform is less important also according to Obert [17]. Now if only the span was varied, the sweep angle and aspect ratio would also change, making it unclear what the driving factor is. As the sweep angle is already varied in the other sensitivity analysis, it would be desirable to keep it constant for this sensitivity analysis. With the sweep angle kept constant there are two options to vary the span. Either through changing the aspect ratio, however, the taper ratio would also change, or through scaling the whole planform. The latter is chosen since this keeps the sweep angle, aspect ratio, and taper ratio constant, isolating the effect of the surface area scaling. An added benefit is that the existing vertical tail does not have to be redesigned, but can simply be enlarged or reduced in size, depending on the requirements.

4.8.1. Sweep variation

For the sweep variation, the quarter-chord sweep angle is varied between 30 and 60 degrees in 5-degree increments. This range was chosen based on the most common design ranges for vertical tailplanes, as shown in Table 2.1. Figure 4.26 visualizes the effect a sweep angle variation has on the vertical tailplane geometry and associated variables. The calculation of the affected variables as well as the assumptions are listed in Table 4.2. One of the assumptions is that the slight downward shift of the whole vertical tailplane relative to the fuselage is not taken into account. This slight shift is the result of the fuselage centerline at the tail cone not being horizontal, but slightly upwards, and the definition of the location of the root chord, where the semi-root chord intersects the fuselage centerline. Another important assumption is that the CG shift due to the new tail is not taken into account.

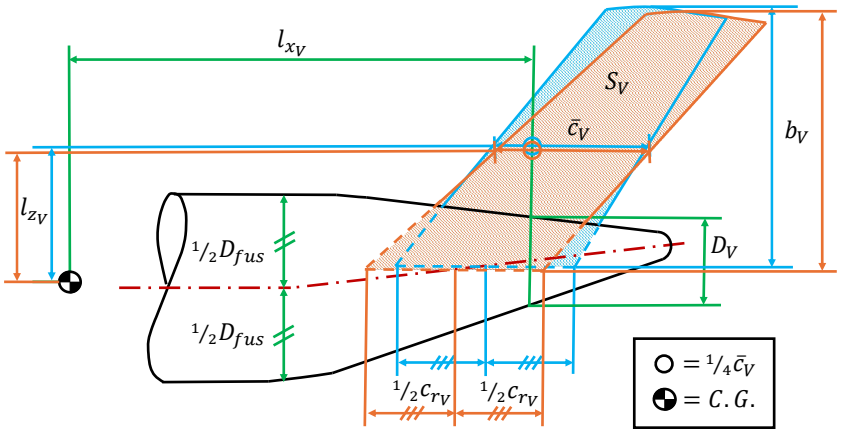

Figure 4.26: Sweep angle variation.

4.8.2. Surface area variation

For the surface area variation, the surface area will be scaled by a surface area scaling factor between 0.5 and 1.2 in 0.1-sized increments. This range is selected to see both the effect of a reduced as well as an enlarged tail. Since an enlarged tail is not desirable due to the associated drag increase, this is only tested up to a 20% increase. For the reduced tail a size reduction of up to 50% is used. Smaller vertical tailplane sizes would seem unlikely, but can always be calculated in future research if deemed useful. Figure 4.27 visualizes the effect a surface area variation has on the vertical tailplane geometry and associated variables. The calculation of the affected variables as well as the assumptions are listed in Table 4.3, and Table 4.4.

Regarding the mounting location of the horizontal stabilizer, special attention is required when it comes to a surface area variation. For both T-tails and conventional tails the horizontal stabilizer will be mounted at the same longitudinal location relative to the vertical tailplane ($\frac{x_H}{c_V}$). However, regarding the spanwise mounting location, $\frac{z_H}{b_V}$, there is a difference. For conventional tails, the mounting location of the horizontal tailplane stays at the same location on the fuselage (often $\frac{z_H}{b_V} = 0$). T-tails are handled differently as seen in Figure 4.28. As the horizontal tailplane geometry is not changed, the spanwise space required to mount it to the vertical tailplane must stay the same. Therefore $b_{V_{top}}$ must stay constant. This has an effect on both $\frac{z_H}{b_V}$ as well as the S_{V_R}.

Another point of attention is the rudder surface area as it is chosen to keep $\frac{c_R}{c_V}$ constant. This was chosen to keep the sensitivity analysis simple as rescaling the rudder to keep the same effective control becomes too complex. Not only the rudder chord reduces due to keeping $\frac{c_R}{c_V}$ constant with a vertical tail surface area reduction, also the rudder span reduces due to the reduction in b_V. To then compensate for the loss in rudder surface area, the rudder control effectiveness should be increased, which is also dependent on $\frac{c_R}{c_V}$. However, for normal rudders the maximum $\frac{c_R}{c_V}$ lies around 0.35 to 0.40 (see Table 2.1), which is partly bound by structural limitations. Therefore it was chosen not to vary the $\frac{c_R}{c_V}$.

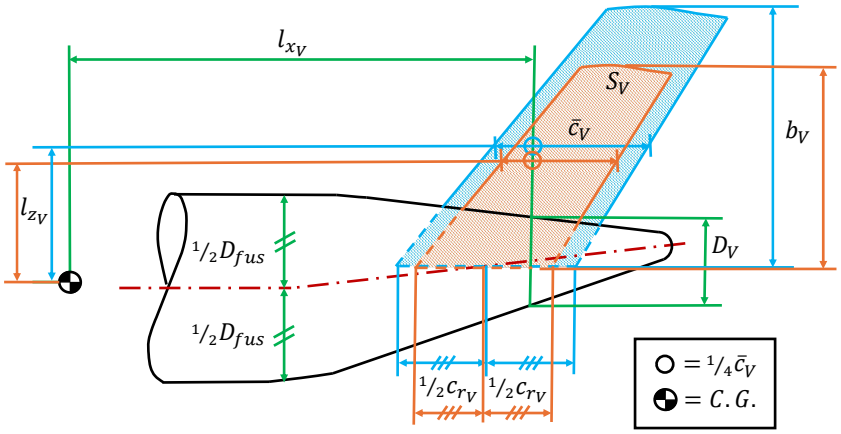

Figure 4.27: Surface area variation

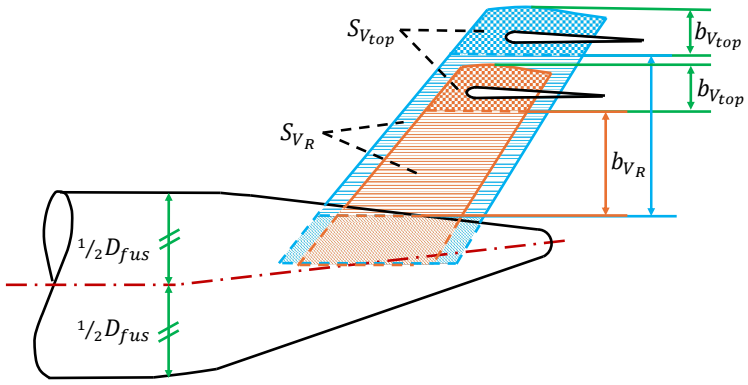

Figure 4.28: Surface area variation T-tail

Table 4.2: Affected variables due to sweep variation

Affected variable	Calculation of new value	Assumptions
$\bar{c}_{V}$	$(\bar{c}_{V})_{new} = (\bar{c}_{V})_{original}$	Kept constant
S_{V}	$(S_{V})_{new} = (S_{V})_{original}$	Kept constant.
b_{V}	$(b_{V})_{new} = (b_{V})_{original}$	Kept constant.
A_{V}	$(A_{V})_{new} = (A_{V})_{original}$	Kept constant.
$\Lambda_{1/4c_{V}}$	Main variable of sensitivity analysis.	-
λ_{V}	$(\lambda_{V})_{new} = (\lambda_{V})_{original}$	Kept constant.
$S_{V_{ref}}$	$\left(S_{V_{ref}}\right)_{new} \approx \left(S_{V_{ref}}\right)_{original}$	Slight change due to fuselage being tapered not taken into account.
$l_{x_{V}}$	$\left(l_{x_{V}}\right)_{new} = \left(l_{x_{V}}\right)_{original}$	CG shift due to new tail not taken into account.
$l_{x_{V_{ref}}}$	$\left(l_{x_{V_{ref}}}\right)_{new} = \left(\left(l_{x_{V_{ref}}}\right)_{original} - \left(l_{x_{V}}\right)_{original}\right) \frac{tan\left(\left(\Lambda_{1/4c_{V}}\right)_{new}\right)}{tan\left(\left(\Lambda_{1/4c_{V}}\right)_{original}\right)} + \left(l_{x_{V}}\right)_{original}$	CG shift due to new tail not taken into account.
$l_{z_{V}}$	$\left(l_{z_{V}}\right)_{new} \approx \left(l_{z_{V}}\right)_{original}$	Slight downward shift due to fuselage being tapered not taken into account. CG shift due to new tail not taken into account.
$\frac{S_{df}}{S_{V}}$	$\left(\frac{S_{df}}{S_{V}}\right)_{new} = \left(\frac{S_{df}}{S_{V}}\right)_{original}$	Assume dorsal fin scales accordingly.
$\frac{b_{V}}{d_{V}}$	$\left(\frac{b_{V}}{d_{V}}\right)_{new} = \left(\frac{b_{V}}{d_{V}}\right)_{original}$	Kept constant.
$\frac{z_{H}}{b_{V}}$	$\left(\frac{z_{H}}{b_{V}}\right)_{new} = \left(\frac{z_{H}}{b_{V}}\right)_{original}$	Kept constant.
$\frac{x_{H}}{c_{V}}$	$\left(\frac{x_{H}}{c_{V}}\right)_{new} = \left(\frac{x_{H}}{c_{V}}\right)_{original}$	Slight downward shift due to fuselage being tapered not taken into account.
$\frac{c_{R}}{c_{V}}$	$\left(\frac{c_{R}}{c_{V}}\right)_{new} = \left(\frac{c_{R}}{c_{V}}\right)_{original}$	Kept constant.
$S_{V_{R}}$	$\left(S_{V_{R}}\right)_{new} = \left(S_{V_{R}}\right)_{original}$	Kept constant.

Table 4.3: Affected variables due to surface area variation part 1/2

Affected variable	Calculation of new value	Assumptions
$\bar{c}_V$	$\left(c_{r_V}\right)_{new} = \frac{2\left(S_V\right)_{new}}{\sqrt{\left(A_V\right)_{original}\left(S_V\right)_{new}\left(1+\left(\lambda_V\right)_{original}\right)}}$ $\left(\bar{c}_V\right)_{new} = \frac{2}{3}\left(c_{r_V}\right)_{new}\frac{\left(1+\left(\lambda_V\right)_{original}+\left(\lambda_V\right)^2_{original}\right)}{\left(1+\left(\lambda_V\right)_{original}\right)}$	Assuming straight-tapered planform, see Equation 2.5.
S_V	Main variable of sensitivity analysis.	-
b_V	$\left(b_V\right)_{new} = \sqrt{\left(A_V\right)_{original}\left(S_V\right)_{new}}$	Kept constant.
A_V	$\left(A_V\right)_{new} = \left(A_V\right)_{original}$	Kept constant.
$\Lambda_{1/4c_V}$	$\left(\Lambda_{1/4c_V}\right)_{new} = \left(\Lambda_{1/4c_V}\right)_{original}$	Kept constant.
λ_V	$\left(\lambda_V\right)_{new} = \left(\lambda_V\right)_{original}$	Kept constant.
$S_{V_{ref}}$	$\left(d_V\right)_{original} = \frac{\left(b_V\right)_{original}}{\left(\frac{b_V}{d_V}\right)_{original}}$ $\left(c_{r_{V_{ref}}}\right)_{new} = \left(c_{r_V}\right)_{new} - \frac{1}{2}\left(d_V\right)_{original}tan(\Lambda_{LE}) + \frac{1}{2}\left(d_V\right)_{original}tan(\Lambda_{TE})$ $\left(S_{V_{ref}}\right)_{new} = \left(S_V\right)_{new} - \frac{1}{2}\left(\left(c_{r_V}\right)_{new} + \left(c_{r_{V_{ref}}}\right)_{new}\right)\frac{1}{2}\left(d_V\right)_{original}$	Slight change to fuselage being tapered not taken into account.
l_{x_V}	$\left(l_{x_V}\right)_{new} = \left(l_{x_V}\right)_{original}$	CG shift due to new tail not taken into account.
$l_{x_{V_{ref}}}$	$\left(l_{z_{V_{ref}}}\right)_{original} = \left(l_{z_V}\right)_{original} + \frac{\left(\left(l_{x_{V_{ref}}}\right)_{original} - \left(l_{x_V}\right)_{original}\right)}{tan\left(\left(\Lambda_{1/4c_V}\right)_{original}\right)}$ $\left(l_{z_{V_{ref}}}\right)_{new} = \left(\left(l_{z_{V_{ref}}}\right)_{original} - \frac{1}{2}\left(d_V\right)_{original}\right)\frac{\left(\left(b_V\right)_{new} - \frac{1}{2}\left(d_V\right)_{original}\right)}{\left(\left(b_V\right)_{original} - \frac{1}{2}\left(d_V\right)_{original}\right)} + \frac{1}{2}\left(d_V\right)_{original}$ $\left(l_{x_{V_{ref}}}\right)_{new} = \left(\left(l_{z_{V_{ref}}}\right)_{new} - \left(l_{z_V}\right)_{new}\right)tan\left(\left(\Lambda_{1/4c_V}\right)_{original}\right) + \left(l_{x_V}\right)_{original}$	CG shift due to new tail not taken into account.
l_{z_V}	$\left(l_{z_V}\right)_{new} = \frac{1}{3}\frac{\left(1+2\left(\lambda_V\right)_{original}\right)}{\left(1+\left(\lambda_V\right)_{original}\right)}\left(b_V\right)_{new} + \left(\frac{1}{2}D_{fus_{max}} - \frac{1}{2}\left(d_V\right)_{original}\right) + \left(\frac{z_W}{D_{fus_{max}}}\right)D_{fus_{max}}$	Slight downward shift due to fuselage being tapered not taken into account. CG shift due to new tail not taken into account.

Table 4.4: Affected variables due to surface area variation part 2/2

Affected variable	Calculation of new value	Assumptions
$\frac{S_{df}}{S_V}$	$\left(\frac{S_{df}}{S_V}\right)_{new} = \left(\frac{S_{df}}{S_V}\right)_{original}$	Assume dorsal fin scales accordingly.
$\frac{b_V}{d_V}$	$\left(\frac{b_V}{d_V}\right)_{new} = \left(\frac{b_V}{d_V}\right)_{original} \left(\frac{(b_V)_{new}}{(b_V)_{original}}\right)$	-
$\frac{z_H}{b_V}$	**T-tail:** $\left(\frac{z_H}{b_V}\right)_{new} = \frac{\left((b_V)_{new} - \left((b_V)_{original} - \left(\left(\frac{z_H}{b_V}\right)_{original} (b_V)_{original}\right)\right)\right)}{(b_V)_{new}}$ **Conventional tail:** $\left(\frac{z_H}{b_V}\right)_{new} = \left(\frac{z_H}{b_V}\right)_{original} \left(\frac{(b_V)_{original}}{(b_V)_{new}}\right)$	**T-tail:** Assume horizontal tailplane stays mounted at same spanwise distance from tip. **Conventional tail:** Assume horizontal tailplane stays mounted at same fuselage mounting location.
$\frac{x_H}{c_V}$	$\left(\frac{x_H}{c_V}\right)_{new} = \left(\frac{x_H}{c_V}\right)_{original}$	Kept constant.
$\frac{c_R}{c_V}$	$\left(\frac{c_R}{c_V}\right)_{new} = \left(\frac{c_R}{c_V}\right)_{original}$	Kept constant.
S_{V_R}	$\left(c_{r_{V_{ref}}}\right)_{original} = \left(c_{r_V}\right)_{original} - \frac{1}{2}(d_V)_{original} tan(\Lambda_{LE}) + \frac{1}{2}(d_V)_{original} tan(\Lambda_{TE})$ $\left(S_{V_{top}}\right)_{original} = (S_V)_{original} - \frac{1}{2}\left(\left(c_{r_V}\right)_{original} + \left(c_{r_{V_{ref}}}\right)_{original}\right)\frac{1}{2}(d_V)_{original} - \left(S_{V_R}\right)_{original}$ **T-tail:** $\left(b_{V_{top}}\right)_{original} = \frac{-B+\sqrt{B^2-4AC}}{2A}$ where $A = \frac{1}{2}tan\left((\Lambda_{LE})_{original}\right) - \frac{1}{2}tan\left((\Lambda_{TE})_{original}\right)$, $B = \left(c_{t_V}\right)_{original}$, $C = -\left(S_{V_{top}}\right)_{original}$ **Conventional tail:** $\left(b_{V_{top}}\right)_{original} = 0$ $\left(c_{t_V}\right)_{new} = (\lambda_V)_{original} * \left(c_{r_V}\right)_{new}$ $\left(c_{r_{V_{top}}}\right)_{new} = \left(c_{t_V}\right)_{new} + \left(b_{V_{top}}\right)_{original} tan\left((\Lambda_{LE})_{original}\right) - \left(b_{V_{top}}\right)_{original} tan\left((\Lambda_{TE})_{original}\right)$ $\left(S_{V_{top}}\right)_{new} = \frac{1}{2}\left(\left(c_{r_{V_{top}}}\right)_{new} + \left(c_{t_V}\right)_{new}\right)\left(b_{V_{top}}\right)_{original}$ $\left(S_{V_R}\right)_{new} = (S_V)_{new} - \frac{1}{2}\left(\left(c_{r_V}\right)_{new} + \left(c_{r_{V_{ref}}}\right)_{new}\right)\frac{1}{2}(d_V)_{original} - \left(S_{V_{top}}\right)_{new}$	Keeping $\left(b_{V_{top}}\right)_{original}$ constant to ensure enough mounting room for the horizontal stabilizer, as seen in Figure 4.28.

5

Verification and validation of method

In this chapter the various components of the method, as proposed in chapter 4, and intermediate results are verified and validated. This chapter can be divided into two main parts: vertical tail aerodynamics and stability analysis. For the vertical tail aerodynamics, first, the wind tunnel experiment pressure distributions are replicated with XFoil, to ensure XFoil is capable to simulate the M3J wing and hump in section 5.1. Second, in section 5.2, Q3D for vertical tailplanes will be verified, by analyzing vertical tailplane lift curve slopes for various aircraft. Third, the transition location simulations are discussed in section 5.3. This includes the calculations and simulations to obtain the transition locations, as well as discussing the transition location results. Also, the effect of tip vortices, boundary conditions, and separation on these results are discussed. For the stability analysis, the implementation of the Fokker / Obert method is validated by comparing the various calculated stability coefficients to wind tunnel- and calculated data from Fokker / Obert in section 5.4.

5.1. Validation of Xfoil with experimental data

As explained in section 4.2, it is proposed to use Q3D for the aerodynamic analyses. To be able to model the DeLaH it is required to use a NLF airfoil. During the wind tunnel experiments with the hump, the M3J airfoil was used, as mentioned in section 4.6. Therefore it is crucial that Q3D is able to replicate the flow around the M3J airfoil. More precisely, XFoil (the 2D viscous analysis of Q3D) must be capable of replicating the pressure distribution of the M3J airfoil as found during wind tunnel experiments.

5.1.1. M3J pressure distribution

Figure 5.1 shows a schematic of the M3J wing in the wind tunnel, with upper and lower pressure taps (without DeLaH). The corresponding measurements taken during the experiments are shown in Figure 5.4. Note that the measurements were only taken on the pressure side of the wing, hence only the lower part of the experimental pressure distribution is shown. Moreover, at the trailing edge, no pressure taps were present, and therefore no pressure data near $x/c_{streamwise} = 1$. Now to replicate this pressure distribution in XFoil, the sweep angle must be accounted for. As XFoil is a 2D analysis, it will only see the normal-to-sweepline flow, shown in orange in Figure 5.1. This affects the flow velocity as well as the angle of attack and the airfoil shape XFoil sees. The freestream velocity U_∞ (streamwise) must be split into a spanwise- and a normal-to-sweepline velocity component. The latter is used for XFoil. The angle of attack can be calculated with Equation 5.1, where $\Lambda_{1/4c} = 45\ deg$ for the M3J wing used in the experiments.

$$\alpha_{normal-to-sweepline} = sin^{-1}\left(\frac{sin(\alpha_{streamwise})}{cos(\Lambda_{1/4c})}\right) \tag{5.1}$$

The effective airfoil shape also changes due to sweep. Figure 5.2 shows the M3J airfoil shape both streamwise and normal-to-sweepline, visualized with the same colors as in Figure 5.1; blue and orange. It can be seen that the chord lengths differ greatly. When normalized by their respective chords in Figure 5.3, it becomes clear that the normal-to-sweepline airfoil has a higher thickness-to-chord ratio.

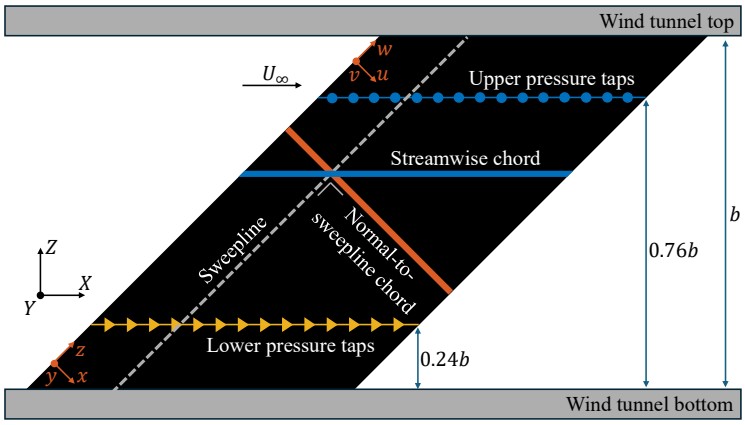

Figure 5.1: M3J wing in wind tunnel, with $b = 1.25\ m$, adapted figure [72] [67].

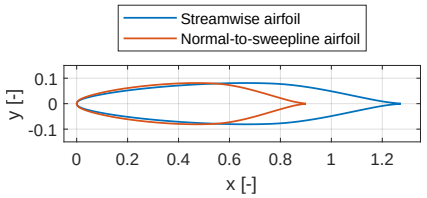

Figure 5.2: M3J airfoil shape, streamwise and normal-to-sweepline.

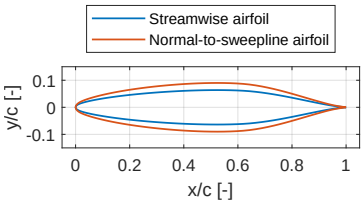

Figure 5.3: M3J airfoil shape, streamwise and normal-to-sweepline, normalized.

Taking all of the above into account, the pressure distribution is simulated with XFoil by setting the transition location (x_{tr}/c) to 0.565 on the pressure side and to free transition on the suction side with the N-factor to its default value of 9. The transition location is based on the value found during the wind tunnel experiments for M3J wing at $\alpha = 3\ deg$ and $Re = 2.29 \cdot 10^6$. After correcting the XFoil pressure distribution for the spanwise velocity component (converting it to the streamwise direction), the purple graph in Figure 5.4 is obtained. It matches the wind tunnel experiments very well. From this, it can be concluded that XFoil can replicate the pressure distribution of the M3J airfoil, as found during wind tunnel experiments, sufficiently well, and therefore XFoil (as part of Q3D) can be used as the aerodynamic analysis tool in this research.

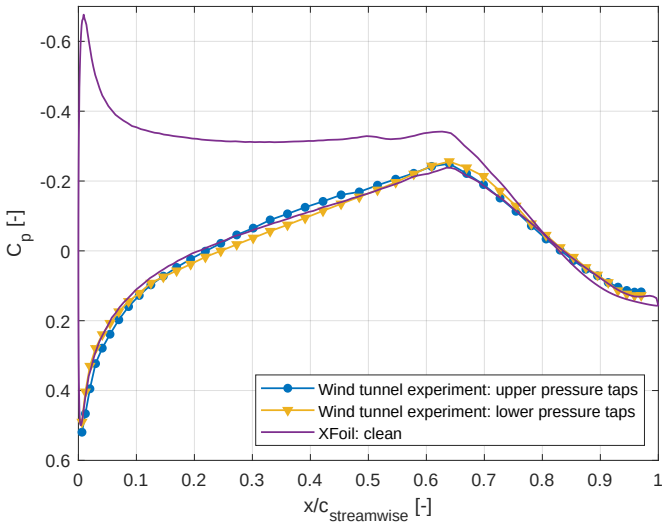

Figure 5.4: M3J pressure distribution from wind tunnel measurements (pressure side only, with DREs) compared to XFoil (pressure side $(x_{tr}/c) = 0.565$, suction side free transition at $N = 9$), $\alpha = 3\ deg$ and $Re = 2.29 \cdot 10^6$.

It is important to note that, based on Drela and Youngren[1], modifying the N-factor in XFoil modifies the transition location. Nevertheless, since the assumptions behind the stability calculations computed in the background by XFoil are unclear, in what follows the N-factor from XFoil will be ignored, only modifying x_{tr}/c to set the transition location based on the experimental observations/solution from the boundary layer solver and stability analysis. As XFoil will always use the most upstream transition

[1] Drela, M., Youngren, H.. (2001). XFOIL 6.9 User Primer. Retrieved February 14, 2025, from `https://web.mit.edu/drela/Public/web/xfoil/xfoil_doc.txt`

location, regardless of the transition method (through N-factor or directly setting x_{tr}/c), the N-factor in XFoil must be set sufficiently high not to interfere with the directly set x_{tr}/c. A more detailed analysis of the transition settings in XFoil is found in Appendix E.

5.1.2. Delft Laminar Hump

Next to the M3J wing, the effect of the DeLaH will also be simulated with XFoil in this research. As explained in subsection 4.2.2, the aerodynamic effect of the hump is represented by a shift in transition location, neglecting the hump geometry. In XFoil this is established by setting the x_{tr}/c to the experimental transition location of the hump $(x_{tr}/c)_{hump}$. From the wind tunnel tests $(x_{tr}/c)_{hump} =$ [redacted] CONFIDENTIAL on the pressure side for M3J wing at $\alpha = 3\ deg$ and $Re = 2.29 \cdot 10^6$, without roughness forcing. The suction side is set to free transition with the N-factor to its default value of 9 in XFoil. Figure 5.5 shows the associated pressure distribution for the hump in light blue, as well as the clean configuration in purple ($(x_{tr}/c)_{clean} = 0.565$), obtained in the previous section.

Figure 5.5: CONFIDENTIAL M3J clean and hump pressure distribution, comparison XFoil (pressure side $(x_{tr}/c)_{clean} = 0.565$ and $(x_{tr}/c)_{hump} =$ [redacted], suction side free transition at $N = 9$) and numerical simulation (no roughness forcing), $\alpha = 3\ deg$ and $Re = 2.29 \cdot 10^6$. Note hump only present on pressure side.

Figure 5.6: CONFIDENTIAL Zoomed M3J clean and hump pressure distribution, comparison XFoil (pressure side $(x_{tr}/c)_{clean} = 0.565$ and $(x_{tr}/c)_{hump} =$ [redacted], suction side free transition at $N = 9$) and numerical simulation (no roughness forcing), $\alpha = 3\ deg$ and $Re = 2.29 \cdot 10^6$. Note hump only present on pressure side.

The pressure distributions for the clean and hump configurations in Figure 5.5 are very similar and largely overlap, except on the suction side around 0.52 x/c, and the pressure side around 0.65 x/c. On the suction side, this is the result of the free transition calculated by XFoil at $N = 9$ even though there is no hump present on the suction side. On the pressure side, a laminar separation bubble occurs, because of the strong adverse pressure gradient, the (laminar) flow separates, transitions, and reattaches. Thus the difference in pressure distribution between XFoil clean and hump around 0.65 x/c is only due to a laminar separation bubble as the geometry of the hump is neglected. This also implies that the $(x_{tr}/c)_{hump} =$ [redacted] CONFIDENTIAL is not the maximum potential transition location due to the hump, but the results of the laminar separation bubble due to the strong adverse pressure gradient of the M3J airfoil. A visualization of this laminar separation bubble is shown in Figure 5.7, which occurs when no roughness forcing is used. Here at the strong convex area around 0.65 x/c laminar separation occurs, directly transitioning and reattaching, forming the laminar separation bubble. This is also what happens in Figure 5.5 at pressure side around 0.65 x/c, where the XFoil clean and hump pressure distributions differ. During the wind tunnel tests roughness forcing was used in the form of discrete roughness elements as well as a distributed roughness patch, as discussed in subsection 4.6.2. The effect of this is shown in Figure 5.8, where the boundary layer transitions further upstream due to the roughness forcing, subsequently turbulent transition occurring before the strong convex area (before the strong adverse pressure region). In this case, there is much more room for the hump to delay transition, before reaching the strong convex area, where a laminar separation bubble would occur. This is why Figure 5.8 is representative of the wind tunnel test, to see the maximum effect of the hump in terms of transition delay. In this research, the laminar boundary layer is maximized for the least overall drag, therefore Figure 5.7 is representative.

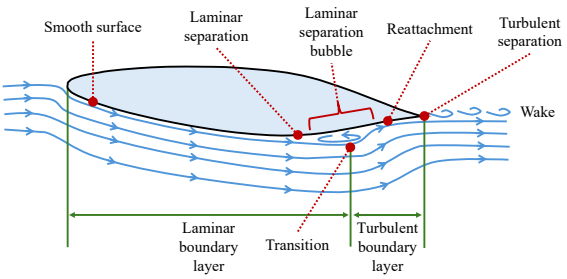

Figure 5.7: M3J airfoil with laminar separation bubble schematic.

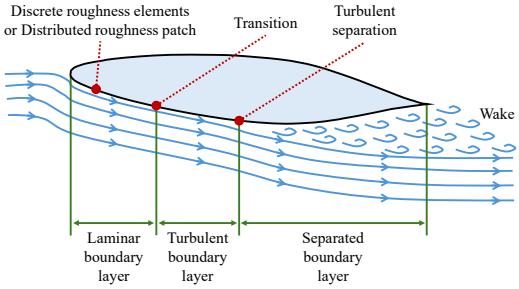

Figure 5.8: M3J airfoil with turbulent separation schematic.

Effect of hump geometry

In this research, the hump is only modeled as a transition shift, however, in reality, the hump is a physical change to the geometry of a wing. Whether this change in geometry can be neglected must be verified. A numerical simulation using the Harmonic Navier Stokes Solver [73] is shown in Figure 5.5, which shows the pressure distribution around the location of the hump. Figure 5.6 gives a zoomed view around this location for the clean and hump configuration, green and orange respectively. Comparing these, it becomes clear that the hump geometry creates a region of pressure gradient change-over (adverse-favorable-adverse-favorable pressure gradient). However, the pressure distribution upstream and downstream of this change-over stays unchanged compared to the clean numerical simulation. The effect of the hump geometry on the pressure drag is calculated following Anderson [29]. Since only the numerical data around the area of the hump on the pressure side is available, the change in pressure drag is calculated between the clean and hump configuration. In Table 5.1, this value is compared to the change in pressure and friction drag due to the transition shift (due to the hump), which is calculated with XFoil. For the comparison, a reference value is defined, namely $(C_D)_{total}$ the total drag coefficient, which does not include the $\left(C_{D_p}\right)_{NumSim}$, as this is the value without hump.

$$(C_D)_{total} = \left(C_{D_p}\right)_{XFoil} + \left(C_{D_f}\right)_{XFoil} \tag{5.2}$$

From Table 5.1, it can be concluded that the effect of the hump geometry on the drag is relatively small. Therefore, it can be argued not to take the hump geometry into account when modeling the hump. Note however, since the hump has only been tested at subsonic Mach numbers, it is yet unknown whether at cruise Mach numbers the pressure gradient change-over along the hump will cause a shock wave. To establish whether the hump causes a shock, dedicated wind tunnel experiments, flight tests, and/or CFD simulations are necessary.

Table 5.1: Comparison effect of hump on drag through transition location shift and geometry. Based on Figure 5.5, using M3J airfoil, XFoil (pressure side $(x_{tr}/c)_{clean} = 0.565$ and $(x_{tr}/c)_{hump} =$ [redacted] CONFIDENTIAL, suction side free transition at $N = 9$) and numerical simulation (no roughness forcing), $\alpha = 3\,deg$ and $Re = 2.29 \cdot 10^6$. Note hump only present on pressure side.

	XFoil		Numerical simulation
	$\left(C_{D_p}\right)_{XFoil}$	$\left(C_{D_f}\right)_{XFoil}$	$\left(C_{D_p}\right)_{NumSim}$
$(C_D)_{total}$ reduction due to hump	1.63%	6.39%	-0.38%

5.2. Verification of Q3D vertical tailplane lift curve slope

Q3D will be used to calculate the vertical tailplane lift curve slope in the method proposed in section 4.2. Therefore it should be verified whether the Q3D calculated values are representative of the actual lift curve slopes.

5.2.1. Verification of isolated Q3D vertical tailplane lift curve slope calculation

To obtain the vertical tailplane lift curve slope with Q3D, the lift coefficient is calculated based on the planform geometry and airfoil shape at varying angles of attack (-1, 0, and 1). By using the calculated lift coefficients at the varying angles of attack the lift curve slope in the linear regime can estimated. Note that Q3D assesses the vertical tailplane as an isolated, free-floating wing, without any walls present (no fuselage or horizontal stabilizer interference, etc.), because the vertical tailplane lift curve slope required for the Fokker / Obert stability analysis (section 2.5) is based on the isolated free-floating vertical tailplane as well.

To verify the Q3D calculation, the calculated values of various existing aircraft are compared with data from the Fokker / Obert report [14], which gives values for the isolated vertical tailplane lift curve slopes. It is assumed that the Fokker / Obert data is closest to the real vertical tailplane lift curve slopes since this contains a lot of data from the actual manufacturers. Moreover, the Fokker aircraft values can be assumed to be very accurate since it is a Fokker report. Nevertheless, the USAF DATCOM method [2] is also used to calculate the lift curve slopes, for extra verification. This will also serve as an extra check whether the Fokker / Obert data has any biases for Fokker aircraft compared to other aircraft.

The planform geometries are based on Fokker / Obert data [14] and for each aircraft, the same planform is used in each lift curve slope analysis method. This is not the case for the airfoil data, since this data is not available. Since for most aircraft, the thickness-to-chord ratio is available, this is converted to the closest simple symmetric NACA 4-digit series airfoil. Moreover, for the USAF DATCOM method also not all of these NACA 4-digit series airfoils are available, therefore the closest equivalent is used. An overview of all the airfoils is given in Table F.1.

Table 5.2: CONFIDENTIAL Vertical tailplane lift curve slope verification. Values in cruise conditions for each aircraft. Fokker / Obert data from [14]. Note: $\epsilon_{a,b}$ states error a relative to b.

Aircraft type	$(C_{L_\alpha})_V$ **Q3D** $[deg^{-1}]$	$(C_{L_\alpha})_V$ **USAF DATCOM (dat)** $[deg^{-1}]$	$(C_{L_\alpha})_V$ **Fokker/ Obert (fok) [14]** $[deg^{-1}]$	$\epsilon_{Q3D,fok}$ [%]	$\epsilon_{dat,fok}$ [%]	$\epsilon_{Q3D,dat}$ [%]
Airbus A300	0.0401	0.0407	[redacted]	[redacted]	[redacted]	-1.45
Airbus A320	0.0444	0.0461	[redacted]	[redacted]	[redacted]	-3.69
Airbus A340-300	0.0388	0.0393	[redacted]	[redacted]	[redacted]	-1.21
Boeing 737-100	0.0457	0.0473	[redacted]	[redacted]	[redacted]	-3.26
Boeing XB-47 (tailplane model)	0.0420	0.0427	[redacted]	[redacted]	[redacted]	-1.63
Douglas DC9-30	0.0306	0.0298	[redacted]	[redacted]	[redacted]	2.86
F-29 model 1-1	0.0325	0.0328	[redacted]	[redacted]	[redacted]	-0.73
F-29 model 2-5	0.0421	0.0451	[redacted]	[redacted]	[redacted]	-6.52
F-29 model 5-3	0.0348	0.0354	[redacted]	[redacted]	[redacted]	-1.71
Fokker F-28 Mk1000 model 8-3	0.0305	0.0301	[redacted]	[redacted]	[redacted]	1.52
Fokker F-28 QC 40 deg model 8-4	0.0280	0.0277	[redacted]	[redacted]	[redacted]	1.16
Fokker F-28 Tailplane model 9	0.0302	0.0301	[redacted]	[redacted]	[redacted]	0.36
Fokker F-28 Wing off model 4	0.0267	0.0262	[redacted]	[redacted]	[redacted]	1.73
SKV-LST-1 (model of subtype F-28)	0.0305	0.0301	[redacted]	[redacted]	[redacted]	1.47
SKV-LST-2 (model of subtype F-28)	0.0264	0.0258	[redacted]	[redacted]	[redacted]	2.12
SKV-LST-3 (II) (model of subtype F-28)	0.0274	0.0270	[redacted]	[redacted]	[redacted]	1.57
VFW-614	0.0362	0.0371	[redacted]	[redacted]	[redacted]	-2.50
mean $\pm$ stdev				**5.47 $\pm$ 4.47**	**6.20 $\pm$ 6.16**	**-0.58 $\pm$ 2.44**

Table 5.2 shows the obtained vertical tailplane lift curve slopes for Q3D, USAF DATCOM (dat), and Fokker / Obert (fok). Note that all results are calculated at cruise conditions and for Q3D, N-factor is set to its default value of 9. The relative errors between each of these methods are also shown. From these results, several conclusions can be drawn. The Q3D analysis is, on average, the closest to the Fokker / Obert data, when comparing $\epsilon_{Q3D,fok}$, and $\epsilon_{dat,fok}$. It stands out that the Q3D analysis performs better for Fokker aircraft compared to aircraft by other manufacturers when checking the error percentages for the individual aircraft in $\epsilon_{Q3D,fok}$. However, this is also the case for the USAF DATCOM values, $\epsilon_{dat,fok}$, which have errors of similar magnitude. As the errors for both Fokker and non-Fokker aircraft between

Q3D and USAF DATCOM are relatively low ($\epsilon_{Q3D,dat}$), it can be argued that the lift curve slopes for non-Fokker aircraft might be underestimated by Fokker / Obert. It is still uncertain whether this is the case as the airfoil shapes used by Q3D and USAF DATCOM are based on thickness-to-chord ratios. It could be that the Fokker / Obert data is based on other airfoil shapes, as this data is not available.

Overall from this analysis, it can be concluded that Q3D can calculate the vertical lift curve slope of existing aircraft reasonably well. Hence Q3D is used to calculate new vertical tailplane designs during the sensitivity analysis (section 6.2) and it can be assumed with some confidence that these values are also representative. In addition, the airfoil shape does not matter as much, as the sensitivity analysis will use the same airfoil throughout and will look at the relative effect of a change in planform geometry.

5.2.2. Comparison vertical tailplane lift curve slope calculation performance and aircraft characteristics

To make the data from Table 5.2 more informative, the data is plotted against various aircraft characteristics. Figure 5.9, Figure 5.10, Figure 5.11, and Figure 5.12 show the percentage errors for the various aircraft, distinguishing between conventional- and T-tail, and comparing for quarter-chord sweep angle, taper ratio and aspect ratio. Other characteristics, such as cruise Mach number, cruise altitude, thickness-to-chord ratio, span, and surface area, were also tested but yielded no clear trends.

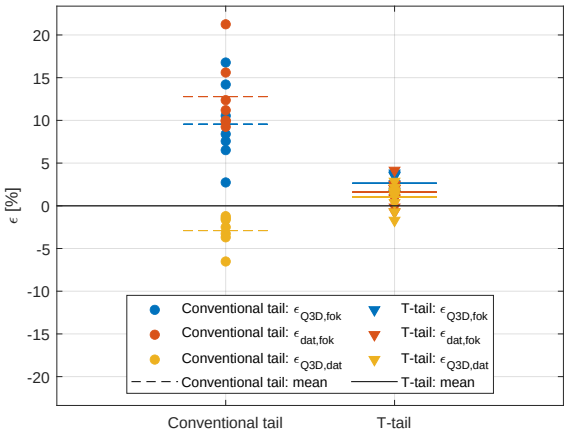

Figure 5.9: Vertical tailplane lift curve slope verification: Conventional vs. T-tail. Values in cruise conditions for each aircraft. Note: $\epsilon_{a,b}$ states error a relative to b.

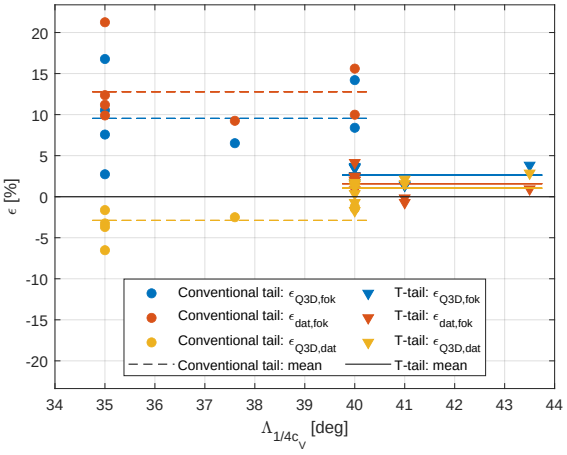

Figure 5.10: Vertical tailplane lift curve slope verification: Conventional vs. T-tail quarter-chord sweep angle. Values in cruise conditions for each aircraft. Note: $\epsilon_{a,b}$ states error a relative to b.

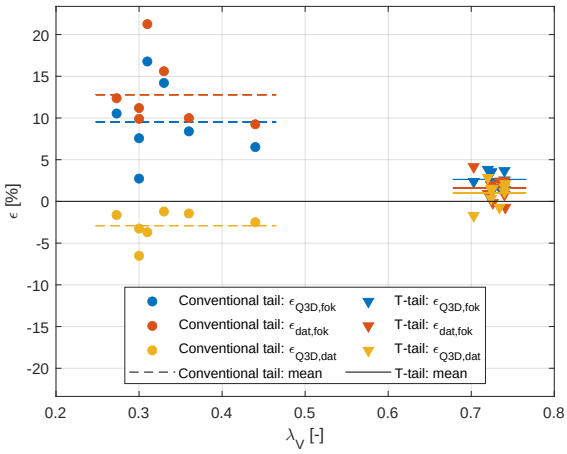

Figure 5.11: Vertical tailplane lift curve slope verification: Conventional vs. T-tail taper ratio. Values in cruise conditions for each aircraft. Note: $\epsilon_{a,b}$ states error a relative to b.

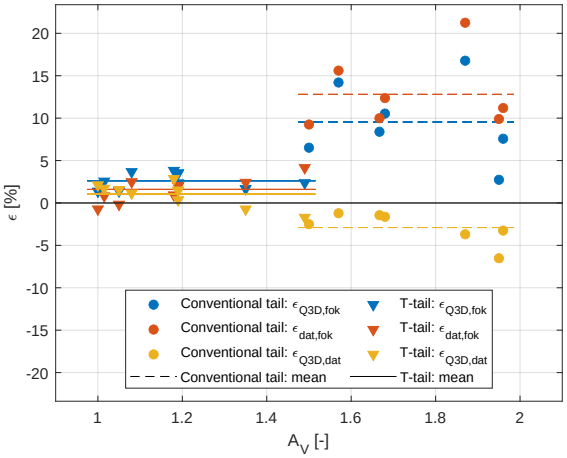

Figure 5.12: Vertical tailplane lift curve slope verification: Conventional vs. T-tail aspect ratio. Values in cruise conditions for each aircraft. Note: $\epsilon_{a,b}$ states error a relative to b.

Figure 5.9 shows a clear difference in lift curve slope error percentage between conventional- and T-tails. The Q3D and USAF DATCOM calculations are much closer to the Fokker / Obert data for T-tails compared to conventional tails. In addition, for the T-tail the Q3D and USAF DATCOM calculations both have a similar error to the Fokker / Obert data, however, for conventional tails Q3D seems to perform better than USAF DATCOM. It also stands out that the error for the conventional tail between the Q3D and USAF DATCOM is much smaller than their respective errors relative to the Fokker / Obert data. As most of the T-tails are Fokker aircraft, this strengthens the suspicion that the Fokker / Obert data is biased for Fokker aircraft or underestimates conventional tail lift curve slopes (non-Fokker aircraft). The exact same trends are witnessed in Figure 5.10, Figure 5.11, and Figure 5.12. Here the data seems clustered for either conventional- or T-tails. This is expected as in general T-tails have more sweep, higher taper ratio, and lower aspect ratios compared to conventional tails.

5.3. Estimating the transition location with the hump

The transition location simulations are an essential part of the aerodynamic analysis since it dictates the magnitude of the transition shift due to the hump depending on flight conditions, and geometry and will form the aerodynamic database for LFC. In this section, the method described in subsection 4.2.2 is followed to obtain the transition location. First, the boundary layer solver and stability analysis, and the N-factor curves are discussed in subsection 5.3.1. Second, the dependence of the transition location with the Reynolds number, obtained from the N-factor curves is presented in subsection 5.3.2. Thereafter, the effects of tip vortices, boundary conditions, and separation on the transition location results are discussed in subsection 5.3.3, subsection 5.3.4, and subsection 5.3.5. Finally, the transition locations results are compared with literature in subsection 5.3.6.

5.3.1. Boundary layer solver and stability analysis

To obtain the N-factor curves for the different configurations tested, a boundary layer solver and stability analysis are used. For this, the numerical tools developed by the Group of Flow Control and Stability within the Delft University of Technology are used. The boundary layer solver needs as input the external velocity over the airfoil. This is obtained from the pressure distributions calculated by XFoil at the airfoil sections as used in Q3D. Thereafter, the baseflow is computed by solving the boundary layer equations [74]. In this work, the flow is assumed incompressible to simplify the formulation and reduce the computational time. Despite the Mach numbers being as high as 0.78 (cruise speeds of aircraft, see section 4.7), it is observed in literature that the dominant instability governing laminar-to-turbulent transition remains unchanged for Mach numbers below Mach 4 [75]. Laminar-to-turbulent transition is initiated by instabilities. This can be modeled by adding perturbations to the baseflow and performing a stability analysis to see the behavior of the perturbations in the baseflow. This is done by first establishing the perturbation equations. By using parallel linear stability theory, where the growth of the boundary layer in streamwise direction is not accounted for (wall-normal velocity zero, stream- and spanwise velocities as a function of y), and spanwise invariant (infinite wing), the perturbation equations are simplified to a so-called 2.5D flow. The 2.5D equations are separable, which allows for the eigenmode solutions. The eigenmode solutions have the form of a complex exponential wave function, which can be used to determine when the flow becomes unstable and how the instabilities amplify in streamwise direction, which eventually causes transition [75][67]. By combining these eigenmode solutions with the e^N-method by Van Ingen [66] the transition locations can be predicted. This method finds the transition location by calculating the maximum amplification factor, N, for each perturbation wavelength, creating an N-factor curve, which can be used to find the transition location.

As explained in subsection 4.2.2 the transition locations are obtained through the N-factor curves taking the location at N_{clean} and N_{hump}, for the clean and hump configurations respectively. N_{clean} is assumed to be 9 and $N_{hump} = N_{clean} + \Delta N$, where $\Delta N \approx$ [redacted] CONFIDENTIAL for the forcing case with a distributed roughness patch. The latter value is estimated from the (confidential) master thesis by Morais [67] and is assumed to be valid for every flight condition. In reality the value of ΔN would vary for different Reynolds numbers, angles of attack, and sweep angles, however, there is no wind tunnel data available on this. The N-factors along the chord of the airfoil sections are calculated for only one side of the airfoil, hence at a non-zero angle of attack, the N-factor curve from one side is based on the opposite angle of attack compared to the other side. This is only possible since the M3J

airfoil is symmetric.

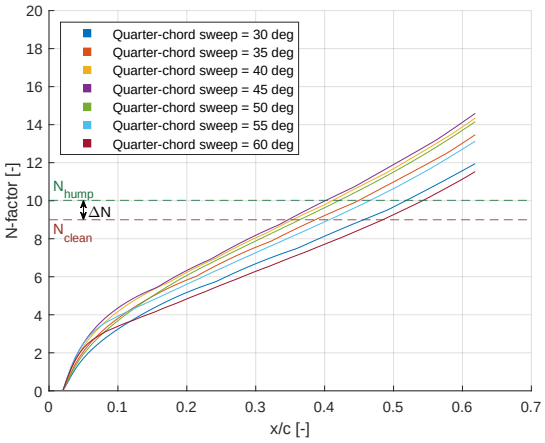

Figure 5.13: Sweep variation, x/c vs. N-factor (Fokker F-28 Mk1000, mid-span section (4 of 8), cruise, $\alpha = 0\ deg$)

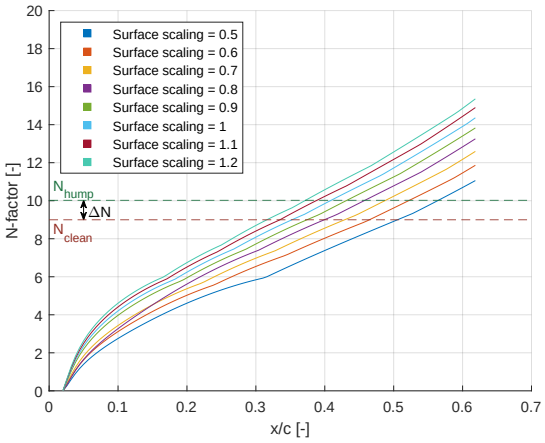

Figure 5.14: Surface area variation, x/c vs. N-factor (Fokker F-28 Mk1000, mid-span section (4 of 8), cruise, $\alpha = 0\ deg$)

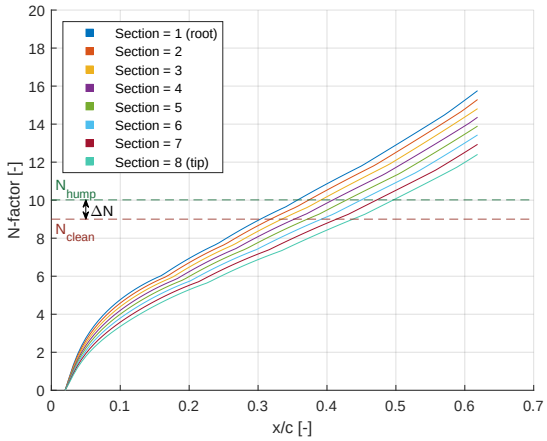

Figure 5.15: Section variation, x/c vs. N-factor (Fokker F-28 Mk1000, cruise, $\alpha = 0\ deg$)

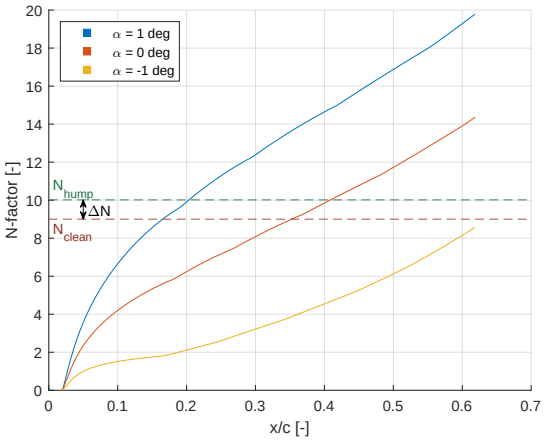

Figure 5.16: Angle-of-attack variation, x/c vs. N-factor (Fokker F-28 Mk1000, mid-span section (4 of 8), cruise)

Several examples of N-factor curves are shown in Figure 5.13, Figure 5.14, Figure 5.15, and Figure 5.16. Note that the same airfoil section at the mid-span location (section 4 of 8) is taken for all the N-factor curves, except of course in Figure 5.15, where the difference in section is evaluated. In Figure 5.13 the effect of the sweep angle is visible. The transition location is at its minimum for the 45-degree sweep angle. Transition is delayed more downstream for sweep angles that are further away from the 45-degree minimum. This is expected as the crossflow velocities and thus also the CFI are at their maximum at 45 deg [75]. Figure 5.14 shows that with increased surface area (and thus an increase in chord length) the Reynolds number increases and the N-factor curve moves to the right, therefore increasing the transition location. For varying sections in Figure 5.15, the N-factor curves behave the same as for the surface variation. This is also expected because when a section is taken closer to the tip, the chord length reduces due to taper. Again, this reduces the local Reynolds number and therefore increases the transition location. Finally, Figure 5.16 shows the effect of changing the angle of attack. Increasing the angle of attack moves the transition location upstream and vice versa, which is expected behavior. Note that the $\alpha = -1$ degree curve shows the special case where the N-factor curve does not intersect the N_{clean} and/or N_{hump} lines. This was already mentioned at the end of subsection 4.2.2 and is regarded as a case where separation occurs at the chordwise location where the curve ends. It is assumed that the transition location coincides with the separation location and behaves like a laminar separation bubble. This assumption will be validated in subsection 5.3.5.

5.3.2. Effect of Reynolds number on transition location

The transition locations are obtained from the N-factor curves in the previous section, following the method explained in subsection 4.2.2. This process is performed for every airfoil section at every required flight condition, for both the clean and hump configuration. The complete transition location results for the Airbus A320 and Fokker F-28 Mk1000 in both cruise and landing conditions are shown in Figure G.1 till Figure G.24, which form the aerodynamic database for LFC. To better see the general trends in this data, plots with less data are shown in this section.

Starting with Figure 5.17, to show the effect of the hump and changing angle of attack for a single vertical tailplane geometry. Before analyzing these effects, the general composition of the figure is discussed. All figures in this section are constructed similarly, consisting of the same main components discussed here. This figure shows the transition locations for one vertical tailplane geometry, namely for the Fokker F-28 Mk1000 in cruise conditions. The angles of attack are indicated on the right-hand side with their respective symbols (diamond, circle, and triangle). The clean and hump configurations are indicated with a continuous and dashed line, respectively. To show which data point belongs to which airfoil section along the span, the planform is shown with the tip and root side indicated. Finally, the plot also shows the separation locations. The flagged (red cross) data points have laminar separation and all other data points have turbulent separation at the trailing edge. Why the laminar separation has a constant location is discussed in subsection 5.3.5.

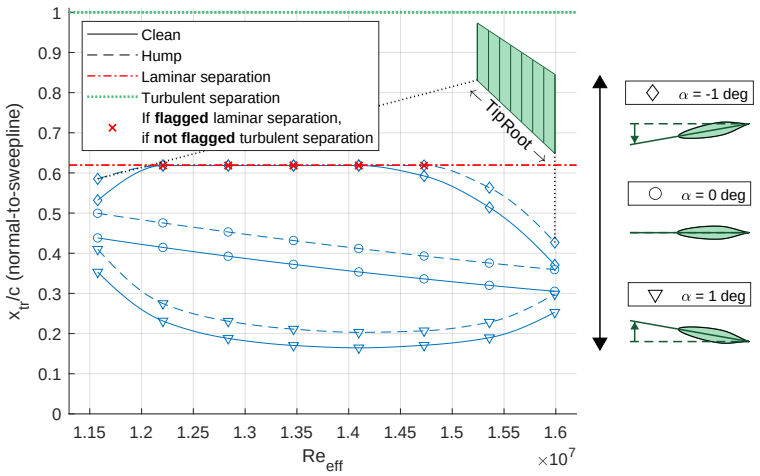

Figure 5.17: Change of transition locations with effective Reynolds number for original Fokker F-28 Mk1000 vertical tailplane planform in cruise for varying angles of attack.

For Figure 5.17 several observations are made. First, overall, the curves all have a negative gradient. This is because as the Reynolds number increases, the flow is more prone to transition and therefore the transition location moves upstream. Second, the effect of the hump is shown for each angle of attack by the dashed line. This clearly shows that the hump moves the transition location downstream compared to the clean configuration (full line). In this case, the hump has the most absolute effect at $\alpha = 0\,deg$, but is still very effective at the other angles of attack. Third, the effect of the angle of attack on the transition location curve is that it shifts the curve vertically and the ends become curved. As the simulated data is for the top side of the wing (when regarding the angle of attack), it is expected that for a positive angle of attack, the transition location moves upstream (the curve moves down), and for the negative angle of attack vice versa. The curved ends at non-zero angles of attack are due to tip vortices. This will be explained in more detail in subsection 5.3.3. Finally, the plot also shows the separation locations. For the angle of attack of -1 deg the mid-span section transition locations are bounded by the laminar separation point. Here the hump will not induce a shift in transition location. Why laminar separation has a constant location is discussed in subsection 5.3.5.

The effect of sweep variation on the transition location can be seen in Figure 5.18. The figure shows four different sweep angles at the top, each with a different color. The corresponding data for each sweep angle uses these same colors. From this figure, it can be observed that for increasing sweep angle the curves shift to the left because the local Reynolds numbers reduce. This is because

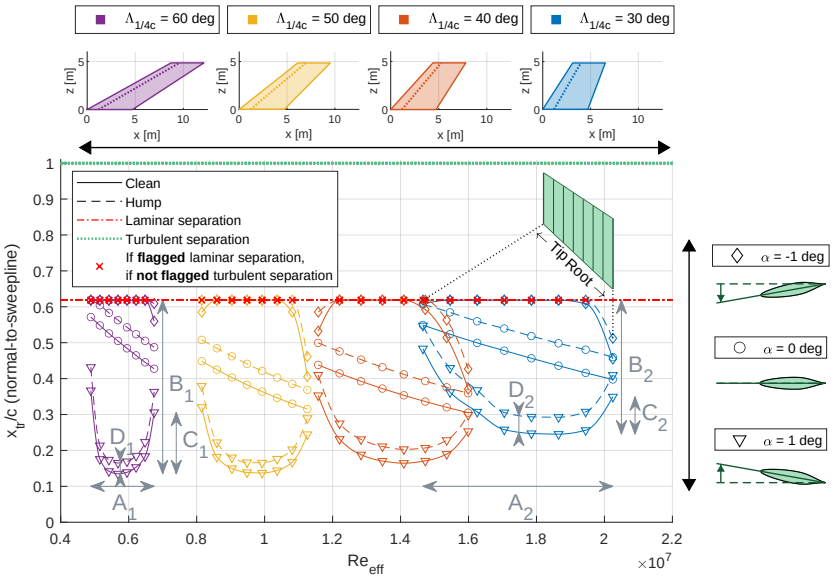

Figure 5.18: Change of transition locations with effective Reynolds number for Fokker F-28 Mk1000 vertical tailplane planform in cruise for varying sweep angles and angles of attack.

the normal-to-sweepline velocity reduces with increasing sweep angle. Another thing that stands out is when the sweep angle is increased (right to left) the Reynolds number range reduces (A1-A2). As the local Reynolds numbers are reduced for all airfoil sections, their relative difference becomes less, resulting in the curves seeming to get 'squeezed' horizontally. Next to that, for increasing sweep angle, the shift in transition location due to a change in angle of attack is much larger (B1-B2). In other words, the transition location becomes more responsive to a change in angle of attack for larger sweep angles. The higher sweep angles are at lower Reynolds numbers, and thus less able to withstand transition and this makes the curves being 'stretched' vertically as the sweep angle increases. Another noticeable effect is that for 1 deg angle of attack, the ends of the curves bend more upwards for increasing sweep angle (C1-C2). Higher sweep angles result in higher tip loading, which increases the strength of the tip vortices, and in turn reduces the effective angle of attack (see subsection 5.3.3). At 0 deg angle of attack, it is observed that the transition location is most upstream between 40 and 50 deg sweep, which is in line with that CFI is most unstable at 45 deg sweep [75]. Finally, for the angle of attack 1 deg the absolute transition shift due to the hump becomes smaller when the sweep angle increases (D1-D2). Similar behavior is seen at -1 deg, but this is partially overshadowed by the laminar separation boundary.

The effect of surface area scaling is visualized in Figure 5.19. At the top it shows the three surface scalings, increasing going from left to right. When increasing the surface area, the general shapes of the transition curves stay the same, but the Reynolds number range increases (A1-A2) similarly to the sweep variation. In contrast with the sweep variation, the Reynolds number does not change due to a velocity change, but due to the change in chord length of the airfoil sections. As the local Reynolds numbers increase for all airfoil sections when the surface area is increased, their relative difference becomes greater. Another thing to notice is at $\alpha = 0°$ the curves for different surface scalings continue in a straight line. As the surface area is scaled the only thing changing at the airfoil sections is the chord length. All the other flow conditions stay the same at $\alpha = 0°$, and therefore the curves merge. This would also be the case for the non-zero angles of attack, were it not that the tip vortices bend the ends of the curves as well as laminar separation occurring for some data points at $\alpha = -1°$. Next to this, a difference in transition shift due to angle of attack is noticed for the surface scaling of 1.2 (B1-B2). Looking at the clean configuration, the absolute shift in transition between 0 and 1 deg is smaller than between 0 and -1 deg. The same is observed for the hump configuration. Due to the laminar separation boundary, it cannot be determined if this also applies to the other surface scalings. Finally, for the angle of attack 1 deg the absolute transition shift due to the hump becomes smaller when the surface area increases (C1-C2). This is the opposite of what is observed for sweep variation, where the absolute

effect of the hump reduces for a decreasing Reynolds number.

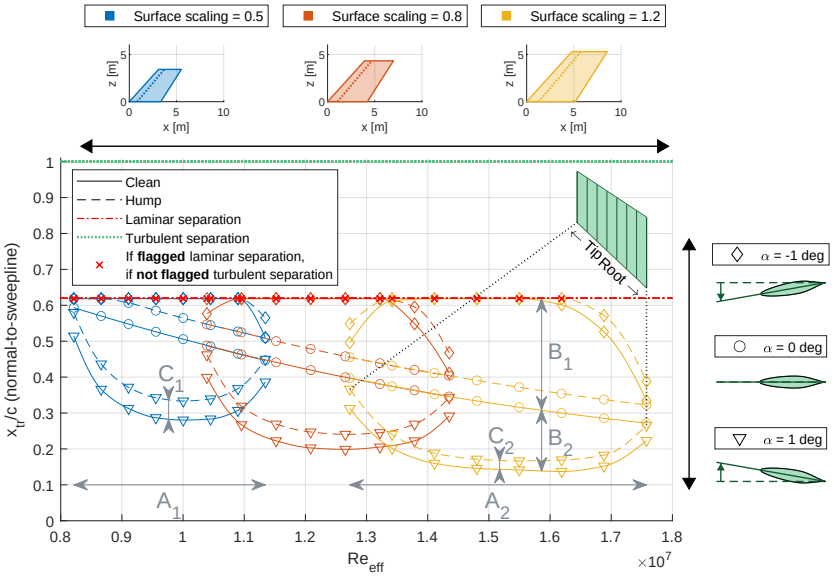

Figure 5.19: Change of transition locations with effective Reynolds number for Fokker F-28 Mk1000 vertical tailplane planform in cruise for varying surface scalings and angles of attack.

The final comparison will be between the Airbus A320 and Fokker F-28 Mk1000 aircraft as they have very different planforms. First, Figure 5.20 shows the data for both aircraft at their original sweep angle, where both original planforms are shown at the top. The large difference in the Reynolds number range for the airfoil section is due to the difference in sweep angle and taper between the Airbus A320 and Fokker F-28 Mk1000. The Airbus A320 has less sweep, and thus a greater relative difference in local velocity between the sections as well as having more taper and thus having a greater difference in chord lengths. Both of these factors affect the Reynolds number range. The vertical difference for the curves can be explained by the difference in sweep angle, as the same behavior was observed in Figure 5.18. Regarding hump effectiveness, the aircraft are similar in absolute transition shift due to the hump. However, in relative terms, the hump has a bigger impact on the Fokker F-28 Mk1000. This is again due to the difference in sweep angle.

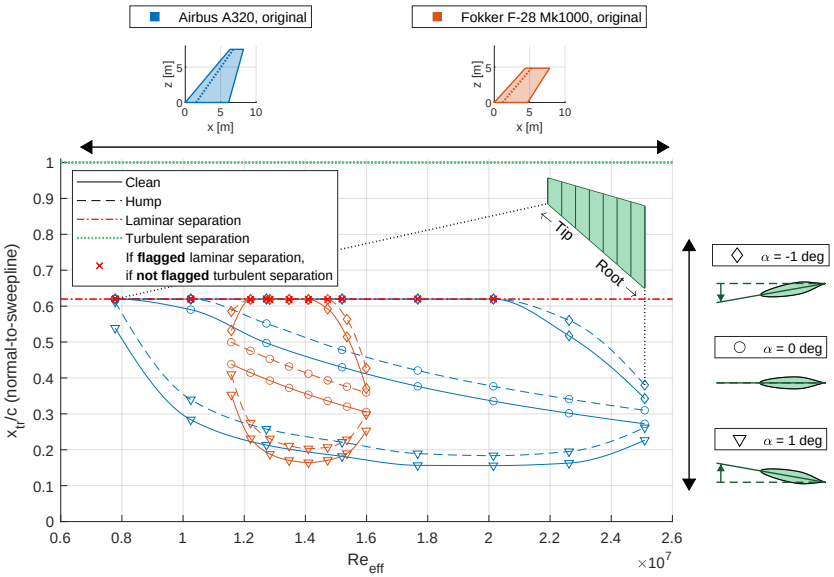

Figure 5.20: Change of transition locations with effective Reynolds number for original Airbus A320 and Fokker F-28 Mk1000 vertical tailplane planform in cruise for varying angles of attack.

Second, when both planforms are changed to the same sweep angle, as seen in Figure 5.21, it would be expected that the zero angle of attack curves overlap, similar to what was observed in Figure 5.19. Since the curves do not overlap in Figure 5.21, there must be another contributor to the difference in transition location curves between the two aircraft. The main differences are surface area, cruise speed, and taper. The former two are incorporated in the Reynolds number, which leaves taper as the most likely explanation for why the curves differ.

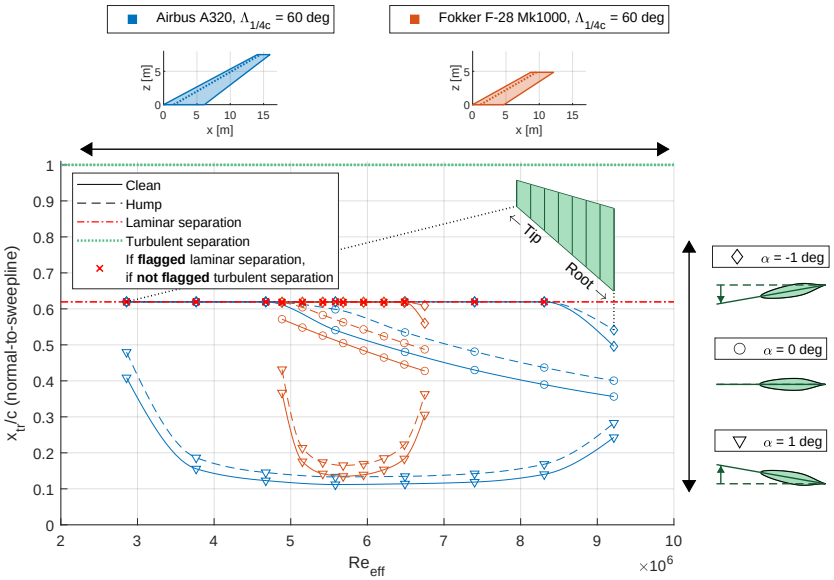

Figure 5.21: Change of transition locations with effective Reynolds number for Airbus A320 and Fokker F-28 Mk1000 vertical tailplane planform in cruise at 60 deg sweep for varying angles of attack.

Third, Figure 5.22, compares the Airbus A320 and Fokker F-28 Mk1000 but scaled in such a way that their surface areas almost are identical, $24.08\ m^2$ and $23.58\ m^2$, respectively. This shows that even for the same surface area, the transition location curves look very different. This shows that the planform plays an important role in the transition location, mainly dependent on sweep angle and taper ratio.

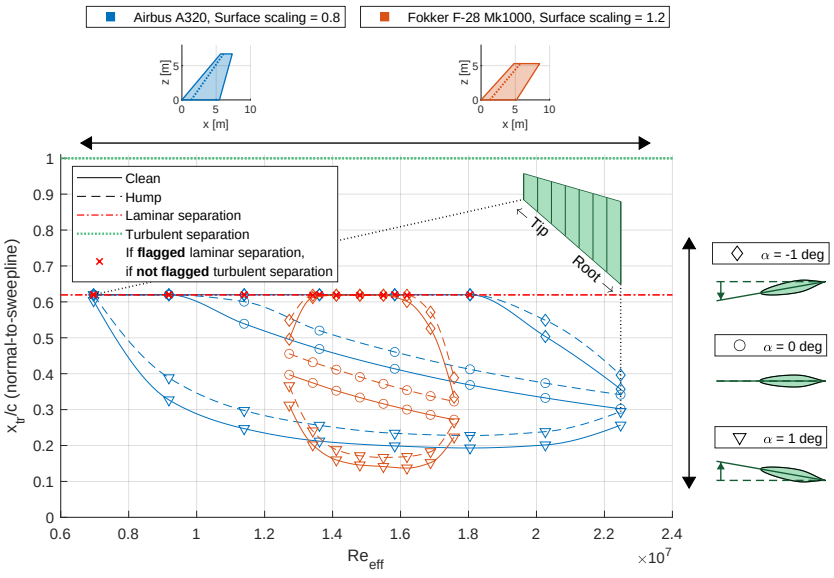

Figure 5.22: Change of transition locations with effective Reynolds number for Airbus A320 and Fokker F-28 Mk1000 vertical tailplane planform in cruise at approximately same surface area ($24.08\ m^2 \approx 23.58\ m^2$) for varying angles of attack.

5.3.3. Effect of tip vortices on the spanwise distribution of the transition front

As observed in the previous section for all the non-zero angle of attack transition location curves, the tip and root values are curved up- and downwards. This modification at the root and tip is caused by the downwash effect of the tip vortices. These vortices influence both the tip and root of the tail because the tail is modeled as a free-floating aerodynamic surface. To understand this better Figure 5.23[2] shows a lifting wing, where due to the pressure difference between the top and bottom, tip vortices occur at either end of the wing. These vortices create a downwash along the wingspan, being most present near the tips and reducing going to the mid-span of the wing. The higher the downwash the lower the local effective angle of attack and thus less lift near the tips. In Q3D, AVL is used to find the local lift coefficient C_l at each wing section and this tip vortex effect is also present there. The C_l at the tips are lower than the mid-span sections.

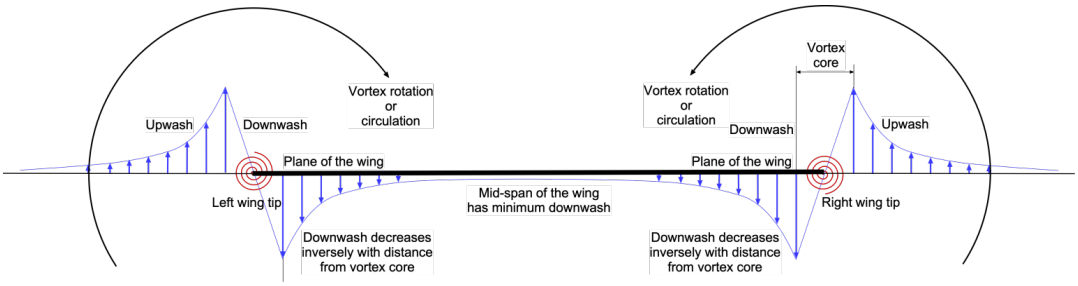

Figure 5.23: Downwash distribution along wingspan due to tip vortices[2].

From the C_l, the effective C_l is calculated and Q3D loops through XFoil to find the corresponding effective angle of attack. When converged, the final effective angle of attack is used to calculate the profile drag. The pressure distributions associated with the effective angle of attack are plotted in Figure 5.24. It becomes clear that due to the tip vortices, the pressure distributions at the root and tip of the vertical tail become less peaky near the leading edge, hence the lower local lift coefficients. These pressure distributions are used in the boundary layer solver and stability analysis to calculate the N-factor curves and from that the transition location curves. Therefore, the up-/downward bending at the tip and root of these curves at non-zero angle of attack are the result of a lower effective angle of attack, induced by the tip vortices. This then also means that for a non-lifting configuration at zero angle of attack, there are no tip vortices. The associated pressure distributions are almost constant for the different sections along the wingspan, as seen in Figure 5.25 and thus is the transition location curve also (almost) linear at zero angle of attack.

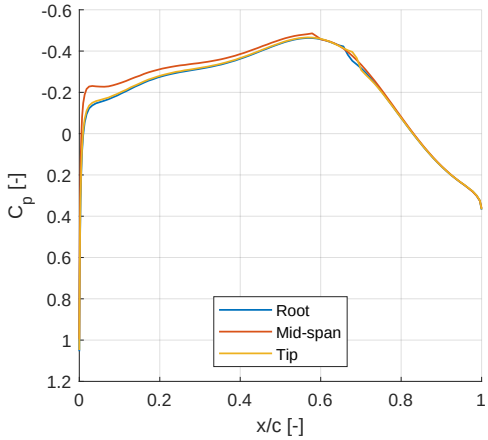

Figure 5.24: Pressure distribution pressure side (Fokker F-28 Mk1000, cruise, $\alpha = 1\ deg$)

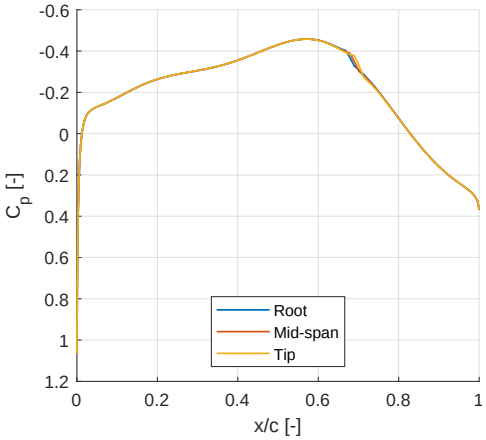

Figure 5.25: Pressure distribution pressure side (Fokker F-28 Mk1000, cruise, $\alpha = 0\ deg$)

[2]Gordon Leishman, J.. (2022). Introduction to Aerospace Flight Vehicles. Aerodynamics of Finite Wings. Embry-Riddle Aeronautical University. Retrieved February 22, 2025, from `https://eaglepubs.erau.edu/introductiontoaerospaceflightvehicles/chapter/finite-wing-characteristics/`

5.3.4. Effect of boundary conditions and interference on drag coefficient

In the aerodynamic analysis, the vertical tailplane is modeled as a free-floating aerodynamic surface. The main reason to model the vertical tailplane as an isolated, free-floating surface is that the vertical tailplane lift curve slope required for the Fokker / Obert stability analysis (section 2.5) is based on the isolated free-floating vertical tailplane as well. The interaction effects with the fuselage and horizontal tailplane endplate effect are incorporated at a later stage as correction factors to the free-floating lift curve slope. As one of the objectives of this research is to analyze the effect of the hump on drag, the question arises whether the drag coefficient can also be based on the free-floating approach and whether it should be corrected for the fuselage and horizontal tailplane interference.

Free-floating vs. wall at root

The alternative to the free-floating approach would be to model the vertical tailplane with a wall at the root as AVL in Q3D provides this option. Figure 5.26 shows a comparison between two identical vertical tails with different boundary conditions at the root. In blue the free-floating tail is shown and in orange the tail with a wall at the root. There are two main things to observe from this figure. First, and most importantly, the transition locations at zero angle of attack are not affected by the wall at the root for both the clean and hump configuration. Second, a wall at the root affects the transition location curves at non-zero angle of attack. The wall continues almost linearly towards the root instead of curving upwards. This confirms the analysis in subsection 5.3.3 that the curving is due to tip vortices, as the wall ensures no tip vortex can be formed, acting like a winglet. It is also observed that the wall at the root also moves the transition more upstream at an angle of attack of 1 deg. At -1 deg it is expected that the wall moves transition more downstream, but laminar separation already occurs in this case.

In this research, the effect of the hump on a vertical tailplane is analyzed in cruise conditions, meaning that there is no sideslip and thus no angle of attack at the vertical tailplane. Based on the observation made earlier that the transition locations do not change for zero angle of attack with a wall at the root, it is argued that modeling the vertical tailplane as a free-floating surface would yield the same results in terms of drag reduction due to the hump. Another argument in favor of the free-floating approach is that, as the vertical tail lift curve slope already requires the free-floating surface approach, it makes sense to analyze the drag coefficient with the same configuration, reducing computational time.

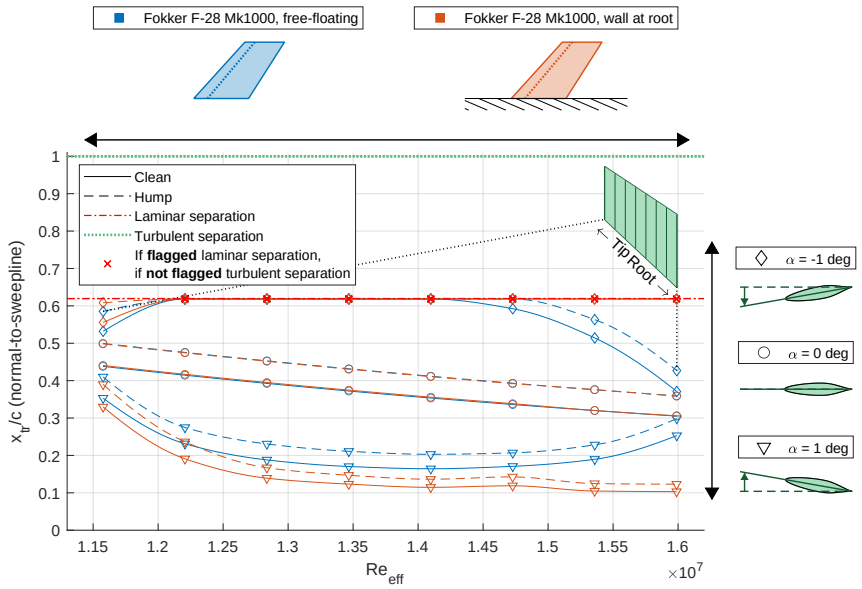

Figure 5.26: Change of transition locations with effective Reynolds number for original Fokker F-28 Mk1000 vertical tailplane planform in cruise for varying boundary conditions and angles of attack.

Full surface area vs. exposed surface area

In continuation of the previous section, when analyzing the drag coefficient it could be argued that only the drag of the exposed vertical tailplane is of interest for the total drag of the aircraft. This is

different from the definition of the vertical tailplane surface area by Fokker / Obert as the tailplane surface continues within the fuselage up to the fuselage centerline (see Figure 2.3). However, according to Torenbeek [15], it is generally accepted to use the full surface area for vertical tailplanes instead of the exposed surface area when the interference effects with the horizontal stabilizer and fuselage are not taken into account. It is assumed that the additional drag due to the extended surface into the fuselage compensates for the lack of interference drag. Moreover, the actual interference drag is hard to estimate as the filleting and fairings are often unknown. It is estimated that unfilleted conventional tailplanes would have an interference (combined fuselage- and horizontal stabilizer interference) of around 4-5%, whilst fin-mounted tailplanes around 6% [76][16]. When properly filleted, the fuselage interference can be reduced by 10% and horizontal stabilizer interference by 20% [76]. According to Obert [17], for modern transport aircraft the areas where interference occurs are optimized for minimum drag (fairings and fillets etc.), thus interference would be relatively small.

Dynamic pressure ratio for drag coefficient

It is established in the previous sections that the vertical tailplane can be modeled as a free-floating aerodynamic surface and the drag coefficient should not be corrected for the fuselage and horizontal tailplane interference when the full surface area is used. To calculate the drag of the vertical tailplane the effective-versus-free-stream dynamic pressure ratio, $\frac{q_V}{q}$, is required (see subsection 4.4.3), which accounts for the fuselage boundary layer effect [14]. Unfortunately, only data is available that also includes the fuselage interference effect, $K_{_{FV}} \frac{q_V}{q}$. $K_{_{FV}}$ is originally intended to adjust the vertical tailplane lift curve slope and not the drag coefficient. Thus it must be assumed that $K_{_{FV}}$ is also applicable to the drag coefficient. The value of $K_{_{FV}} \frac{q_V}{q} \approx 0.94$ CONFIDENTIAL in cruise conditions (no flaps, no sideslip, zero aircraft angle of attack) for both baseline aircraft. This value is comparable to the dynamic pressure ratio of fin-mounted horizontal stabilizers, $\frac{q_H}{q} = 0.95$ [15], as the aerodynamic centers of the vertical tailplane and fin-mounted horizontal stabilizer are relatively close to each other. This justifies the assumption that $K_{_{FV}} \frac{q_V}{q}$ will suffice for the drag coefficient calculation.

5.3.5. Flow separation at the M3J airfoil

Already introduced in subsection 4.2.2, there are two main cases wherefore transition locations are obtained from the N-factor curves. To test if the separation behavior is modeled as expected by XFoil (Q3D), both of these cases will be analyzed in terms of separation and a third case will be added. The first case, seen in Figure 4.5, is where transition takes place where the N-factor curve intersects with N_{clean} or N_{hump}. The second case, seen in Figure 4.6, is when the N-factor curve does not reach the values of N_{clean} or N_{hump}. Here it is assumed that the transition location coincides with the point of separation at x_{sep}. The third and final case that will be tested is forcing transition far downstream of the separation point x_{sep}, at the trailing edge.

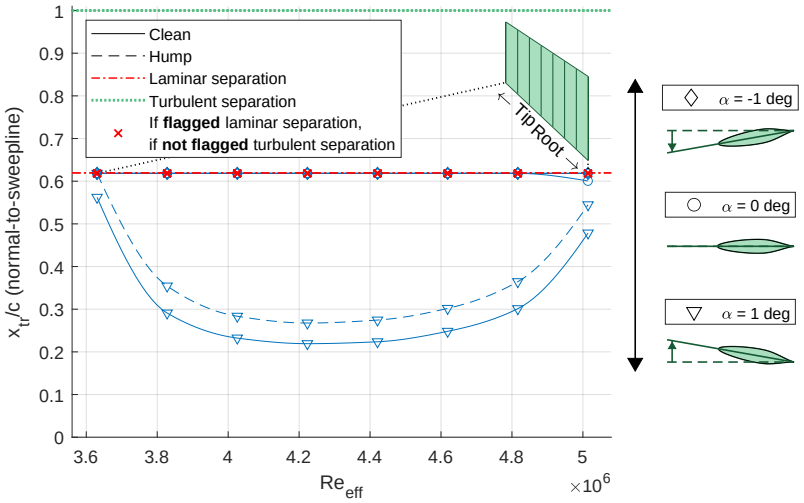

Figure 5.27: Change of transition locations with effective Reynolds number for Fokker F-28 Mk1000 vertical tailplane planform in landing at 60 deg sweep for varying angles of attack.

To test the three cases the configuration and flight conditions at the lowest Reynolds number are chosen, as the flow is more prone to separate at lower Reynolds numbers. If the separation analysis shows correct behavior for this case, it will also hold for higher Reynolds numbers. The lowest Reynolds number data used in this research is for the Fokker F-28 Mk1000 in landing with a sweep angle of 60 deg, shown in Figure 5.27. The separation location cannot be extracted directly from XFoil, therefore the friction coefficient along the chord length is used. When the friction coefficient becomes zero or negative, separation occurs. Based on this, the separation locations, together with the transition locations are plotted and analyzed for each of the three aforementioned cases.

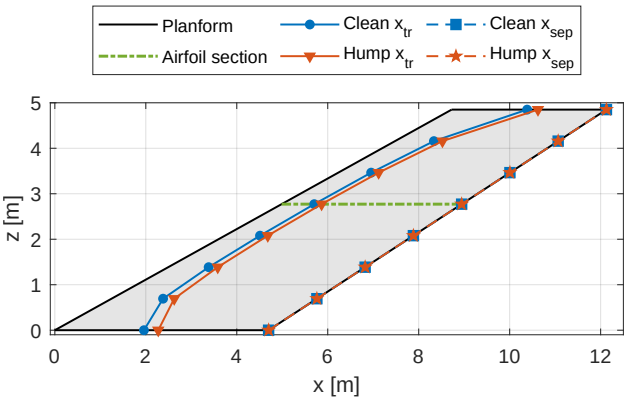

Figure 5.28: Separation and transition locations Fokker F-28 Mk1000, landing, sweep $60\ deg$, $\alpha = 1\ deg$ suction side, clean and hump.

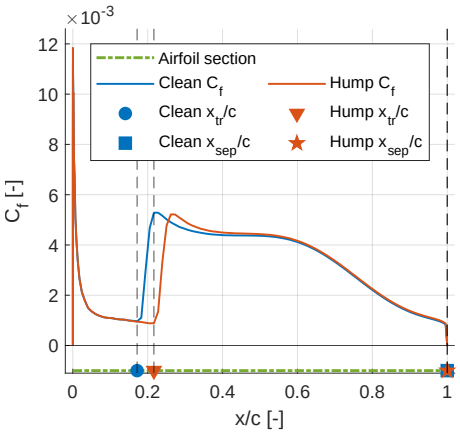

Figure 5.29: Friction coefficient distribution along mid-span airfoil section Fokker F-28 Mk1000, landing, sweep $60\ deg$, $\alpha = 1\ deg$ suction side, clean and hump.

The separation front of first case, where transition takes place where the N-factor curve intersects with N_{clean} or N_{hump}, is shown in Figure 5.28, with the corresponding friction coefficient distribution for the mid-span section in Figure 5.29 for both the clean and hump configuration. The effect of the hump on the transition front is the transition location moving downstream relative to the clean configuration. Separation occurs at the trailing edge (for both configurations), downstream of the transition location, making it turbulent separation. Separation at the trailing edge is expected since the turbulent flow is less likely to separate. This is reinforced by wind tunnel experiments, separation would also occur at the trailing edge for M3J wings in cases where the flow already transitioned [68]. These wind tunnel tests were performed at lower Reynolds numbers than the ones used in this research. Since the flow is less likely to separate at higher Reynolds numbers, separation at the trailing edge is expected here.

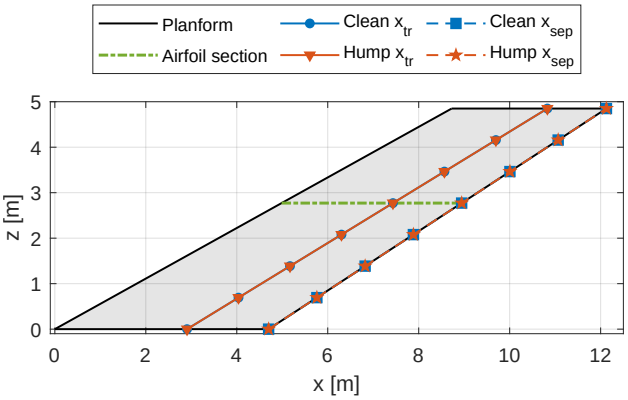

Figure 5.30: Separation and transition locations Fokker F-28 Mk1000, landing, sweep $60\ deg$, $\alpha = 1\ deg$ pressure side, clean and hump.

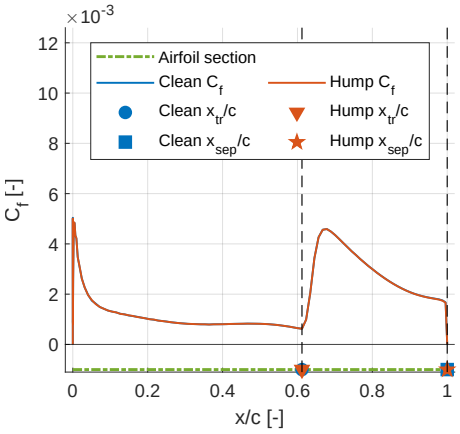

Figure 5.31: Friction coefficient distribution along mid-span airfoil section Fokker F-28 Mk1000, landing, sweep $60\ deg$, $\alpha = 1\ deg$ pressure side, clean and hump.

The second case is when the N-factor curve does not reach the values of N_{clean} or N_{hump}. Here it is assumed that the transition location coincides with the point of separation at x_{sep}. The separation front is shown in Figure 5.30 and the friction coefficient distribution in Figure 5.31. These plots show that when the transition location coincides with the separation location as simulated with the boundary layer stability solver, the separation behavior is similar to the first case, where transition occurs before separation. It might be the case that the XFoil estimate for the separation location is slightly further downstream than the value obtained with the boundary layer stability solver. This means that this specific case does not behave as a laminar separation bubble as suggested in subsection 4.2.2.

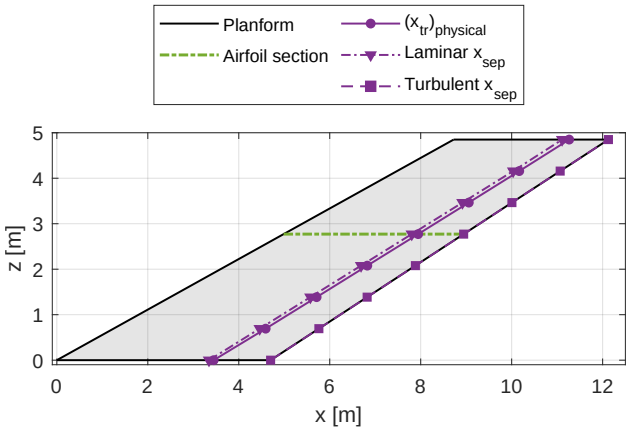

Figure 5.32: Friction coefficient distribution along mid-span airfoil section Fokker F-28 Mk1000, landing, sweep $60\ deg$, $\alpha = 1\ deg$ pressure side, at $(x_{tr}/c)_{forced} = 1$.

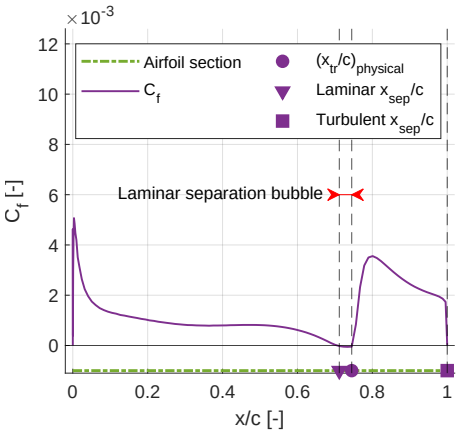

Figure 5.33: Friction coefficient distribution along mid-span airfoil section Fokker F-28 Mk1000, landing, sweep $60\ deg$, $\alpha = 1\ deg$ pressure side, at $(x_{tr}/c)_{forced} = 1$.

The third case is forcing transition far downstream of the separation point x_{sep}, at the trailing edge. The reason for this is to see if the expected laminar separation bubble, which was not observed in the second case, will occur. Again, Figure 5.32 shows the separation front and Figure 5.33 the corresponding friction coefficient distribution. By forcing $(x_{tr}/c)_{forced} = 1$, the flow remains laminar up to the point of separation (laminar separation), which also directly results in transition and reattachment, which forms the laminar separation bubble. Note that this $(x_{tr}/c)_{phycical}$ lies right after the laminar separation location, which is upstream of the $(x_{tr}/c)_{forced}$ location. Due to the (physical) transition, the boundary layer will reattach, after which turbulent separation will happen further downstream or even stay attached up until at the trailing edge (as is the case here). This reinforces the suspicion that the XFoil estimate for the separation location is slightly further downstream than the value obtained with the boundary layer stability solver. Based on experimental evidence [68], it is known that a laminar separation bubble forms around $x/c \approx 0.70$ ($\alpha = 0\ deg$ and $Re = 2.12 \cdot 10^6$). This behavior is also observed in Figure 5.33, where the laminar $x_{sep}/c \approx 0.70$. As the laminar flow reaches the adverse pressure gradient region of the airfoil (see Figure 5.4 around $x/c \approx 0.65$, the adverse pressure gradient is so strong the flow will always separate and a laminar separation bubble will occur. Therefore the laminar separation location is relatively constant for varying Reynolds numbers.

After analyzing the three transition location cases, it is shown that XFoil can simulate the separation behavior realistically. Even though XFoil estimates the separation location is slightly further downstream than the boundary layer stability solver, it is still able to simulate the laminar separation bubble.

5.3.6. Comparison of transition location results with literature

Figure 5.34 shows the transition location curves for an unswept NACA0012 wing. This is one of the few sources with a symmetric airfoil at a similar Reynolds range as the cases in this research. The closest case in terms of Reynolds range in this research is the Fokker F-28 Mk1000 in cruise, as seen in Figure 5.35. A comparison can be made at $\alpha = 0\ deg$ since this is the same as $C_l = 0$ in the experimental NACA 0012 data. The angles of attack corresponding to the other C_l values of the experimental NACA 0012 data are unknown. Even though this is not a direct comparison, due to the

difference in sweep angle and airfoil shapes, it is observed that as the Reynolds number increases, the transition location shifts upstream in an exponential manner. This shows that the trend found for the transition location curves in this research is supported by the literature, to a certain extent.

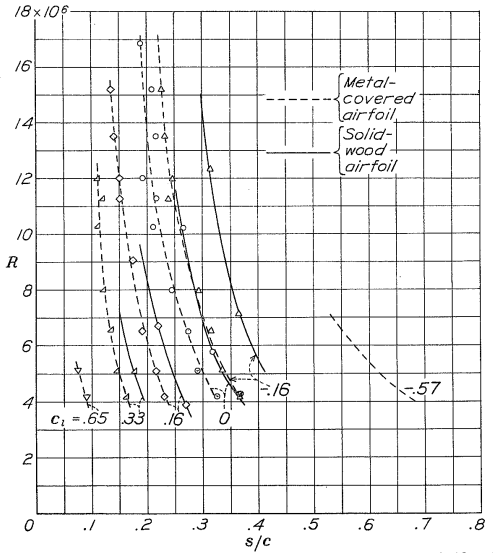

Figure 5.34: Transition location curves for unswept 8-foot span wing with 5-foot-chord NACA 0012 airfoil (solid-wood and metal-covered) [77].

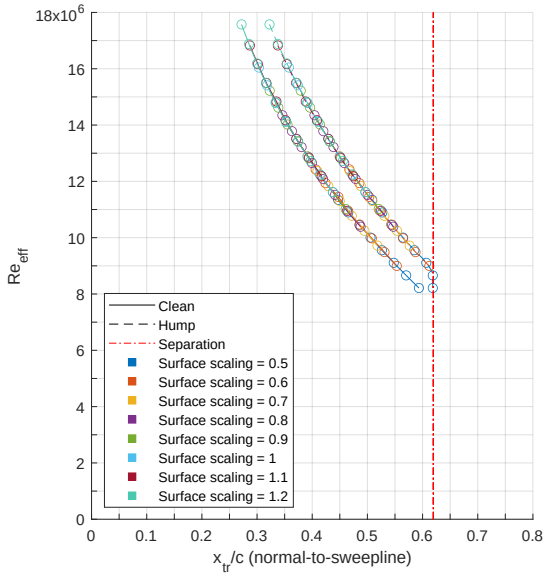

Figure 5.35: Transition location curves for $40\ deg$ swept wing with M3J airfoil (Fokker F-28 Mk1000, cruise, $\alpha = 0\ deg$)

Figure 5.36 shows an overview of laminar flow tests performed in Europe with their respective free-stream Reynolds numbers and leading edge sweep angles by Schrauf [8]. For comparison with this research, the Reynolds-sweep range of the vertical tail of the Airbus A320 and Fokker F-28 Mk1000 tested with the DeLaH are added. This research increases the maximum investigated sweep angle from 40 to just over 60 deg. Also, note that the Airbus A320 with hump is right on the A320 Laminar Fin in terms of Reynolds number, but the Laminar Fin was tested for a broader range.

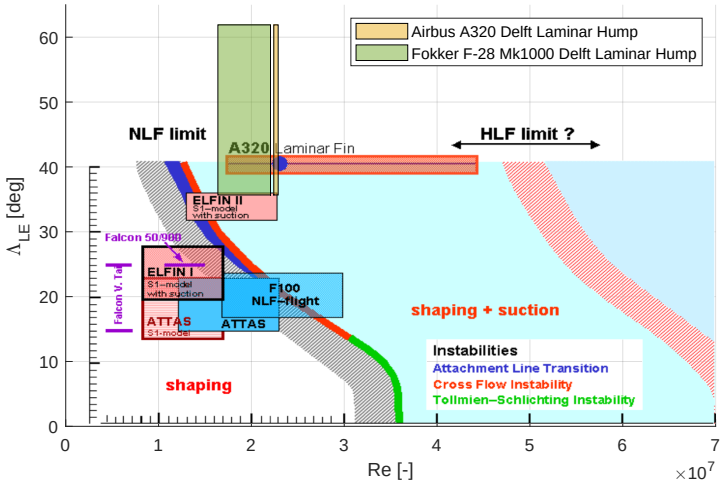

Figure 5.36: Free-stream Reynolds number vs. leading edge sweep, comparison of wind tunnel- and flight tests in Europe [8] and simulations of Delft Laminar Hump in cruise. Note free-stream Reynolds number based on MAC of the vertical tailplane.

5.4. Validation of stability analysis with wind tunnel data

To validate the stability coefficients calculated with the Fokker / Obert method [14], a comparison is made between available wind tunnel data and the calculated values. In the results discussed in this

section, a distinction is made between two types of calculated values. The exact calculated values are the values calculated by Fokker / Obert, which uses the actual values for each aircraft instead of using the average curves of the generalized method. The calculated values based on average curves are the result of the implementation of the generalized Fokker / Obert method in this research, as discussed in section 2.5. The generalized Fokker / Obert method based on the average curves is used in this research because it makes it possible to assess other geometries next to the ones of existing aircraft. This will be used during the sensitivity analysis section 6.2, where different geometric variables are varied to see the effect on various aircraft characteristics, such as the stability coefficients. In this section, the results make it possible to see the difference between the wind tunnel data and the exact and average curve calculations.

There are two aircraft evaluated in this section, namely the Airbus A320 and the Fokker F-28 Mk 1000 since these are the baseline cases as discussed in section 4.7. Both aircraft are considered to be in cruise. The original flight conditions and geometry can be found in Table H.1 till Table H.6. Note that these validation values of the stability coefficients are not all evaluated for the same geometry and flight conditions. These validation results are therefore not the same as the stability coefficient results shown in subsection 6.1.1. The changes to the original flight conditions and geometry specific for the stability analysis validation in this section are found in Table I.1, Table I.2 and Table I.3. For both of these aircraft, not all data was available to fully validate the stability coefficients. The data of the Fokker / Obert method [14] does not show any rolling moment coefficient data, most likely since this derivative is often neglected during the initial design stages of the vertical tailplane, due to the relatively small contribution. In addition, the aileron derivatives are calculated with a method by Roskam [22] (subsection 2.5.8), and no data was found to validate these values. Finally, for the vertical tail components, the $(C_{L_\alpha})_V$ from Fokker / Obert data [14] was used in the generalized calculations with the average curves, and not the calculated values by Q3D, otherwise additional errors are introduced. Note that in all the other results after this section, the $(C_{L_\alpha})_V$ will be calculated with Q3D unless stated otherwise.

Airbus A320 stability coefficient validation

In Table 5.3 it can be seen that almost all stability coefficients calculated based on average curves match reasonably well with both the wind tunnel and exact calculated values ($\epsilon_{avg,wt}$ and $\epsilon_{avg,ex}$). Most of the errors are within 15%, and many even lower. The only outlier is the $\left(C_{l_\beta}\right)_{T-O}$, which is a good match to the exact calculated value, however, there is a mismatch compared to the wind tunnel data. This is also the case for the exact calculated values compared to the wind tunnel data ($\epsilon_{ex,wt}$). Therefore the calculation based on the average curves is probably correct, but the Fokker / Obert method simply does not match with wind tunnel experiments. No potential explanation was identified.

Since there is so much data missing an additional comparison is made to validate the tail-off stability coefficients. There is data available for the Fokker F-29 model 1-2, which is very comparable to the Airbus A320 in terms of geometry. Especially comparable for the driving geometry characteristics involved in the calculation of $\left(C_{y_\beta}\right)_{T-O}$ and $\left(C_{n_\beta}\right)_{T-O}$ as seen in Table 5.5. For $\left(C_{l_\beta}\right)_{T-O}$, however, there is a large discrepancy between the wing lift coefficients as well as the wing dihedral, which makes the aircraft not comparable for this stability coefficient. Fortunately the $\left(C_{l_\beta}\right)_{T-O}$ for the Airbus A320 is already validated in Table 5.3. The stability coefficients for the F-29 (wind tunnel and exact values) compared to the Airbus A320 (average curves) are compared Table 5.4. $\left(C_{y_\beta}\right)_{T-O}$ and $\left(C_{n_\beta}\right)_{T-O}$ coefficients match very well when looking at $\epsilon_{avg,ex}$. Therefore it can be assumed that the Fokker F-29 model 1-2 and Airbus A320 are also comparable in terms of stability coefficients and that the Fokker F-29 model 1-2 wind tunnel values should be indicative of the magnitude of the Airbus A320 wind tunnel values. $\epsilon_{avg,wt}$ shows that the error of the stability coefficients Airbus A320 relative to wind tunnel values would lie around 20 and 27%, which is deemed reasonable.

Fokker F-28 Mk1000 stability coefficient validation

In Table 5.6 it can be seen that again most of the stability coefficients calculated based on average curves are within 15% of both the wind tunnel and exact calculated values ($\epsilon_{avg,wt}$ and $\epsilon_{avg,ex}$). The exceptions are the $\left(C_{y_\beta}\right)_{T-O}$, $\left(1+\frac{\delta\sigma}{\delta\beta}\right)\frac{q_V}{q}K_{FV}$ from $\left(\Delta C_{n_\beta}\right)_{V+H}$ and the $C_{l_{\delta_a}}$. For the $\left(C_{y_\beta}\right)_{T-O}$,

it is again the case that the average curve value matches the exact calculated value and that they both have a similar error to the wind tunnel value. This implies that the Fokker / Obert method does not match with wind tunnel experiments for this stability derivative, but no potential explanation could be identified. In case of the $\left(1+\frac{\delta\sigma}{\delta\beta}\right)\frac{q_V}{q}K_{FV}$ from $\left(\Delta C_{n_\beta}\right)_{V+H}$, the error is still reasonable, moreover the same value obtained through $\left(\Delta C_{y_\beta}\right)_{V+H}$ wind tunnel measurements is much lower. As this value is comprised of many different sidewash components, the error seems to be the accumulation of many smaller errors, since no main driving contributor to this error could be identified. Regarding the $C_{l_{\delta_a}}$, the error is very large, which is unexpected. The calculated value overestimates the effectiveness of the aileron greatly. The only potential explanation for this discrepancy is that the aileron dimensions are incorrectly assumed as these are estimated from drawings.

Stability analysis for DeLaH implementation

Overall the average curve calculation performs reasonably well compared to both the exact calculation as well as the wind tunnel values. The majority of stability coefficients are within 15%. Larger errors are observed for tail-off- and aileron stability derivatives. As this research focuses on the impact of the hump on the vertical tail, the only stability derivatives affected by the implementation of the hump are the vertical tail derivatives through the vertical tailplane lift curve slope. This means all other stability derivatives stay constant when implementing the hump on the vertical tail. When redesigning the vertical tail in the sensitivity analysis only the vertical tail- and rudder stability coefficients are affected. As the vertical tail- and rudder stability coefficients are within 15%, which is deemed sufficient, the relative effect of the hump and vertical tail redesign on the total stability coefficients of the aircraft can still be properly observed.

Table 5.3: CONFIDENTIAL Airbus A320 stability coefficient validation. Flight conditions and geometry see Table H.1, Table H.2, Table H.5, and Table I.1. Note: * unit is not $[deg^{-1}]$, but $[-]$. Note: $\epsilon_{a,b}$ states error a relative to b.

	Stability derivative	**Wind tunnel (wt)** $[deg^{-1}]$ **[14]**	**Calc. exact values (ex)** $[deg^{-1}]$ **[14]**	**Calc. average curves (avg)** $[deg^{-1}]$	$\epsilon_{ex,wt}$ [%]	$\epsilon_{avg,wt}$ [%]	$\epsilon_{avg,ex}$ [%]
Tail-off	$\left(C_{y_\beta}\right)_{T-O}$	-	-	-0.0089	-	-	-
	$\left(C_{l_\beta}\right)_{T-O}$	[redacted]	[redacted]	-0.00104	[redacted]	[redacted]	[redacted]
	$\left(C_{n_\beta}\right)_{T-O}$	-	-	-0.00240	-	-	-
Horizontal tail	$\left(C_{l_\beta}\right)_H$	-	-	-0.00008	-	-	-
Vertical tail	$\left(C_{y_\beta}\right)_V$	[redacted]	-	-0.0125	-	[redacted]	-
	$\left(C_{l_\beta}\right)_V$	-	-	-0.00172	-	-	-
	$\left(C_{n_\beta}\right)_V$	[redacted]	-	0.00589	-	[redacted]	-
Sidewash	$\left(\frac{\delta\sigma}{\delta\beta}\right)_{tot}$	[redacted]*	[redacted]*	0.347*	[redacted]	[redacted]	[redacted]
	$\left(1+\frac{\delta\sigma}{\delta\beta}\right)\frac{q_V}{q}K_{FV}$ from $\left(\Delta C_{y_\beta}\right)_{V+H}$	[redacted]*	-	1.238*	-	[redacted]	-
	$\left(1+\frac{\delta\sigma}{\delta\beta}\right)\frac{q_V}{q}K_{FV}$ from $\left(\Delta C_{n_\beta}\right)_{V+H}$	[redacted]*	-	1.238*	-	[redacted]	-
Rudder	$C_{y_{\delta_R}}$	-	[redacted]	0.0045	-	-	[redacted]
	$C_{l_{\delta_R}}$	-	-	0.00075	-	-	-
	$C_{n_{\delta_R}}$	-	[redacted]	-0.00236	-	-	[redacted]
Aileron	$C_{y_{\delta_a}}$	-	-	0	-	-	-
	$C_{l_{\delta_a}}$	-	-	-0.00287	-	-	-
	$C_{n_{\delta_a}}$	-	-	0.00009	-	-	-

Table 5.4: CONFIDENTIAL Airbus A320 stability coefficient validation compared to F-29 model 1-2 with wing-mounted nacelles. Flight conditions and geometry see Table H.1, Table H.2, Table H.5, and Table I.2. Note: * unit is not $[deg^{-1}]$, but $[-]$. Note: $\epsilon_{a,b}$ states error a relative to b.

	Stability derivative	Wind tunnel (wt) $[deg^{-1}]$ [14]	Calc. exact values (ex) $[deg^{-1}]$ [14]	Calc. average curves (avg) $[deg^{-1}]$	$\epsilon_{ex,wt}$ [%]	$\epsilon_{avg,wt}$ [%]	$\epsilon_{avg,ex}$ [%]
Aircraft	-	F-29 model 1-2	F-29 model 1-2	Airbus A320	-	-	-
Tail-off	$\left(C_{y_\beta}\right)_{T-O}$	[redacted]	[redacted]	-0.0089	[redacted]	[redacted]	[redacted]
	$\left(C_{l_\beta}\right)_{T-O}$	[redacted]	[redacted]	-0.00104	[redacted]	[redacted]	[redacted]
	$\left(C_{n_\beta}\right)_{T-O}$	[redacted]	[redacted]	-0.00240	[redacted]	[redacted]	[redacted]

Table 5.5: CONFIDENTIAL Comparison of driving geometry characteristics for tail-off stability coefficients of Airbus A320 and F-29 model 1-2 with wing-mounted nacelles [17]. Note: $\epsilon_{a,b}$ states error a relative to b.

	Stability derivative	Driving geometry characteristic	Airbus A320	F-29 model 1-2	$\epsilon_{F-29,A320}$ [%]
Tail-off	$\left(C_{y_\beta}\right)_{T-O}$	$\frac{S_{fus.cross}}{S_W}$	[redacted]	[redacted]	-4.85
	$\left(C_{l_\beta}\right)_{T-O}$	C_{L_W}	[redacted]	[redacted]	156.25
		Γ_W	[redacted] deg	[redacted] deg	37.25
	$\left(C_{n_\beta}\right)_{T-O}$	l_B	[redacted] m	[redacted] m	4.90
		b_W	[redacted] m	[redacted] m	-3.07

Table 5.6: CONFIDENTIAL Fokker F-28 Mk1000 stability coefficient validation. Flight conditions and geometry see Table H.3, Table H.4, Table H.6, and Table I.3. Note: * unit is not $[deg^{-1}]$, but $[-]$. Note: † from [17]. Note: $\epsilon_{a,b}$ states error a relative to b.

	Stability derivative	Wind tunnel (wt) $[deg^{-1}]$ [14]	Calc. exact values (ex) $[deg^{-1}]$ [14]	Calc. average curves (avg) $[deg^{-1}]$	$\epsilon_{ex,wt}$ [%]	$\epsilon_{avg,wt}$ [%]	$\epsilon_{avg,ex}$ [%]
Tail-off	$\left(C_{y_\beta}\right)_{T-O}$	[redacted]	[redacted]	-0.0062	[redacted]	[redacted]	[redacted]
	$\left(C_{l_\beta}\right)_V$	[redacted]	[redacted]	-0.00014	[redacted]	[redacted]	[redacted]
	$\left(C_{n_\beta}\right)_V$	[redacted]	[redacted]	-0.00146	[redacted]	[redacted]	[redacted]
Horizontal tail	$\left(C_{l_\beta}\right)_H$	-	-	0	-	-	-
Vertical tail	$\left(C_{y_\beta}\right)_V$	[redacted]	-	-0.0109	-	[redacted]	-
	$\left(C_{l_\beta}\right)_V$	-	-	-0.00188	-	-	-
	$\left(C_{n_\beta}\right)_V$	[redacted]	-	0.00436	-	[redacted]	-
Sidewash	$\left(\frac{\delta\sigma}{\delta\beta}\right)_{tot}$	[redacted]*	[redacted]*	0.276*	[redacted]	[redacted]	[redacted]
	$\left(1+\frac{\delta\sigma}{\delta\beta}\right)\frac{q_V}{q}K_{FV}$ from $\left(\Delta C_{y_\beta}\right)_{V+H}$	[redacted]*	-	1.199*	-	[redacted]	-
	$\left(1+\frac{\delta\sigma}{\delta\beta}\right)\frac{q_V}{q}K_{FV}$ from $\left(\Delta C_{n_\beta}\right)_{V+H}$	[redacted]*	-	1.199*	-	[redacted]	-
Rudder	$C_{y_{\delta_R}}$	-	[redacted]	0.0030	-	-	[redacted]
	$C_{l_{\delta_R}}$	-	-	0.00058	-	-	-
	$C_{n_{\delta_R}}$	-	[redacted]	-0.00138	-	-	[redacted]
Aileron	$C_{y_{\delta_a}}$	-	-	0	-	-	-
	$C_{l_{\delta_a}}$	[redacted]†	-	-0.00582	-	[redacted]	-
	$C_{n_{\delta_a}}$	-	-	0.00016	-	-	-

6

Results baseline and sensitivity analysis

In this chapter, starting with section 6.1, the baseline configurations will be assessed, as introduced in section 4.7. This will show both the effect of retrofitting the DeLaH on existing aircraft as well as the effect of changing the original vertical tailplane airfoil shape to the M3J, as the M3J is required for implementing the hump. Moreover, it will provide a ground truth to compare the geometry changes due to the sensitivity analysis. This sensitivity analysis is presented in the second part of this chapter in section 6.2, section 6.3, and section 6.4, where the effect of a change in sweep angle as well as scaling the surface area on the effectiveness of the hump is analyzed.

All results in this chapter are calculated based on original geometry and flight conditions as provided by Table H.1 till Table H.6. In addition, the vertical tailplane lift curve slope $(C_{L_\alpha})_V$ and drag coefficient $(C_D)_V$ are calculated with Q3D. This makes it possible to vary the vertical tailplane airfoil shape and the vertical tailplane planform geometry, and asses for both landing- and cruise conditions.

6.1. Baseline results

The baseline results will use three vertical tailplane configurations:

1. Original airfoil (depending on the aircraft)
2. M3J airfoil in clean configuration
3. M3J airfoil with the hump

The transition locations for the original airfoil are calculated by XFoil with free transition at $N = 9$, whilst the transition locations for both M3J configurations are obtained from the N-factor curves calculated with the boundary layer solver and stability analysis (see subsection 5.3.1) at $N_{clean} = 9$ and $N_{hump} = N_{clean} + \Delta N$, where $\Delta N \approx$ [redacted] CONFIDENTIAL. By analyzing these three configurations the effect of changing the original airfoil to the M3J airfoil can be observed, as well as the effect of the hump. The results are divided into four sections. First, the stability coefficients are shown in subsection 6.1.1. Second, in subsection 6.1.2, the critical design requirements are checked based on the provided stability coefficients. Third, the full aircraft results are presented in subsection 6.1.3. Finally, the full aircraft results for the original airfoil shape will be validated in subsection 6.1.4.

6.1.1. Baseline results stability coefficients

The baseline results for the stability coefficients for the three vertical tailplane configurations are provided in Table 6.1 and Table 6.2, for both landing and cruise conditions because both flight conditions will be required when assessing the critical design requirements in subsection 6.1.2. Note that the side force due to bank angle, C_{y_ϕ}, and yawing moment due to one engine inoperative, $(C_n)_{OEI}$, are only shown for landing conditions as they are only used for the critical design requirements that use landing conditions.

Table 6.1: Stability and control coefficient results for baseline configuration Airbus A320 for varying vertical tailplane configurations at landing and cruise conditions. Flight conditions and geometry see Table H.1, Table H.2, and Table H.5. Vertical tailplane aerodynamics calculated with Q3D. Note: * unit is not $[deg^{-1}]$, but $[-]$.

		Original airfoil $[deg^{-1}]$	**M3J clean** $[deg^{-1}]$	**M3J hump** $[deg^{-1}]$	$\epsilon_{clean,orig}$ [%]	$\epsilon_{hump,orig}$ [%]	$\epsilon_{hump,clean}$ [%]
Flight condition		**Landing**					
Sideslip	C_{y_β}	-0.0230	-0.0230	-0.0230	-0.000018	-0.000005	0.000013
	C_{l_β}	-0.00497	-0.00497	-0.00497	-0.000008	-0.000002	0.000006
	C_{n_β}	0.00406	0.00406	0.00406	-0.000050	-0.000015	0.000035
Rudder	$C_{y_{\delta_R}}$	0.0051	0.0051	0.0051	-0.000035	-0.000010	0.000025
	$C_{l_{\delta_R}}$	0.00061	0.00061	0.00061	-0.000035	-0.000010	0.000025
	$C_{n_{\delta_R}}$	-0.00274	-0.00274	-0.00274	-0.000035	-0.000010	0.000025
Aileron	$C_{y_{\delta_a}}$	0	0	0	0.00	0.00	0.00
	$C_{l_{\delta_a}}$	-0.00287	-0.00287	-0.00287	0.00	0.00	0.00
	$C_{n_{\delta_a}}$	0.00108	0.00108	0.00108	0.00	0.00	0.00
Bank angle	C_{y_ϕ}	0.4557	0.4557	0.4557	0.00	0.00	0.00
Other	$(C_n)_{OEI}$	0.01310*	0.01310*	0.01310*	0.00	0.00	0.00
Flight condition		**Cruise**					
Sideslip	C_{y_β}	-0.0230	-0.0230	-0.0230	-0.000029	-0.000023	0.000006
	C_{l_β}	-0.00312	-0.00312	-0.00312	-0.000030	-0.000024	0.000006
	C_{n_β}	0.00448	0.00448	0.00448	-0.000071	-0.000057	0.000014
Rudder	$C_{y_{\delta_R}}$	0.0052	0.0052	0.0052	-0.000046	-0.000037	0.000009
	$C_{l_{\delta_R}}$	0.00088	0.00088	0.00088	-0.000046	-0.000037	0.000009
	$C_{n_{\delta_R}}$	-0.00276	-0.00276	-0.00276	-0.000046	-0.000037	0.000009
Aileron	$C_{y_{\delta_a}}$	0	0	0	0.00	0.00	0.00
	$C_{l_{\delta_a}}$	-0.00287	-0.00287	-0.00287	0.00	0.00	0.00
	$C_{n_{\delta_a}}$	0.00009	0.00009	0.00009	0.00	0.00	0.00

Table 6.2: Stability and control coefficient results for baseline configuration Fokker F-28 Mk1000 for varying vertical tailplane configurations at landing and cruise conditions. Flight conditions and geometry see Table H.3, Table H.4, and Table H.6. Vertical tailplane aerodynamics calculated with Q3D. Note: * unit is not $[deg^{-1}]$, but $[-]$.

		Original airfoil $[deg^{-1}]$	**M3J clean** $[deg^{-1}]$	**M3J hump** $[deg^{-1}]$	$\epsilon_{clean,orig}$ [%]	$\epsilon_{hump,orig}$ [%]	$\epsilon_{hump,clean}$ [%]
Flight condition		**Landing**					
Sideslip	C_{y_β}	-0.0183	-0.0183	-0.0183	-0.000011	-0.000013	-0.000002
	C_{l_β}	-0.00380	-0.00380	-0.00380	-0.000007	-0.000008	-0.000001
	C_{n_β}	0.00328	0.00328	0.00328	-0.000025	-0.000029	-0.000004
Rudder	$C_{y_{\delta_R}}$	0.0032	0.0032	0.0032	-0.000020	-0.000024	-0.000003
	$C_{l_{\delta_R}}$	0.00049	0.00049	0.00049	-0.000020	-0.000024	-0.000003
	$C_{n_{\delta_R}}$	-0.00152	-0.00152	-0.00152	-0.000020	-0.000024	-0.000003
Aileron	$C_{y_{\delta_a}}$	0	0	0	0.00	0.00	0.00
	$C_{l_{\delta_a}}$	-0.00582	-0.00582	-0.00582	0.00	0.00	0.00
	$C_{n_{\delta_a}}$	0.00206	0.00206	0.00206	0.00	0.00	0.00
Bank angle	C_{y_ϕ}	0.4162	0.4162	0.4162	0.00	0.00	0.00
Other	$(C_n)_{OEI}$	0.00732*	0.00732*	0.00732*	0.00	0.00	0.00
Flight condition		**Cruise**					
Sideslip	C_{y_β}	-0.0171	-0.0171	-0.0171	-0.000098	-0.000106	-0.000007
	C_{l_β}	-0.00210	-0.00210	-0.00210	-0.000139	-0.000149	-0.000010
	C_{n_β}	0.00305	0.00305	0.00305	-0.000220	-0.000237	-0.000017
Rudder	$C_{y_{\delta_R}}$	0.0031	0.0031	0.0031	-0.000149	-0.000160	-0.000011
	$C_{l_{\delta_R}}$	0.00060	0.00060	0.00060	-0.000149	-0.000160	-0.000011
	$C_{n_{\delta_R}}$	-0.00143	-0.00143	-0.00143	-0.000149	-0.000160	-0.000011
Aileron	$C_{y_{\delta_a}}$	0	0	0	0.00	0.00	0.00
	$C_{l_{\delta_a}}$	-0.00582	-0.00582	-0.00582	0.00	0.00	0.00
	$C_{n_{\delta_a}}$	0.00016	0.00016	0.00016	0.00	0.00	0.00

The first thing to notice is that the sideslip and rudder derivatives are the only derivatives affected by a change in airfoil and/or hump, as expected. However, the effect of the airfoil and/or hump is very small. The differences in stability coefficients between the three configurations are so small that they are only visible when looking at the error percentages with at least three to six decimals. As the derivatives are only changed through the change in $(C_{L_\alpha})_V$, this implies that the lift curve slope is almost not affected by the change in airfoil/hump. Also, the aileron- and bank angle derivatives, and yawing moment due to one engine inoperative are not affected by the airfoil change since these are not dependent on the vertical tail lift curve slope.

The effect of the change in airfoil going from the original NACA 4-digit series airfoil to the M3J airfoil (clean) is represented by $\epsilon_{clean,orig}$. When comparing landing and cruise conditions, the cruise conditions have a slightly higher error, which is expected due to the higher velocity. Comparing the values of the Airbus A320 and the Fokker F-28 Mk1000, the differences are the result of differences in flight speed, planform as well as airfoil shape. No clear trend is identified, however.

The effect of the hump is represented by $\epsilon_{hump,clean}$, and shows that the hump almost does not affect the vertical tailplane lift curve slope and stability coefficients. This is desirable because this also means that the hump does not reduce the overall stability of the aircraft. With this, retrofitting the hump on an existing aircraft becomes a viable option. Again when comparing the values of the Airbus A320 and the Fokker F-28 Mk1000, no clear trend is observed. The only thing that stands out is that the effect of the hump is a small increase for the Airbus A320 and a decrease for the Fokker F-28 Mk1000 in terms of stability coefficients. However, such small errors can be neglected.

All in all, the analysis of the very small differences in stability coefficients between the three configurations needs to be taken with caution as the vertical tailplane lift curve slope is calculated with Q3D. Q3D loops through XFoil to find the effective angle of attack that matches the local lift coefficient for each airfoil section. This process repeats until the termination criterium is reached when the difference between two consecutive values of the induced angle of attack falls below a threshold ($\Delta\alpha_i \leq 0.05$). Therefore differences in lift curve slope are potentially (partially) the result of this threshold. Nevertheless, it is concluded that the effect of the hump on the vertical tailplane lift curve slope and stability coefficients is negligible.

6.1.2. Baseline results critical design requirements

The critical design requirements are also evaluated for all three vertical tail configurations. However, since the differences in stability coefficients between the three configurations are very small, as established in the previous section, the values obtained for the critical design requirements are the same for the three cases. Therefore, in Table 6.3, the results for the critical design requirements are shown once for each aircraft, but are valid for all three vertical tail configurations. Each of the requirements uses either landing or cruise conditions as denoted for the requirement type, as well as the implementation of the requirement itself, the associated values, and whether the requirement is met for both aircraft individually.

All critical design requirements are met with some margin left, which was expected as these results are valid for the original airfoil and vertical tail configuration. The original configuration should fulfill the CS-25 regulations for Large Aeroplanes by EASA since these aircraft are already certified. The only exception is the stall angle for full rudder sideslips, where the sideslip angle, $\beta_{_{CWL,FRS}}$, exceeds the maximum stall angle, $\alpha_{_{C_{L_{max}}}}$. Note however that this stall angle is calculated with the USAF DATCOM approach laid out in subsection 2.6.4. This method assumes that the vertical tailplane is an isolated wing without any interference from other components. In reality, the flow at the base of the vertical tail will be turbulent due to the vicinity of the fuselage, which opposes separation. Moreover, the Fokker F-28 Mk1000 has a dorsal fin, which also increases the stall angle [17][14]. The exact effect of the dorsal fin on maximum stall angle is hard to quantify but can be in the order of 10 degrees [17][14][78][79]. Therefore these values are deemed close enough to meet the critical design requirement for not stalling at full rudder sideslip crosswind landing. A final thing to notice is that the maximum stall angle is different for the one engine inoperative and the crosswind landing for steady straight sideslips and full rudder sideslips. The reason for this is that the maximum stall angle is adjusted for the rudder deflection. The magnitude of the adjustment of the stall angle is proportional to the amount of rudder deflection.

Table 6.3: Results baseline critical design requirements (based on CS-25 for Large Aeroplanes by EASA). Airbus A320 stability coefficient values from Table 6.1. Fokker F-28 Mk1000 stability coefficient values from Table 6.2.

Critical design requirement		Airbus A320		Fokker F-28 Mk1000	
Type	**Requirement**	**Values**	**Req. met**	**Values**	**Req. met**
Static stability (Cruise)	$C_{y_\beta} < 0$	C_{y_β} = -0.0230 deg^{-1}	yes	C_{y_β} = -0.0171 deg^{-1}	yes
	$C_{l_\beta} < 0$	C_{l_β} = -0.00312 deg^{-1}	yes	C_{l_β} = -0.00210 deg^{-1}	yes
	$C_{n_\beta} > 0$	C_{n_β} = 0.00448 deg^{-1}	yes	C_{n_β} = 0.00305 deg^{-1}	yes
One engine inoperative (OEI) (Landing)	$\beta_{OEI} = arcsin\left(\frac{V_{CW}}{V}\right)$	β_{OEI} = 11.91 deg, V_{CW} = 30 $KCAS$	yes	β_{OEI} = 15.27 deg, V_{CW} = 30 $KCAS$	yes
	$\delta_R \leq \delta_{R_{max}}$	δ_R = 15.61 deg, $\delta_{R_{max}}$ = 35 deg	yes	δ_R = 27.44 deg, $\delta_{R_{max}}$ = 35 deg	yes
	$\delta_a \leq \delta_{a_{max}}$	δ_a = -17.29 deg, $\delta_{a_{max}}$ = 25 deg	yes	δ_a = -7.69 deg, $\delta_{a_{max}}$ = 25 deg	yes
	$\phi \leq \phi_{max}$	ϕ = 0.43 deg, ϕ_{max} = 3 deg	yes	ϕ = 0.46 deg, ϕ_{max} = 3 deg	yes
Crosswind landing for steady, straight sideslips (CWL,SSS) (Landing)	$\beta_{CWL,SSS} = arcsin\left(\frac{V_{CW}}{V}\right)$	$\beta_{CWL,SSS}$ = 11.91 deg, V_{CW} = 30 $KCAS$	yes	$\beta_{CWL,SSS}$ = 15.27 deg, V_{CW} = 30 $KCAS$	yes
	$\delta_R = \delta_{R_{max}}/2$	δ_R = 17.5 deg, $\delta_{R_{max}}/2$ = 17.5 deg	yes	δ_R = 17.5 deg, $\delta_{R_{max}}/2$ = 17.5 deg	yes
	$\delta_a \leq \delta_{a_{max}}$	δ_a = -14.82 deg, $\delta_{a_{max}}$ = 25 deg	yes	δ_a = -8.84 deg, $\delta_{a_{max}}$ = 25 deg	yes
	$\phi \leq \phi_{max}$	ϕ = 0.41 deg, ϕ_{max} = 3 deg	yes	ϕ = 0.54 deg, ϕ_{max} = 3 deg	yes
Crosswind landing for full rudder sideslips (CWL,FRS) (Landing)	$(\beta_{CWL,FRS} \cdot \beta_{CWL,SSS}) > 0$, $\beta_{CWL,FRS} > \beta_{CWL,SSS}$	$\beta_{CWL,FRS}$ = 22.16 deg, $\beta_{CWL,SSS}$ = 11.91 deg	yes	$\beta_{CWL,FRS}$ = 37.13 deg, $\beta_{CWL,SSS}$ = 15.27 deg	yes
	$\delta_R = \delta_{R_{max}}$	δ_R = 35 deg, $\delta_{R_{max}}$ = 35 deg	yes	δ_R = 35 deg, $\delta_{R_{max}}$ = 35 deg	yes
	$\delta_a = \delta_{a_{max}}$	δ_a = -25 deg, $\delta_{a_{max}}$ = 25 deg	yes	δ_a = -25 deg, $\delta_{a_{max}}$ = 25 deg	yes
	$\phi \leq \phi_{max}$	ϕ = 0.77 deg, ϕ_{max} = 3 deg	yes	ϕ = 1.39 deg, ϕ_{max} = 3 deg	yes
Stall (Landing)	$\beta_{OEI} \leq \alpha_{C_{L_{max}}}$	β_{OEI} = 11.91 deg, $\alpha_{C_{L_{max}}}$ = 23.03 deg	yes	β_{OEI} = 15.27 deg, $\alpha_{C_{L_{max}}}$ = 32.70 deg	yes
	$\beta_{CWL,SSS} \leq \alpha_{C_{L_{max}}}$	$\beta_{CWL,SSS}$ = 11.91 deg, $\alpha_{C_{L_{max}}}$ = 22.81 deg	yes	$\beta_{CWL,SSS}$ = 15.27 deg, $\alpha_{C_{L_{max}}}$ = 33.47 deg	yes
	$\beta_{CWL,FRS} \leq \alpha_{C_{L_{max}}}$	$\beta_{CWL,FRS}$ = 22.16 deg, $\alpha_{C_{L_{max}}}$ = 20.76 deg	no	$\beta_{CWL,FRS}$ = 37.13 deg, $\alpha_{C_{L_{max}}}$ = 32.12 deg	no

6.1.3. Baseline results full aircraft

The full aircraft results for the baseline aircraft are presented in Table 6.4 and Table 6.5, for the Airbus A320 and Fokker F-28 Mk1000, respectively. Starting with the effect of changing the airfoil from the original to M3J ($\epsilon_{clean,orig}$), the vertical tailplane lift curve slope is not affected. However, the drag coefficient is significantly affected and reduced by 12.20% for the Airbus A320 and 2.63% for the Fokker F-28 Mk1000. A potential explanation for the difference in drag coefficient reduction, apart from differences in planform and flight speeds, is that the Airbus A320 and Fokker F-28 Mk1000 have a different thickness-to-chord ratio for the original airfoil, 9 and 10% respectively. The vertical tailplane weight is not affected as it is based on an empirical relationship using the design dive speed and planform geometry (see subsection 4.4.1), thus the airfoil shape does not play a role in this estimate. The full aircraft drag coefficient is reduced by 0.33% for the Airbus A320 and 0.11% for the Fokker F-28 Mk1000 and is the direct result of the drag reduction of the vertical tailplane. The drag reduction in turn increases the lift-to-drag ratio and decreases the fuel weight, volume, and CO_2 emission, the latter three all directly related, hence the same error percentages.

With the effect of the change in airfoil known, the effect of the hump can now be analyzed. Starting again with the vertical tailplane results, it can be seen that the vertical tailplane lift curve slope is not affected by the implementation of the hump. This is desirable since this means that a retrofit of the hump will not affect the stability of the aircraft. In contrast, the vertical tailplane drag coefficient is affected by the hump. It greatly reduces the vertical tailplane drag coefficient by 6.73% and 8.72% for the Airbus A320 and Fokker F-28 Mk1000, respectively. The reduction in vertical tailplane drag is also reflected by the full aircraft drag coefficient, which is reduced by 0.17% and 0.34%. This then translated into an

increase in lift-to-drag ratio of the same magnitude and a reduction of fuel weight, volume, and CO_2 emission slightly lower. The vertical tailplane weight is not affected for the same reason as explained for the change in airfoil. It is assumed that the added weight due to the hump itself is negligible.

From these results, it can be concluded that the DeLaH has a significant drag-reducing effect on the overall aircraft, whilst not affecting the aircraft's stability. Even though the fuel savings for an individual aircraft are not very large, on a fleet level this would be significant. The hump can be retrofitted on existing aircraft by simply gluing it on the outer skin, making it a relatively simple and cheap way to improve efficiency for aircraft manufacturers.

Table 6.4: Results baseline Airbus A320 in cruise, no sideslip. Flight conditions and geometry see Table H.1, Table H.2, and Table H.5. Vertical tailplane aerodynamics calculated with Q3D. Note: $\epsilon_{a,b}$ states error a relative to b.

	Original airfoil	**M3J clean**	**M3J hump**	$\epsilon_{clean,orig}$ [%]	$\epsilon_{hump,orig}$ [%]	$\epsilon_{hump,clean}$ [%]
$(C_{L_\alpha})_V$	0.0444	0.0444	0.0444	0.00	0.00	0.00
$(C_D)_V$	0.0047	0.0042	0.0039	-12.20	-19.75	-6.73
Vertical tailplane weight	494 kg	494 kg	494 kg	0.00	0.00	0.00
C_D	0.0363	0.0362	0.0361	-0.33	-0.50	-0.17
$\frac{L}{D}$	17.300	17.356	17.386	0.32	0.49	0.17
Fuel weight	8311 kg	8285 kg	8272 kg	-0.31	-0.47	-0.16
Fuel volume	10337 l	10305 l	10289 l	-0.31	-0.47	-0.16
CO_2 emission	26179 kg	26099 kg	26057 kg	-0.31	-0.47	-0.16

Table 6.5: Results baseline Fokker F-28 Mk1000 in cruise, no sideslip. Flight conditions and geometry see Table H.3, Table H.4, and Table H.6. Vertical tailplane aerodynamics calculated with Q3D. Note: $\epsilon_{a,b}$ states error a relative to b.

	Original airfoil	**M3J clean**	**M3J hump**	$\epsilon_{clean,orig}$ [%]	$\epsilon_{hump,orig}$ [%]	$\epsilon_{hump,clean}$ [%]
$(C_{L_\alpha})_V$	0.0305	0.0305	0.0305	0.00	0.00	0.00
$(C_D)_V$	0.0047	0.0045	0.0042	-2.63	-11.58	-8.72
Vertical tailplane weight	332 kg	332 kg	332 kg	0.00	0.00	0.00
C_D	0.0261	0.0260	0.0260	-0.11	-0.45	-0.34
$\frac{L}{D}$	14.600	14.616	14.666	0.11	0.45	0.34
Fuel weight	2442 kg	2439 kg	2431 kg	-0.11	-0.43	-0.32
Fuel volume	3037 l	3034 l	3024 l	-0.11	-0.43	-0.32
CO_2 emission	7692 kg	7684 kg	7659 kg	-0.11	-0.43	-0.32

6.1.4. Baseline results validation

To validate the baseline results, the original airfoil results from the previous section are compared to values found in literature, presented in Table 6.6 and Table 6.7. The vertical tail lift curve slope matches relatively well for the Fokker F-28 Mk1000, however, the Airbus A320 has a larger error. A potential explanation is discussed in section 5.2, where it is argued that the Fokker / Obert data [14] might underestimate the vertical tail lift curve for non-Fokker aircraft. However, it could be that the Fokker / Obert data is based on other airfoil shapes, as this data is not available. The vertical tail weight matches quite well within a 7% error for both aircraft. The full aircraft drag coefficients match better for the Fokker F-28 Mk1000 than for the Airbus A320. The full aircraft drag coefficient is calculated with the cruise L/D from literature and the lift coefficient for mid-cruise weight, which might not be fully representative. Also, the drag coefficient from literature for the A320 is taken at the design lift coefficient of the Boeing 737, as Obert [14] states their similarity, however, whether the design lift coefficient is also similar, is uncertain. The fuel weight does not match literature very well. The fuel weight is a direct result of the drag coefficient. Therefore, a relatively large error for the Airbus A320 is expected, but not for the Fokker F-28 Mk1000 as its drag coefficient is close to literature. This implies that there must be another reason for the discrepancy in fuel weight. The TSFC of the engine could be underestimated. Another explanation is that the fuel weight is calculated for cruise conditions only, whilst take-off, landing, loiter,

etc., are not accounted for. Incorporating these would result in a value closer to literature.

Table 6.6: Validation original Airbus A320 in cruise. Calculated values from Table 6.4. Note: $\epsilon_{a,b}$ states error a relative to b.

	Calculated (calc)	**Literature (lit)**	$\epsilon_{calc,lit}$ [%]	**Source**
$(C_{L_\alpha})_V$	0.0444 deg^{-1}	[redacted] deg^{-1}	[redacted]	[14] CONFIDENTIAL
Vertical tailplane weight	494 kg	463 kg	-6.68	Figure 42.25 [17]
C_D	0.0363	0.0306	-18.64	Figure 24.123, at $C_{L_{des}} = 0.5$ (assumed same as Boeing 737) at cruise Mach [17]
Fuel weight	8311 kg	13000 kg	36.07	$MTOW - MZFW$ (WV000) [80]

Table 6.7: Validation original Fokker F-28 Mk1000 in cruise. Calculated values from Table 6.5. Note: $\epsilon_{a,b}$ states error a relative to b.

	Calculated (calc)	**Literature (lit)**	$\epsilon_{calc,lit}$ [%]	**Source**
$(C_{L_\alpha})_V$	0.0305 deg^{-1}	[redacted] deg^{-1}	[redacted]	[14] CONFIDENTIAL
Vertical tailplane weight	332 kg	322 kg	-3.18	Figure 42.26 (Fokker F-28 Mk4000) [17]
C_D	0.0261	0.0248	-5.14	Figure 24.142, at $C_{L_{des}} = 0.23$ at cruise Mach [17]
Fuel weight	2442 kg	4560 kg	46.45	$MTOW - MZFW$ (original maximum weights Fokker F-28 Mk 1000) [81]

6.2. Sensitivity analysis

There are two sensitivity analyses performed as described in section 4.8, namely sweep angle variation and surface area scaling. The details specific to each of the sensitivity analyses are discussed in their respective chapters, section 6.3 and section 6.4. The common denominator is that both analyses (similar to the baseline results) will evaluate each of the three vertical tail configurations as described in section 6.1. By analyzing these three configurations the effect of changing the original airfoil to the M3J airfoil can be observed, as well as the effect of the hump. Note when no difference is observed between the original, M3J clean, and M3J hump configuration, the results will only be shown once and be denoted with 'all configurations'. The configurations will be evaluated for cruise conditions as described in Table H.5 and Table H.6. Both analyses will follow the same structure. First, the effect on the vertical tailplane aerodynamics will be assessed. Second, the effect on the stability coefficients is discussed and the critical design requirements, based on CS-25 for Large Aeroplanes by EASA, are checked for each vertical tailplane configuration. This is followed by the effect on the full aircraft aerodynamics. Finally, the changes in weight and fuel consumption are presented.

6.3. Sensitivity analysis: sweep variation

For the first sensitivity analysis, the quarter-chord sweep angle is the main sensitivity variable. Why this is chosen and how it is implemented can be found in section 4.8. The variation range lies between 30 and 60 degrees with 5-degree increments. This range was chosen based on the most common design ranges for vertical tailplanes, as shown in Table 2.1. The effect of the sweep angle variation on the planform shapes of the two baseline aircraft is shown in Figure 6.1. Note that the mean aerodynamic quarter-chord is kept constant as this is assumed to coincide with the aerodynamic center and therefore the rolling- and yawing moment arms will stay constant. Also, note how the horizontal tailplane mounting location shifts along with the changed geometry, keeping the vertical-horizontal tailplane interaction the same.

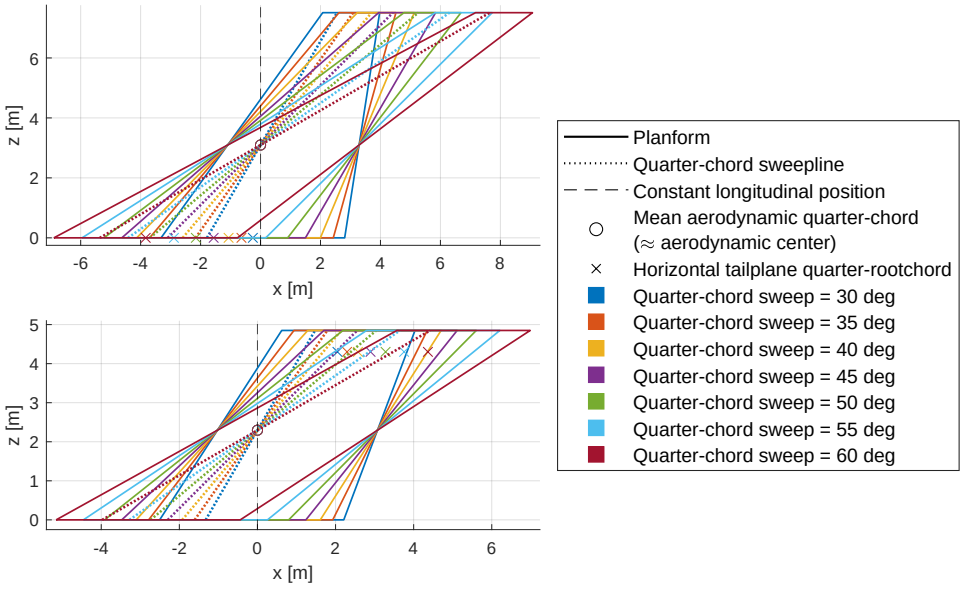

Figure 6.1: Sweep variation Airbus A320 (top) and Fokker F-28 Mk1000 (bottom).

6.3.1. Effect on vertical tailplane aerodynamics

As vertical tailplane geometry changes with sweep angle, the main aerodynamic characteristics that change are the vertical tailplane lift curve slope, $(C_{L_\alpha})_V$, and vertical tailplane drag coefficient, $(C_D)_V$. Note that the latter is evaluated at zero angle of attack, which essentially means non-sideslipping flight, as in cruise conditions no sideslip is assumed.

The effect of sweep variation on the vertical tail lift curve slope is shown in Figure 6.2. The lift curve slope reduces for increasing sweep angle, which is expected as the increased sweep angle the local Mach number reduced, which reduces the amount of lift generated. What stands out for the lift curve slope is there is no difference observed between the original, M3J clean, and M3J hump configuration, which is reflected by the stability coefficients staying constant in subsection 6.1.1. Thus the vertical tail lift curve slope is not affected by the hump. Comparing the two aircraft, the Airbus A320 is more dependent on sweep angle than the Fokker F-28 Mk1000. This is most likely the result of differences in taper-, aspect ratio, and/or cruise speed.

The vertical tail drag coefficient does change with the original, M3J clean and M3J hump configuration as seen in Figure 6.4 and Figure 6.5. It can be seen that going from the original to the M3J airfoil reduces the drag significantly, which is expected. Also, the relationship between sweep angle and vertical tailplane drag coefficient changes from linear to exponential. Moving from clean to hump configuration creates an additional drag coefficient reduction. The vertical tailplane drag coefficient reduction due to the hump is also expressed as a percentage, where only M3J clean and M3J hump are compared to show the effect of the hump, shown in Figure 6.3. This shows that the hump reduces the vertical tail drag coefficient by at least 5.79%, and even up to 11.31%. In the simulated range, the hump is most effective at lower sweep angles. However, keep in mind that since the hump attenuates the growth of the CFI, it requires a condition where CFI is the dominant transition mechanism to be effective. Generally, CFI dominate when the wing sweep is greater than 30-35 deg [12]. These results are based on a shift in transition location due to the hump and it is assumed that the CFI dominate for all sweep angles. In Figure 6.3, the sweep angle has an exponential relationship with the drag-reducing effect of the hump. The dependency on sweep for the effectiveness of the hump is more pronounced for the Fokker F-28 Mk1000, compared to the Airbus A320. This is again most likely the result of differences in taper-, aspect ratio, and/or cruise speed. The Fokker F-28 Mk1000 has less taper and is therefore closer to the spanwise invariant assumption of the boundary layer solver in terms of taper. The minima lie around 45 and 50 deg sweep, for the Fokker F-28 Mk1000 and Airbus A320, respectively, which coincides with the sweep angle where the CFI are at their maximum (45 deg sweep) [75].

Main takeaways:

- Vertical tail lift curve slope is not affected by the hump.
- Effect of the hump on vertical tail drag coefficient has an exponential relationship with sweep angle.
- In the simulated range, the hump is most effective at the lowest sweep angle (30 deg).
- Overall lower sweep angles are beneficial (for the M3J wing) since low drag and a high lift curve slope are desired. Moreover, at lower sweep angles the hump is more effective.

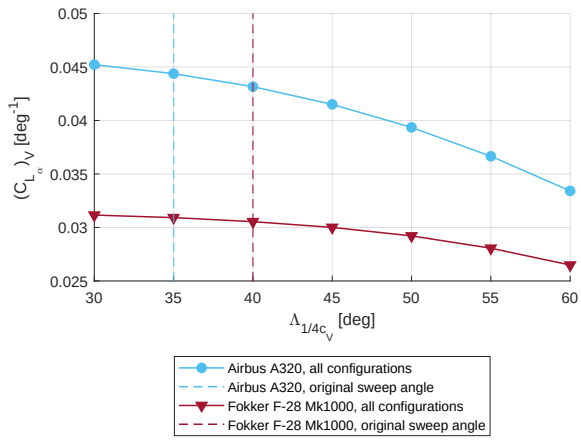

Figure 6.2: Airbus A320 and Fokker F-28 Mk1000, $(C_{L_\alpha})_V$ vs. sweep

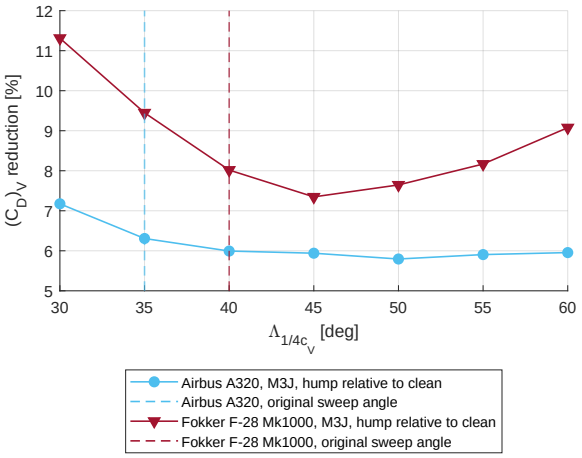

Figure 6.3: Airbus A320 and Fokker F-28 Mk1000, $(C_D)_V$ reduction due to hump vs. sweep

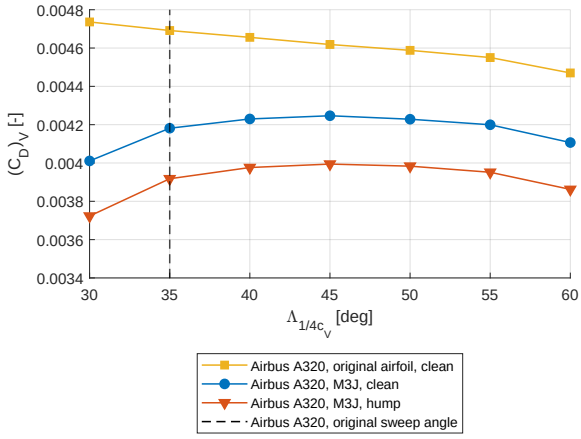

Figure 6.4: Airbus A320, $(C_D)_V$ vs. sweep

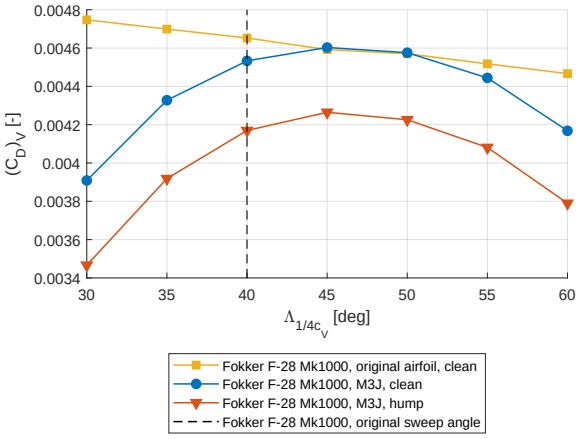

Figure 6.5: Fokker F-28 Mk1000, $(C_D)_V$ vs. sweep

6.3.2. Effect on stability coefficients

The effect of sweep on the stability coefficients (due to sideslip) is shown in Figure 6.6, Figure 6.7, and Figure 6.8. As sweep increases, the stability coefficients reduce (get closer to the stability boundary). This dependency on sweep is expected as stability coefficients are directly related to the vertical tail lift curve slope. As the vertical tail lift curve slope changes, the vertical tail component of the stability coefficient changes and therefore also the stability coefficient. Similarly for the effect of the hump, as the hump does not affect the vertical tail lift curve slope, it also does not affect the stability coefficients. This is desired, as this would imply that the hump can be retrofitted on an existing aircraft without compromising the aircraft's stability. Comparing the aircraft types, the Airbus A320 has a larger margin to the stability boundary. This can mean that either this larger margin is desired, i.e. a larger restoring response in terms of static stability, but it can also be interpreted that there is more room for a redesign of the vertical tail. The latter is a realistic option when comparing the Airbus A320 to the original Fokker

F-28 Mk1000, where even the lowest stability coefficients of the Airbus A320 (at 60 deg) are equal to or larger than the stability coefficients of the original Fokker F-28 Mk1000. This implies that the stability coefficients of the Airbus A320 could be significantly lowered. Moreover, based on the takeaways of the previous section, where less sweep is better (for the M3J and hump), the stability coefficients would increase, creating even more room for a redesign.

Regarding the critical design requirements, it was found that both aircraft meet all critical design requirements for all sweep angles, except the full rudder sideslip stall requirement. Therefore, the full rudder sideslip angle for varying sweep angles is plotted in combination with the maximum stall angle of attack in Figure 6.9. This figure shows that the Airbus A320 only meets the requirement for sweep angles of 45 deg and higher, but the remaining sweep angles are very close. For the Fokker F-28 Mk1000 the full rudder sideslip is consistently around 5 deg above the maximum stall angle. Nevertheless, this is most likely still sufficient for the same reasoning as provided in subsection 6.1.2, as the dorsal fin and other interference effects are not taken into account.

Main takeaways:

- Lower sweep increases the margin with stability boundary.
- The hump does not affect the stability coefficients.
- All critical design requirements are met for the range of sweep angles, except the full rudder sideslip stall requirement, but is still deemed sufficient.

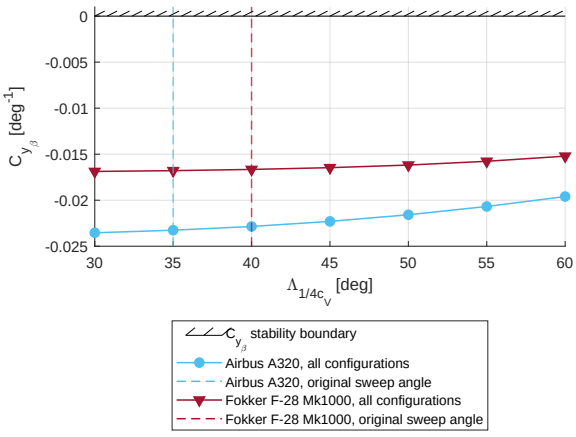

Figure 6.6: Airbus A320 and Fokker F-28 Mk1000, C_{y_β} vs. sweep

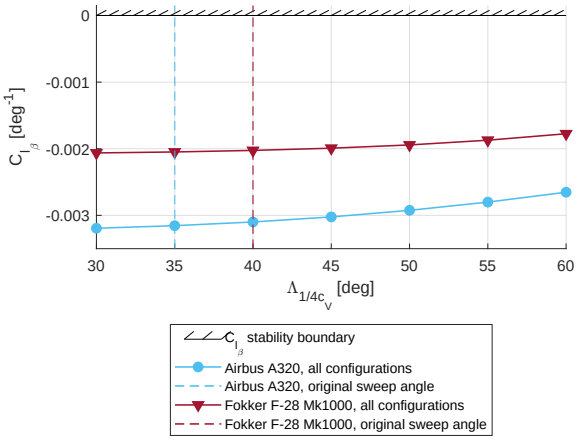

Figure 6.7: Airbus A320 and Fokker F-28 Mk1000, C_{l_β} vs. sweep

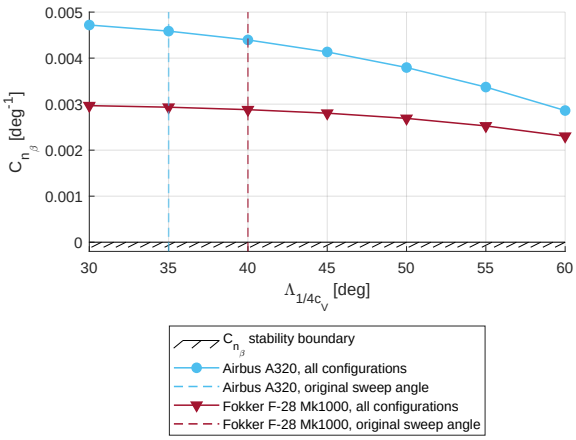

Figure 6.8: Airbus A320 and Fokker F-28 Mk1000, C_{n_β} vs. sweep

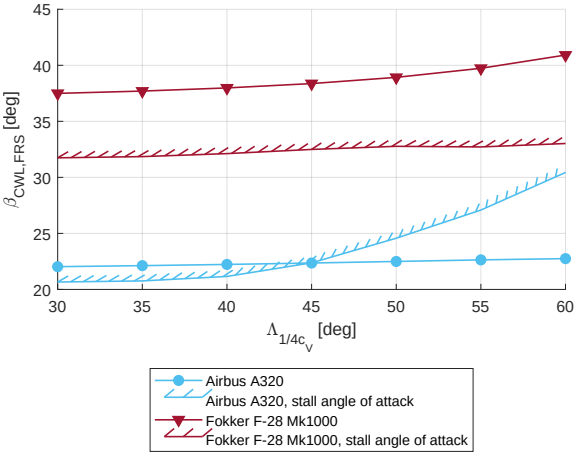

Figure 6.9: Airbus A320 and Fokker F-28 Mk1000, $\beta_{CWL,FRS}$ vs. sweep

6.3.3. Effect on full aircraft aerodynamics

The effect of sweep on the full aircraft drag coefficient, seen in Figure 6.10 and Figure 6.11, follows the same trends as for the vertical tailplane drag coefficient since the only drag reduction is that of the vertical tailplane. Going from the original airfoil to the M3J changes the relationship of sweep angle with drag coefficient from linear to exponential and reduces the drag. The hump induces an added drag reduction. This drag reduction due to hump is relatively small, as shown in Figure 6.12, because vertical tailplane drag is a very small part of total drag. The overall relationship is still the same, the effect of the hump on the drag coefficient with sweep angle is exponential and the hump is more effective at lower sweep for the given range. At the sweep angle of 30 deg a maximum drag reduction due to the hump of 0.41% is achieved. However, lowering the vertical tailplane sweep angle has less of an impact on the full aircraft drag reduction compared to the vertical tailplane drag reduction (seen before in Figure 6.3) due to the relatively small contribution of the vertical tailplane drag to the full aircraft drag. This is best seen for the Airbus A320, where the drag reduction curve almost seems constant at around 0.16%. Thus on vertical tailplane drag sweep angle has a large impact, but on full aircraft drag, the vertical tailplane sweep angle is less important. The difference in drag reduction due to the hump between the Airbus A320 and Fokker F-28 Mk1000 is again most likely due to the difference in taper-, aspect ratio, and/or cruise speed.

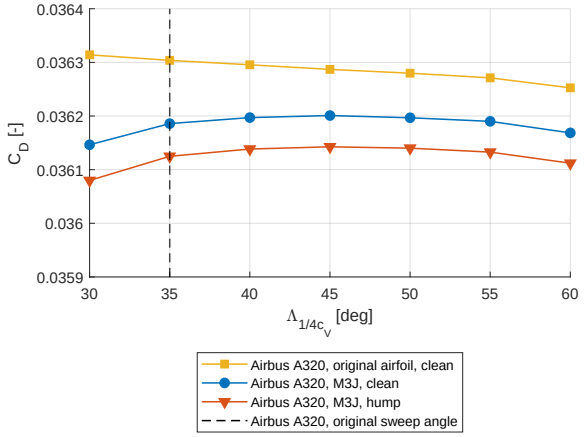

Figure 6.10: Airbus A320, C_D vs. sweep

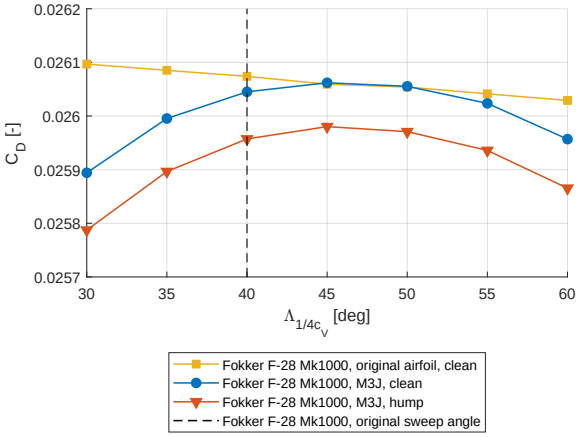

Figure 6.11: Fokker F-28 Mk1000, C_D vs. sweep

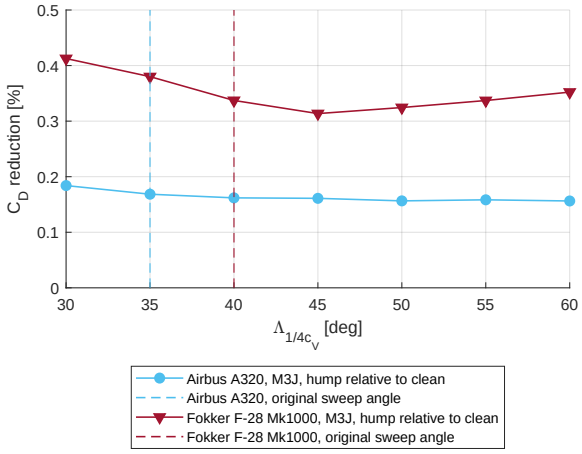

Figure 6.12: Airbus A320 and Fokker F-28 Mk1000, C_D reduction due to hump vs. sweep

The change in drag coefficient also affects other aerodynamic characteristics such as the lift-to-drag ratio. The lift-to-drag ratio is also only slightly increased due to the small overall drag reduction and shows the same behavior as the drag coefficient curves but inverted for obvious reasons. The increase in lift-to-drag-ratio due to the hump is therefore also equivalent in magnitude to the drag coefficient reduction in Figure 6.12. For reference, the figures for lift-to-drag ratio are added to section J.1.

Main takeaways:

- For the given range, the hump is most effective at reducing the drag coefficient at the lowest sweep angle (30 deg).
- The effectiveness of the hump on the overall drag coefficient is less affected by the vertical tailplane sweep angle due to the relatively small contribution of the vertical tailplane drag to the full aircraft.
- Overall lower sweep angles are beneficial (for the M3J wing) since this produces the least drag and highest lift-to-drag ratio as well as the hump being most effective.

6.3.4. Effect on weight and fuel consumption

The effect of sweep on vertical tailplane weight is shown in Figure 6.13. Weight increases for increasing sweep angle as it requires more material to make a wing of equal span with more sweep. Torenbeek (see Equation 4.1) is used to calculate the vertical tail weight, which uses planform geometry and design dive speed and is therefore independent of airfoil shape. Technically the weight of the vertical tailplane would also be dependent on airfoil, but that is negligible. Next to airfoil shape is the vertical tailplane weight also independent of the hump, as the change in aerodynamics does not affect the weight, assuming the structure can handle the different aerodynamic loads. The weight of the hump itself can also be neglected. Of course, when the hump is implemented on aircraft on a commercial scale the material might change from what is used in the wind tunnel tests. This then may change the current assumption of neglecting the hump's weight.

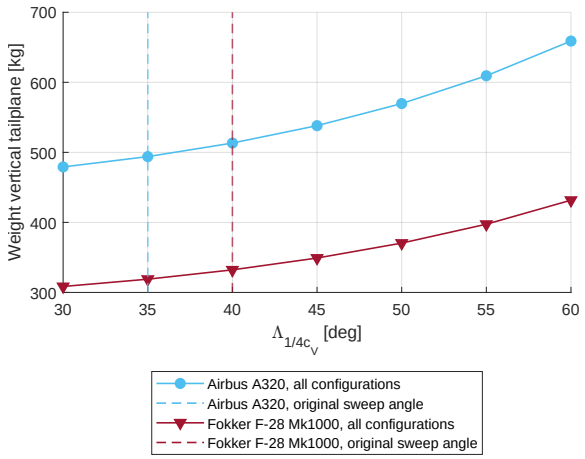

Figure 6.13: Airbus A320 and Fokker F-28 Mk1000, Vertical tailplane weight vs. sweep

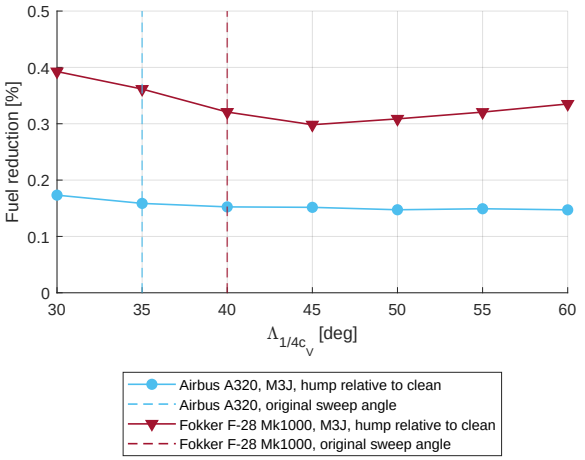

Figure 6.14: Airbus A320 and Fokker F-28 Mk1000, Fuel reduction due to hump vs. sweep

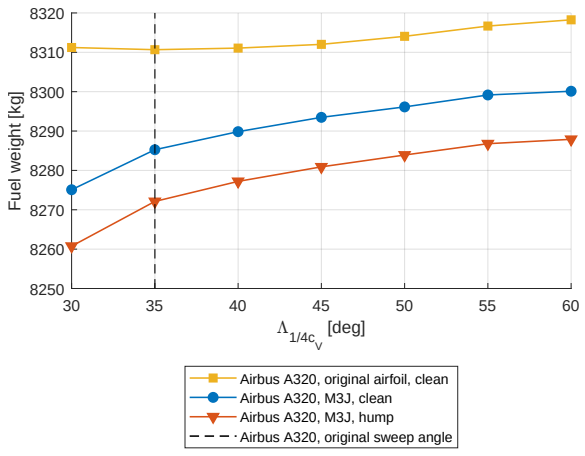

Figure 6.15: Airbus A320, Fuel weight vs. sweep

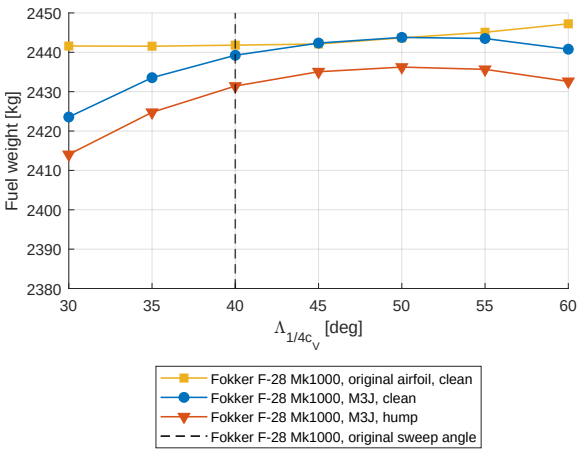

Figure 6.16: Fokker F-28 Mk1000, Fuel weight vs. sweep

The fuel weight is based on the range equation (Equation 4.5) at the harmonic range, which incorporates the change in weight of the vertical tailplane and the full aircraft drag coefficient from the previous section. The latter is incorporated through the lift-to-drag ratio. The relationship between sweep angle and fuel weight, seen in Figure 6.15 and Figure 6.16, are very similar to the drag coefficient curves, however at sweep angles above 40-45 deg the effect of the vertical tailplane weight starts showing, increasing the fuel weight. This results in that the fuel weight is lowest for the lowest vertical tail sweep angle. Isolating the effect of the hump in Figure 6.14 shows that the hump is most effective at low sweep angles in terms of fuel reduction. The curves have the same shape as what is observed for the drag reduction, but the curves are slightly lower in magnitude. For the Airbus A320 the maximum fuel reduction is 0.17% and for the Fokker F-28 Mk1000 is 0.39%, both at 30 deg sweep.

Fuel volume and CO_2 emission are directly related to the fuel weight, both obtained by a simple conversion for Jet-A1 fuel and a fuel conversion factor, respectively. Therefore these both show the same curves as the fuel weight, but at their respective magnitudes, which are added to section J.1 as reference. Overall the fuel- and CO_2 emission reduction is modest since the vertical tail is a relatively small component. Still, the hump is useful as it is a cheap and easy way to reduce fuel and can be retrofitted, and (almost) no weight penalty for the hump itself. Moreover, on fleet level this small impact can become significant.

Main takeaways:

- Low sweep angles result in the lightest vertical tailplane.
- The vertical tailplane weight is not affected by the hump.
- Low sweep angles result in lower fuel weight.
- The hump is most effective in reducing fuel weight at lower sweep angles.
- Modest fuel reduction obtained due to the hump, but potentially significant on fleet level.

6.4. Sensitivity analysis: surface area variation

For the second sensitivity analysis, the surface area is the main sensitivity variable. This is varied by scaling the surface area. Why this variable is chosen and how it is implemented can be found in section 4.8. The variation range lies between 0.5 and 1.2 with 0.1-sized increments. This range is selected to see both the effect of a reduced as well as an enlarged tail. The changes to the geometry due to surface area scaling are visualized in Figure 6.17 for the planform shapes of the two baseline aircraft. Note that the mean aerodynamic quarter-chord is kept at a constant longitudinal position as this is assumed to coincide with the aerodynamic center and therefore the yawing moment arms will stay constant. In contrast to the sweep variation, the rolling moment arm will change here. Also, note how the horizontal tailplane mounting location stays relatively constant for the Airbus A320 (conventional tail), whilst it shifts along with the changed geometry for the Fokker F-28 Mk1000 (T-tail).

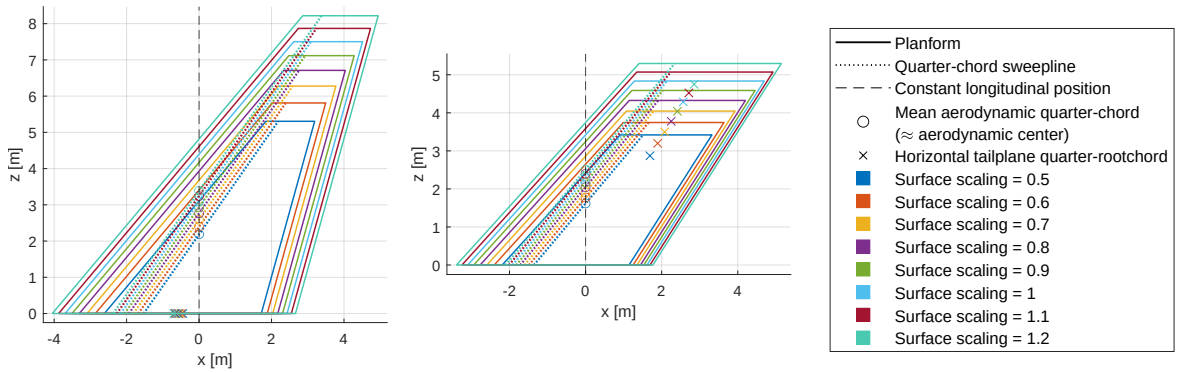

Figure 6.17: Surface area Airbus A320 (left) and Fokker F-28 Mk1000 (right).

6.4.1. Effect on vertical tailplane aerodynamics

As vertical tailplane geometry changes due to scaling the surface area, the main aerodynamic characteristics that change are the vertical tailplane lift curve slope, $(C_{L_\alpha})_V$, and vertical tailplane drag

coefficient, $(C_D)_V$. Note that the latter is again evaluated at zero angle of attack, which essentially means non-sideslipping flight, as in cruise conditions no sideslip is assumed.

The effect of surface scaling on the vertical tail lift curve slope is shown in Figure 6.18. As the vertical tailplane planform is only scaled and the other characteristics (sweep, taper- and aspect ratio) stay constant, the vertical tailplane lift curve slope also stays constant. No difference is observed between the original, M3J clean and M3J hump configuration, which is reflected by the stability coefficients staying constant in subsection 6.1.1. This also shows that the hump does not affect the vertical tailplane lift curve slope as established before.

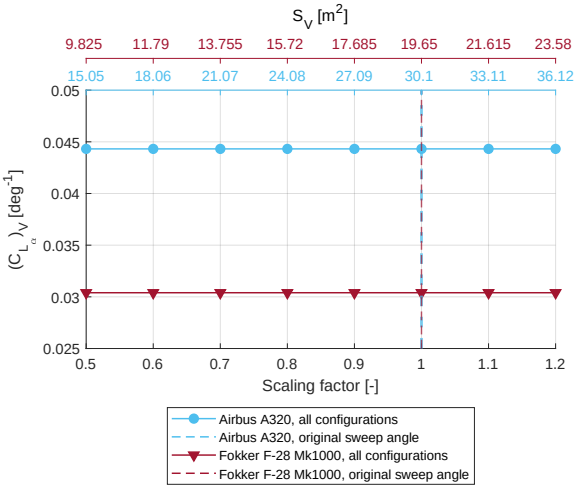

Figure 6.18: Airbus A320 and Fokker F-28 Mk1000, $(C_{L_\alpha})_V$ vs. surface area

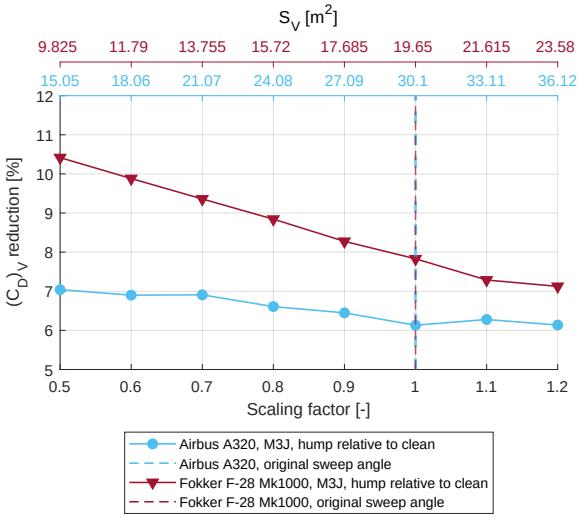

Figure 6.19: Airbus A320 and Fokker F-28 Mk1000, $(C_D)_V$ reduction due to hump vs. surface area

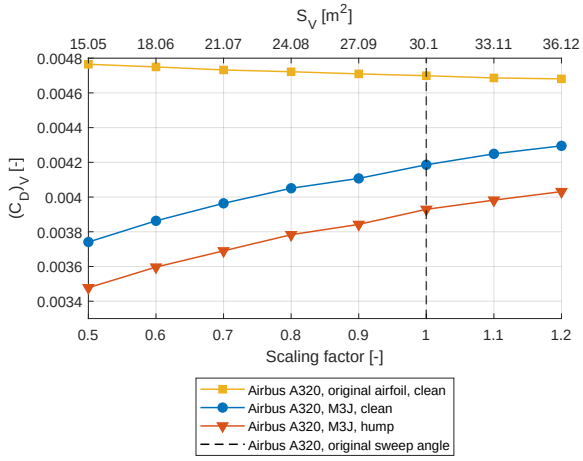

Figure 6.20: Airbus A320, $(C_D)_V$ vs. surface area

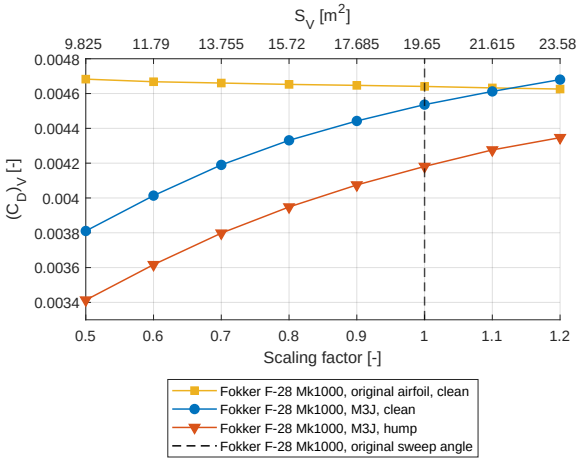

Figure 6.21: Fokker F-28 Mk1000, $(C_D)_V$ vs. surface area

In contrast to the lift curve slope, the vertical tailplane drag coefficient is affected by surface scaling, in Figure 6.20 and Figure 6.21. The original airfoil has a linear reducing vertical tailplane drag coefficient for increasing surface area. The increased surface area increases the local chords at each airfoil section and thus also the local Reynolds number. Comparing to experimental data for the NACA 4-digit airfoils [82] it is found that indeed the drag coefficient (at zero angle of attack) reduces slightly with increasing Reynolds number. Most likely due to an increased resistance to separation. In contrast, the M3J airfoil has the opposite relation with increasing surface area. This is reflected by Figure 5.19 where with increasing Reynolds number the transition location moves upstream increasing drag. A drag reduction is established by the hump. The drag coefficient reduction due to the hump is also expressed as a percentage shown in Figure 6.19. The smaller the surface area the higher the relative impact of the hump, where the maximum drag reduction is 7.04% for the Airbus A320 and 10.41%

for the Fokker F-28 Mk1000 and at its minimum still 6.14% and 7.12%, respectively. Comparing both aircraft, the Fokker F-28 Mk1000 seems to be more dependent on a change in surface area in terms of the hump effectiveness than the Airbus A320, as it has a higher gradient. This is most likely the result of differences in taper-, aspect ratio, and/or cruise speed. The Fokker F-28 Mk1000 has less taper and is therefore closer to the spanwise invariant assumption of the boundary layer solver in terms of taper. Also, the hump effectiveness is higher for all surface scaling of the Fokker F-28 Mk1000. This is probably the result of the Fokker F-28 Mk1000 having 40 deg sweep, which is closer to the maximum CFI at 45 deg [75], than the Airbus A320 with 35 deg sweep. The drag coefficient reduction curve for Airbus A320 flattens towards lower scaling factors. This is the result of reaching the laminar separation point, i.e. the laminar flow maximum for the M3J airfoil as visualized in Figure G.8.

Main takeaways:

- The vertical tailplane lift curve slope is not affected by surface area change.
- The hump does not affect the vertical tailplane lift curve slope.
- Smaller surface area results in a lower vertical tailplane drag coefficient (for the M3J airfoil).
- Smaller surface area makes the hump more effective in terms of vertical tailplane drag coefficient reduction.

6.4.2. Effect on stability coefficients

The effect of surface scaling on the stability coefficients (due to sideslip) is shown in Figure 6.22, Figure 6.23, and Figure 6.24. All three stability coefficients are linearly affected by surface area. As the surface area increases, the stability coefficients reduce and get closer to the stability boundary. The dependency on surface area is expected as stability coefficients are directly related to the vertical tail surface area. As the vertical tail surface area changes, the vertical tail component of the stability coefficient changes and therefore also the stability coefficient. Note that this is different than the sweep variation, where the vertical tailplane lift curve slope is the driving factor behind the change in stability coefficients. The hump does not affect the stability coefficients, which is expected as the aerodynamic effect would be passed down by the lift curve slope, which is also not affected by the hump. This is desired, as this would imply that the hump can be retrofitted on an existing aircraft without compromising the aircraft's stability. Comparing both aircraft, the Airbus A320 again has a larger margin to the stability boundary. This can mean that either this larger margin is desired, i.e. a larger restoring response in terms of static stability, or that there is more room for a redesign. When halving the surface area of the Airbus A320 vertical tail, the C_{y_β} and C_{l_β} are still as high as the original Fokker F-28 Mk1000 coefficients. The limiting coefficient for the Airbus A320 is the C_{n_β}, which has the steepest gradient and therefore most responsive to a change in surface area.

All critical design requirements for all surface area scaling are met for both aircraft, except the full rudder sideslip stall requirement. Figure 6.25 shows the full rudder sideslip angle for varying sweep angles in combination with the maximum stall angle of attack. For the Airbus A320, only the surface scaling of 0.5 meets the requirement, but the remaining surface scalings are very close. For the Fokker F-28 Mk1000, the full rudder sideslip decreases for increasing surface scaling but never reaches the stall angle limit in the given range. For the same reasoning as provided in subsection 6.1.2, most of the surface scaling would still pass the requirement, as the dorsal fin and other interference effects are not taken into account. Only the lower surface scalings for the Fokker F-28 Mk1000 are potentially too far over the maximum stall limit, but a more elaborate stall angle estimation is required to determine this.

Main takeaways:

- A smaller vertical tailplane surface area decreases static stability linearly, where C_{n_β} is the most responsive to surface scaling and therefore limiting.
- The hump does not affect the stability coefficients.
- All critical design requirements are met for the range of surface areas, except the full rudder sideslip stall requirement. Especially the lower surface scalings for Fokker F-28 Mk1000 are potentially over the limit, but an improved stall angle estimation is required.

6.4.3. Effect on full aircraft aerodynamics

The effect of surface scaling on the full aircraft drag coefficient is seen in Figure 6.26 and Figure 6.27. The drag coefficient increases linearly with increasing surface area. In the case of the original airfoil this

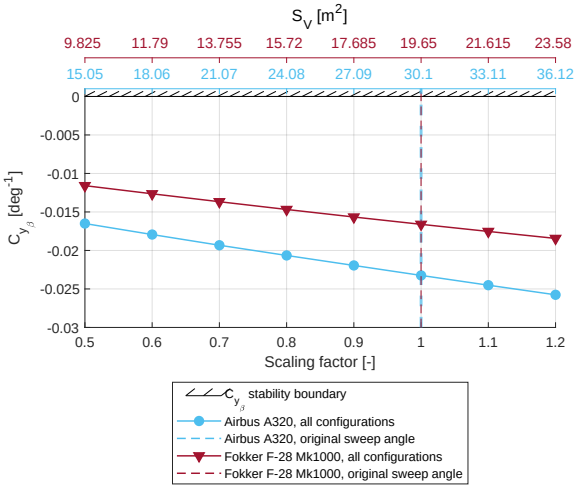

Figure 6.22: Airbus A320 and Fokker F-28 Mk1000, C_{y_β} vs. surface area

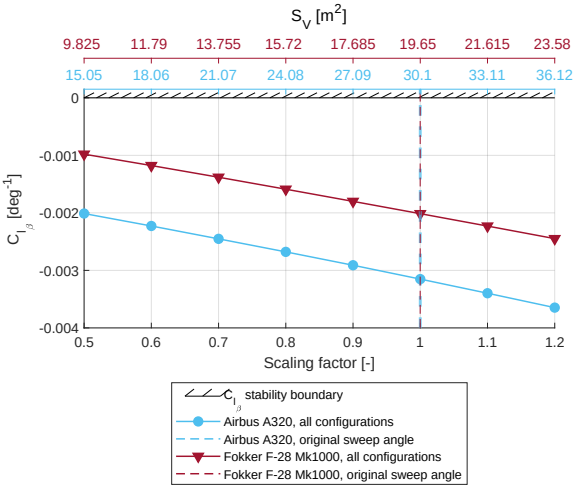

Figure 6.23: Airbus A320 and Fokker F-28 Mk1000, C_{l_β} vs. surface area

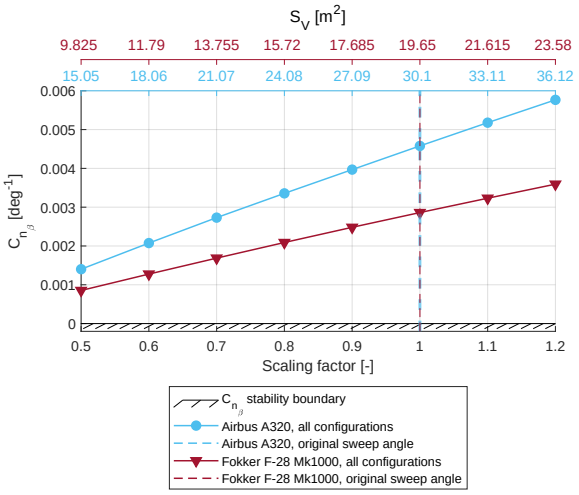

Figure 6.24: Airbus A320 and Fokker F-28 Mk1000, C_{n_β} vs. surface area

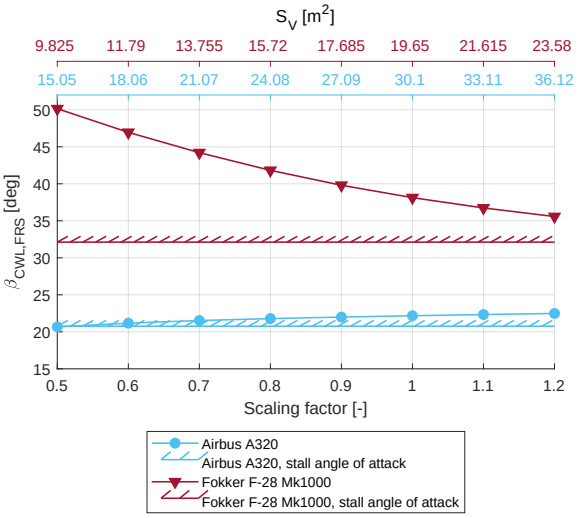

Figure 6.25: Airbus A320 and Fokker F-28 Mk1000, $\beta_{CWL,FRS}$ vs. surface area

is the opposite trend from what was seen for the vertical tail drag coefficient. For the M3J airfoil (clean and hump) the gradient becomes positive compared to the vertical tail drag coefficient. The reason for this is that the vertical tailplane drag coefficient is normalized with the vertical tailplane surface area, whilst the total drag coefficient is normalized with the wing surface area. The former changes for each surface scaling, whilst the latter stays constant. Looking at Figure 6.28 a similar effect is seen for the drag coefficient reduction, where the (almost) linear relationship changes to a positive gradient compared to the vertical tailplane drag coefficient reduction (seen in Figure 6.19). However, here it is due to the combined effect of the surface area normalization and the relative magnitude of the vertical tailplane drag coefficient compared to the full aircraft drag coefficient. The full aircraft drag coefficient reduction due to the hump now has become more effective for larger surface areas. Comparing both aircraft, the Fokker F-28 Mk1000 is still more reactive to a change in surface area with its steeper gradient compared to the Airbus A320, most likely due to the difference in taper-, aspect ratio, and/or cruise speed. The maximum drag coefficient reduction for this range is found to be 0.37% and 0.20% and the minimum 0.19% and 0.09% for the Fokker F-28 Mk1000 and Airbus A320, respectively.

Again the lift-to-drag ratio is shown for reference in section J.2, showing the same, but inverted, behavior as the drag coefficient curves. The increase in lift-to-drag ratio due to the hump is therefore

also equivalent in magnitude to the drag coefficient reduction in Figure 6.28.

Main takeaways:

- The full aircraft drag coefficient increases with increasing vertical tailplane surface area.
- The hump is more effective in reducing the full aircraft drag coefficient for larger surface areas.
- The lift-to-drag ratio increases for reducing surface area.
- For the least drag and high lift-to-drag ratio, a smaller vertical tailplane is preferred, however, the hump effectiveness will be reduced.

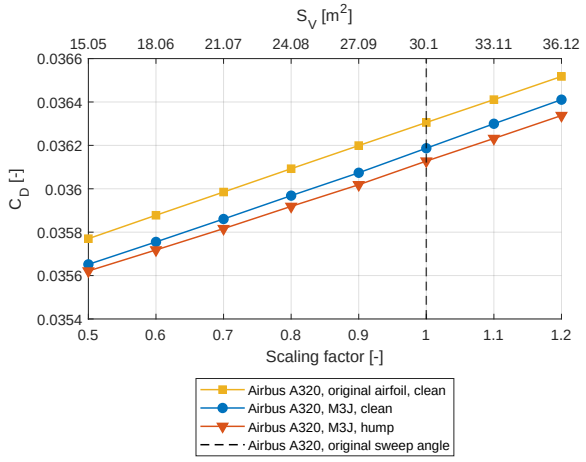

Figure 6.26: Airbus A320, C_D vs. surface area

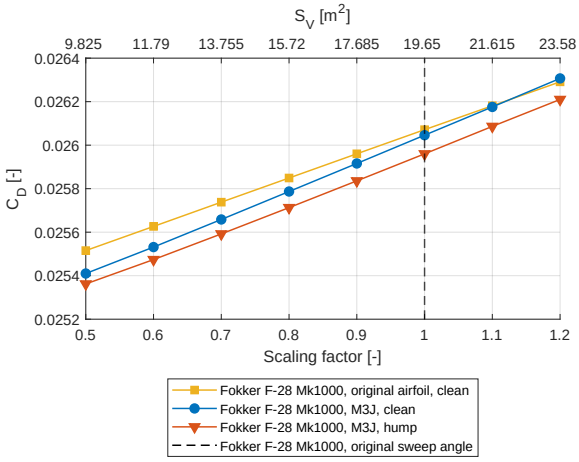

Figure 6.27: Fokker F-28 Mk1000, C_D vs. surface area

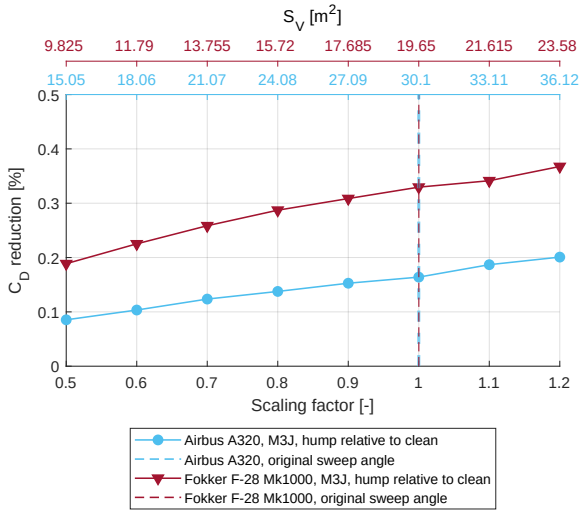

Figure 6.28: Airbus A320 and Fokker F-28 Mk1000, C_D reduction due to hump vs. surface area

6.4.4. Effect on weight and fuel consumption

The effect of surface area scaling on vertical tailplane weight is shown in Figure 6.29. The weight increases linearly with increasing surface area, as expected. As discussed in subsection 6.3.4, the vertical tail weight is independent of airfoil shape as well as the hump due to the nature of the weight estimate by Torenbeek (see Equation 4.1). The weight of the hump itself can also be neglected.

The fuel weight for surface area scaling is visualized in Figure 6.31 and Figure 6.32, where through the range equation (Equation 4.5), the change in vertical tailplane weight and the full aircraft drag coefficient from the previous section are incorporated. The fuel weight increases linearly with increasing surface area. The effect of the hump on fuel weight reduction in Figure 6.30 shows increasing effectiveness for larger surface areas, which has the same shape as Figure 6.28 at a slightly lower magnitude.

Thus the Fokker F-28 Mk1000 is also here more responsive to the change in surface area compared to the Airbus A320. For the given range, the fuel reduction varies between 0.18% and 0.35% for the Fokker F-28 Mk1000 and between 0.08% and 0.19% for the Airbus A320. The smallest surface area is preferred for the lowest drag coefficient, but the effectiveness of the hump is lowest at this point.

The fuel volume and CO_2 emission curves are again added to section J.2 for reference. These have the same relation to surface area as the fuel weight but at their respective magnitudes. A similar conclusion as drawn for the sweep sensitivity analysis can be drawn here for surface area scaling. Even though the overall fuel- and CO_2 emission reduction due to the hump is modest, on fleet level this is still considerable.

Main takeaways:

- The smaller the surface area, the lighter the vertical tailplane is.
- A smaller surface area results in less fuel weight.
- For fuel reduction the hump effectiveness increases for increasing vertical tailplane surface area.
- The smallest surface area is preferred for the lowest fuel consumption, but the effectiveness of the hump is lowest at this point.

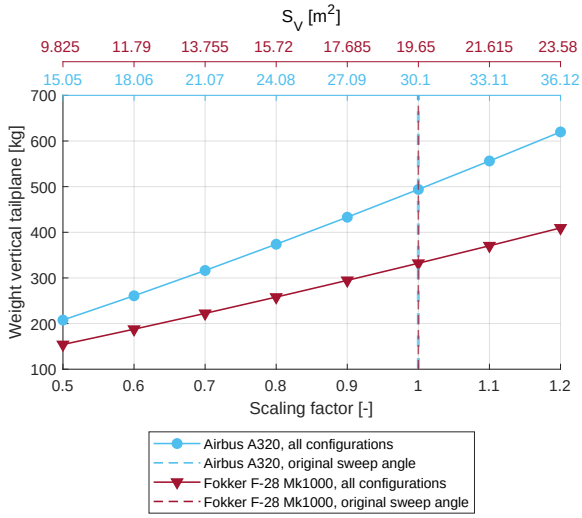

Figure 6.29: Airbus A320 and Fokker F-28 Mk1000, Vertical tailplane weight vs. surface area

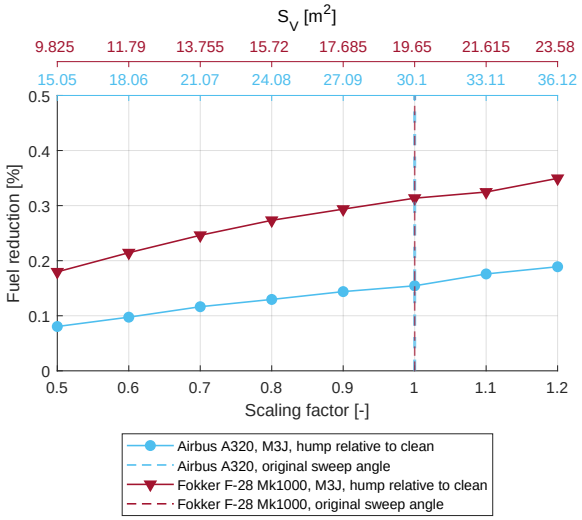

Figure 6.30: Airbus A320 and Fokker F-28 Mk1000, Fuel reduction due to hump vs. surface area

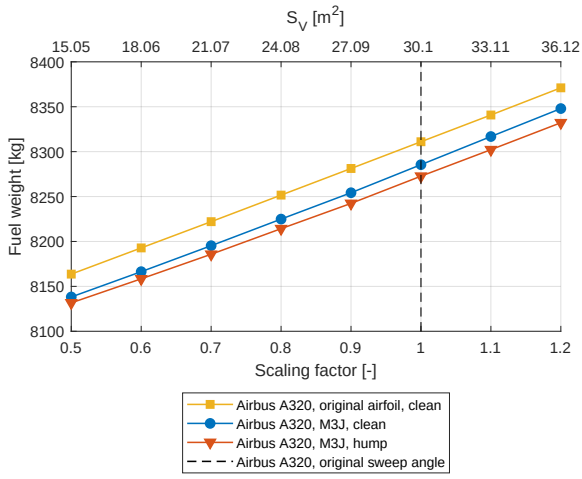

Figure 6.31: Airbus A320, Fuel weight vs. surface area

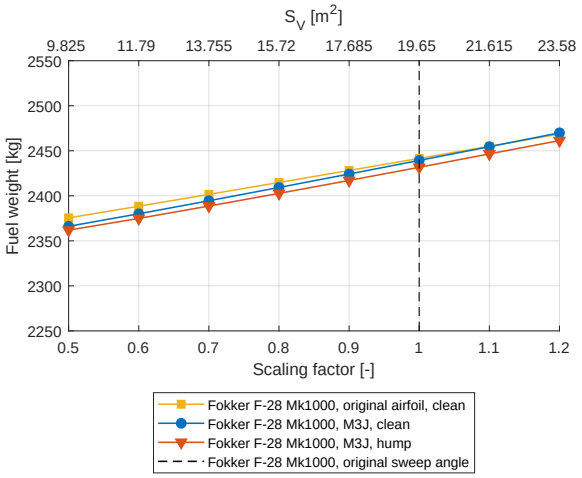

Figure 6.32: Fokker F-28 Mk1000, Fuel weight vs. surface area

7

Conclusion and discussion

The objective of this research was to investigate the implementation of the Delft Laminar Hump on a vertical stabilizer by answering the following research question: *What is the impact of the Delft Laminar Hump, implemented on the vertical stabilizer, on conceptual subsonic transport aircraft design and performance in terms of weight and drag?*. To answer this question, this research implements the DeLaH on the vertical stabilizer of subsonic transport aircraft by modeling the effect of the hump as a shift in transition location. By using a Quasi-3D aerodynamic analysis by Mariens [61] in combination with a transition location database, constructed with a boundary layer solver and stability analysis developed by the Group of Flow Control and Stability within the Delft University of Technology, the effect of the hump on the lift and drag coefficient of the vertical stabilizer is analyzed. To evaluate these aerodynamic changes on the full aircraft directional and lateral stability a stability analysis based on a method by Fokker / Obert [14] is performed and checked against the CS-25 for Large Aeroplanes regulations by EASA [25]. To evaluate the effect of the hump on weight and fuel consumption, additional weight, drag, and mission analyses are performed. In addition to, retrofitting the hump on an existing vertical stabilizer, a sensitivity analysis is used to see how the hump effectiveness changes when the geometry of the vertical tailplane changes, showing the potential of a redesign of the vertical tailplane to enhance the hump effectiveness. The main conclusions from this analysis are presented in section 7.1, and subsequently points of discussion and suggestions to improve and/or continue this research are discussed in section 7.2.

7.1. Conclusion

In this research, it was found that the DeLaH on the vertical stabilizer of a subsonic transport aircraft does not affect the vertical tailplane lift curve slope. This is desirable since this means that a retrofit of the hump will not affect the stability of the aircraft. In contrast, the vertical tailplane drag coefficient is reduced by the hump. As a baseline, the Airbus A320 and the Fokker F-28 Mk1000 were evaluated, since they are considered to be representative of the two most common tail configurations, namely a conventional tail with a fuselage-mounted stabilizer and a T-tail. Retrofitting the hump on the vertical stabilizer of these aircraft results in a reduction of the vertical tailplane drag coefficient of 6.73% and 8.72% for the Airbus A320 and Fokker F-28 Mk1000, respectively. Translating this vertical tail drag coefficient reduction to the full aircraft drag coefficient a reduction of 0.17% and 0.34% was found for the baseline aircraft. Evaluating the harmonic range, an fuel reduction due to the hump of 0.16% and 0.32% is established. The aircraft weight is reduced by the same percentage through the fuel reduction, as it is assumed that the added weight due to the hump itself is negligible. From these results, it can be concluded that the DeLaH has a significant drag-reducing effect on the overall aircraft, whilst not affecting the aircraft's stability. Even though the fuel savings for an individual aircraft are not very large, on a fleet level this would be significant. The hump can be retrofitted on existing aircraft by simply gluing it on the outer skin, making it a relatively simple and cheap way to improve efficiency for aircraft manufacturers.

Additionally, two sensitivity analyses are performed, namely, sweep angle variation and surface area scaling. By varying the quarter-chord sweep angle (30 to 60 degrees in 5-degree increments)

and scaling the surface area (scaling factor 0.5 to 1.2 in 0.1-sized increments), the effectiveness of the hump for different vertical tailplane geometries is analyzed.

The following conclusions can be drawn for the effect of sweep variation on the hump:

- The vertical tailplane lift curve slope is not affected by the hump regardless of the sweep angle.
- The effect of the hump on the vertical tail drag coefficient has an exponential relationship with sweep angle.
- In the simulated range, the hump is most effective in reducing the vertical tailplane drag coefficient at the lowest sweep angle of 30 deg (up to 11.31%).
- The hump does not affect the stability coefficients, thus not affecting the critical design requirements based on CS-25 for Large Aeroplanes by EASA [25] for the simulated range of sweep angles.
- Effectiveness of the hump on the full aircraft drag coefficient is less affected by sweep angle compared to the vertical tailplane drag coefficient due to the relatively small contribution of the vertical tailplane drag to the full aircraft.
- For the simulated range, the hump is most effective in reducing the full aircraft drag coefficient at the lowest sweep angle of 30 deg (up to 0.41%).
- Since the weight of the hump itself is negligible, the vertical tailplane weight is not affected by the hump. Regardless of the hump, lower sweep angles result in lighter vertical tailplanes.
- The fuel reduction is the result of the combined effect of the reduction in drag and vertical tailplane weight. Therefore, the hump is most effective in reducing fuel weight at lower sweep angles.
- Overall, lower sweep angles are beneficial as the hump is most effective. In addition, regardless of the hump, lower sweep angles result in lower drag (for the M3J airfoil), reduced vertical tailplane weight, less fuel weight as well as an increased stability margin.

Analyzing the effect of surface area scaling on the hump resulted in the following findings:

- The hump has no effect on the vertical tailplane lift curve slope regardless of surface scaling.
- Smaller surface area makes the hump more effective in terms of vertical tailplane drag coefficient reduction. However, this is the result of the vertical tailplane drag coefficient being normalized by the respective vertical tailplane surface it is evaluated for (changes for each surface scaling) and therefore not indicative of the hump's effect on the full aircraft.
- The hump does not affect the stability coefficients, thus not affecting the critical design requirements based on CS-25 for Large Aeroplanes by EASA [25] for the simulated range of surface area scaling factors.
- In contrast to the vertical tailplane drag coefficient, for the full aircraft drag coefficient the hump effectiveness increases linearly for increasing surface area.
- Since the weight of the hump itself is negligible, the vertical tailplane weight is not affected by the hump. Smaller surface areas result in lighter vertical tailplanes (regardless of the hump).
- The hump becomes more effective in reducing fuel weight for increasing surface area, again because the fuel reduction is the result of the combined effect of the reduction in drag and vertical tailplane weight.
- Overall, there will be an optimal vertical tailplane surface area, since the hump effectiveness increases for increasing surface area, whilst for the full aircraft drag, vertical tailplane weight, and thus fuel weight, a smaller surface area is preferred. The stability margin becomes the limiting factor as a minimum surface area is required for sufficient stability.

Comparing the baseline aircraft, the hump is more effective for the Fokker F-28 Mk1000 over the entire range of scaling factors and sweep angles compared to the Airbus A320. As the drag coefficient is not corrected for endplate effects, the difference in horizontal tailplane mounting location (conventional vs. T-tail) cannot be the reason for this difference. This leads to the suspicion that, next to the sweep angle of the Fokker F-28 Mk1000 being closer to the sweep angle of the CFI maximum, taper- and aspect ratio, and cruise speed play an important role in the effectiveness of the hump, but more research is required.

7.2. Discussion and future work

In continuation of the conclusions in the previous section, several suggestions for new research are formulated as well as parts that may be improved. They are grouped per subject.

Prerequisites and assumptions for the DeLaH

For the hump to be effective, laminar flow is required as it delays transition. However, at the root of the vertical tailplane, the flow is affected by the fuselage (and potentially a dorsal fin), which makes the flow turbulent, making the hump useless in that area. A similar problem occurs near the horizontal tailplane, where due to interference the flow is most likely not laminar in that area. This would reduce the overall effectiveness of the hump on the vertical tailplane and the results in this research are therefore overestimating the drag and fuel reduction. In addition to this, to ensure laminar flow, in the wind tunnel test of the hump, the NLF airfoil M3J was used. Generally, aircraft do not use NLF airfoil for the vertical tailplane, thus making a direct retrofit of the hump difficult, diminishing the hump's potential slightly.

Since the hump has only been tested at low subsonic Mach numbers, it is yet unknown whether at cruise Mach numbers the pressure gradient change-over along the hump will cause a shock wave. In addition, the hump has only been tested on the pressure side of the wing. It has not been tested whether the hump works on the suction side or even has detrimental effects in terms of lift (side force) and drag. It would make sense to install the hump on either side of the vertical tail, as it uses a symmetrical airfoil shape. This is important since the vertical tail should be able to deal with both positive well as negative sideslip angles. To establish whether the hump works on the suction side as well as whether the hump causes a shock, dedicated wind tunnel experiments, flight tests, and/or CFD simulations are necessary.

Aerodynamic analysis

Q3D, which is used to assess the vertical tailplane aerodynamics, has several limitations, which could have an impact on the results. According to Mariens [61], Q3D over-predicts the lift coefficient and Q3D under-predicts the drag coefficient. The over-prediction of the lift coefficient would result in an over-prediction of the vertical tailplane lift curve slope used in the vertical tailplane stability coefficients. In other words, the vertical tailplane effectiveness in stabilizing the aircraft is over-estimated, and therefore one should be cautious for cases in the sensitivity analysis where the stability coefficients get closer to the stability boundary because the stability margin is most likely smaller than calculated. The under-predicts the drag coefficient especially occurs at lower angles of attack. In this research, the vertical tailplane drag coefficient at zero angle of attack is of importance as this resembles cruise conditions. In the validation of Q3D by Mariens [61] the order of magnitude of under-prediction of the drag coefficient at zero angle of attack lies around 1%. For this research, this would mean that the vertical tailplane drag coefficient is underestimated. However, this might be more nuanced. As the vertical tailplane is symmetric, at zero angle of attack the drag coefficients only consist of profile drag, which can be split into its respective components, skin friction drag and pressure drag. The earlier mentioned 1% under-prediction of drag is the combined effect of an under-estimation of skin friction drag and over-estimated pressure drag. The under-prediction of the skin friction drag can be explained by the overestimation of the transition location calculated by XFoil according to Mariens [61]. In this research, however, the transition location is set directly based on the boundary layer and stability solver results. This makes the transition location more likely to be representative of the real world and therefore also the skin friction drag closer to the actual value. This would mean that the 1% under-prediction of the overall drag coefficient by Q3D is reduced in this research. More research would be required to verify this reasoning. Nevertheless, the relative impact of the hump on the drag coefficient will still be valid.

For the boundary layer solver and stability analysis the flow is assumed to be incompressible, however in reality at cruise Mach numbers compressibility does play a role. More research is required to see whether compressibility affects the results. Another assumption is that the constant value of ΔN used to estimate N_{hump}, is valid for all flight conditions. In reality the value of ΔN would vary for different Reynolds numbers, angles of attack, and sweep angles. However, to find the actual ΔN value for each flight condition many wind tunnel tests would be required, which is not feasible.

Stability analysis

In the stability analysis, the CG shift due to fuel and varying tail geometries (during the sensitivity analysis) is not taken into account. Also, CG location taken at 25% wing mean aerodynamic chord

(30% for Fokker aircraft) following the Fokker / Obert method [14]. In reality, the CG would shift during flight and the most critical CG location would be the most aft location, which creates the shortest yawing moment arm, making the vertical tail least effective. Therefore some margin must be taken for the stability coefficient results and/or the CG shift should be added to the stability analysis.

Regarding critical design requirements, the full rudder sideslip stall requirement is not met by the baseline aircraft. This could be the result of an underestimation of the stall angle by neglecting the dorsal fin and other interference effects. Therefore an improved stall estimation would be useful.

Vertical tailplane geometry and DeLaH

As mentioned in the conclusion, it is suspected that taper- and aspect ratio, and cruise speed play an important role in the effectiveness of the hump. Additional sensitivity analyses for these variables could be performed to determine the main driving factor behind the effectiveness of the hump. Other, more complex, variables that could be investigated are for instance the vertical position of the horizontal tail or rudder size. One other thing that would also be interesting to analyze is other airfoil shapes, different from the M3J airfoil used in the wind tunnel test with the hump. Do note that the hump has the prerequisite that a NLF airfoil is used.

Another option, at a secondary stage, would be to redesign/resize the vertical tail once the hump is installed. This can of course be done with an optimizer, iterating to obtain a smaller and more efficient tailplane as shown in Figure 7.1. This can also be integrated into existing aircraft design tools such as the Aircraft Design Initiator [83][84]. A disadvantage of this approach is that this provides only an optimum for one specific aircraft and set of flight conditions. In addition, there are quite a lot of geometric parameters to optimize for, making this very computationally intensive.

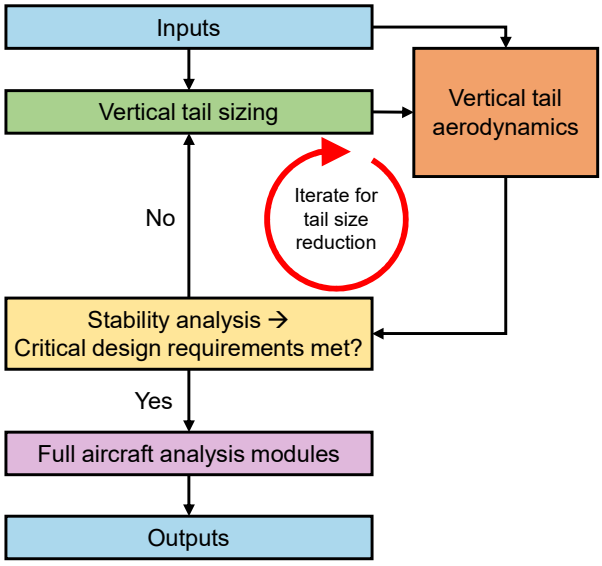

Figure 7.1: Iterative redesign of vertical tailplane added to the existing method.

References

[1] ESDU, "Contribution of fin to sideforce, yawing moment and rolling moment derivatives due to sideslip,(yv) f,(nv) f,(lv) f, in the presence of body, wing and tailplane," *ESDU Item 82010*, 2017.

[2] Finck, R., "Usaf (united states air force) stability and control datcom (data compendium)," *Defense Technical Information Center*, 1978.

[3] Nicolosi, F., Ciliberti, D., Della Vecchia, P., Corcione, S., and Cusati, V., "A comprehensive review of vertical tail design," *Aircraft Engineering and Aerospace Technology*, vol. 89, no. 4, pp. 547–557, 2017.

[4] United Nations Framework Convention on Climate Change, "Paris agreement," 2015.

[5] ICAO, "Resolution A41-21: Consolidated statement of continuing icao policies and practices related to environmental protection — climate change," 2022.

[6] ICAO CAEP, "Report on the feasibility of a long-term aspirational goal (ltag) for international civil aviation co2 emission reductions," 2022.

[7] Thibert, J., Reneaux, J., and Schmitt, V., "ONERA activities on drag reduction," *Office National d'Etudes et de Recherches Aérospatiales*, 1990.

[8] Schrauf, G., "Status and perspectives of laminar flow," *Aeronautical Journal*, vol. 109, 1102 2005, ISSN: 00019240. DOI: 10.1017/S000192400000097X.

[9] Braslow, A., "History of suction-type laminar-flow control with emphasis on flight resrearch: Monographs in aerospace history number 13," 1999.

[10] Joslin, R. D., "Overview of laminar flow control," *NASA/TP-1998-208705*, 1998.

[11] Rius-Vidales, A. F. and Kotsonis, M., "Impact of a forward-facing step on the development of crossflow instability," *Journal of Fluid Mechanics*, vol. 924, A34, 2021.

[12] Joslin, R. D., "Aircraft laminar flow control," *Annual review of fluid mechanics*, vol. 30, no. 1, pp. 1–29, 1998.

[13] Cook, M. V., *Flight dynamics principles*. Butterworth-Heinemann, 2012.

[14] Obert, E., "Static directional stability and control of transport aircraft," *11th European Workshop on Aircraft Design Education*, 2013.

[15] Torenbeek, E., *Synthesis of subsonic airplane design*. Springer Science & Business Media, 1982.

[16] Raymer, D. P., *Aircraft design: a conceptual approach*. American Institute of Aeronautics and Astronautics, Inc., 1993.

[17] Obert, E., *Aerodynamic design of transport aircraft*. IOS press, 2009.

[18] ESDU, "Rudder sideforce, yawing moment and rolling moment control derivatives at low speeds: Yζ, nζ and lζ," *ESDU Item 87008*, 2014.

[19] Roskam, J., *Airplane Design: Part 2-Preliminary Configuration Design and Integration of the Propulsion System*. DARcorporation, 1985.

[20] Ciliberti, D., Della Vecchia, P., Nicolosi, F., and De Marco, A., "Aircraft directional stability and vertical tail design: A review of semi-empirical methods," *Progress in Aerospace Sciences*, vol. 95, pp. 140–172, 2017.

[21] Scholz, D., "Empennage sizing with the tail volume complemented with a method for dorsal fin layout," *INCAS bulletin*, vol. 13, no. 3, pp. 149–164, 2021.

[22] Roskam, J., *Airplane flight dynamics and automatic flight controls*. DARcorporation, 2001, vol. Part 1.

[23] Mulder, J., Staveren, W. van, Vaart, J. van der, *et al.*, "AE3202 flight dynamics lecture notes," *Delft University of Technolgy, Faculty of Aerospace Engineering*, 2013.

[24] Wolowicz, C. H. and Yancey, R. B., "Lateral-directional aerodynamic characteristics of light, twin-engine, propeller driven airplanes," *NASA-TN-D-6946*, 1972.

[25] EASA, "Certification specifications and acceptable means of compliance for large aeroplanes," *CS-25, Amendment 28*, 2023.

[26] Gale, L. J. and Jones, I. P., "Effects of antispin fillets and dorsal fins on the spin and recovery characteristics of airplanes as determined from free-spinning-tunnel tests," *NACA TN No. 1779*, 1948.

[27] Prandtl, L., "Uber flussigkeitsbewegung bei sehr kleiner reibung," *Verhandl. 3rd Int. Math. Kongr. Heidelberg (1904), Leipzig*, 1905.

[28] Schlichting, H. and Gersten, K., *Boundary-layer theory*. springer, 2016.

[29] Anderson, J. D., *Fundamentals of Aerodynamics (SI units)*. McGraw hill, 2011.

[30] White, F. M., *Fluid mechanics*. The McGraw Hill Companies, 2008.

[31] Zalovcik, J. A., Wetmore, J., and Vondoenhoff, A. E., "Flight investigation of boundary-layer control by suction slots on an naca 35-215 low-drag airfoil at high reynolds numbers," *NACA ACR No. 4B29*, 1944.

[32] Voogt, N., "Flight testing of a fokker 100 test aircraft with laminar flow glove," *Fokker Aircraft B.V.*, 1992.

[33] Saric, W. S., West, D. E., Tufts, M. W., and Reed, H. L., "Experiments on discrete roughness element technology for swept-wing laminar flow control," *AIAA Journal*, vol. 57, no. 2, pp. 641–654, 2019.

[34] Lemarechal, J., Costantini, M., Klein, C., *et al.*, "Investigation of stationary-crossflow-instability induced transition with the temperature-sensitive paint method," *Experimental Thermal and Fluid Science*, vol. 109, p. 109 848, 2019.

[35] Saric, W. S., Carpenter, A. L., and Reed, H. L., "Passive control of transition in three-dimensional boundary layers, with emphasis on discrete roughness elements," *Philosophical Transactions of the Royal Society A: Mathematical, Physical and Engineering Sciences*, vol. 369, no. 1940, pp. 1352–1364, 2011.

[36] Krishnan, K. S., Bertram, O., and Seibel, O., *Review of hybrid laminar flow control systems*, 2017. DOI: 10.1016/j.paerosci.2017.05.005.

[37] Bushnell, D. M. and Tuttle, M. H., *Survey and bibliography on attainment of laminar flow control in air using pressure gradient and suction, volume 1*. National Aeronautics, Space Administration, Scientific, and Technical Information Branch NASA-RP-1035, 1979, vol. 1.

[38] Brooks Jr, C. W., Harris, C. D., and Harvey, W. D., "The nasa langley laminar-flow-control experiment on a swept, supercritical airfoil," *NASA Technical Memorandum 4096*, 1989.

[39] Dannenberg, R. E., Gambucci, B. J., and Weiberg, J. A., "Perforated sheets as a porous material for distributed suction and injection," *NACA TN 3669*, 1956.

[40] Boeing Commercial Airplane Group, "High reynolds number hyrbid laminar flow control (hlfc) flight experiment ii. aerodynamic design," *NASA/CR-1999-209324*, 1999.

[41] Schrauf, G. and Geyr, H. von, "Simplified hybrid laminar flow control for transport aircraft," *European Congress on Computational Methods in Applied Sciences and Engineering (ECCOMAS 2012)*, 2012.

[42] Schrauf, G. H. and Geyr, H. von, "Simplified hybrid laminar flow control for the a320 fin-aerodynamic and system design, first results," *AIAA Scitech 2020 Forum*, 2020.

[43] Schrauf, G. H. and Geyr, H. von, "Simplified hybrid laminar flow control for the a320 fin. part 2: Evaluation with the en-method," *AIAA Scitech 2021 Forum*, p. 1305, 2021.

[44] Henke, R., ""a 320 hlf fin" flight tests completed," *Air & Space Europe*, vol. 1, no. 2, pp. 76–79, 1999.

[45] Lekoudis, S. G., "Stability of the boundary layer on a swept wing with wall cooling spyridon," *AIAA Journal*, vol. 18, no. 9, pp. 1029–1035, 1980.

[46] Mack, L. M., “On the stabilization of three-dimensional boundary layers by suction and cooling,” in *Laminar-turbulent transition*. 1980.

[47] Bertolotti, F. and Bieler, H., “Stability analysis of two-and three-dimensional boundary layer flows with varied wall temperatures,” in *New Results in Numerical and Experimental Fluid Mechanics: Contributions to the 10th AG STAB/DGLR Symposium Braunschweig, Germany 1996*. 1997, pp. 64–70.

[48] Reshotko, E., “Drag reduction by cooling in hydrogen-fueled aircraft,” *Journal of Aircraft*, vol. 16, no. 9, pp. 584–590, 1979.

[49] Stuber, V. L., Mkhoyan, T., De Breuker, R., and Zwaag, S. van der, “In-situ boundary layer transition detection on multi-segmental (a) synchronous morphing wings,” *Measurement: Sensors*, vol. 19, p. 100 356, 2022.

[50] Lammering, T., Risse, K., Franz, K., and Stumpf, E., “Assessment of an innovative morphing leading edge considering uncertainties in conceptual design,” *12th AIAA Aviation Technology, Integration, and Operations (ATIO) Conference and 14th AIAA/ISSMO Multidisciplinary Analysis and Optimization Conference*, 2012.

[51] Malik, M., Weinstein, L., and Hussaini, M., “Ion wind drag reduction,” *21st Aerospace Sciences Meeting*, p. 231, 1983.

[52] Roth, J. R., Sherman, D. M., and Wilkinson, S. P., “Electrohydrodynamic flow control with a glow-discharge surface plasma,” *AIAA journal*, vol. 38, no. 7, pp. 1166–1172, 2000.

[53] Tol, H., De Visser, C., and Kotsonis, M., “Experimental model-based estimation and control of natural tollmien–schlichting waves,” *AIAA Journal*, vol. 57, no. 6, pp. 2344–2355, 2019.

[54] Chernyshev, S., Kiselev, A. P., and Kuryachii, A., “Laminar flow control research at tsagi: Past and present,” *Progress in Aerospace Sciences*, vol. 47, no. 3, pp. 169–185, 2011.

[55] Boeing Commercial Airplane Group, “High reynolds number hybrid laminar flow control (hlfc) flight experiment iv. suction system design and manufacture,” *NASA/CR-1999-209326*, 1999.

[56] Collier Jr., F., “An overview of recent subsonic laminar flow control flight experiments,” *23rd Fluid Dynamics, Plasmadynamics, and Lasers Conference*, 1993.

[57] Schmitt, V., Archambaud, J., Hortstmann, K., and Quast, A., “Hybrid laminar fin investigations,” in *Proceedings of the RTO AVT Symposium on Active Control Technology for Enhanced Performance Operational Capabilities of Military Aircraft, Land Vehicles and Sea Vehicles, Braunschweig, Germany*. 2001, vol. 8.

[58] Schrauf, G. and Geyr, H. von, “Hybrid laminar flow control on a320 fin: Retrofit design and sample results,” *Journal of Aircraft*, vol. 58, no. 6, pp. 1272–1280, 2021.

[59] Schrauf, G., “Large-scale laminar flow tests evaluated with linear stability theory,” *Journal of Aircraft*, vol. 41, no. 2, pp. 224–230, 2004.

[60] Hansen, H., “Laminar flow technology-the airbus view,” *27th International Congress of the Aeronautical Sciences*, 2010.

[61] Mariens, J., Elham, A., and Van Tooren, M., “Quasi-three-dimensional aerodynamic solver for multidisciplinary design optimization of lifting surfaces,” *Journal of Aircraft*, vol. 51, no. 2, pp. 547–558, 2014.

[62] Méheut, M. and Bailly, D., “Drag-breakdown methods from wake measurements,” *AIAA journal*, vol. 46, no. 4, pp. 847–862, 2008.

[63] Flandro, G. A., McMahon, H. M., and Roach, R. L., *Basic aerodynamics: incompressible flow*. Cambridge University Press, 2011, vol. 31.

[64] Wright, J. R. and Cooper, J. E., *Introduction to aircraft aeroelasticity and loads*. John Wiley & Sons, 2008, vol. 20.

[65] ESDU, “Introduction to transonic aerodynamics of aerofoils and wings,” *ESDU Item 90008*, 1990.

[66] Van Ingen, J., “The en method for transition prediction. historical review of work at tu delft,” in *38th AIAA Fluid Dynamics Conference and Exhibit*, 2008, p. 3830.

[67] Morais, L., “Confidential master thesis,” *Delft University of Technology*, 2023.

[68] Serpieri, J., “Cross-flow instability: Flow diagnostics and control of swept wing boundary layers,” English, Dissertation (TU Delft), Delft University of Technology, 2018, ISBN: 978-94-6186-879-4. DOI: 10.4233/uuid:3dac1e78-fcc3-437f-9579-048b74439f55.

[69] EASA, “Sustainable Aviation Fuel ‘Monitoring System’,” *Grant Agreement EASA.2015.FC21*, 2019.

[70] Risse, K. and Stumpf, E., “Conceptual aircraft design with hybrid laminar flow control,” *CEAS Aeronautical Journal*, vol. 5, pp. 333–343, 2014.

[71] Risse, K., Schueltke, F., Stumpf, E., and Schrauf, G. H., “Conceptual wing design methodology for aircraft with hybrid laminar flow control,” *52nd Aerospace Sciences Meeting*, 2014.

[72] Vidales, A. R., “Influence of a forward-facing step on crossflow instability and transition: An experimental study in a swept wing boundary-layer,” 2022.

[73] Westerbeek, S., Hulshoff, S., Schuttelaars, H., and Kotsonis, M., “Dehnsso: The delft harmonic navier-stokes solver for nonlinear stability problems with complex geometric features,” *Computer Physics Communications*, vol. 302, p. 109 250, 2024.

[74] Anderson, D., Tannehill, J. C., Pletcher, R. H., Munipalli, R., and Shankar, V., *Computational fluid mechanics and heat transfer*. CRC press, 2020.

[75] Mack, L. M., “Boundary-layer linear stability theory,” *Agard rep*, vol. 709, 1984.

[76] Hoerner, S. F., *Fluid-dynamic drag*. Published by the Author, 1965.

[77] Becker, J. V., “Boundary-layer transition on the naca 0012 and 23012 airfoils in the 8-foot high-speed wind tunnel,” *NACA-SR-137*, 1940.

[78] Ciliberti, D., De Luca, L., and Nicolosi, F., “An improved preliminary design methodology for aircraft directional stability prediction and vertical tailplane sizing,” *University of Naples “Federico II*, 2016.

[79] Barua, P., Sousa, T., and Scholz, D., “Empennage statistics and sizing methods for dorsal fins,” *Hamburg University of Applied Sciences, Hamburg, Germany*, 2013.

[80] Airbus S.A.S., “A320 aircraft characteristics airport and maintenance planning,” *Customer Services, Technical Data Support and Services*, 2020.

[81] EASA, “Type-certificate data sheet for Fokker F28,” *No. EASA.A.037*, 2022.

[82] Goett, H. J. and Bullivant, W. K., *Tests of NACA 0009, 0012, and 0018 airfoils in the full-scale tunnel*. US Government Printing Office Washington, DC, USA, 1938.

[83] Elmendorp, R., Vos, R., and La Rocca, G., “A conceptual design and analysis method for conventional and unconventional airplanes,” *29th Congress of the International Council of the Aeronautical Sciences*, vol. 1, 2014.

[84] Hoogreef, M., Vries, R. de, Sinnige, T., and Vos, R., “Synthesis of aero-propulsive interaction studies applied to conceptual hybrid-electric aircraft design,” in *AIAA Scitech 2020 Forum*, 2020, p. 0503.

[85] Campbell, J. P. and Mckinney, M. O., “Summary of methods for calculating dynamic lateral stability and response and for estimating aerodynamic stability derivatives,” *NACA-TR-1098*, 1952.

[86] Luckring, J. M., “Theoretical and experimental analysis of longitudinal and lateral aerodynamic characteristics of skewed wings at subsonic speeds to high angles of attack,” *NASA TN D-8512*, 1977.

[87] Schrauf, G., “On allowable step heights: Lessons learned from the f100 and attas flight tests,” *6th European Conference on Computational Mechanics: Solids, Structures and Coupled Problems, ECCM 2018 and 7th European Conference on Computational Fluid Dynamics, ECFD 2018*, 2018.

[88] Sakurai, S. and Fevergeon, M., *Door assembly for laminar flow control system*, European Patent Office, EP2208669A2, 2010.

[89] Gibson, T., Soucheleau, B., and Rogers, N., “BLADE - natural laminar flow flight testing,” *32nd Congress of the International Council of the Aeronautical Sciences, ICAS*, 2021.

[90] EASA, “Type-certificate data sheet for CFM56-5B and CFM56-5C series engines,” *No. E.003*, 2023.

A

Comparison of stability analyses

Table A.1: Comparison of stability analyses.

	USAF DATCOM [2]	**ESDU** [1]	**Fokker / Obert** [14]	**VeDSC** [3]
Method	· Semi-empirical method	· Semi-empirical method	· Semi-empirical method (uses DATCOM, ESDU, and NACA TM D-6946)	· Semi-empirical method (uses ESDU)
Input	· Vertical tail geometry · Wing + fuselage geometry · $\left(C_{L_\alpha}\right)_V$	· Vertical tail geometry · Wing + fuselage geometry · $\left(C_{L_\alpha}\right)_V$ · Location center of pressure	· Vertical tail geometry · Wing + fuselage geometry · $\left(C_{L_\alpha}\right)_V$	· Vertical tail geometry · Wing + fuselage geometry · $\left(C_{L_\alpha}\right)_V$
Output	· $C_{y_\beta}, C_{l_\beta}, C_{n_\beta}$	· $C_{y_\beta}, C_{l_\beta}, C_{n_\beta}$	· $C_{y_\beta}, C_{l_\beta}, C_{n_\beta}$	· $C_{y_\beta}, C_{l_\beta}, C_{n_\beta}$
Conditions	· Subsonic speeds · Low angles of attack · Linear angle of attack range	· Subsonic speeds (freestream) · The flow over the configuration is fully attached and wholly subsonic. · Small angles of attack · Linear variation of the side force, yawing moment and rolling moment with the angle of sideslip	· Subsonic speeds	· Subsonic speeds
Configurations	· Horizontal tail must be mounted to the body or no horizontal tail · No dorsal fins	· Single fin is located on top of the aircraft rear-body, and in the plane of symmetry. · The shape of the fin is assumed to approximate to a trapezium. · Bodies with circular or nearly-circular cross-sections · Small aspect ratios and close to zero twist due to assumption of constant induced sidewash · Dorsal fins can be implemented	· Dorsal fins and endplate effects of horizontal tailplane can be taken into account	
Remarks	· Build-up procedure · Includes interference effects of other vehicle components · Uses apparent-mass concept to deal with side wash and crossflow	· The predicted contributions include allowances for interference between the body, wing, tailplane, and fin and represent the effect of adding a fin. In particular, the additional load induced on the body by the fin is taken into account	· Includes interference effects of other vehicle components · DATCOM and ESDU consider only fuselage cross flow and the effect of the vertical position of the wing on the fuselage and of the wing dihedral on this cross flow, all at zero angle of attack. Fokker/E.Obert considers also different contributions to the cross-flow or sidewash at the tail	· Focus on turboprops · Synthesis of hundreds of numerical RANS simulations involving many different regional turboprop transport aircraft configurations and validated through wind tunnel tests

B

CONFIDENTIAL Figures for stability analysis

B.1. Stability derivatives: Tail-off components

Figure B.1: CONFIDENTIAL

Figure B.2: CONFIDENTIAL [redacted]

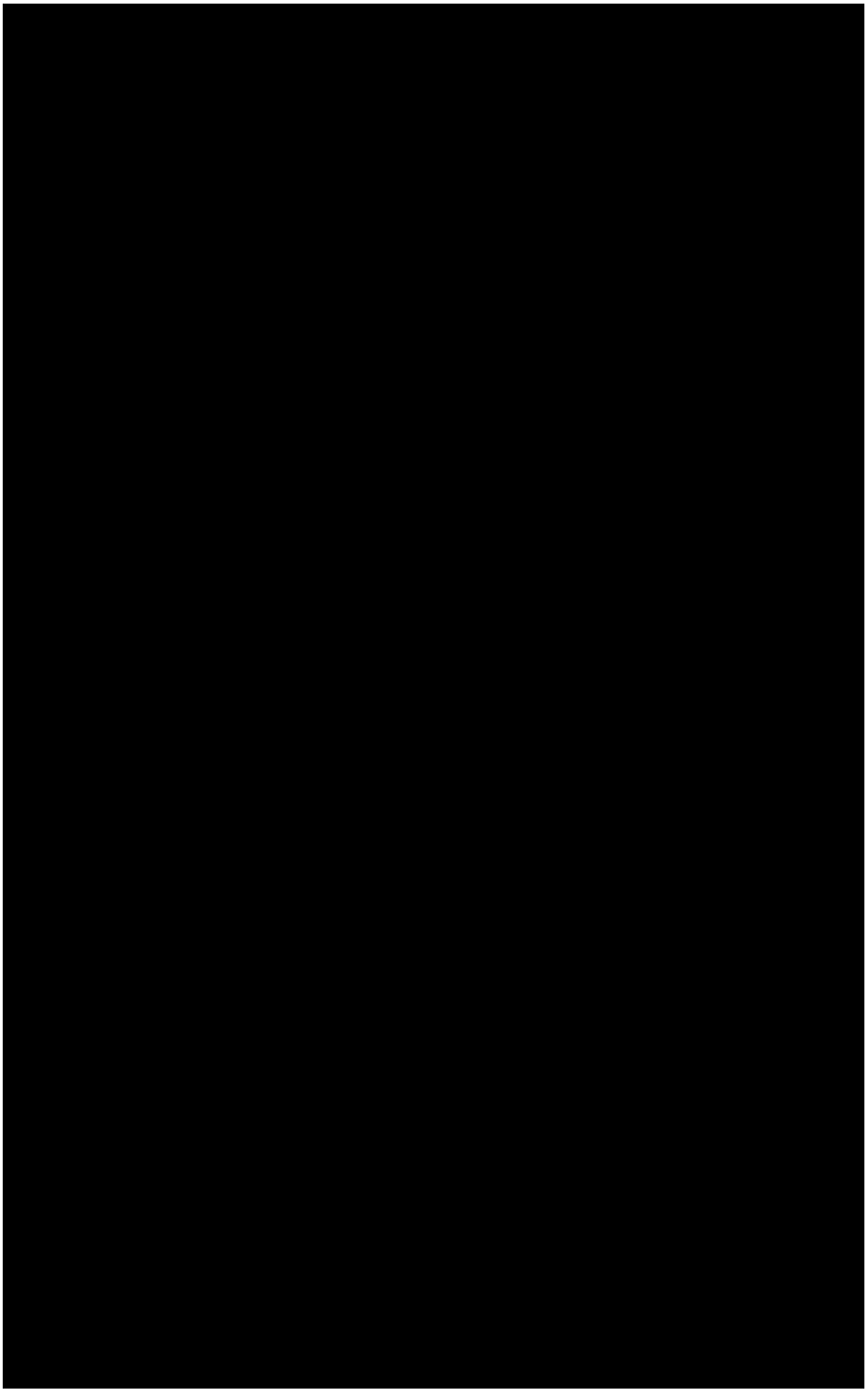

Figure B.3: CONFIDENTIAL [redacted]

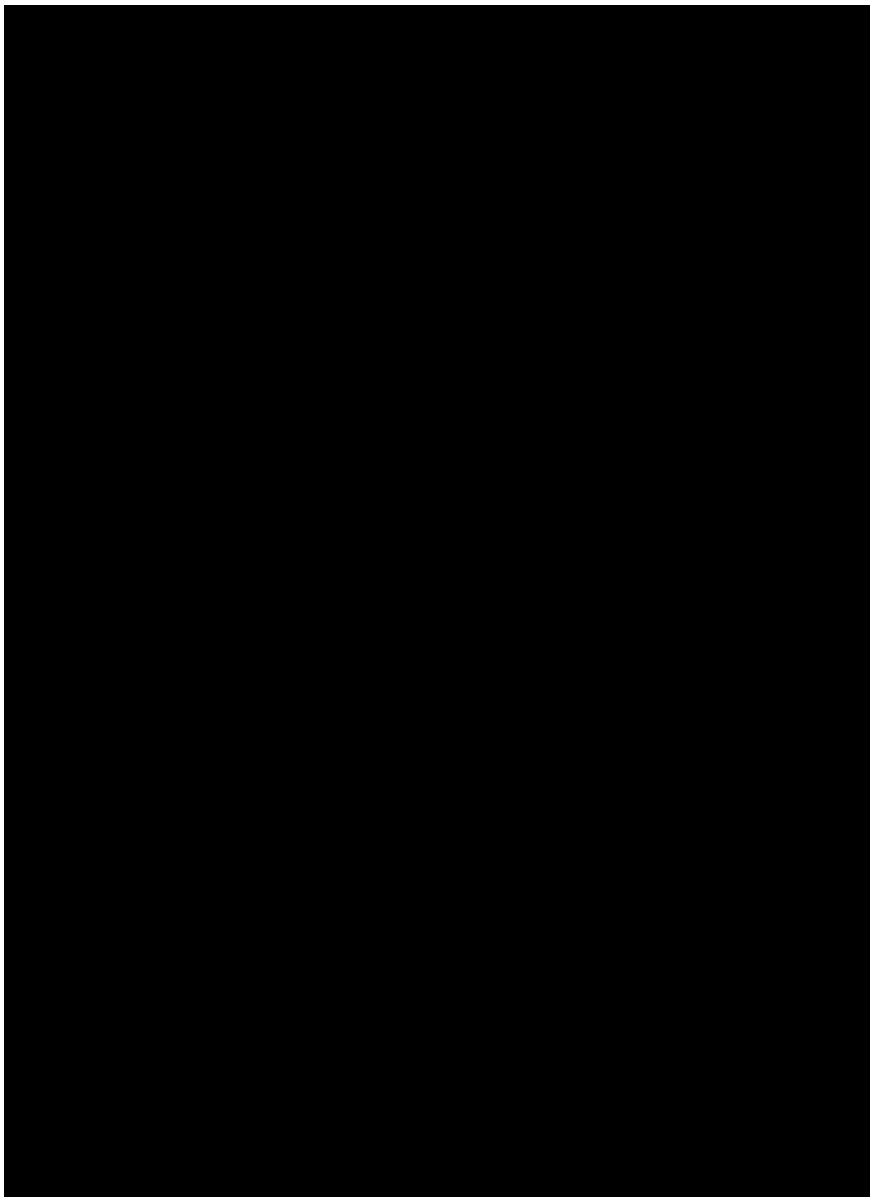

Figure B.4: CONFIDENTIAL [redacted]

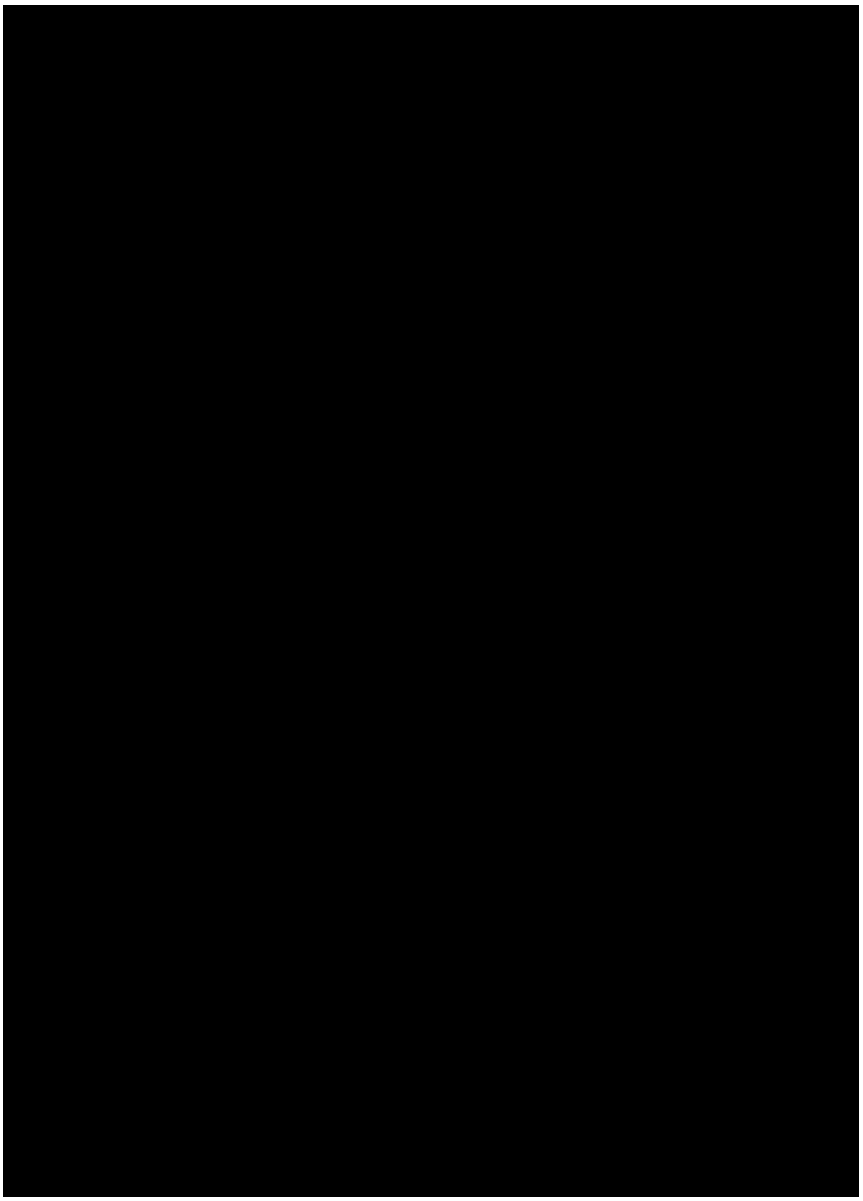

Figure B.5: CONFIDENTIAL [redacted]

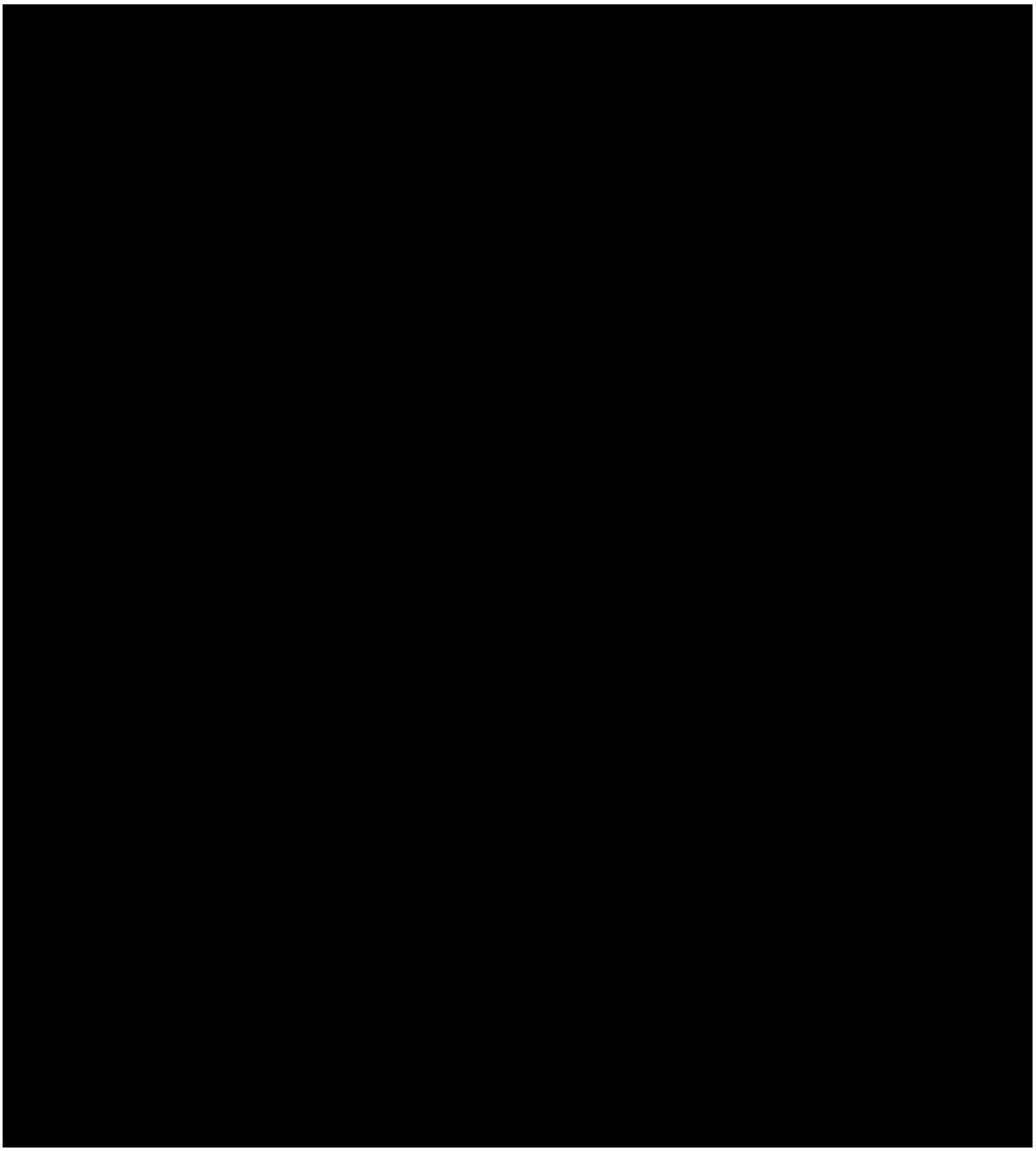

Figure B.6: CONFIDENTIAL [redacted]

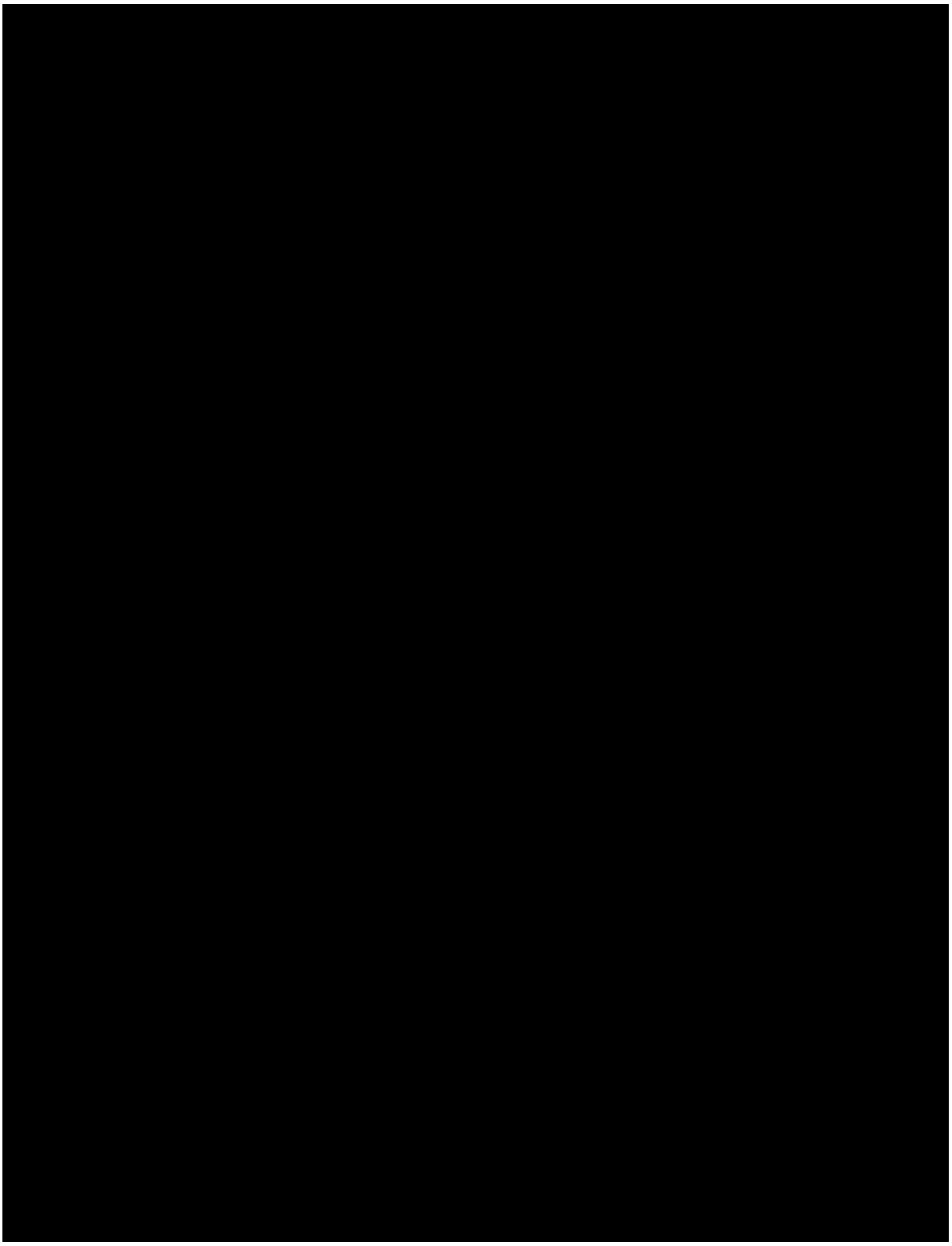

Figure B.7: CONFIDENTIAL [redacted]

B.2. Stability derivatives: Horizontal tail component

Figure B.8: CONFIDENTIAL [redacted]

B.3. Stability derivatives: Vertical tailplane lift curve slope

B.3.1. Effect of vertical tailplane geometry on vertical tailplane lift curve slope

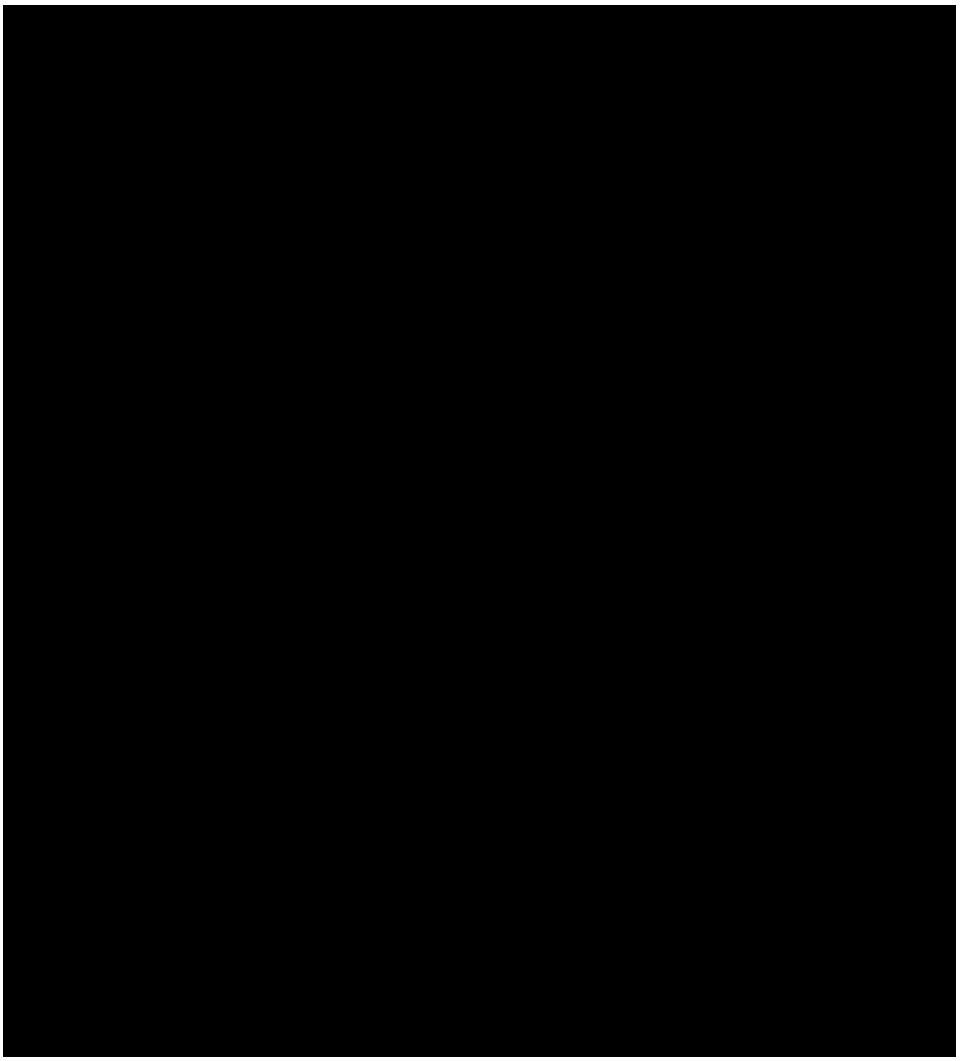

Figure B.9: CONFIDENTIAL [redacted]

Figure B.10: CONFIDENTIAL [redacted]

Figure B.11: CONFIDENTIAL [redacted]

B.3.2. Effect of dorsal fin on vertical tailplane lift curve slope

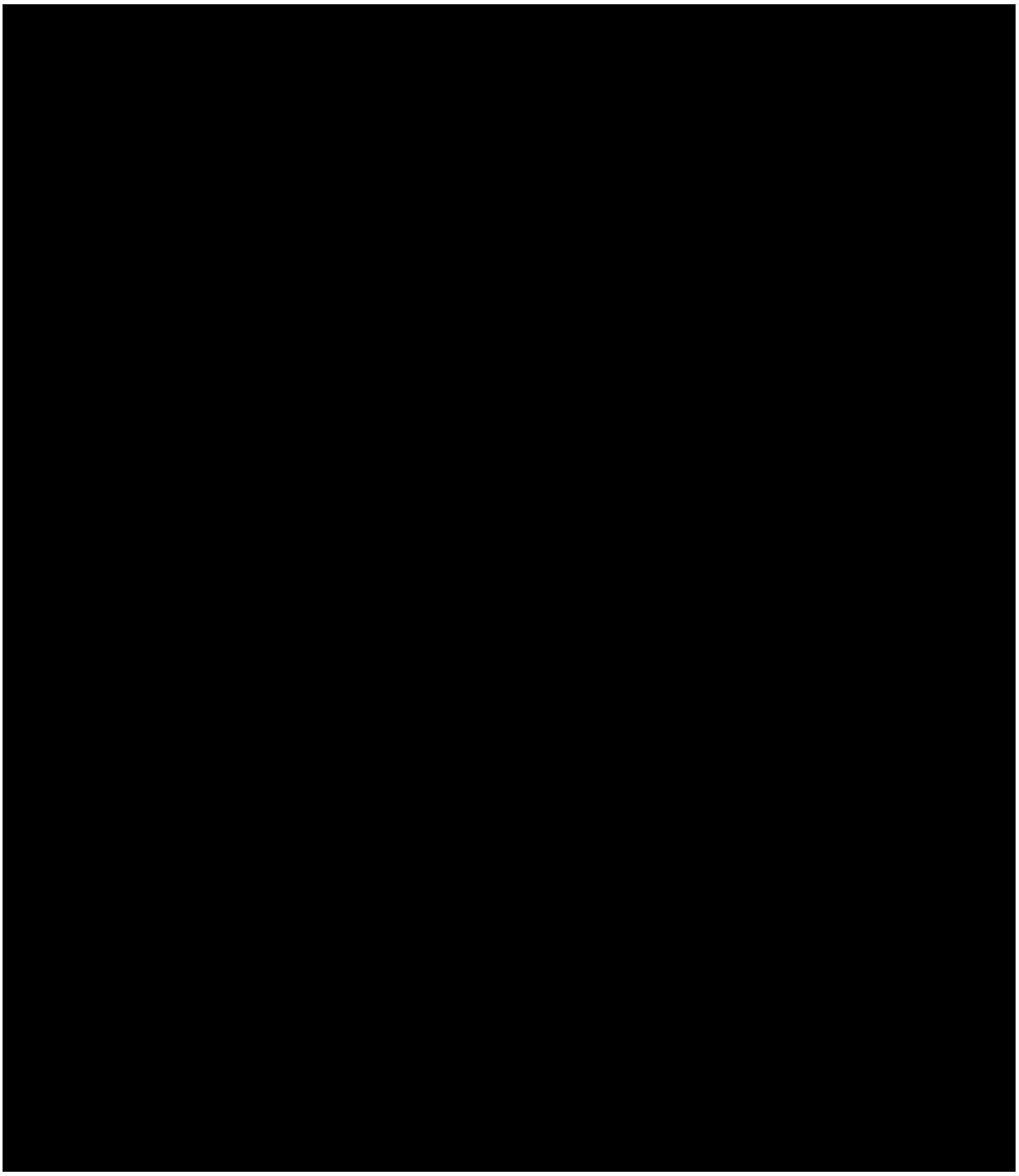

Figure B.12: CONFIDENTIAL [redacted]

Figure B.13: CONFIDENTIAL [redacted]

Figure B.14: CONFIDENTIAL [redacted]

Figure B.15: CONFIDENTIAL [redacted]

Figure B.16: CONFIDENTIAL [redacted]

B.3.3. Endplate effect on vertical tailplane lift curve slope

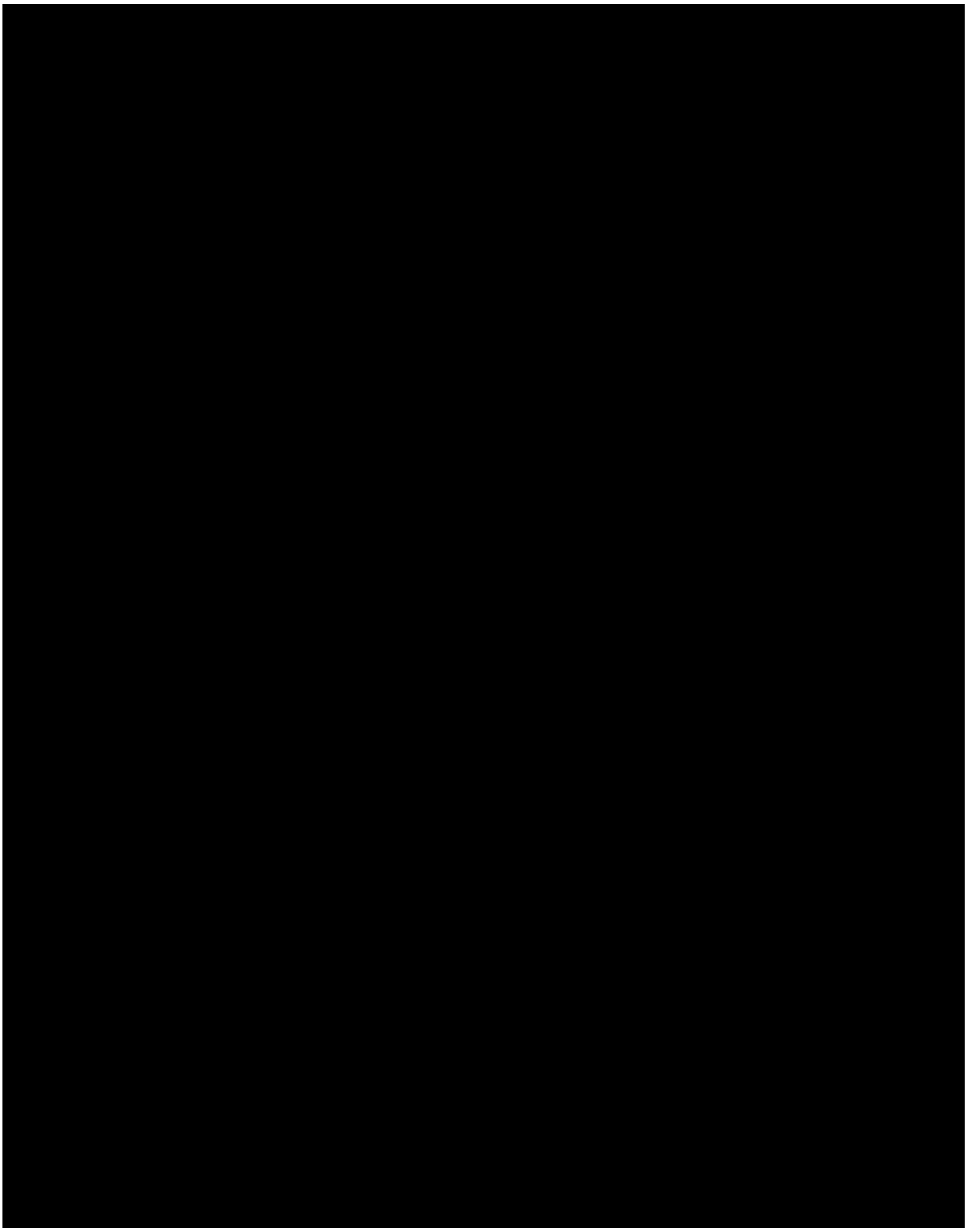

Figure B.17: CONFIDENTIAL [redacted]

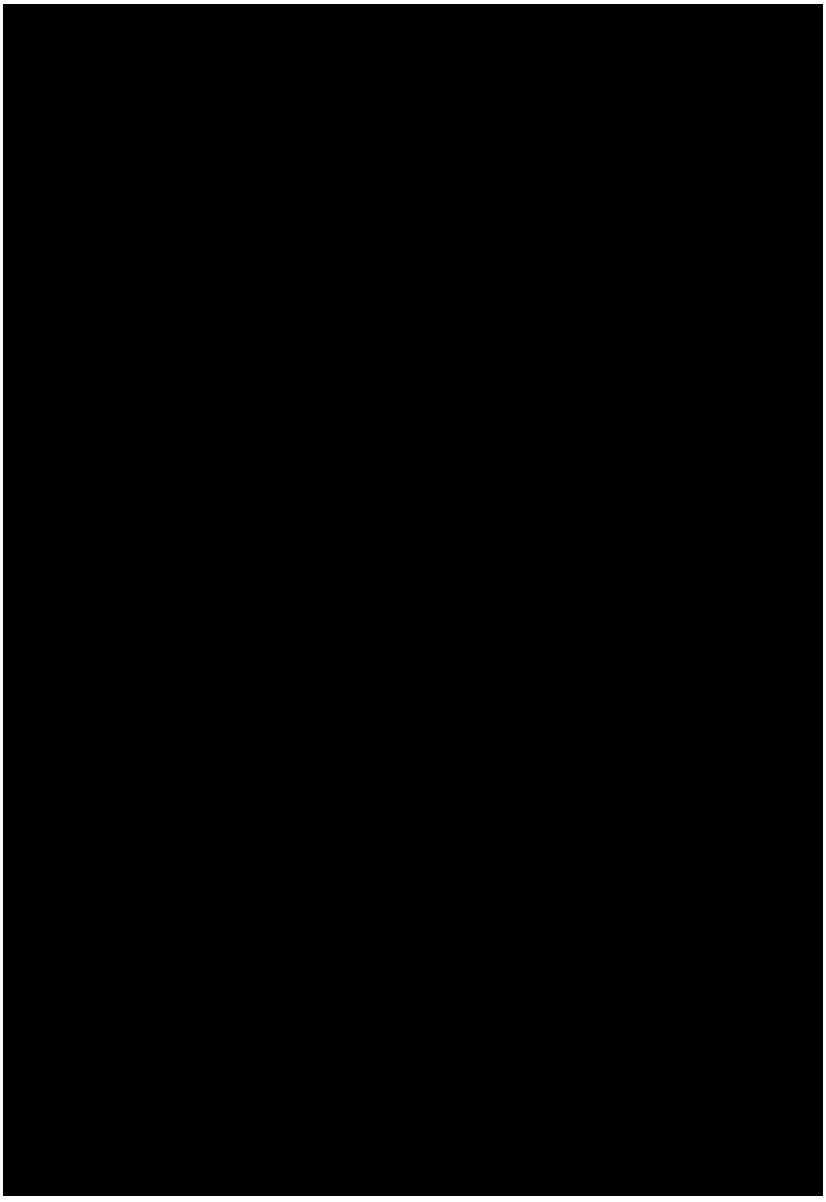

Figure B.18: CONFIDENTIAL [redacted]

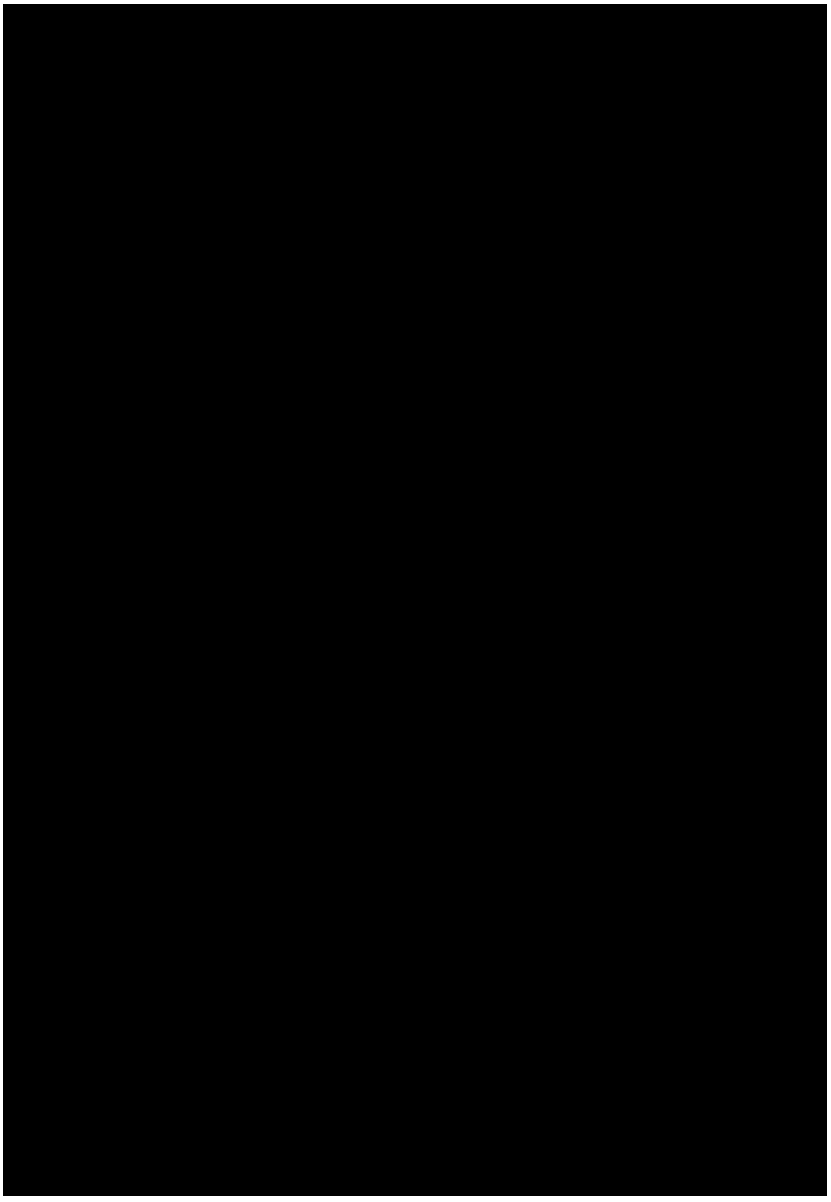

Figure B.19: CONFIDENTIAL [redacted]

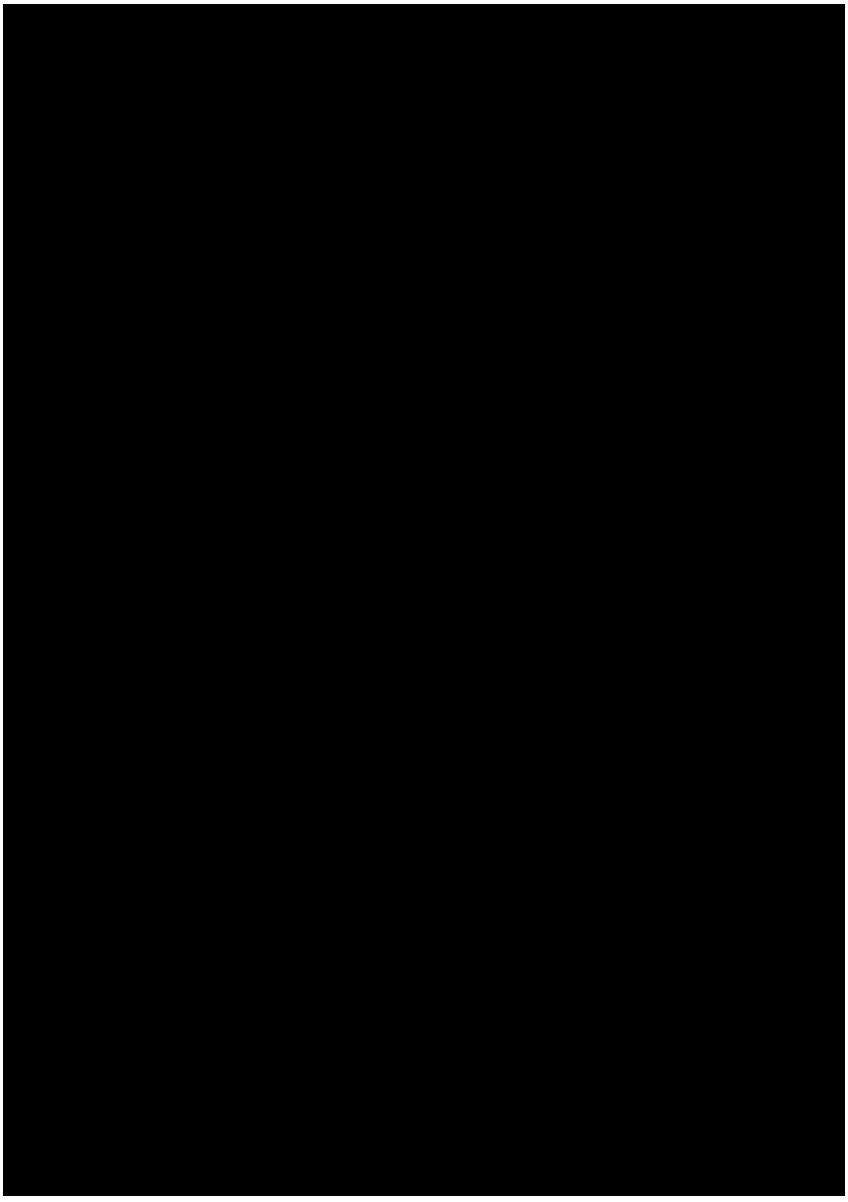

Figure B.20: CONFIDENTIAL [redacted]

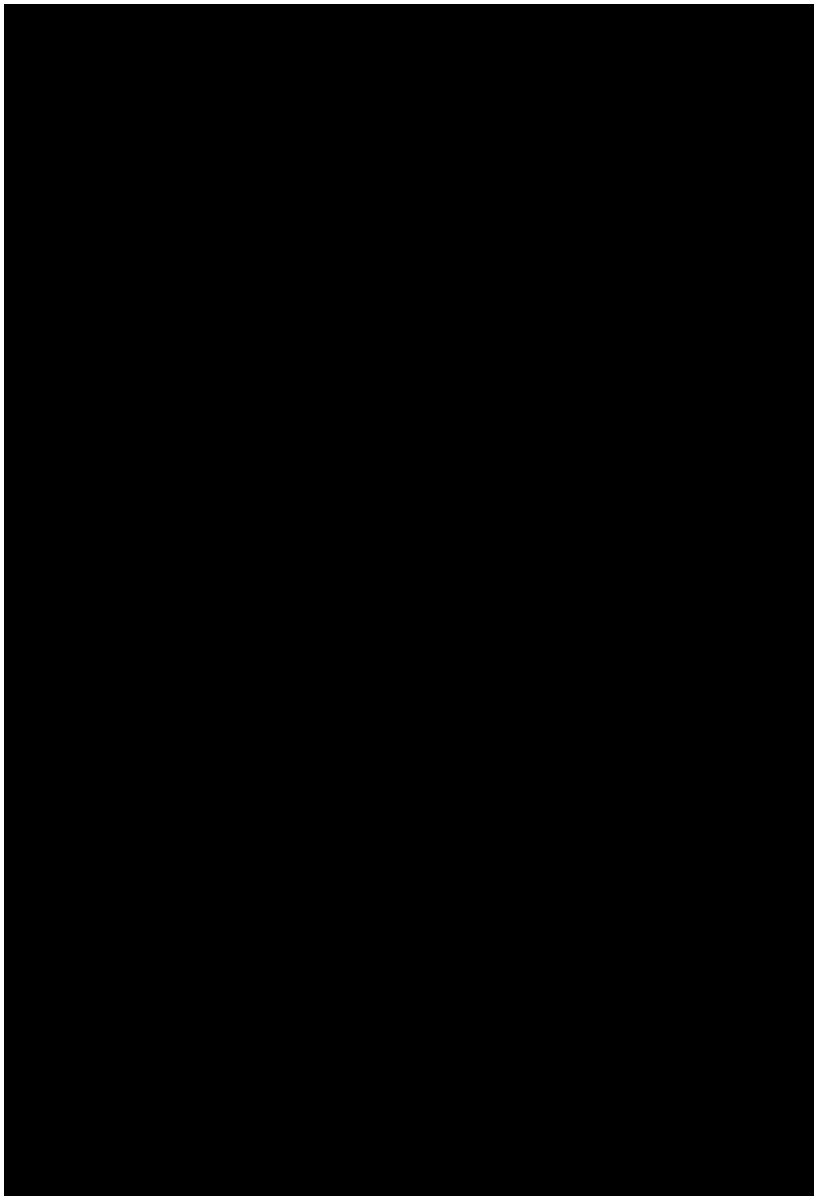

Figure B.21: CONFIDENTIAL [redacted]

Figure B.22: CONFIDENTIAL [redacted]

Figure B.23: CONFIDENTIAL [redacted]

Figure B.24: CONFIDENTIAL [redacted]

B.4. Stability derivatives: Sidewash

B.4.1. Effective-versus-free-stream dynamic pressure ratio and fuselage-vertical-tailplane lift carry-over effect

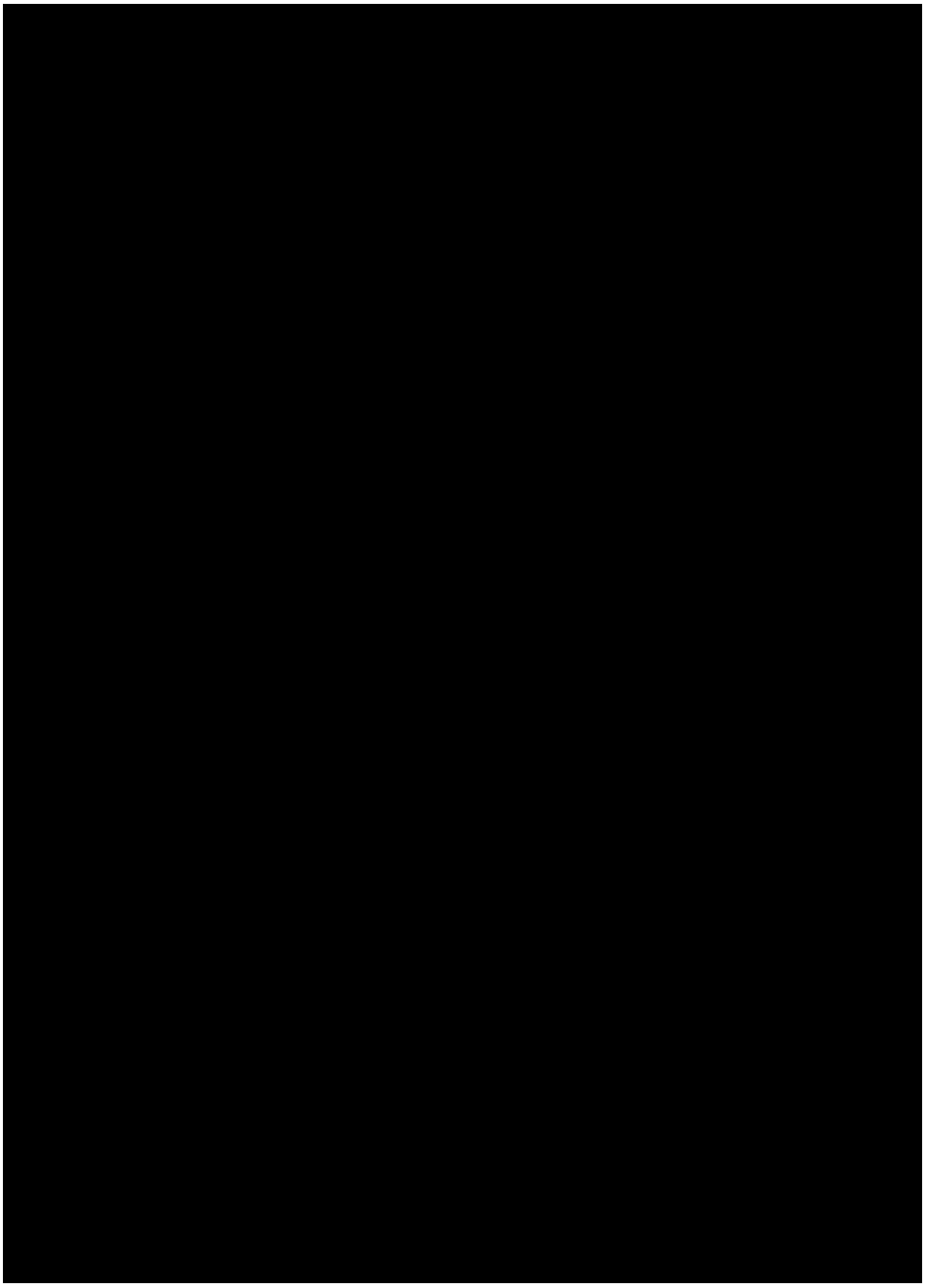

Figure B.25: CONFIDENTIAL [redacted]

B.4.2. Effect of fuselage-vertical-tailplane interference on sidewash

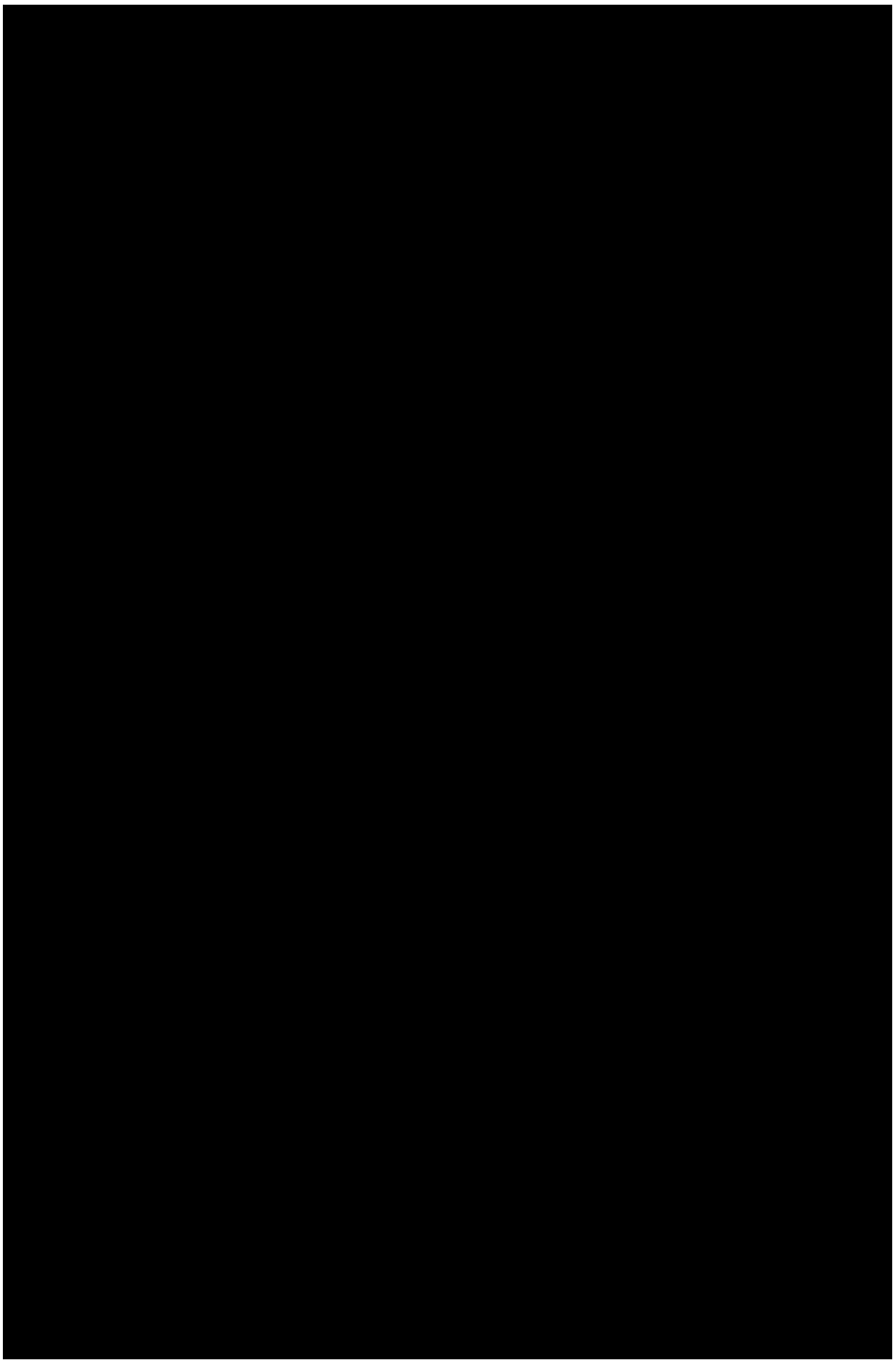

Figure B.26: CONFIDENTIAL [redacted]

B.4.3. Effect of wing-fuselage interference on sidewash

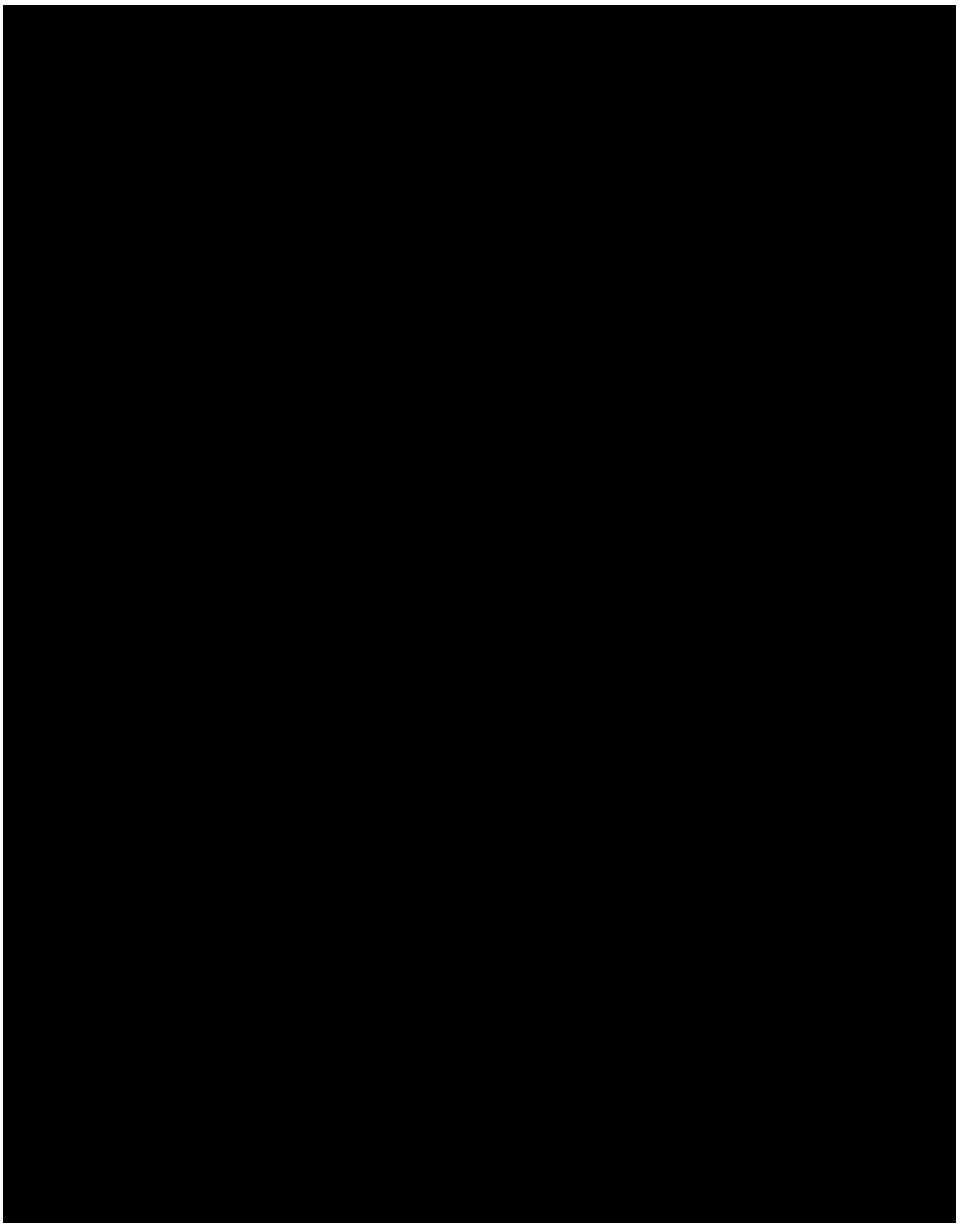

Figure B.27: CONFIDENTIAL [redacted]

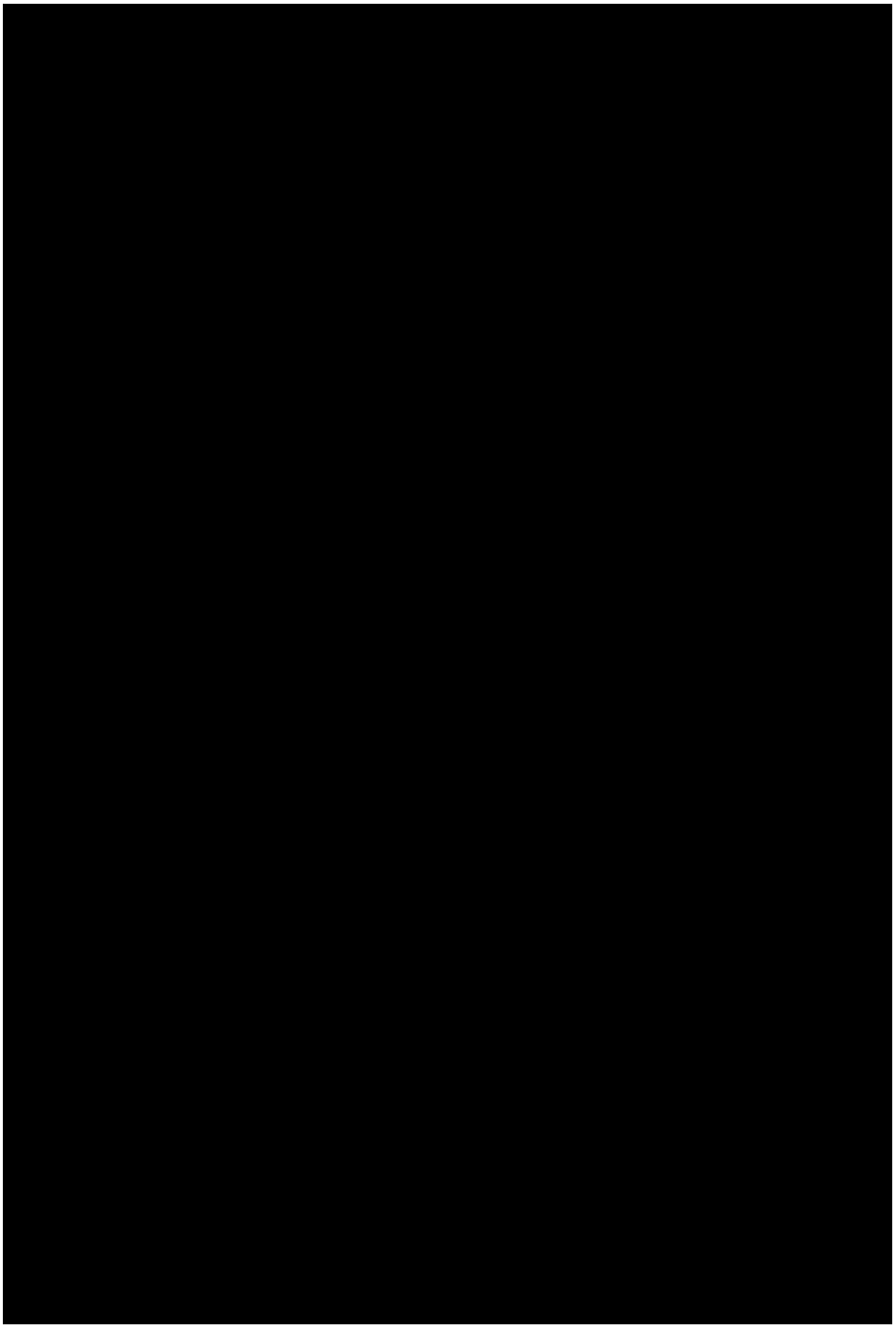

Figure B.28: CONFIDENTIAL [redacted]

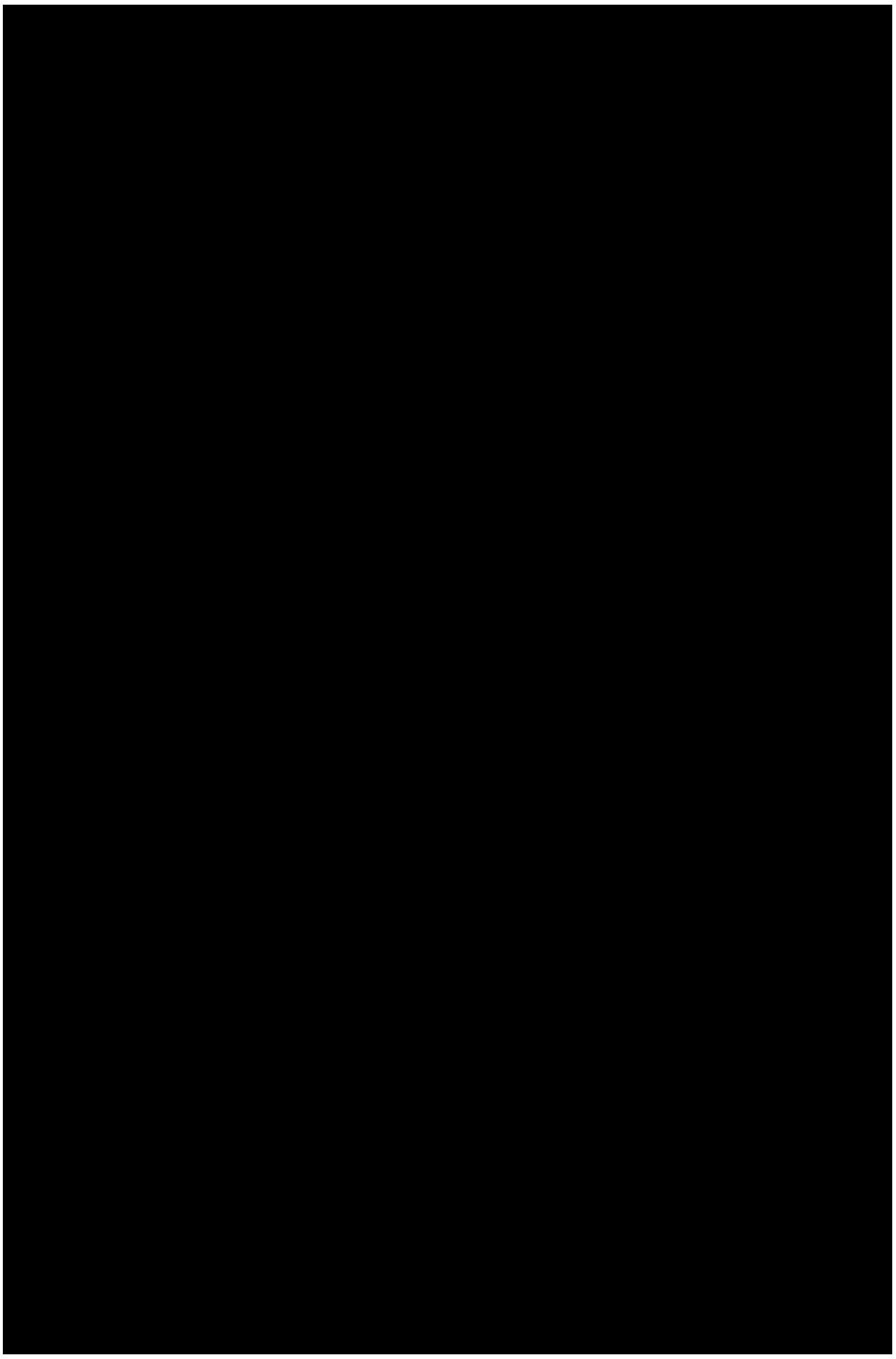

Figure B.29: CONFIDENTIAL [redacted]

B.4.4. Effect of wing dihedral and sweep on sidewash

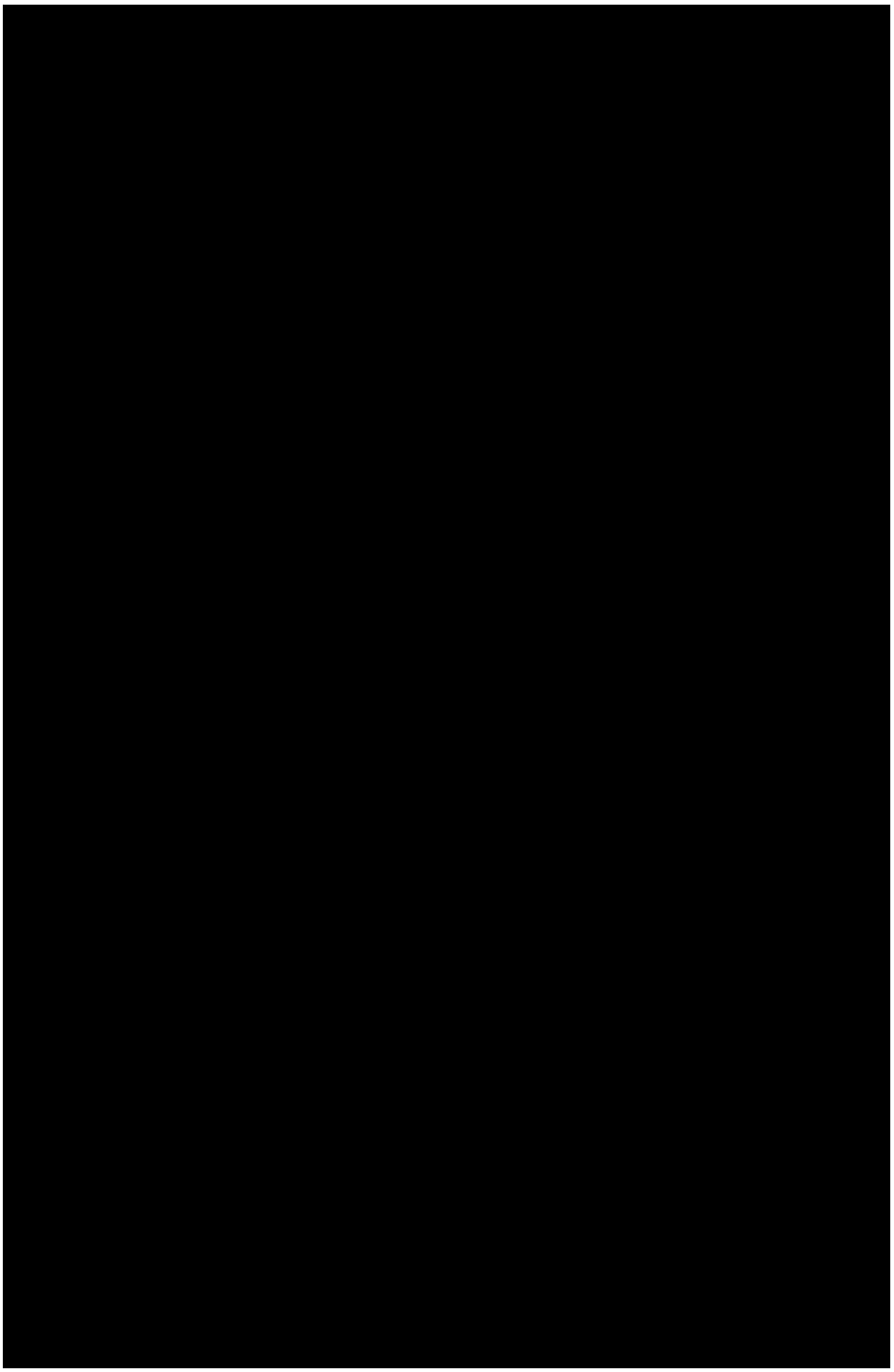

Figure B.30: CONFIDENTIAL [redacted]

B.4.5. Effect of wing flap deflection in landing position on sidewash

Figure B.31: CONFIDENTIAL [redacted]

B.4.6. Effect of engine nacelles on the wing on sidewash

Figure B.32: CONFIDENTIAL [redacted]

B.4.7. Effect of engine nacelles on the rear-fuselage on sidewash

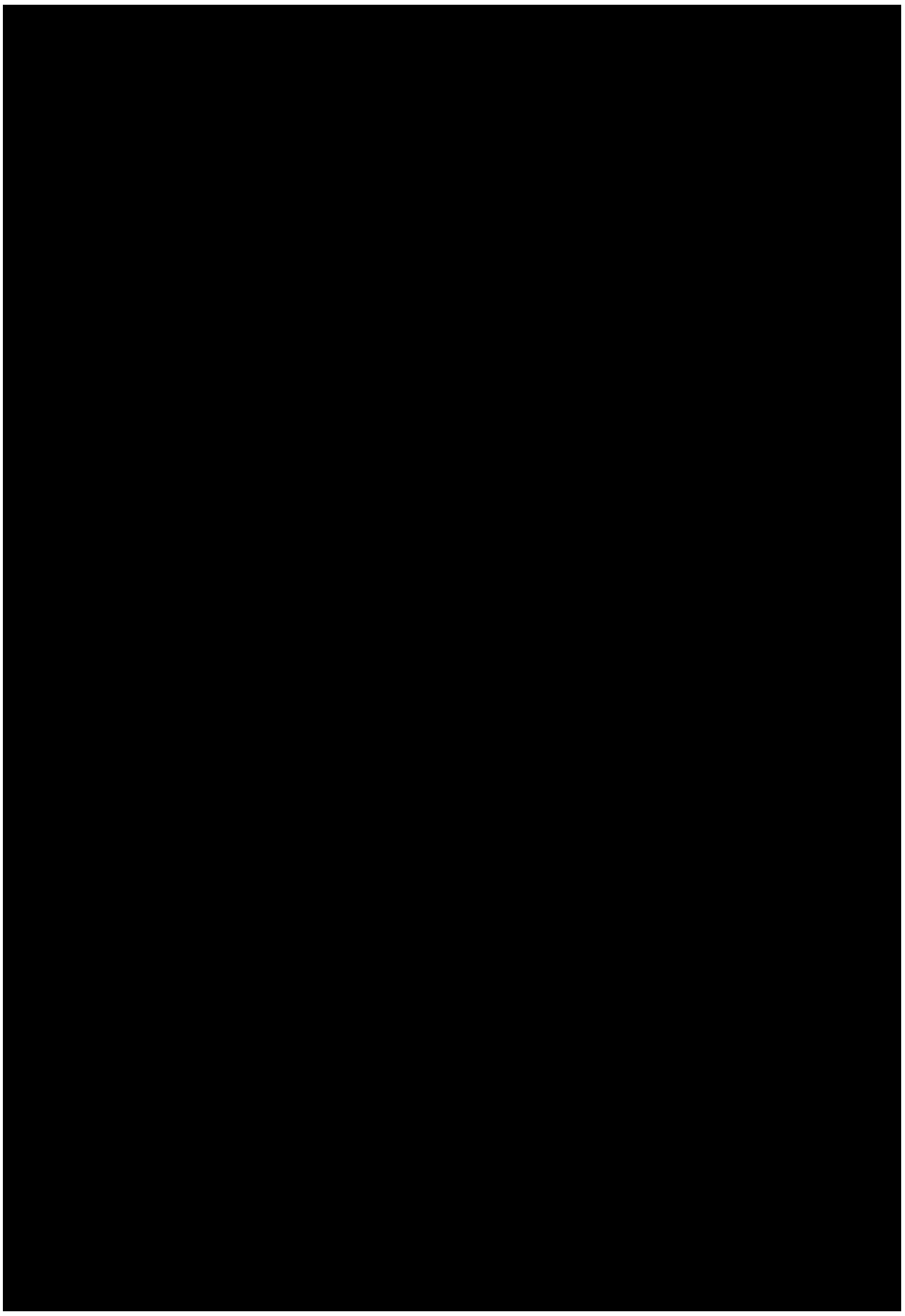

Figure B.33: CONFIDENTIAL [redacted]

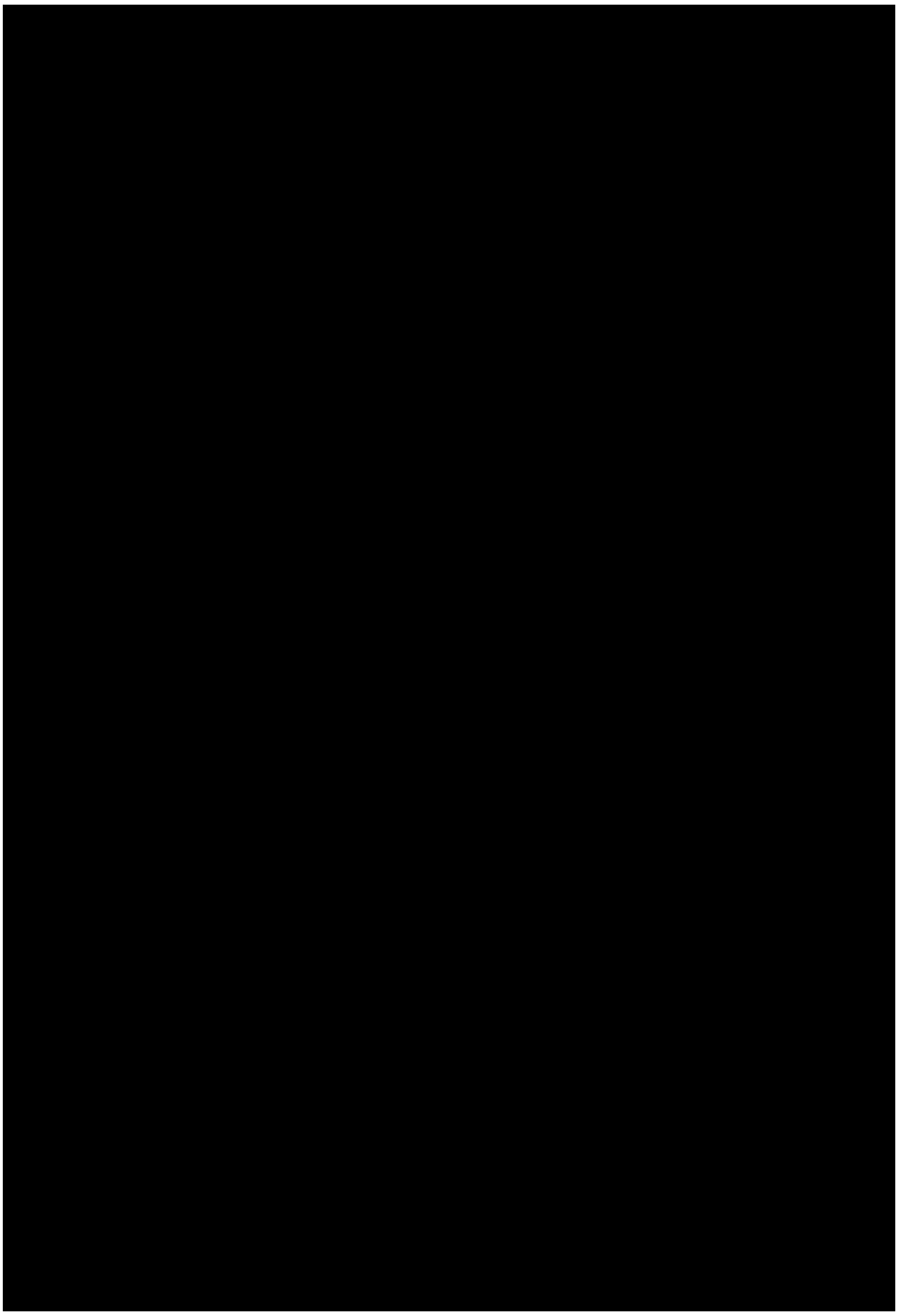

Figure B.34: CONFIDENTIAL [redacted]

Figure B.35: CONFIDENTIAL [redacted]

B.5. Control derivatives: Rudder

Figure B.36: CONFIDENTIAL [redacted]

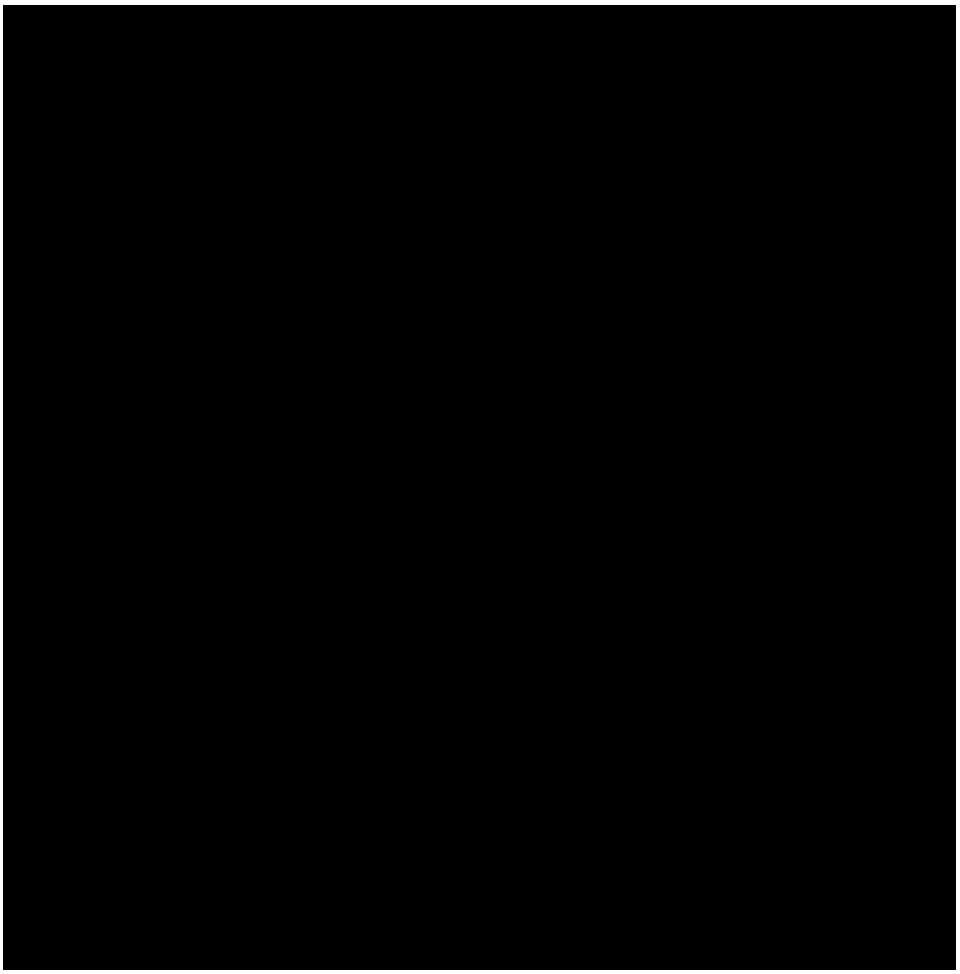

Figure B.37: CONFIDENTIAL [redacted]

B.6. Control derivatives: Aileron

Figure B.38: CONFIDENTIAL [redacted]

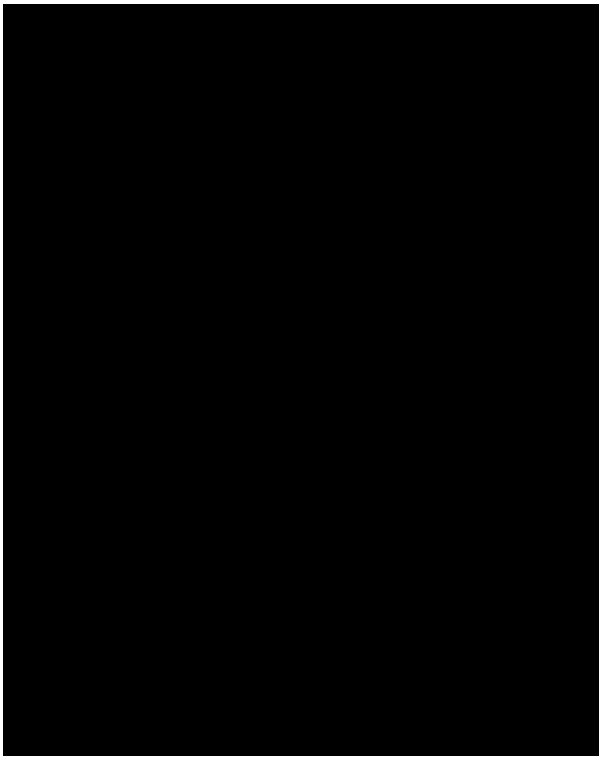

Figure B.39: CONFIDENTIAL [redacted]

C

Timeline of laminar flow control research

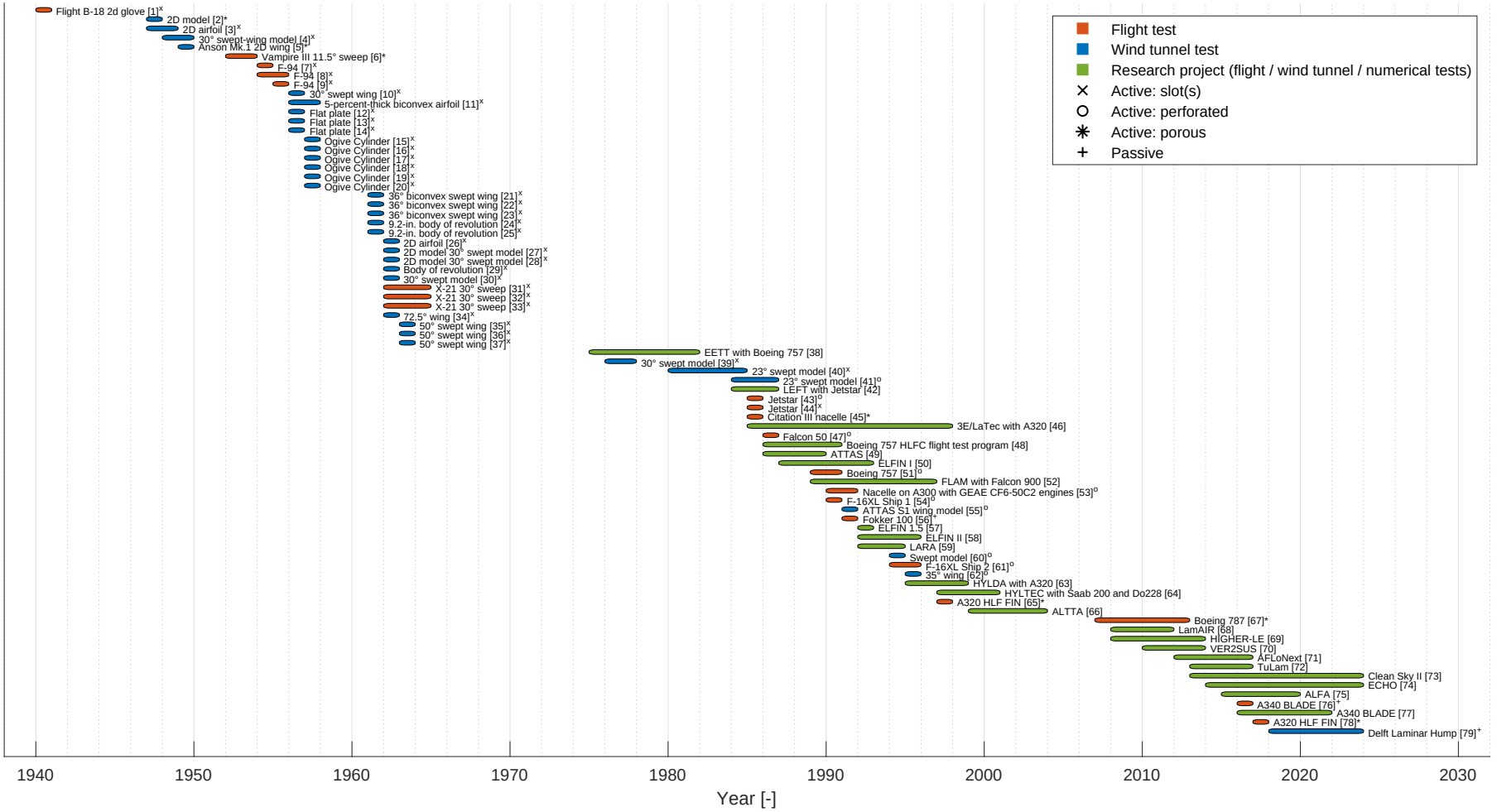

Figure C.1: LFC research: Timeline based on [10][36][59][8],[60] (Note: research project is a collaborative research which may include flight, wind tunnel and/or numerical tests. Some of the flight and wind tunnel tests shown in the figure are also part of the research projects shown in the same figure).

D

Laminar flow control in modern subsonic transport aircraft

D.1. Boeing 757 - HLFC

In 1990 Boeing performed flight tests with a Boeing 757 with an HLFC system on the wing, shown in Figure D.1. The HLFC system consists of a perforated titanium leading edge through which suction can be applied. In addition, a Krueger flap is placed in front, visualized in Figure D.2. The Krueger flap is of importance since it is not only there for high lift purposes, but it also houses the thermal anti-icing system as well as being an insect shield [40][55][56][10]. This solves some major problems with HLFC suction devices since they tend to clog due to insects and debris and do not have room for anti-icing systems.

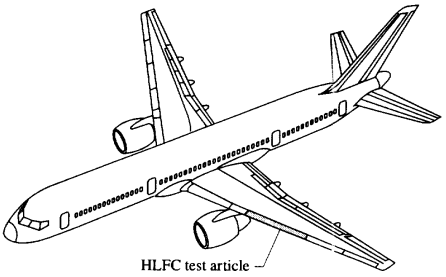

Figure D.1: Boeing 757 with HLFC system on wing [10].

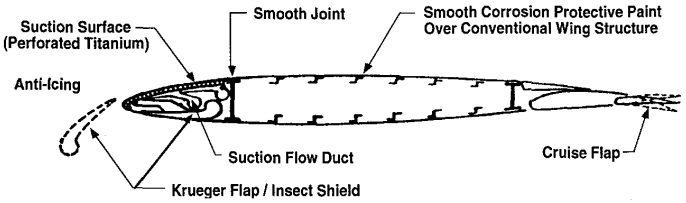

Figure D.2: Airfoil section with HLFC system and Krueger flap [56].

The actual suction system is seen in Figure D.3 shows that it consists of a perforated outer skin and an inner panel sandwich, with stringers in between. The spaces in between the stringers form the flutes (suction chambers). The flutes are connected with spanwise ducts to a pump providing the suction [40][55][10]. Figure D.4 show the laminar and turbulent areas for a specific set of flight conditions obtained with hot film sensors, which proves laminar flow is obtained over a large part of the wing. In addition to hot-film sensors, pressure taps, wake survey probes, attachment line flow sensors, and infrared transition detection systems were used to obtain data during flight tests. Based on this data it was found that a local drag reduction of 29% could be obtained, which equates to a 6% overall drag reduction of the aircraft [56].

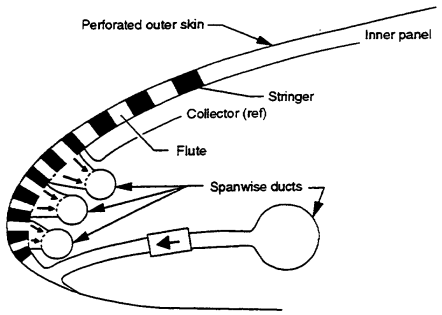

Figure D.3: Suction system [55].

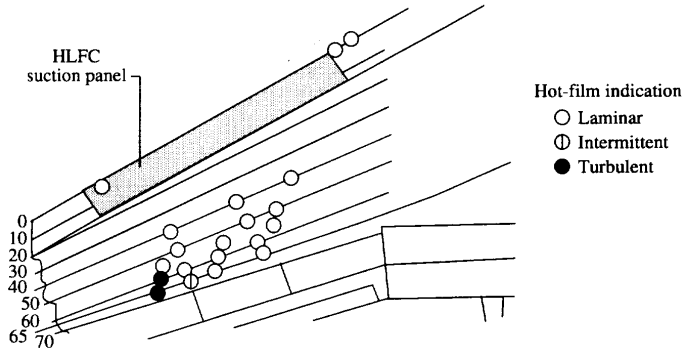

Figure D.4: Laminar and turbulent areas on wing at M=0.82, altitude=38600 ft, and C_L=0.48 [10].

D.2. Fokker 100 - Laminar flow glove

A passive NLF system was tested during the Fokker 100 flight tests in 1992 using a natural laminar flow glove. The tests were part of the European Laminar Flow Investigation (ELFIN) project. The glove is a NLF wing shape, constructed by fitting a composite (foam and glass fiber) layer around the existing wing with fairings on either side, as shown in Figure D.5a, Figure D.5b, and Figure D.5c. The latter figure also shows a carbon fiber heater mat to create a heat gradient, which was required to better visualize the laminar and turbulent flow, when using infrared cameras [32]. The flight test conditions were at a Reynolds number between $17 - 30 \cdot 10^6$ and a Mach number between $0.50 - 0.80$ [59].

(a) Fokker 100 with glove [87].

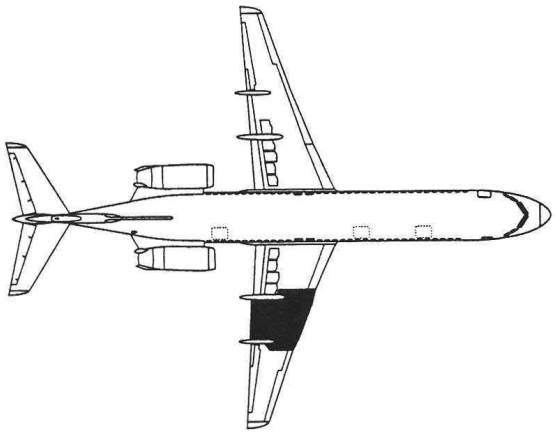

(b) Glove location on Fokker 100 [32].

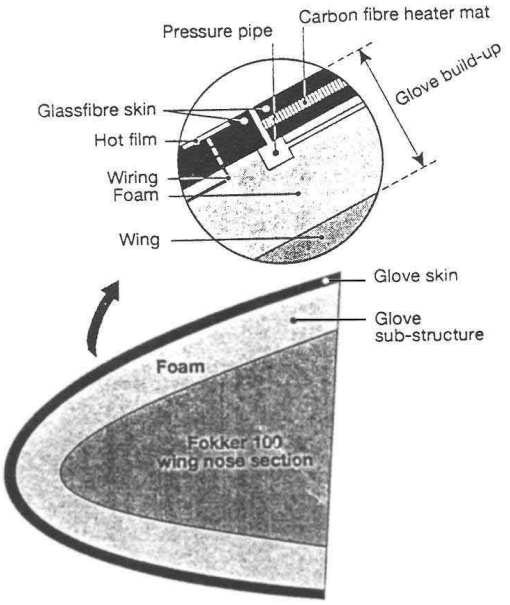

(c) Glove build-up [32].

Figure D.6 shows the effect of the glove on the pressure distribution of the wing, creating a much flatter pressure distribution and more gradual pressure gradient. This should enhance laminar flow, however, during flight testing, it was found that the initial glove did not result in the expected transition delay. The reason for this was surface imperfections (waviness), although being well within surface quality requirements for commercial aircraft. A refinished glove was made and the transition delay was increased by 10 to 15%, as seen in Figure D.7. Overall, it was concluded that for laminar flow wings to be effective, they require proper NLF aerodynamic design, and a high surface quality [32][60].

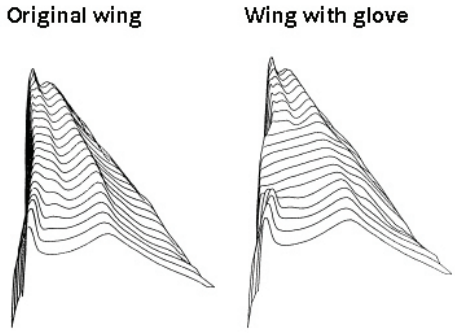

Figure D.6: Pressure distribution of wing with and without glove [8].

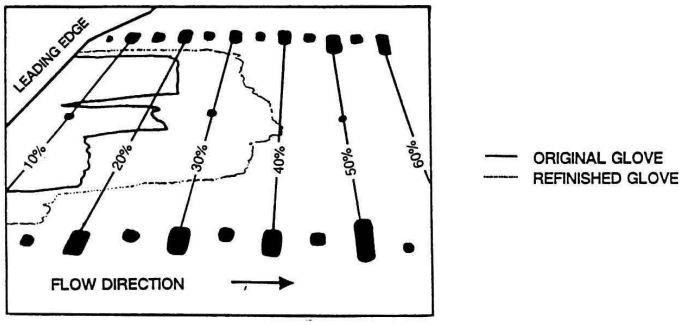

Figure D.7: Transition location original and refinished glove [32].

D.3. Airbus A320 - Hybrid laminar flow fin

A major effort was made to implement a HLFC suction system in the vertical stabilizer of an Airbus A320, under the name of the A320 HLF fin project. Numerous flight tests and configurations have been tested. Starting in 1998 with flight tests as part of the Laminar Technology (LATEC) program, which was part of the Energy, Economy, Environment (3E) Technology Plan. At the same time, additional tests were performed under the Hybrid Laminar Flow Demonstration on Aircraft (HYLDA) program [44][57]. Later a simpler version of the suction system was developed and in 2018 more flight tests were performed as part of Application of Hybrid Laminar Flow Technology on Transport Aircraft (ALTTA) program [43][41][58][42]. For all images used in this section, the left images refer to the 1998 flight tests and system, and the right images to the 2018 version. Figure D.8 and Figure D.9 show the respective airplanes with the hybrid laminar flow fin installed, shown in more detail in Figure D.10 and Figure D.11.

Figure D.8: Airbus A320 with HLF fin during 1998 flight tests [8].

Figure D.9: Airbus A320 with HLF fin during 2018 flight tests [42].

Figure D.10: Hybrid laminar flow fin during 1998 flight tests [41].

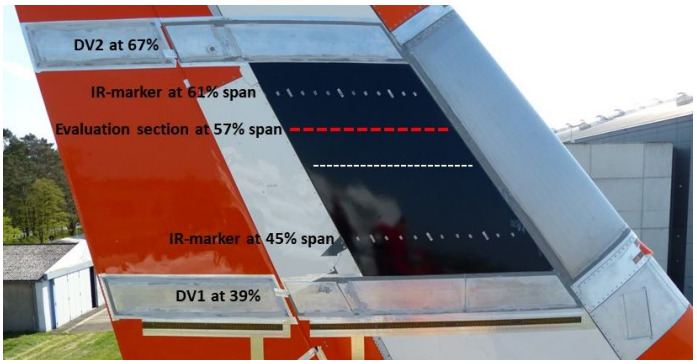

Figure D.11: Hybrid laminar flow fin during 2018 flight tests [42].

The hybrid laminar flow fin uses a combination of wing shaping (NLF wing) and suction at the leading edge through a porous wall [41]. This concept is the same for the 1998 and 2018 tests, however, the suction systems differ. Figure D.12 shows the suction system used in 1998. It consists of porous panels with laser-drilled holes. The porous leading edge extends up to 20% of the chord length. Inside the leading edge suction chambers are located and are connected via ducts, tubes, and valves to a pump. The Gaster-bump at the bottom is implemented to create a stagnation point to divert flow disturbances coming from the fuselage and to start a laminar boundary layer [57]. An actual photo of the system is shown in Figure D.14, which shows that the chambers along the porous skin and the ducting take up a lot of space, and are rather heavy and complex. With the 1998 flight tests, it was proven that laminar flow could be obtained with such a system. However, they did not provide an overall gain due to its weight and complexity. Because of this, a new suction system was designed for the 2018 flight tests, shown in Figure D.13. This system consists of a titanium porous panel with an inner sheet relatively close to the outer one with stringers in between, creating very small chambers. The empty volume within the inner sheet is the suction duct, which is connected to a pump. Figure D.15 shows the new suction system, which is significantly smaller and simpler. The main difference with the 1998 system is that the suction chambers are a lot smaller and thinner and that the complex and heavy suction

ducts, tubes, and valves are removed. This does take away the possibility of customizing the suction distribution. However, it was found that the reduction in weight and complexity outweighed this [41].

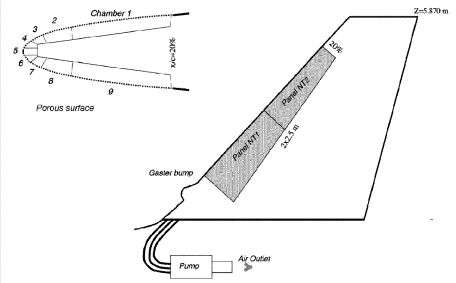

Figure D.12: Schematic of suction system during 1998 flight tests [57].

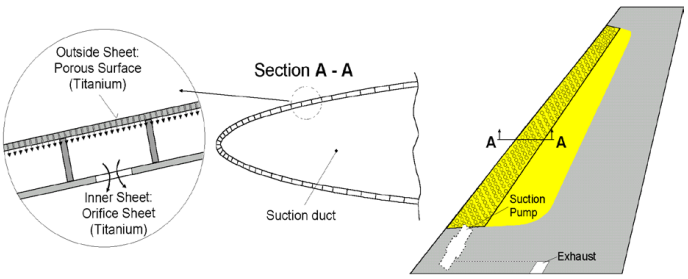

Figure D.13: Schematic of suction system during 2018 flight tests [41].

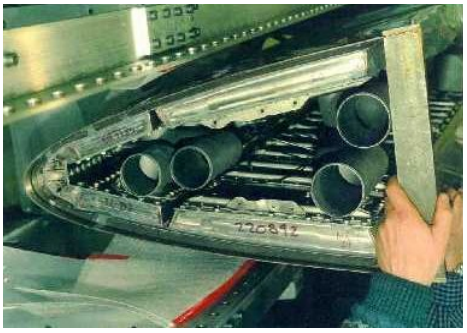

Figure D.14: Suction system during 1998 flight tests [41].

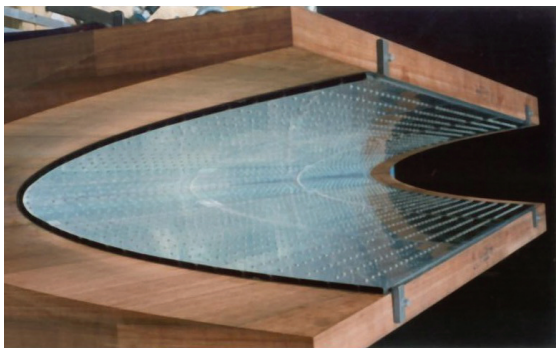

Figure D.15: Suction system during 2018 flight tests [8].

The 1998 tests found that transition roughly occurred between 24 and 52% of the chord [57]. For the 2018 tests it was found that the transition location lies between 36.5 to 50% [42], based on the limited data that is available in literature. For both tests, the results are very dependent on flight conditions, such as Mach number, altitude, sideslip angle, and rudder angle. However, the transition is still delayed significantly [42]. Nevertheless, there are still some problems left to be able to implement this system in commercial aircraft. For example, the problems of contamination (insects, debris, etc.) and the combining of the system with anti-icing systems still need to be tackled [8].

D.4. Boeing 787 - Passive suction system

A very recent development is a passive suction system tested on the Boeing 787. Not a lot of information on this device is publicly available, but still enough to discuss. This passive suction system consists of a special door located on the horizontal- and vertical tailplanes as seen in Figure D.16 and Figure D.17[1]. This door can be opened and, via an internal duct, it creates a low-pressure zone behind the porous wall at the leading edge. In addition to suction, the door can also be used as a scoop to create a high-pressure zone behind the porous wall, resulting in blowing. The suction is used to delay the transition, whilst the blowing is suggested to be used to clean the leading edge and pores[2,3]. Although the suction system is passive, the door must be powered by an actuator, making the system not completely passive [36]. The device was patented in the EU by Boeing in 2010, which provided some drawings on how the device works. This is shown in Figure D.18. Figure D.19[4] shows the device implemented on the tail of a Boeing 787, with the porous leading edge in green and the door at the bottom of the black area. Apart from the general mechanism, it is unknown how much the transition is delayed with this system and how large the reduction in drag is.

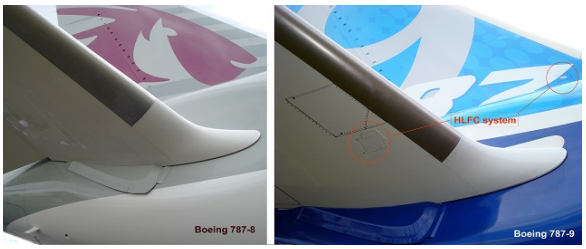

Figure D.16: Tail with and without the doors[1].

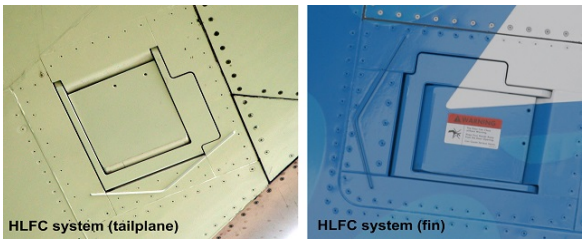

Figure D.17: Door for passive suction system[1].

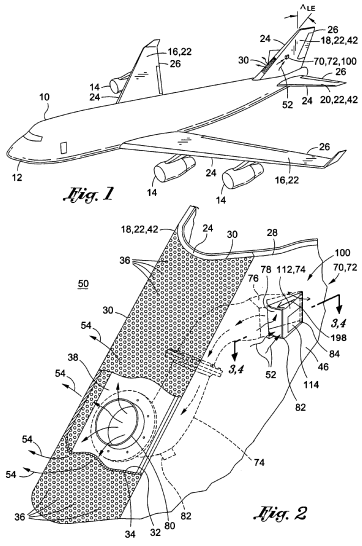

Figure D.18: Patent drawing of door assembly for laminar flow control system [88].

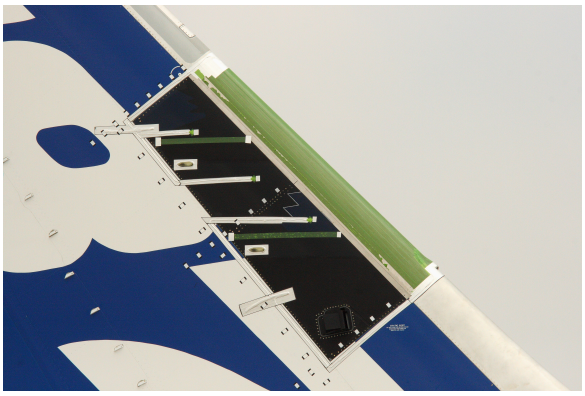

Figure D.19: Passive suction system on vertical tail[4].

[1]Kingsley-Jones, M. (2014). FARNBOROUGH: Aero secrets of Boeing's new Dreamliner. Retrieved January 28, 2024, from https://www.flightglobal.com/farnborough-aero-secrets-of-boeings-new-dreamliner/113955.article

[2]Unknown Stack Exchange user. (2021), What is the purpose of the tiny doors used by the 787's laminar control?, Retrieved January 28, 2024, from https://aviation.stackexchange.com/questions/89513/what-is-the-purpose-of-the-tiny-doors-used-by-the-787s-laminar-control

[3]Lustublog. (2017). 787 épisode 2 : génialement simple. Retrieved January 28, 2024, from https://lustublog.com/2017/11/13/787-episode-2-genialement-simple/

[4]KSBD Photo. (2011). "Boe 03" B787-8 N787BX. Retrieved January 28, 2024, from https://www.flickr.com/photos/ksbdphotos/5813364256

D.5. Airbus A340 - BLADE

A very recent development is the Breakthrough Laminar Demonstrator in Europe (BLADE) project as part of the Cleansky II[5]. The BLADE project is used to investigate NLF wings at near full-scale, continuing on the Fokker 100 flight tests. The BLADE uses NLF panels, which are basically small-sized NLF wings. To test these NLF panels, they are placed at the tip of a so-called parent wing as seen in Figure D.20. This was done so that minimal alterations to the test aircraft were required, but the flight conditions and envelope still represent short-medium range aircraft. The NLF panels are designed with several fairings as visualized in Figure D.21. The wing aerodynamic fairing is used to minimize interference from the parent wing and to achieve more laminar flow on the inboard side of the panel. The wing tip pod helps to achieve laminar flow as far outboard as possible. The first flight test was performed in 2017[6]. During the flight test infrared images were made to determine the transition location as seen in Figure D.22. The BLADE project not only assesses the performance NLF wings but also the impact of manufacturing techniques. To test this, a small difference between the right and left NLF panel is made in terms of cover panels (skin construction). The right panel uses a leading edge connected to a separate upper cover panel, which is the common method used in the industry. The left panel uses a single continuous leading edge and upper cover panel. Also, an effort was made to investigate the impact of surface imperfections on NLF wings. Forward-facing steps, aft-facing steps, discrete imperfections, and waviness were all tested. It was found that all of these surface imperfections have a considerable impact on the transition location and laminar flow [89].

Figure D.20: Airbus A340 with BLADES [89].

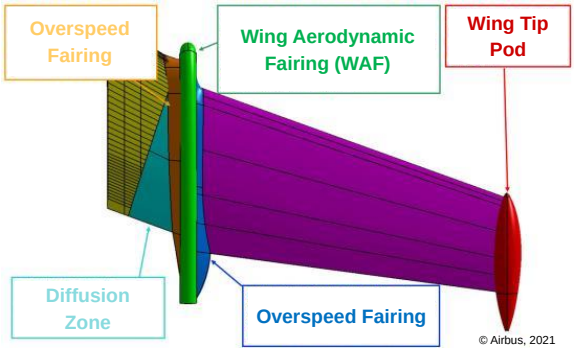

Figure D.21: BLADE design [89].

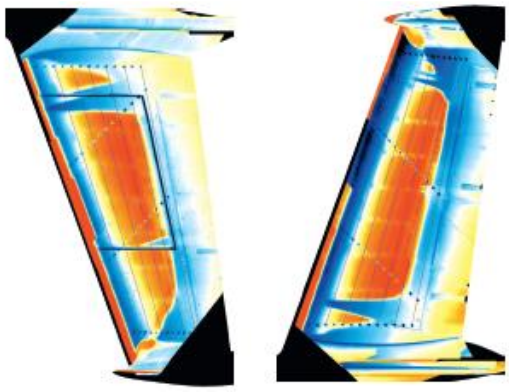

Figure D.22: Infrared images of BLADE from the flight tests [89].

[5]Clean Aviation. (2022). BLADE Flight Test Data results, analysis and Exploitation Conclusive workshop. Retrieved January 28, 2024, from https://www.clean-aviation.eu/blade-flight-test-data-results-analysis-and-exploitation-conclusive-workshop

[6]Airbus. (2017). Airbus' "BLADE" laminar flow wing demonstrator makes first flight. Retrieved January 28, 2024, from https://www.airbus.com/en/newsroom/press-releases/2017-09-airbus-blade-laminar-flow-wing-demonstrator-makes-first-flight

E

Analysis of transition settings in XFoil

Having established the M3J airfoil can be modeled with XFoil in subsection 5.1.1, the full M3J wing should also be simulated with Q3D (and thus XFoil). To see the aerodynamic effect of the hump on the full M3J wing, an analysis was performed by varying the x_{tr}/c. The M3J wing simulated in this section uses the dimensions shown in Figure 5.1, which has a constant chord length of 1.2728 m (no sweep or taper). As Q3D analyzes airfoil sections along the span of the wing, the x_{tr}/c will be set the same for all of these airfoil sections on both the pressure- and suction side. The drag- and lift coefficients found with Q3D are seen in Figure E.1 and Figure E.2. The drag coefficient reduces when the transition location is moved downstream, as expected, but after a slight dip around 0.75 x/c, it plateaus at around 0.8 x/c, which needs to be further investigated. The lift coefficient stays constant throughout all x_{tr}/c values for both the inviscid and viscous solutions. It also shows the viscous effects, reducing the lift coefficient.

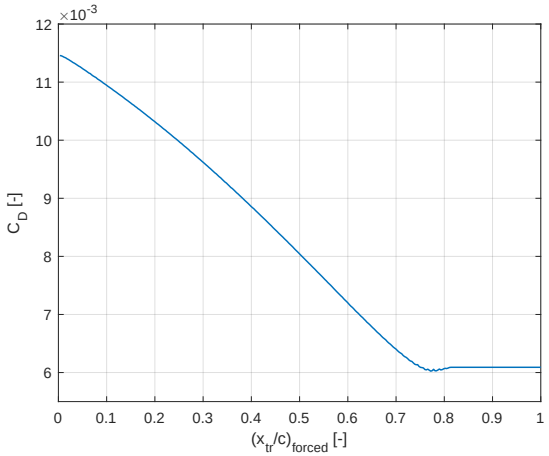

Figure E.1: Forced transition location vs. drag coefficient, M3J wing, $N = 9$, $\alpha = 3\ deg$ and $Re = 2.29 \cdot 10^6$.

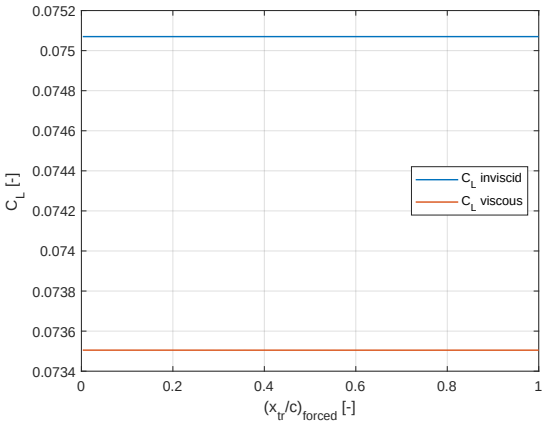

Figure E.2: Forced transition location vs. lift coefficient, M3J wing, at $N = 9$, $\alpha = 3\ deg$ and $Re = 2.29 \cdot 10^6$.

Further investigating the behavior of the drag coefficient from 0.75 x/c to the trailing edge, the $(x_{tr}/c)_{forced}$ is plotted against the $(x_{tr}/c)_{physical}$ in Figure E.3. XFoil uses the most upstream transition location through to either the directly set $(x_{tr}/c)_{forced}$ or through the N-factor, the dominating transition setting is denoted as $(x_{tr}/c)_{physical}$. As the N-factor is kept constant to its default value of 9 in Figure E.3, it is found that the N-factor dictates transition from 0.75 x/c onward. This is represented by the $(x_{tr}/c)_{physical}$ becoming constant after 0.75 x/c on the suction side and slightly more downstream on the pressure side. Note that these are the values taken at a mid-span section of the full M3J wing and assumed to be approximately representative of the full wing.

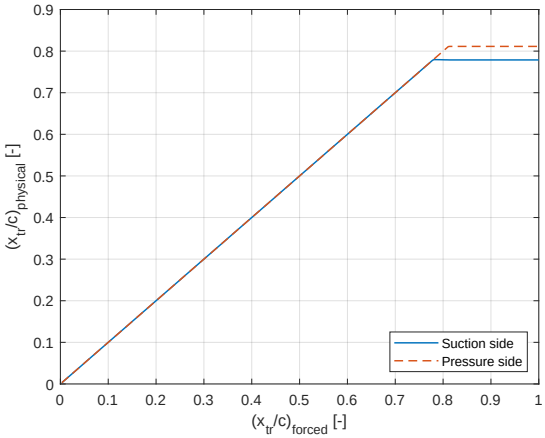

Figure E.3: Forced transition location vs. physical transition location, mid-span section of M3J wing, at $N = 9$, $\alpha = 3\ deg$ and $Re = 2.29 \cdot 10^6$.

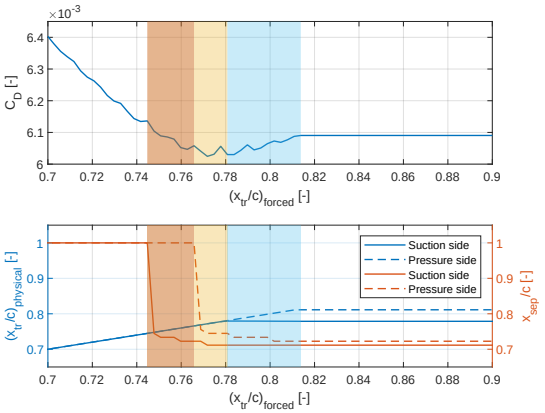

Figure E.4: Forced transition location vs. drag coefficient, physical transition location, and separation location, mid-span section of M3J wing, at $N = 9$, $\alpha = 3\ deg$ and $Re = 2.29 \cdot 10^6$.

This still leaves the question of why there is a short dip before the drag coefficient plateaus. A better visualization of this dip in drag coefficient is seen in the upper plot of Figure E.4. As it is found that the constant $(x_{tr}/c)_{physical}$ due to the N-factor is responsible for the plateauing of the curve after the dip, it raises the question what triggers the transition at that point. The bottom plot of Figure E.4 shows the answer. Laminar separation occurs at the location where the dip in drag coefficient is observed. The separation locations are obtained from the friction coefficient in XFoil since no direct method exists. The location where the friction coefficient becomes negative is taken as the separation location. To better explain what is happening area of the dip, where the separation and transition location curves intersect, three shaded areas are indicated in red, yellow, and blue. The red area is the onset of separation at the suction side moving upstream and becoming the limiting over the transition (intersecting below the transition curve), reflected by the drag coefficient curve having a slightly less steep downward gradient compared to upstream. The yellow area shows the same behavior for the separation curve as the red area, but now for the pressure side. Here separation has become the limiting on both sides of the wing. This is represented by the drag coefficient curve reaching its minimum. Finally, the blue area shows the separation location on both the suction and pressure side becoming constant as well as the transition location curves. This is seen in the drag coefficient as a slight upward gradient becoming a constant line going downstream.

It can be concluded that at the dip in drag coefficient, separation becomes limiting at the given flight conditions and N-factor. In this case, it is laminar separation, since the flow is laminar before the separation location and the separation induces transition slightly downstream of the separation location. As the separation location stays constant, so does the induced transition, explaining the plateaus in Figure E.1 and Figure E.3 respectively.

F

Vertical tailplane airfoils

Table F.1: CONFIDENTIAL Note all Fokker models are based on Fokker F-28 Mk1000 and assumed all to be the same since all these variants are similar types of aircraft. For all other aircraft, the t/c ratio % is converted to a simple symmetrical NACA airfoil, since actual airfoils are unknown, except for the VFW-614. For DATCOM also not all NACA thicknesses are available, therefore closest equivalent is chosen.

Aircraft type	**t/c ratio % from sources**	**Airfoils used for Q3D, Fokker/Obert**	**Closest equivalent used for USAF DATCOM**
Airbus A300	12.5% [15]	NACA 0012	NACA 0012
Airbus A320	9%	NACA 0009	NACA 0009
Airbus A340-300	[redacted]% [14]	[redacted]	[redacted]
Boeing 737-100	12% [15]	NACA 0012	NACA 0012
Boeing XB-47 (tailplane model)	11%	NACA 0011	NACA 0012
Douglas DC9-30	11% [15]	NACA 0011	NACA 0012
F-29 model 1-1	10.15% [15]	NACA 0010	NACA 0009
F-29 model 2-5	10.15% [15]	NACA 0010	NACA 0009
F-29 model 5-3	10.15% [15]	NACA 0010	NACA 0009
Fokker F-28 Mk1000 model 8-3	10.15% [15]	NACA 0010	NACA 0009
Fokker F-28 QC 40 deg model 8-4	10.15% [15]	NACA 0010	NACA 0009
Fokker F-28 Tailplane model 9	10.15% [15]	NACA 0010	NACA 0009
Fokker F-28 Wing off model 4	10.15% [15]	NACA 0010	NACA 0009
SKV-LST-1 (model of subtype F-28)	10.15% [15]	NACA 0010	NACA 0009
SKV-LST-2 (model of subtype F-28)	10.15% [15]	NACA 0010	NACA 0009
SKV-LST-3 (II) (model of subtype F-28)	10.15% [15]	NACA 0010	NACA 0009
VFW-614	[redacted]% [14]	[redacted]	[redacted]

G

Transition location data (aerodynamic database for LFC)

G.1. Airbus A320, cruise, sweep variation

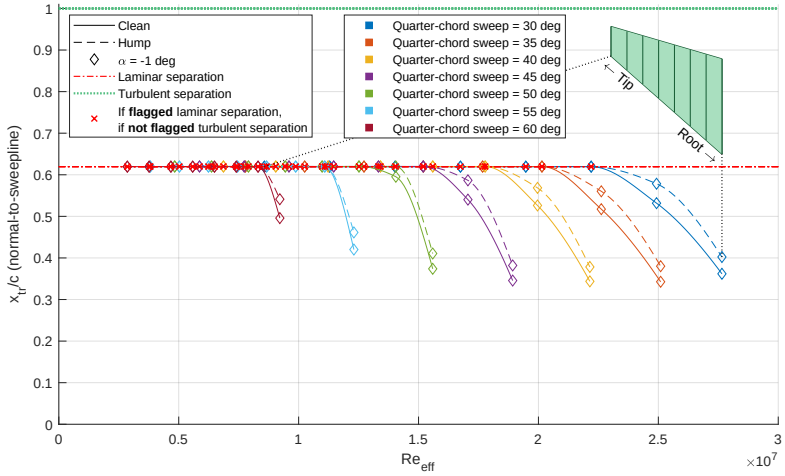

Figure G.1: Transition locations Airbus A320, cruise $\alpha = -1\ deg$ (sweep variation)

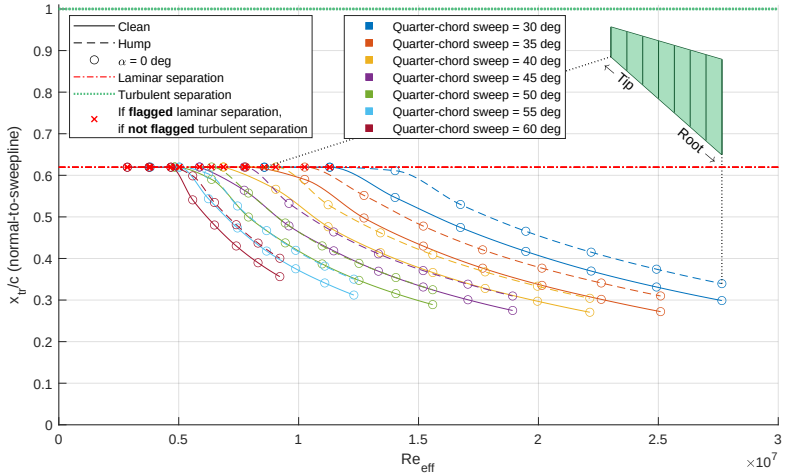

Figure G.2: Transition locations Airbus A320, cruise $\alpha = 0\ deg$ (sweep variation)

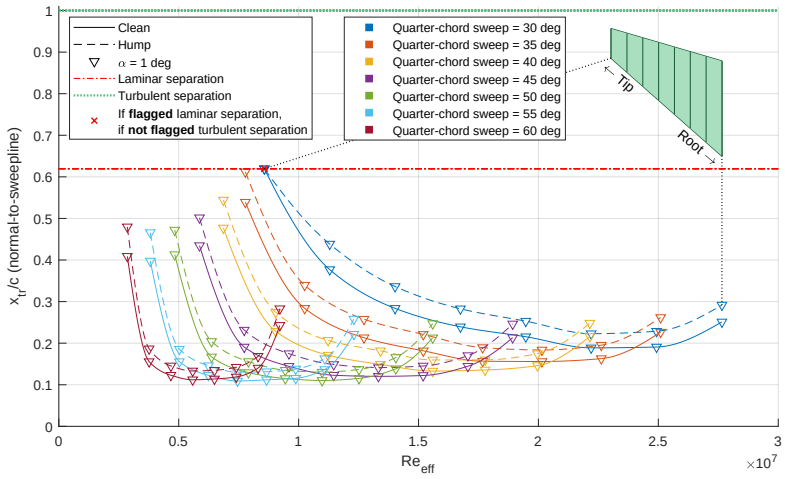

Figure G.3: Transition locations Airbus A320, cruise $\alpha = 1\ deg$ (sweep variation)

G.2. Airbus A320, landing, sweep variation

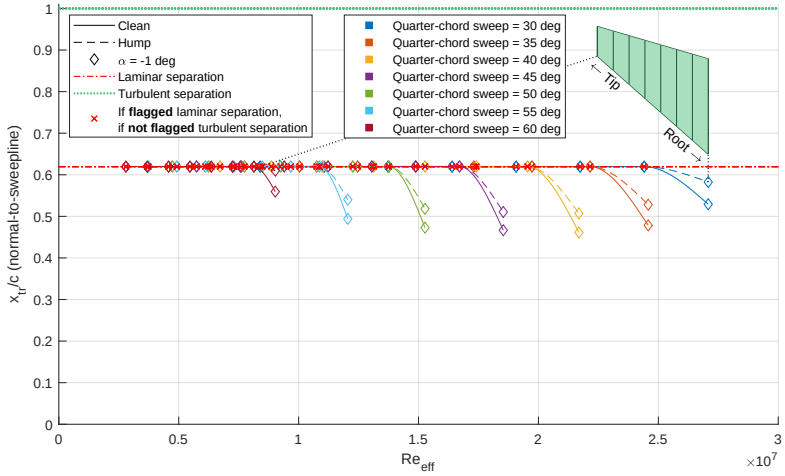

Figure G.4: Transition locations Airbus A320, landing $\alpha = -1\ deg$ (sweep variation)

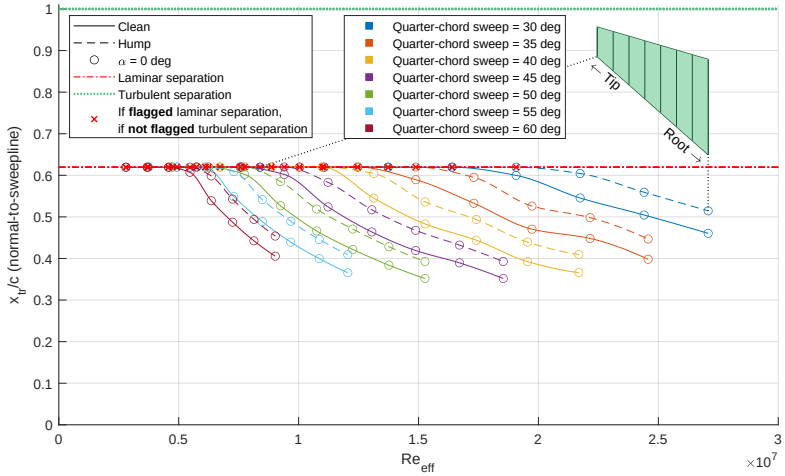

Figure G.5: Transition locations Airbus A320, landing $\alpha = 0\ deg$ (sweep variation)

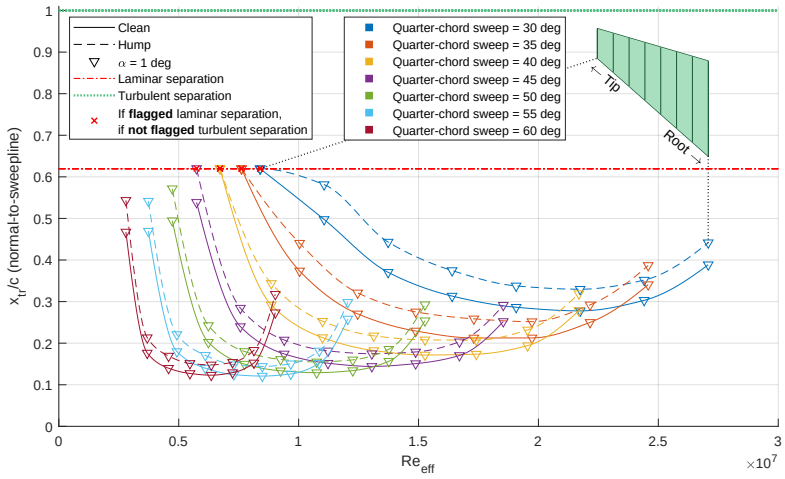

Figure G.6: Transition locations Airbus A320, landing $\alpha = 1\ deg$ (sweep variation)

G.3. Airbus A320, cruise, surface area variation

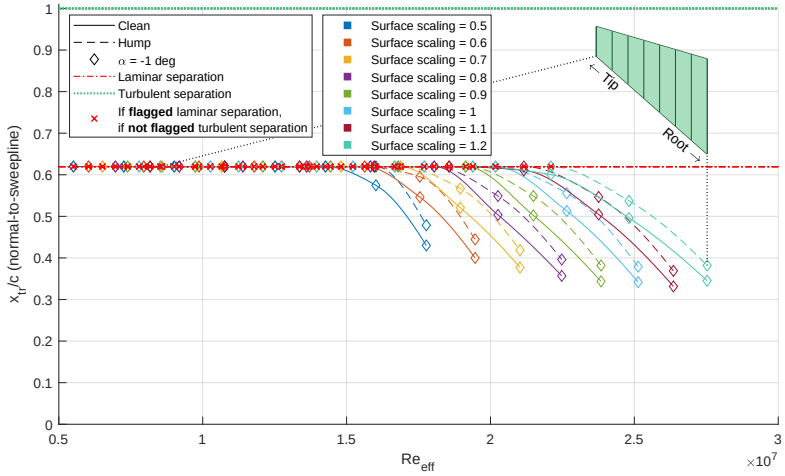

Figure G.7: Transition locations Airbus A320, cruise $\alpha = -1\ deg$ (surface variation)

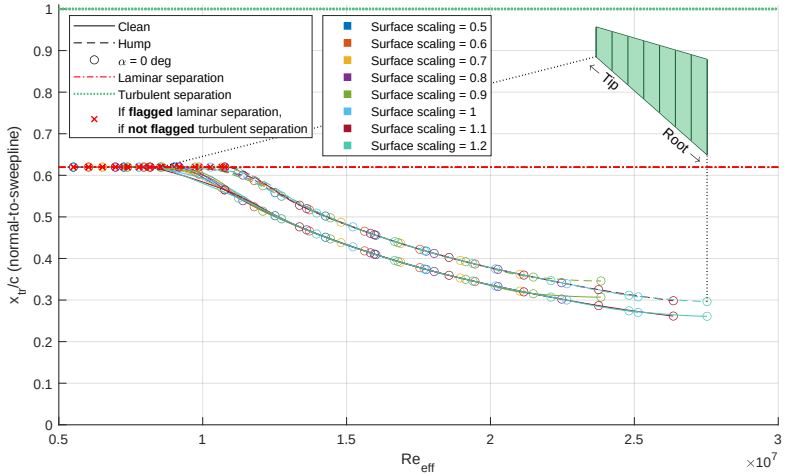

Figure G.8: Transition locations Airbus A320, cruise $\alpha = 0\ deg$ (surface variation)

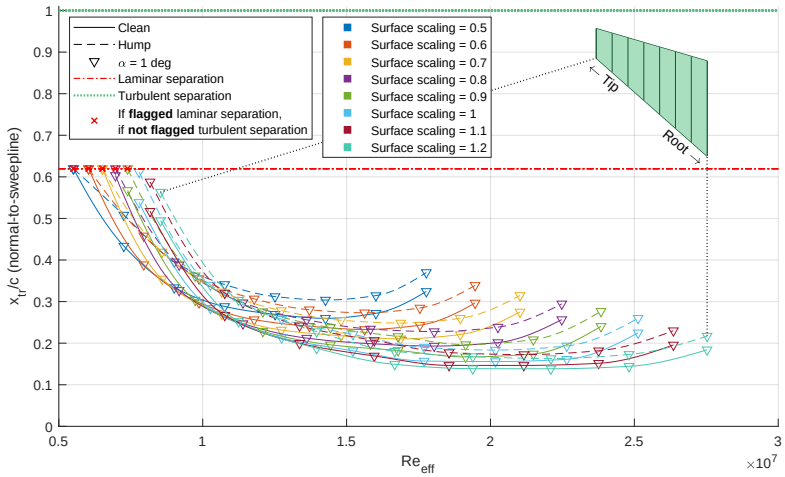

Figure G.9: Transition locations Fokker Airbus A320, cruise $\alpha = 1\ deg$ (surface variation)

G.4. Airbus A320, landing, surface area variation

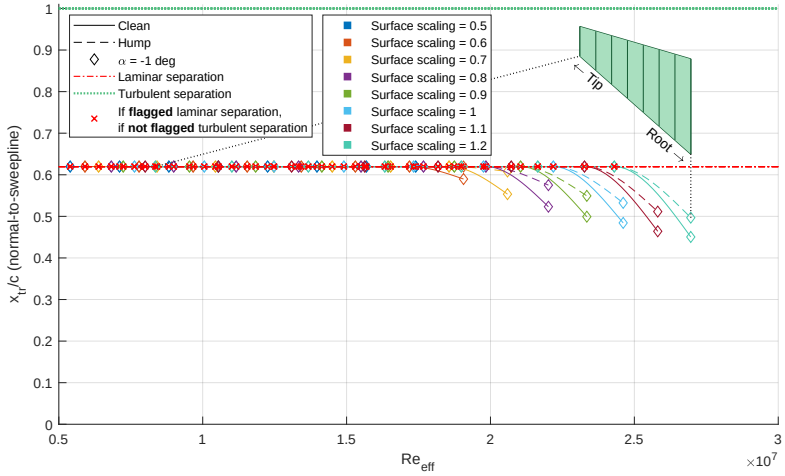

Figure G.10: Transition locations Airbus A320, landing $\alpha = -1\ deg$ (surface variation)

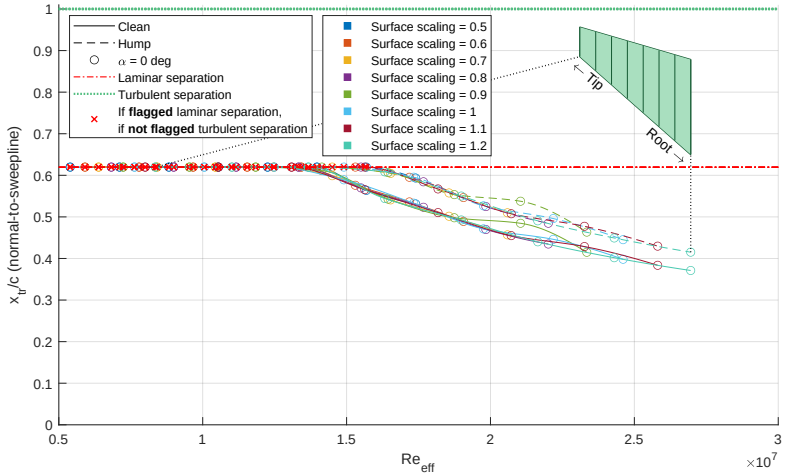

Figure G.11: Transition locations Airbus A320, landing $\alpha = 0\ deg$ (surface variation)

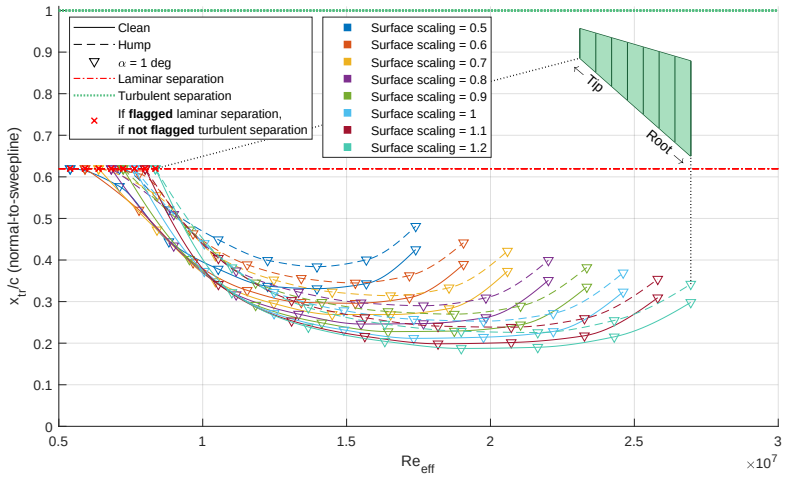

Figure G.12: Transition locations Airbus A320, landing $\alpha = 1\ deg$ (surface variation)

G.5. Fokker F-28 Mk1000, cruise, sweep variation

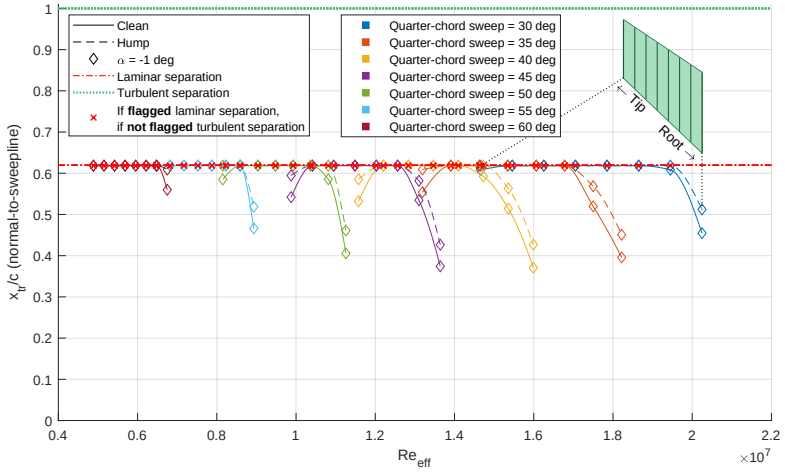

Figure G.13: Transition locations Fokker F-28 Mk1000, cruise $\alpha = -1\ deg$ (sweep variation)

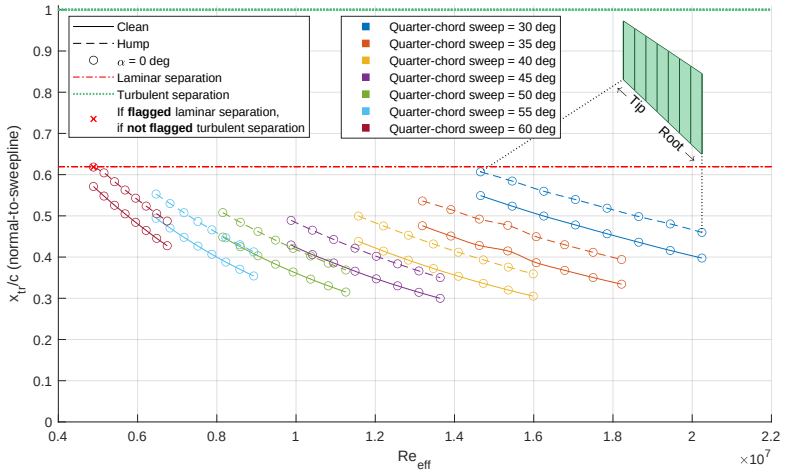

Figure G.14: Transition locations Fokker F-28 Mk1000, cruise $\alpha = 0\ deg$ (sweep variation)

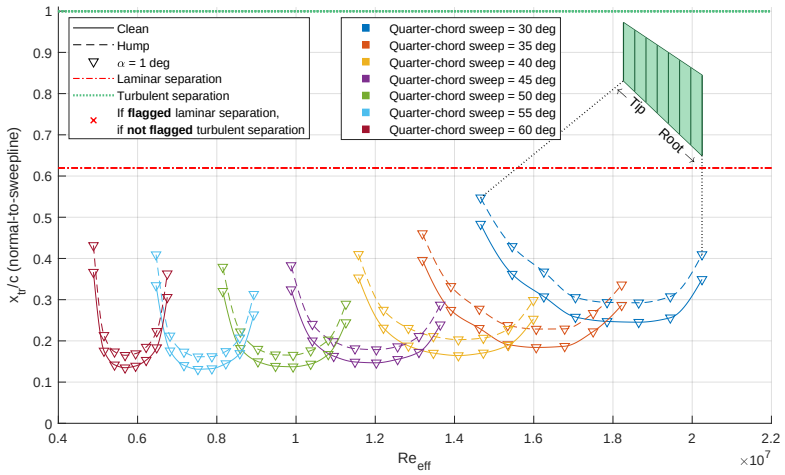

Figure G.15: Transition locations Fokker F-28 Mk1000, cruise $\alpha = 1\ deg$ (sweep variation)

G.6. Fokker F-28 Mk1000, landing, sweep variation

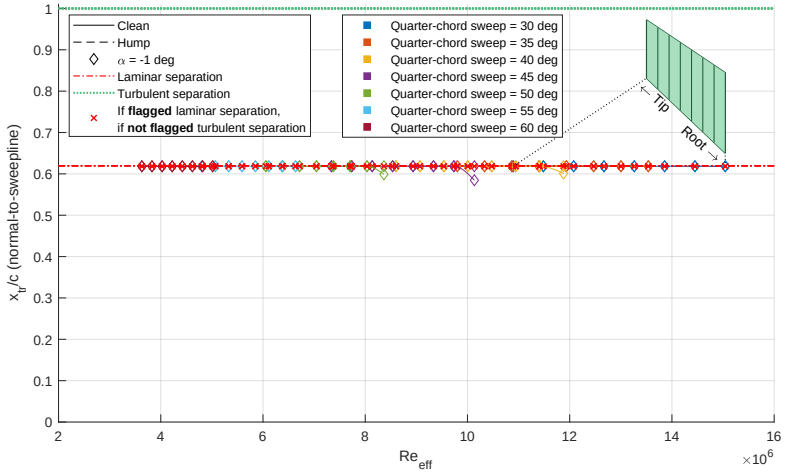

Figure G.16: Transition locations Fokker F-28 Mk1000, landing $\alpha = -1\ deg$ (sweep variation)

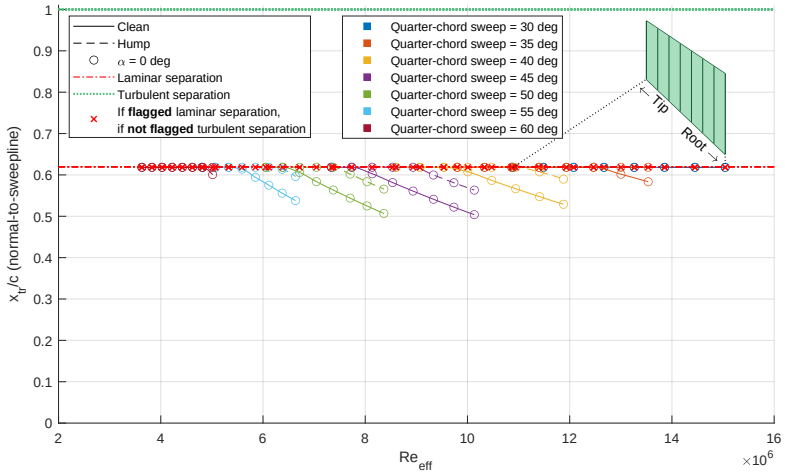

Figure G.17: Transition locations Fokker F-28 Mk1000, landing $\alpha = 0\ deg$ (sweep variation)

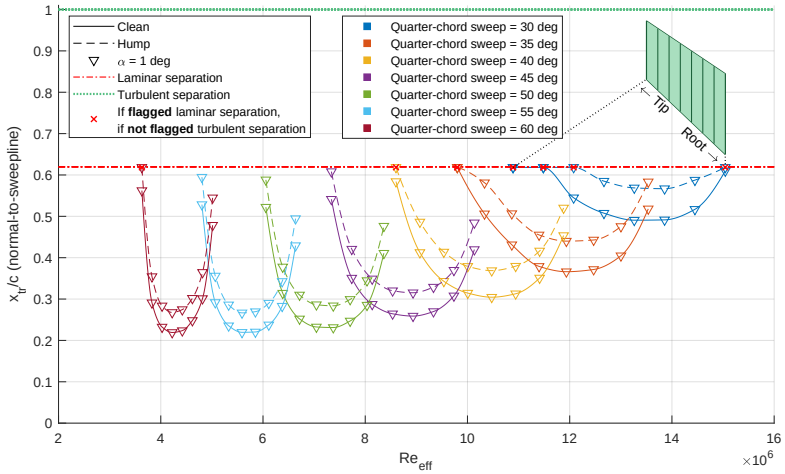

Figure G.18: Transition locations Fokker F-28 Mk1000, landing $\alpha = 1\ deg$ (sweep variation)

G.7. Fokker F-28 Mk1000, cruise, surface area variation

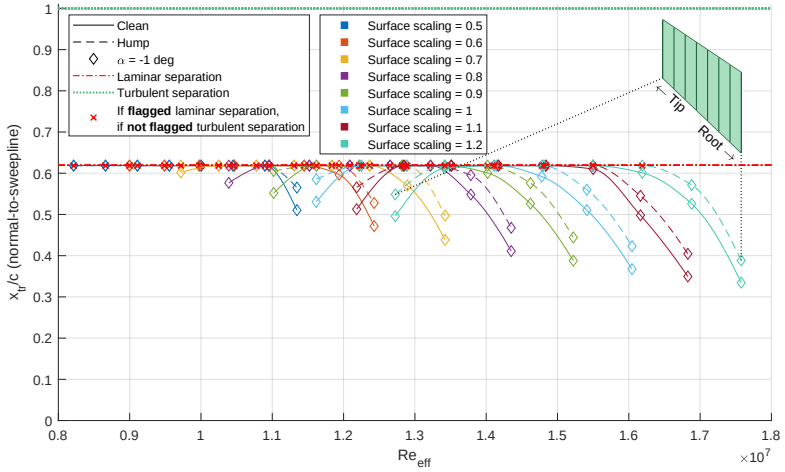

Figure G.19: Transition locations Fokker F-28 Mk1000, cruise $\alpha = -1\ deg$ (surface variation)

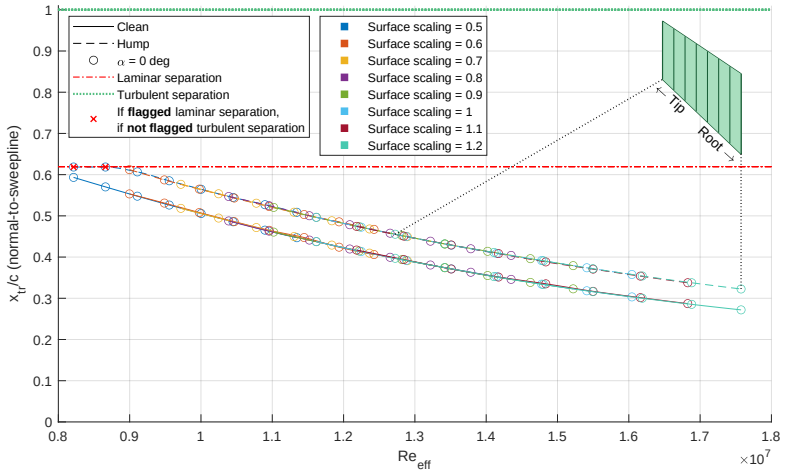

Figure G.20: Transition locations Fokker F-28 Mk1000, cruise $\alpha = 0\ deg$ (surface variation)

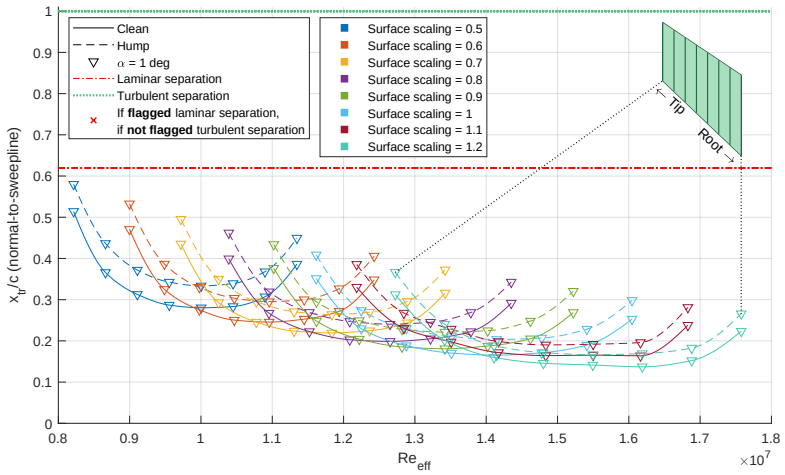

Figure G.21: Transition locations Fokker F-28 Mk1000, cruise $\alpha = 1\ deg$ (surface variation)

G.8. Fokker F-28 Mk1000, landing, surface area variation

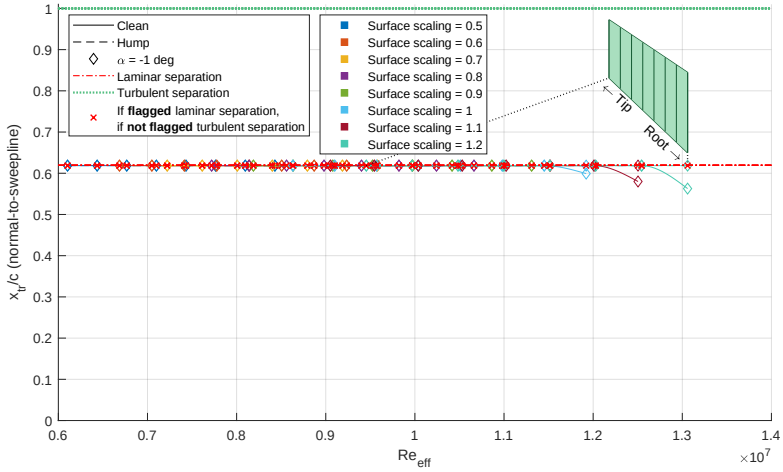

Figure G.22: Transition locations Fokker F-28 Mk1000, landing $\alpha = -1\ deg$ (surface variation)

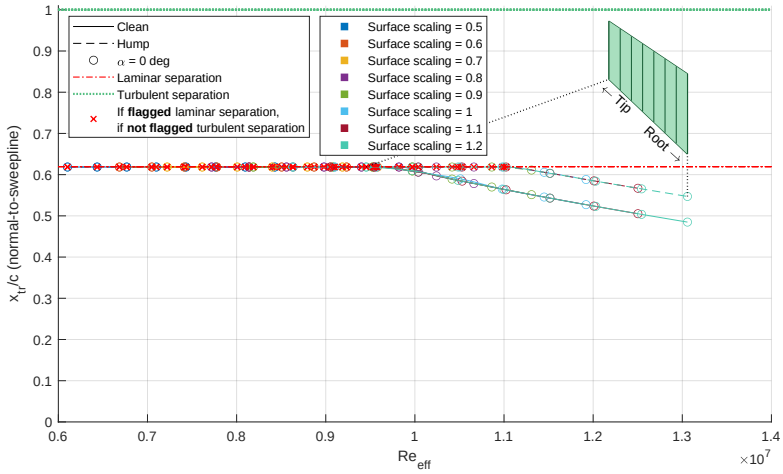

Figure G.23: Transition locations Fokker F-28 Mk1000, landing $\alpha = 0\ deg$ (surface variation)

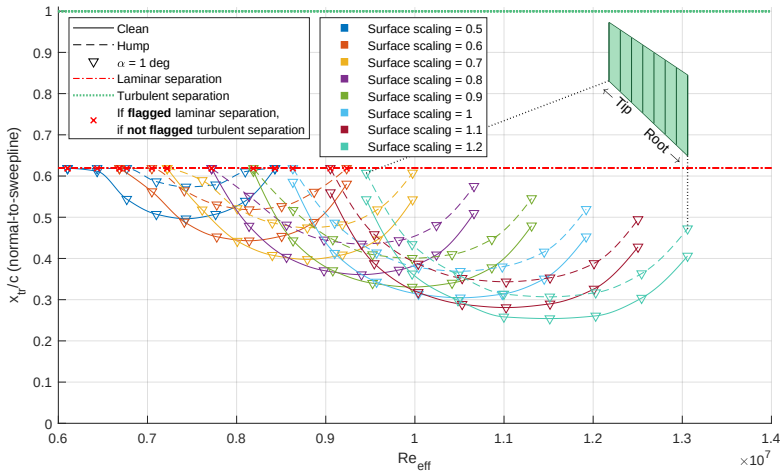

Figure G.24: Transition locations Fokker F-28 Mk1000, landing $\alpha = 1\ deg$ (surface variation)

H

Baseline configuration: geometries and flight conditions

H.1. Estimation of vertical tailplane rolling moment arm

Equation H.1 shows the vertical tailplane rolling moment arm estimation. It is assumed that the CG is at wing root chord height and the fuselage is assumed to continue straight on at the top side near the vertical tail. Thus assuming no cone angle at the top side of the tail cone, since tail cone angles are unknown. Also, a straight-tapered planform is assumed. The first term, $\bar{z}_{_V}$, accounts for the distance between the spanwise location of the MAC and the vertical tailplane root chord and is calculated with Equation 2.7. The second term, $\left(\frac{1}{2}D_{fus_{max}} - \frac{1}{2}d_{_V}\right)$ accounts for the distance between the root chord of the vertical tailplane and the fuselage centerline. The third term, $z_{_W}$, accounts for the distance between the fuselage centerline and the wing root height.

$$l_{z_{_V}} = \bar{z}_{_V} + \left(\frac{1}{2}D_{fus_{max}} - \frac{1}{2}d_{_V}\right) + z_{_W} \tag{H.1}$$

H.2. Aircraft geometries

Table H.1: CONFIDENTIAL Original geometry Airbus A320 part 1/2

	Variable	Value	Source	Note
Wing	S_W	[redacted] m^2	[14]	
	b_W	[redacted] m	[14]	
	A_W	[redacted]	[14]	
	$\Lambda_{1/4c_W}$	[redacted] deg	[14]	
	λ_W	[redacted]	[14]	
	Γ_W	[redacted] deg	[14]	
	C_{L_W}	[redacted]	[14]	[redacted]
	y^*	[redacted]	[14]	
Vertical tail	S_V	[redacted] m^2	[14]	
	Airfoil	NACA 0009	-	Assumed
	b_V	[redacted] m	[14]	
	A_V	[redacted]	[14]	
	$\Lambda_{1/4c_V}$	[redacted] deg	[14]	
	λ_V	[redacted]	[14]	
	$S_{V_{ref}}$	[redacted] m^2	[14]	
	$(C_{L_\alpha})_V$	[redacted] deg^{-1}	[14]	Only used when Q3D is not used
	$\bar{c}_V$	[redacted]	[14]	
	K_{VH}	[redacted]	[14]	
Dorsal fin	$\frac{S_{df}}{S_V}$	[redacted]	[14]	No dorsal fin
Horizontal tail	S_H	[redacted] m^2	[14]	
	b_H	[redacted] m	[14]	
	A_H	[redacted]	[14]	
	$\Lambda_{1/4c_H}$	[redacted] deg	[14]	
	λ_H	[redacted]	[14]	
	Γ_H	6 deg	[15]	Table 9-2, assumed to be the same as the Airbus A300
	i_H	[redacted] deg	[14]	Estimated from drawings
Fuselage	$S_{fus.cross}$	[redacted] m^2	[14]	
	$\frac{D_{fus_{max}}}{b_W}$	[redacted]	[14]	
	x_m	[redacted] m	[14]	From drawings
	l_B	[redacted] m	[14]	
	S_{B_S}	[redacted] m^2	[14]	Estimated from drawings
	h_1	[redacted]	[14]	Estimated from drawings
	h_2	[redacted]	[14]	Estimated from drawings
	h	[redacted]	[14]	Estimated from drawings
	w	[redacted]	[14]	Estimated from drawings
Nacelles	$(n_{nac})_W$	[redacted]	[14]	
	$(n_{nac})_F$	[redacted]	[14]	
	$\left(\Delta\frac{\delta\sigma}{\delta\beta}\right)_{NW}$	[redacted]	[14]	
	$\frac{x_{exh}-0\%c_{r_V}}{c_{r_V}}$	[redacted]	[14]	N.A. since wing-mounted nacelles
	$\frac{z_{cl,nac}}{D_{fus}}$	[redacted]	[14]	N.A. since wing-mounted nacelles
Relative component positioning	$\frac{b_V}{d_V}$	[redacted]	[14]	
	$\frac{z_H}{b_V}$	[redacted]	[14]	
	$\frac{x_H}{c_V}$	[redacted]	[14]	Estimated from drawings
	$\frac{z_W}{D_{fus_{max}}}$	[redacted]	[14]	
Moment arms	l_{x_V}	[redacted] m	[14]	[redacted]
	$l_{x_{V_{ref}}}$	[redacted] m	[14]	[redacted]
	l_{z_V}	4.657 m	-	Obtained through Equation H.1

Table H.2: CONFIDENTIAL Original geometry Airbus A320 part 2/2

	Variable	Value	Source	Note
Flaps	$\frac{b_{fl}}{b_W}$	[redacted]	[14]	Estimated from drawings
Rudder	$\frac{c_R}{c_V}$	[redacted]	[14]	
	S_{V_R}	[redacted] m^2	[14]	
Ailerons	$\frac{c_a}{c_W}$	[redacted]	[14]	Estimated from drawings, assumed ailerons have constant flap chord to wing chord ratio over full aileron span
	$\frac{y_{a_r}}{b_W/2}$	[redacted]	[14]	Estimated from drawings
	$\frac{y_{a_t}}{b_W/2}$	[redacted]	[14]	Estimated from drawings
	$\left(\frac{t}{c}\right)_{W,a}$	0.11	[17]	Figure 24.121
	Hinge gap	Sealed	-	Assumed
Engines	Engine	CFM56-5B4	[80][1]	
	$A_{i_{primary}}$	0.24 m^2	[80]	Estimated from drawings
	$A_{i_{fan}}$	2.29 m^2	[80]	Estimated from drawings
	$A_{nz_{primary}}$	0.36 m^2	[80]	Estimated from drawings
	$A_{nz_{fan}}$	1.41 m^2	[80]	Estimated from drawings
	l_{y_E}	[redacted] m	[14]	Estimated from drawings
	ΔT_{E_o}	120·10^3 N	[90]	Take-off thrust used
Weight	$MTOW$	73500 kg	[80][17]	Weight variant WV000 and Figure 42.25
	$MTOW - W_V$	73037 kg	[80][17]	Weight variant WV000 and W_V from Figure 42.25
	$MZFW$	60500 kg	[80]	Weight variant WV000
Drag	$\frac{L}{D}$	17.3	[17]	Figure 40.17 and Figure 40.37 (85%) at cruise Mach
	$(C_D)_V$	0.004692	-	Calculated with Q3D for original airfoil NACA 0009
	$(C_D)_{V_{ref}}$	0.004723	-	Calculated with Q3D for original airfoil NACA 0009
	$S_{V_{ref}}$ for $(C_D)_{V_{ref}}$	21.8784 m^2	-	Calculated by assuming $b_{V_{ref}} = b_V - (b_V/\frac{b_V}{d_V})/2$. Calculated for consistency, actual $S_{V_{ref}}$ not used, due to ambiguous definition
Range	R	3161·10^3 m	[80]	Harmonic range estimated from figure
	$TSFC$	15.4·10^{-6} $kg/(Ns)$	-[1]	

[1] Meier, N.. (2021). Jet Engine Specification Database. Retrieved December 12, 2024, from `https://www.jet-engine.net/`

Table H.3: CONFIDENTIAL Original geometry Fokker F-28 Mk1000 part 1/2

	Variable	Value	Source	Note
Wing	S_W	[redacted] m^2	[14]	
	b_W	[redacted] m	[14]	
	A_W	[redacted]	[14]	
	$\Lambda_{1/4c_W}$	[redacted] deg	[14]	
	λ_W	[redacted]	[14]	
	Γ_W	[redacted] deg	[14]	
	C_{L_W}	[redacted]	[14]	[redacted]
	y^*	[redacted]	[14]	
Vertical tail	S_V	[redacted] m^2	[14]	
	Airfoil	NACA 0010	[15]	Closest to original $\left(\frac{t}{c}\right)_V = 10.15\%$
	b_V	[redacted] m	[14]	
	A_V	[redacted]	[14]	
	$\Lambda_{1/4c_V}$	[redacted] deg	[14]	
	λ_V	[redacted]	[14]	
	$S_{V_{ref}}$	[redacted] m^2	[14]	
	$(C_{L_\alpha})_V$	[redacted] deg^{-1}	[14]	Only used when Q3D is not used
	$\bar{c}_V$	[redacted]	[14]	
	K_{VH}	[redacted]	[14]	
Dorsal fin	$\frac{S_{df}}{S_V}$	[redacted]	[14]	Reverse-engineered from data
Horizontal tail	S_H	[redacted] m^2	[14]	
	b_H	[redacted] m	[14]	
	A_H	[redacted]	[14]	
	$\Lambda_{1/4c_H}$	[redacted] deg	[14]	
	λ_H	[redacted]	[14]	
	Γ_H	0 deg	[15]	Table 9-2
	i_H	[redacted] deg	[14]	Estimated from drawings
Fuselage	$S_{fus.cross}$	[redacted] m^2	[14]	Based on values of smaller wind tunnel model scaled to full-size model
	$\frac{D_{fus_{max}}}{b_W}$	[redacted]	[14]	
	x_m	[redacted] m	[14]	Based on values of smaller wind tunnel model scaled to full-size model
	l_B	[redacted] m	[14]	
	S_{B_S}	[redacted] m^2	[14]	Based on values of smaller wind tunnel model scaled to full-size model
	h_1	[redacted]	[14]	Based on values of smaller wind tunnel model scaled to full-size model
	h_2	[redacted]	[14]	Based on values of smaller wind tunnel model scaled to full-size model
	h	[redacted]	[14]	Based on values of smaller wind tunnel model scaled to full-size model
	w	[redacted]	[14]	Based on values of smaller wind tunnel model scaled to full-size model
	K_N	[redacted]	[14]	
Nacelles	$(n_{nac})_W$	[redacted]	[14]	
	$(n_{nac})_F$	[redacted]	[14]	
	$\left(\Delta\frac{\delta\sigma}{\delta\beta}\right)_{NW}$	[redacted]	[14]	N.A. since fuselage-mounted nacelles
	$\frac{x_{exh}-0\%c_{r_V}}{c_{r_V}}$	[redacted]	[14]	
	$\frac{z_{cl,nac}}{D_{fus}}$	[redacted]	[14]	
Relative component positioning	$\frac{b_V}{d_V}$	[redacted]	[14]	
	$\frac{z_H}{b_V}$	[redacted]	[14]	
	$\frac{x_H}{c_V}$	[redacted]	[14]	Estimated from drawings
	$\frac{z_W}{D_{fus_{max}}}$	[redacted]	[14]	
Moment arms	l_{x_V}	[redacted] m	[14]	[redacted]
	$l_{x_{V_{ref}}}$	[redacted] m	[14]	[redacted]
	l_{z_V}	4.090 m	-	Obtained through Equation H.1

Table H.4: CONFIDENTIAL Original geometry Fokker F-28 Mk1000 part 2/2

	Variable	Value	Source	Note
Flaps	$\frac{b_{fl}}{b_W}$	[redacted]	[14]	Estimated from drawings
Rudder	$\frac{c_R}{c_V}$	[redacted]	[14]	[redacted]
	S_{V_R}	[redacted] m^2	[14]	[redacted]
Ailerons	$\frac{c_a}{c_W}$	0.32	[15]	Table 7.1
	$\frac{y_{a_r}}{b_W/2}$	[redacted]	[14]	Estimated from drawings
	$\frac{y_{a_t}}{b_W/2}$	[redacted]	[14]	Estimated from drawings
	$\left(\frac{t}{c}\right)_{W,a}$	0.13	[15]	Table 7.1
	Hinge gap	Sealed	-	Assumed
Engines	Engine	RB.183 Mk.555-15/15N Spey Jr.	[81][2,3]	
	$A_{i_{primary}}$	0.1458 m^2	-[2,3]	Estimated from images, assumed full fan diameter = 0.8255 m
	$A_{i_{fan}}$	0.5006 m^2	-[2,3]	Estimated from images, assumed full fan diameter = 0.8255 m
	$A_{nz_{primary}}$	0.0660 m^2	-[2,3]	Estimated from images, assumed exhaust area to be split evenly between primary and fan
	$A_{nz_{fan}}$	0.0660 m^2	-[2,3]	Estimated from images, assumed exhaust area to be split evenly between primary and fan
	l_{y_E}	[redacted] m	[14]	Based on values of smaller wind tunnel model scaled to full-size model
	ΔT_{E_o}	43.8·10^3 N	[81]	Take-off thrust of RB 183 Mk555-15/15N
Weight	$MTOW$	25720 kg	[81]	First model
	$MTOW - W_V$	25398 kg	[81][17]	First model and W_V from Figure 42.26, assumed F-28 Mk4000 data also holds for F-28 Mk1000
	$MZFW$	21160 kg	[81]	First model
Drag	$\frac{L}{D}$	14.6	[17]	Figure 40.17 and Figure 40.37 (85%) at cruise Mach
	$(C_D)_V$	0.004652	-	Calculated with Q3D for original airfoil NACA 0010
	$(C_D)_{V_{ref}}$	0.004659	-	Calculated with Q3D for original airfoil NACA 0010
	$S_{V_{ref}}$ for $(C_D)_{V_{ref}}$	15.9138 m^2	-	Calculated by assuming $b_{V_{ref}} = b_V - (b_V/\frac{b_V}{d_V})/2$. Calculated for consistency, actual $S_{V_{ref}}$ not used, due to ambiguous definition
Range	R	1705·10^3 m	-[4]	Range max. payload
	$TSFC$	17.8·10^{-6} $kg/(Ns)$	[81][4]	Assuming 43.8 kN thrust and 2800 kg/h fuel consumption

[2] Meier, N.. (2021). Jet Engine Specification Database. Retrieved December 12, 2024, from https://www.jet-engine.net/

[3] Wikipedia. (2024). Rolls-Royce Spey. Retrieved December 13, 2024, from https://en.wikipedia.org/wiki/Rolls-Royce_Spey

[4] Wikipedia. (2024). Fokker F28 Fellowship. Retrieved December 13, 2024, from https://en.wikipedia.org/wiki/Fokker_F28_Fellowship

H.3. Flight conditions

Table H.5: CONFIDENTIAL Flight conditions Airbus A320

	Variable	Value	Source	Note
Landing	M	0.2200	[25]	V_{REF} used, see Table 2.3
	$altitude$	15 m	[25]	
	α	5 deg	-	Assumed
	δ_{sl}	[redacted] deg	[14]	
	δ_{fl}	[redacted] deg	[14]	
	$\delta_{fl,2}$	[redacted] deg	[14]	No double-hinged flap
	ϵ	-	-	No downwash data available, no downwash correction for K_{VH} used
	$\frac{q_V}{q} K_{FV}$	[redacted]	[14]	Linearized for small angles of attack
	$C_{L_{max_{1-g}}}$	2.6	[17]	Figure 26.13
	$(altitude)_{C_{L_{max_{1-g}}}}$	0 m	[17]	At sea-level
Cruise	M	0.78	-[5]	
	$altitude$	11760 m	-[5]	
	α	0 deg	-	Assumed
	δ_{sl}	[redacted] deg	[14]	
	δ_{fl}	[redacted] deg	[14]	
	$\delta_{fl,2}$	[redacted] deg	[14]	No double-hinged flap
	ϵ	-	-	No downwash data available, no downwash correction for K_{VH} used
	$\frac{q_V}{q} K_{FV}$	[redacted]	[14]	Linearized for small angles of attack

Table H.6: CONFIDENTIAL Flight conditions Fokker F-28 Mk1000

	Variable	Value	Source	Note
Landing	M	0.1957	[25]	V_{REF} used, see Table 2.3
	$altitude$	15 m	[25]	
	α	5 deg	-	Assumed
	δ_{sl}	[redacted] deg	[14]	
	δ_{fl}	[redacted] deg	[14]	
	$\delta_{fl,2}$	[redacted] deg	[14]	No double-hinged flap
	ϵ	[redacted]	[14]	
	$\frac{q_V}{q} K_{FV}$	[redacted]	[14]	Linearized for small angles of attack
	$C_{L_{max_{1-g}}}$	2.375	[17]	Figure 26.17, assumed F-28 Mk4000 data also holds for F-28 Mk1000
	$(altitude)_{C_{L_{max_{1-g}}}}$	0 m	[17]	At sea-level
Cruise	M	0.69	-[6]	
	$altitude$	10700 m	[81]	Maximum operating altitude
	α	0 deg	-	Assumed
	δ_{sl}	[redacted] deg	[14]	
	δ_{fl}	[redacted] deg	[14]	
	$\delta_{fl,2}$	[redacted] deg	[14]	No double-hinged flap
	ϵ	[redacted]	[14]	
	$\frac{q_V}{q} K_{FV}$	[redacted]	[14]	Linearized for small angles of attack

[5] Wikipedia. (2024). Airbus A320 family. Retrieved December 12, 2024, from `https://en.wikipedia.org/wiki/Airbus_A320_family`

[6] Wikipedia. (2024). Fokker F28 Fellowship. Retrieved December 13, 2024, from `https://en.wikipedia.org/wiki/Fokker_F28_Fellowship`

I

Validation of stability analysis: flight conditions and geometry changes

Table I.1: CONFIDENTIAL Flight conditions, geometry changes (compared to baseline configuration as in Table H.1, Table H.2, and Table H.5) and notes for all the stability derivatives of Airbus A320 used in validation Table 5.3.

	Stability derivative	Flight conditions & geometry changes
Tail-off	$\left(C_{y_\beta}\right)_{T-O}$	Flight conditions: Cruise with $\alpha =$ [redacted], $\delta_{sl} =$ [redacted], $\delta_{fl} =$ [redacted] Geometry changes: $z_W/D_{fus} =$ [redacted], $K_i =$ [redacted] $(C_{L_\alpha})_V$ from [14] used, not Q3D $(C_{L_\alpha})_V$
	$\left(C_{l_\beta}\right)_{T-O}$	Flight conditions: Cruise with $\alpha =$ [redacted], $\delta_{sl} =$ [redacted], $\delta_{fl} =$ [redacted] $(C_{L_\alpha})_V$ from [14] used, not Q3D $(C_{L_\alpha})_V$
	$\left(C_{n_\beta}\right)_{T-O}$	Flight conditions: Cruise with $\alpha =$ [redacted], $\delta_{sl} =$ [redacted], $\delta_{fl} =$ [redacted] $(C_{L_\alpha})_V$ from [14] used, not Q3D $(C_{L_\alpha})_V$
Horizontal tail	$\left(C_{l_\beta}\right)_H$	Flight conditions: Cruise with $\alpha =$ [redacted], $\delta_{sl} =$ [redacted], $\delta_{fl} =$ [redacted] $(C_{L_\alpha})_V$ from [14] used, not Q3D $(C_{L_\alpha})_V$
Vertical tail	$\left(C_{y_\beta}\right)_V$	Flight conditions: Cruise with $\alpha =$ [redacted], $\delta_{sl} =$ [redacted], $\delta_{fl} =$ [redacted] $(C_{L_\alpha})_V$ from [14] used, not Q3D $(C_{L_\alpha})_V$
	$\left(C_{l_\beta}\right)_V$	Flight conditions: Cruise with $\alpha =$ [redacted], $\delta_{sl} =$ [redacted], $\delta_{fl} =$ [redacted] $(C_{L_\alpha})_V$ from [14] used, not Q3D $(C_{L_\alpha})_V$
	$\left(C_{n_\beta}\right)_V$	Flight conditions: Cruise with $\alpha =$ [redacted], $\delta_{sl} =$ [redacted], $\delta_{fl} =$ [redacted] $(C_{L_\alpha})_V$ from [14] used, not Q3D $(C_{L_\alpha})_V$
Sidewash	$\left(\frac{\delta\sigma}{\delta\beta}\right)_{tot}$	Flight conditions: Cruise with $\alpha =$ [redacted], $\delta_{sl} =$ [redacted], $\delta_{fl} =$ [redacted] $(C_{L_\alpha})_V$ from [14] used, not Q3D $(C_{L_\alpha})_V$
	$\left(1+\frac{\delta\sigma}{\delta\beta}\right)\frac{q_V}{q}K_{FV}$ from $\left(C_{y_\beta}\right)_V$	Flight conditions: Cruise with $\alpha =$ [redacted], $\delta_{sl} =$ [redacted], $\delta_{fl} =$ [redacted] $(C_{L_\alpha})_V$ from [14] used, not Q3D $(C_{L_\alpha})_V$
	$\left(1+\frac{\delta\sigma}{\delta\beta}\right)\frac{q_V}{q}K_{FV}$ from $\left(C_{n_\beta}\right)_V$	Flight conditions: Cruise with $\alpha =$ [redacted], $\delta_{sl} =$ [redacted], $\delta_{fl} =$ [redacted] $(C_{L_\alpha})_V$ from [14] used, not Q3D $(C_{L_\alpha})_V$
Rudder	$C_{y_{\delta_R}}$	Flight conditions: Cruise with $\alpha =$ [redacted], $\delta_{sl} =$ [redacted], $\delta_{fl} =$ [redacted] $(C_{L_\alpha})_V$ from [14] used, not Q3D $(C_{L_\alpha})_V$
	$C_{l_{\delta_R}}$	Flight conditions: Cruise with $\alpha =$ [redacted], $\delta_{sl} =$ [redacted], $\delta_{fl} =$ [redacted] $(C_{L_\alpha})_V$ from [14] used, not Q3D $(C_{L_\alpha})_V$
	$C_{n_{\delta_R}}$	Flight conditions: Cruise with $\alpha =$ [redacted], $\delta_{sl} =$ [redacted], $\delta_{fl} =$ [redacted] $(C_{L_\alpha})_V$ from [14] used, not Q3D $(C_{L_\alpha})_V$
Aileron	$C_{y_{\delta_a}}$	Flight conditions: Cruise with $\alpha =$ [redacted], $\delta_{sl} =$ [redacted], $\delta_{fl} =$ [redacted] $(C_{L_\alpha})_V$ from [14] used, not Q3D $(C_{L_\alpha})_V$
	$C_{l_{\delta_a}}$	Flight conditions: Cruise with $\alpha =$ [redacted], $\delta_{sl} =$ [redacted], $\delta_{fl} =$ [redacted] $(C_{L_\alpha})_V$ from [14] used, not Q3D $(C_{L_\alpha})_V$
	$C_{n_{\delta_a}}$	Flight conditions: Cruise with $\alpha =$ [redacted], $\delta_{sl} =$ [redacted], $\delta_{fl} =$ [redacted] $(C_{L_\alpha})_V$ from [14] used, not Q3D $(C_{L_\alpha})_V$

Table I.2: CONFIDENTIAL Flight conditions, geometry changes (compared to baseline configuration as in Table H.1, Table H.2, and Table H.5) and notes for all the stability derivatives of Airbus A320 compared to F-29 model 1-2 with wing-mounted nacelles used in validation Table 5.4.

	Stability derivative	Flight conditions & geometry changes
Tail-off	$\left(C_{y_\beta}\right)_{T-O}$	Flight conditions: Cruise with $\alpha =$ [redacted], $\delta_{sl} =$ [redacted], $\delta_{fl} =$ [redacted] Geometry changes: $z_w/D_{fus} = 0.4, K_i = 1.4$ $(C_{L_\alpha})_V$ from [14] used, not Q3D $(C_{L_\alpha})_V$
	$\left(C_{l_\beta}\right)_{T-O}$	Flight conditions: Cruise with $\alpha =$ [redacted], $\delta_{sl} =$ [redacted], $\delta_{fl} =$ [redacted] $(C_{L_\alpha})_V$ from [14] used, not Q3D $(C_{L_\alpha})_V$
	$\left(C_{n_\beta}\right)_{T-O}$	Flight conditions: Cruise with $\alpha =$ [redacted], $\delta_{sl} =$ [redacted], $\delta_{fl} =$ [redacted] $(C_{L_\alpha})_V$ from [14] used, not Q3D $(C_{L_\alpha})_V$

Table I.3: CONFIDENTIAL Flight conditions, geometry changes (compared to baseline configuration as in Table H.3, Table H.4, and Table H.6) and notes for all the stability derivatives of Fokker F-28 Mk1000 used in validation Table 5.6.

	Stability derivative	Flight conditions & geometry changes
Tail-off	$\left(C_{y_\beta}\right)_{T-O}$	Flight conditions: Cruise with $\alpha =$ [redacted], $\delta_{sl} =$ [redacted], $\delta_{fl} =$ [redacted] Geometry changes: $z_w/D_{fus} =$ [redacted], $K_i =$ [redacted] $(C_{L_\alpha})_V$ from [14] used, not Q3D $(C_{L_\alpha})_V$
	$\left(C_{l_\beta}\right)_{T-O}$	Flight conditions: Cruise with $\alpha =$ [redacted], $\delta_{sl} =$ [redacted], $\delta_{fl} =$ [redacted] $(C_{L_\alpha})_V$ from [14] used, not Q3D $(C_{L_\alpha})_V$
	$\left(C_{n_\beta}\right)_{T-O}$	Flight conditions: Cruise with $\alpha =$ [redacted], $\delta_{sl} =$ [redacted], $\delta_{fl} =$ [redacted] $(C_{L_\alpha})_V$ from [14] used, not Q3D $(C_{L_\alpha})_V$
Horizontal tail	$\left(C_{l_\beta}\right)_H$	Flight conditions: Cruise with $\alpha =$ [redacted], $\delta_{sl} =$ [redacted], $\delta_{fl} =$ [redacted] $(C_{L_\alpha})_V$ from [14] used, not Q3D $(C_{L_\alpha})_V$
Vertical tail	$\left(C_{y_\beta}\right)_V$	Flight conditions: Cruise with $\alpha =$ [redacted], $\delta_{sl} =$ [redacted], $\delta_{fl} =$ [redacted] $(C_{L_\alpha})_V$ from [14] used, not Q3D $(C_{L_\alpha})_V$
	$\left(C_{l_\beta}\right)_V$	Flight conditions: Cruise with $\alpha =$ [redacted], $\delta_{sl} =$ [redacted], $\delta_{fl} =$ [redacted] $(C_{L_\alpha})_V$ from [14] used, not Q3D $(C_{L_\alpha})_V$
	$\left(C_{n_\beta}\right)_V$	Flight conditions: Cruise with $\alpha =$ [redacted], $\delta_{sl} =$ [redacted], $\delta_{fl} =$ [redacted] $(C_{L_\alpha})_V$ from [14] used, not Q3D $(C_{L_\alpha})_V$
Sidewash	$\left(\frac{\delta\sigma}{\delta\beta}\right)_{tot}$	Flight conditions: Cruise with $\alpha =$ [redacted], $\delta_{sl} =$ [redacted], $\delta_{fl} =$ [redacted] $(C_{L_\alpha})_V$ from [14] used, not Q3D $(C_{L_\alpha})_V$
	$\left(1+\frac{\delta\sigma}{\delta\beta}\right)\frac{q_V}{q}K_{FV}$ from $\left(C_{y_\beta}\right)_V$	Flight conditions: Cruise with $\alpha =$ [redacted], $\delta_{sl} =$ [redacted], $\delta_{fl} =$ [redacted] $(C_{L_\alpha})_V$ from [14] used, not Q3D $(C_{L_\alpha})_V$
	$\left(1+\frac{\delta\sigma}{\delta\beta}\right)\frac{q_V}{q}K_{FV}$ from $\left(C_{n_\beta}\right)_V$	Flight conditions: Cruise with $\alpha =$ [redacted], $\delta_{sl} =$ [redacted], $\delta_{fl} =$ [redacted] $(C_{L_\alpha})_V$ from [14] used, not Q3D $(C_{L_\alpha})_V$
Rudder	$C_{y_{\delta_R}}$	Flight conditions: Cruise with $\alpha =$ [redacted], $\delta_{sl} =$ [redacted], $\delta_{fl} =$ [redacted] $(C_{L_\alpha})_V$ from [14] used, not Q3D $(C_{L_\alpha})_V$
	$C_{l_{\delta_R}}$	Flight conditions: Cruise with $\alpha =$ [redacted], $\delta_{sl} =$ [redacted], $\delta_{fl} =$ [redacted] $(C_{L_\alpha})_V$ from [14] used, not Q3D $(C_{L_\alpha})_V$
	$C_{n_{\delta_R}}$	Flight conditions: Cruise with $\alpha =$ [redacted], $\delta_{sl} =$ [redacted], $\delta_{fl} =$ [redacted] $(C_{L_\alpha})_V$ from [14] used, not Q3D $(C_{L_\alpha})_V$
Aileron	$C_{y_{\delta_a}}$	Flight conditions: Cruise with $\alpha =$ [redacted], $\delta_{sl} =$ [redacted], $\delta_{fl} =$ [redacted] $(C_{L_\alpha})_V$ from [14] used, not Q3D $(C_{L_\alpha})_V$
	$C_{l_{\delta_a}}$	Flight conditions: Cruise with $\alpha =$ [redacted], $\delta_{sl} =$ [redacted], $\delta_{fl} =$ [redacted] $(C_{L_\alpha})_V$ from [14] used, not Q3D $(C_{L_\alpha})_V$ Wind tunnel value from graph flight speed against C_l due to δ_a from [17] estimated in linear range between $0 \leq \delta_a \leq 10$ between wind tunnel and flight test data
	$C_{n_{\delta_a}}$	Flight conditions: Cruise with $\alpha =$ [redacted], $\delta_{sl} =$ [redacted], $\delta_{fl} =$ [redacted] $(C_{L_\alpha})_V$ from [14] used, not Q3D $(C_{L_\alpha})_V$

J

Sensitivity analysis: additional figures

J.1. Sweep variation

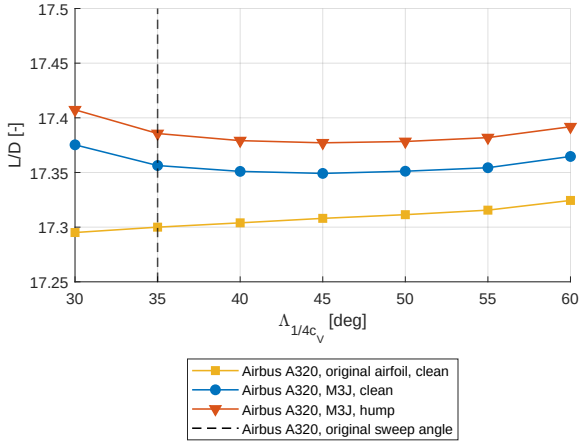

Figure J.1: Airbus A320, $\frac{L}{D}$ vs. sweep

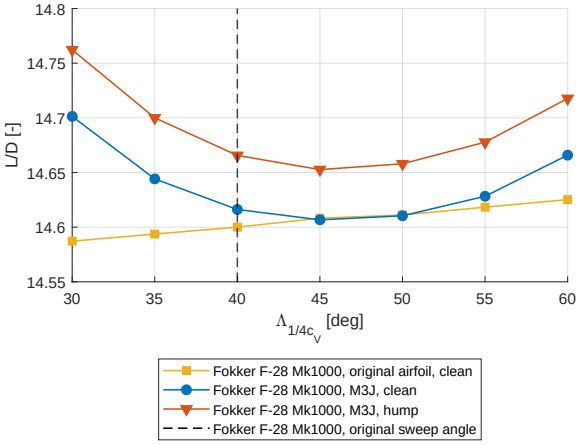

Figure J.2: Fokker F-28 Mk1000, $\frac{L}{D}$ vs. sweep

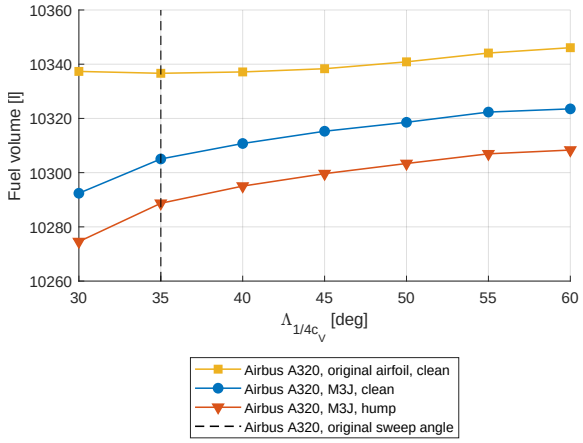

Figure J.3: Airbus A320, Fuel volume vs. sweep

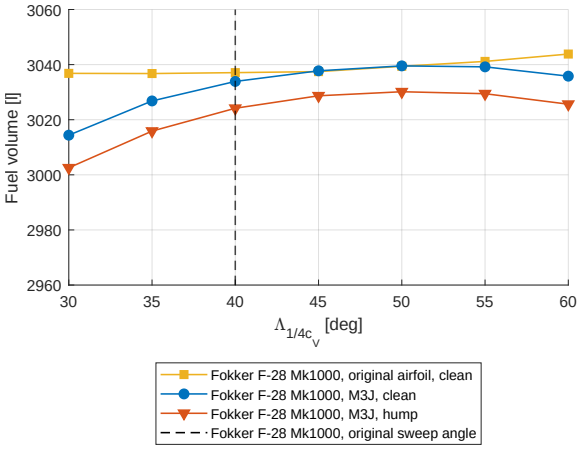

Figure J.4: Fokker F-28 Mk1000, Fuel volume vs. sweep

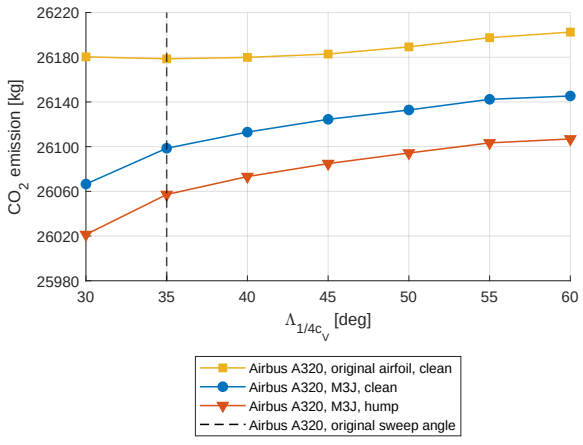

Figure J.5: Airbus A320, CO_2 emission vs. sweep

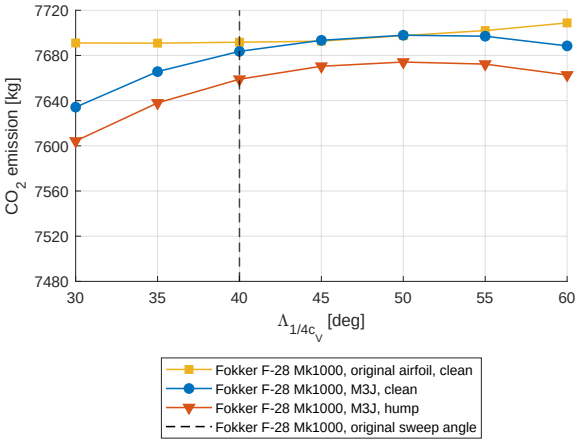

Figure J.6: Fokker F-28 Mk1000, CO_2 emission vs. sweep

J.2. Surface variation

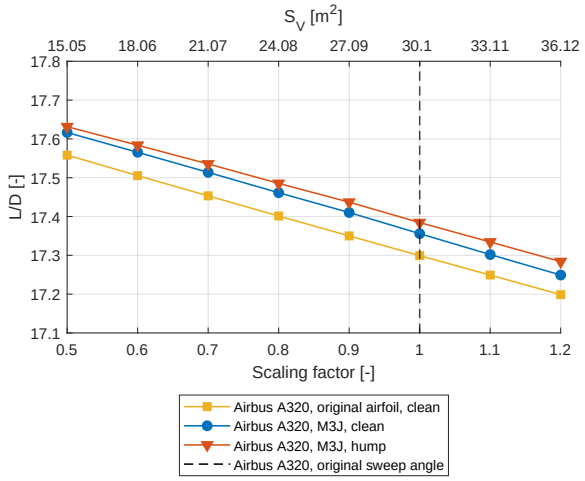

Figure J.7: Airbus A320, $\frac{L}{D}$ vs. surface area

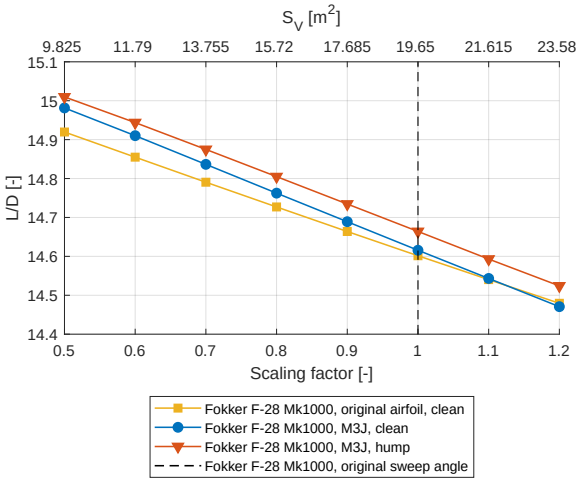

Figure J.8: Fokker F-28 Mk1000, $\frac{L}{D}$ vs. surface area

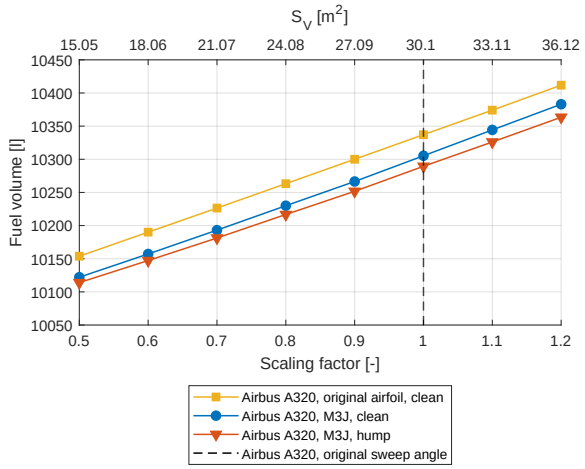

Figure J.9: Airbus A320, Fuel volume vs. surface area

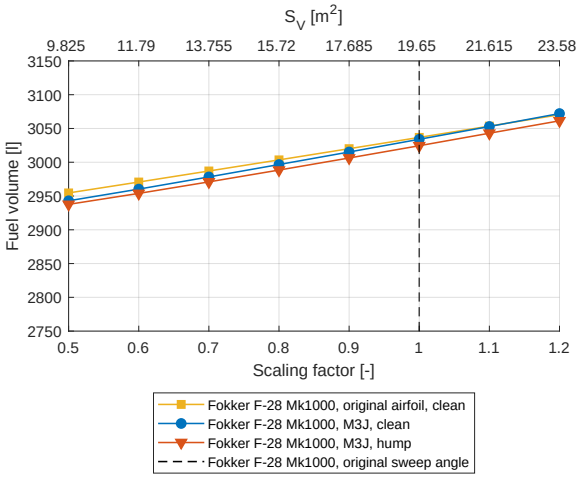

Figure J.10: Fokker F-28 Mk1000, Fuel volume vs. surface area

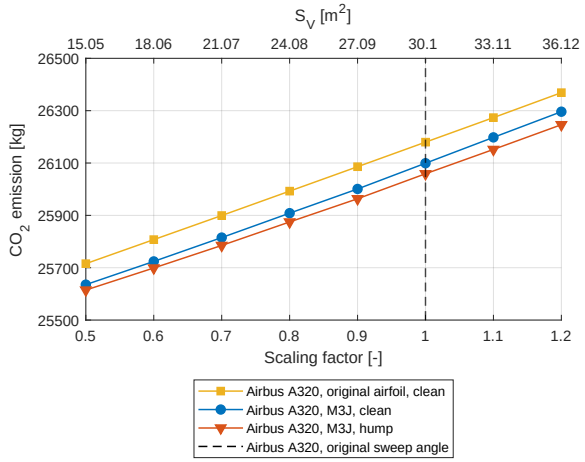

Figure J.11: Airbus A320, CO_2 emission vs. surface area

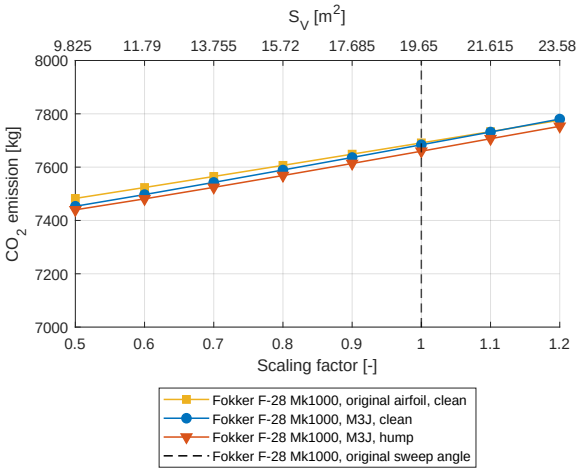

Figure J.12: Fokker F-28 Mk1000, CO_2 emission vs. surface area